OUKA
The University of Osaka
Institutional Knowledge Archive

| | |
|---|---|
| Title | Development of highly-efficient slurryless ultrasonic vibration assisted electrochemical mechanical polishing for silicon carbide wafers |
| Author(s) | 楊, 暁喆 |
| Citation | 大阪大学, 2022, 博士論文 |
| Version Type | VoR |
| URL | https://doi.org/10.18910/87734 |
| rights | |
| Note | |

*The University of Osaka Institutional Knowledge Archive : OUKA*

https://ir.library.osaka-u.ac.jp/

The University of Osaka

Doctoral Dissertation

# Development of highly-efficient slurryless ultrasonic vibration assisted electrochemical mechanical polishing for silicon carbide wafers

Xiaozhe Yang

July 2021

Graduate School of Engineering,
Osaka University

# Table of Contents

Page

**Chapter 1 Background** ..... **1**

1.1 Introduction ..... 1

1.2 The third-generation semiconductor material SiC ..... 2

1.2.1 A brief history of SiC ..... 2

1.2.2 Structure of SiC ..... 3

1.2.3 Advantages of SiC ..... 4

1.2.4 Requirements for SiC substrates in electronic applications ..... 7

1.3 Motivation of this study ..... 8

1.4 Thesis organization ..... 9

References ..... 9

**Chapter 2 Proposal of slurryless ultrasonic vibration assisted electrochemical mechanical polishing** ..... **12**

2.1 Introduction ..... 12

2.2 Current SiC wafer manufacturing process ..... 12

2.2.1 Slicing ..... 13

2.2.2 Grinding ..... 14

2.2.3 Lapping ..... 14

2.2.4 Rough polishing ..... 15

2.3 Current fine polishing techniques for SiC wafers ..... 16

2.3.1 Chemical mechanical polishing (CMP) ..... 16

2.3.2 Plasma-assisted polishing (PAP) ..... 18

2.3.3 Tribochemical polishing (TCP) ..... 19

2.3.4 Catalyst-referred etching (CARE) ..... 20

2.3.5 Ultraviolet-assisted polishing ..... 21

2.4 Electrochemical machining ..... 23

2.4.1 Electrochemical polishing ..... 23

2.4.2 Electrochemical mechanical polishing ..... 25

2.5 Sonochemistry ..... 27

2.6 Ultrasonic vibration assisted machining ..... 29

2.6.1 Ultrasonic machining (USM) ..... 30

2.6.2 Rotation ultrasonic machining (RUM) ..... 31

2.6.3 Ultrasonic vibration assisted CMP ..... 32
2.7 Proposal of slurryless ultrasonic assisted ultrasonic assisted electrochemical mechanical polishing (UAECMP) ..... 33
2.8 Summary ..... 36
References ..... 37

**Chapter 3 Anodic oxidation mechanism of 4H-SiC (0001) ..... 41**
3.1 Introduction ..... 41
3.2 Anodic oxidation and ECMP setup ..... 41
3.2.1 Anodic oxidation setup ..... 41
3.2.2 ECMP setup ..... 42
3.3 Effects of electrolyte type and concentration ..... 43
3.4 Charge utilization efficiency in the anodic oxidation of SiC ..... 51
3.4.1 Relationship between current density and charge utilization efficiency ..... 51
3.4.2 Modeling of the anodic oxidation system of SiC ..... 53
3.4.3 The role of $Cl^-$ and $Na^+$ in SiC anodic oxidation ..... 62
3.5 Summary ..... 63
References ..... 65

**Chapter 4 Dominant factors and their action mechanisms on MRR in the ECMP of the 4H-SiC (0001) surface ..... 66**
4.1 Introduction ..... 66
4.2 Temperature-controllable anodic oxidation setup ..... 67
4.3 Temperature-controllable slurryless ECMP setup ..... 68
4.4 Effects of electrolyte temperature ..... 69
4.4.1 Effects of electrolyte temperature on the anodic oxidation of SiC ..... 69
4.4.2 Effects of electrolyte temperature on the ECMP of SiC ..... 71
4.5 Effects of doping concentration and damage on the anodic oxidation of SiC ..... 75
4.6 Effects of strain ..... 79
4.6.1 Effects of strain on the anodic oxidation of SiC ..... 79
4.6.2 Effect of strain on the ECMP of SiC ..... 82
4.6.3 Action mechanism of strain in the anodic oxidation of SiC ..... 88
4.7 Summary ..... 93
References ..... 95

**Chapter 5 Ultrasonic vibration assisted anodic oxidation of the 4H-SiC (0001) surface ..... 97**

5.1 Introduction ..... 97
5.2 Application of ultrasonic vibration to the electrolyte during anodic oxidation of the 4H-SiC (0001) surface ..... 97
5.2.1 Anodic oxidation setup ..... 97
5.2.2 Effects of ultrasonic vibration in electrolyte on the anodic oxidation rate of the SiC surface ..... 98
5.2.3 Effects of ultrasonic vibration in electrolyte on the anodic oxidation state of the SiC surface ..... 100
5.2.4 Discussion of the promotional mechanism of SiC anodic oxidation when applying ultrasonic vibration to the electrolyte ..... 103
5.2.5 Investigation of the promotional mechanism of ultrasonic vibration by electrochemical impedance spectroscopy (EIS) ..... 105
5.3 Application of ultrasonic vibration to SiC wafer during anodic oxidation ..... 109
5.3.1 Introduction ..... 109
5.3.2 Anodic oxidation setup ..... 110
5.3.3 Effects of ultrasonic vibration on the anodic oxidation of the SiC surface ..... 111
5.4 Summary ..... 114
References ..... 115

**Chapter 6 Application of slurryless UAECMP to SiC wafers ..... 116**
6.1 Introduction ..... 116
6.2 Development of a slurryless UAECMP machine ..... 116
6.2.1 Outline of the slurryless UAECMP machine ..... 116
6.2.2 Structure of the slurryless UAECMP machine ..... 117
6.3 Slurryless UAECMP of 4H-SiC wafers ..... 120
6.3.1 Experimental parameters ..... 120
6.3.2 Characterization methods ..... 121
6.3.3 Effect of ultrasonic vibration on MRR ..... 122
6.3.4 Effect of ultrasonic vibration on SiC surface topography ..... 125
6.3.5 Effects of vibration amplitude on MRR and SiC surface topography ..... 127
6.4 Promotional mechanism of ultrasonic vibration on MRR ..... 129
6.4.1 Temperature increase in UAECMP ..... 129
6.4.2 Effects of ultrasonic vibration on the removal of oxide layer ..... 133
6.4.3 Impacts between abrasives and SiC surface in UAECMP ..... 134
6.4.4 Modeling of the UAECMP process ..... 139
6.5 Summary ..... 141

References ..... 142

**Chapter 7 Summary** ..... **144**

**Acknowledgments** ..... **152**

# Chapter 1
# Background

## 1.1 Introduction

Science is a revolutionary power that promotes the progress of human civilization and is also the cornerstone and driving force for future sustainable development of mankind. From a historical perspective, scientific progress has continuously created new products, lifestyles, and developmental concepts that have promoted human civilization to newer and higher levels. Especially since the mid-18th century, scientific discoveries have led to technological revolutions, which in turn have led to industrial revolutions and social changes, promoting human society to enter the “steam age”, “electric age”, and “information age”. With the development of biotechnology, internet, and artificial intelligence, human society has entered into its fourth industrial revolution. The speed of technological development, as well as the depth and breadth of its impact on human society, are far beyond the previous three industrial revolutions. In this revolution, electronic devices play an important role in information processing and transformation.

The core of power electronics technology is power devices based on semiconductor materials. At present, the vast majority of core electrical power devices are based on silicon (Si) materials. After entering the 21st century, the field of human exploration has expanded greatly; from seas, with depths of tens of thousands of meters, to the universe, hundreds of millions of light-years away, and from nuclear reactions of hundreds of millions of degrees to the extreme ice-cold temperatures of Antarctica. These harsh environments have put forward higher requirements for electronic devices. At the same time, energy conservation and emission reduction have become an important theme of social development. The expectations of society for effective energy conversion have gradually increased, which also puts forward higher requirements for power electronics technologies, especially for the performance of power semiconductor devices. However, after decades of rapid development, traditional Si-based power devices have approached their performance limits, making it difficult to meet the growing demand for electronic device applications. At present, power devices based on third-generation semiconductors, which includes wide-bandgap semiconductors such as silicon carbide (SiC) and gallium nitride (GaN), have become the strategic direction of next-generation technologies in this field. SiC is currently the most mature third-generation wide-bandgap semiconductor material. SiC power devices are expected to trigger a new technological revolution in the field of power

electronics in the next few decades and promote the development of power electronics technology in the direction of more efficient use of electrical energy and miniaturization of equipment.

In applications of SiC in electronic devices, quality and accuracy of the SiC surface directly affect the quality of the subsequent epitaxial film and the performance of the electronic devices. Therefore, in order to meet application requirements, the SiC wafer surface is required to be ultra-smooth (surface roughness below the sub-nanometer level) and damage-free. However, due to the high hardness and chemical stability of SiC single-crystal material, SiC single-crystal polishing is extremely difficult. Currently, chemical mechanical polishing (CMP) has been widely used in ultra-precision polishing of SiC, but its efficiency is low and its cost is high [1,2]. Therefore, the efficient production of SiC wafers with ultra-smooth and damage-free surfaces has important scientific significance and prospective market applications.

## 1.2 The third-generation semiconductor material SiC

### 1.2.1 A brief history of SiC

SiC has a long history; it is a type of carbide that was accidentally discovered by Acheson during the electrofusion of diamond in 1891. In 1893, Acheson developed a method for industrial smelting of silicon carbide, which is known as the Acheson furnace. However, owing to the poor crystallinity and small size of the generated SiC, it was used only in polishing and cutting fields at that time [3]. In the 1950s, more and more of the excellent properties of SiC were being discovered, especially its excellent electrical and thermal properties, which led to it being widely studied as a promising material for electronic devices. However, it was difficult to grow large high-quality SiC crystals, which hindered the development of SiC applications [4]. In 1955, Lely grew bulk SiC crystals by heating SiC powder to 2500 °C and recrystallizing in a low-temperature area. This is known as the Lely method, which laid the foundation for SiC development. However, only ~10-$mm^2$ crystals were obtained by this method and it was difficult to control their polymorphism [5]. In 1978, the invention of physical vapor transport (PVT), namely, the modified Lely mothed, opened the door to the production of large SiC wafers [6]. In this method, SiC powder is placed in the bottom of a closed graphite crucible and then heated to 2300 °C under air atmosphere. The sublimated Si and C gas recrystallize on the seed SiC crystal surface owing to the temperature gradient. This method improved the gas transport stability and nucleation process during the SiC crystallization process. The PVT method has been commercialized and is almost exclusively used to manufacture SiC wafers today. Currently, SiC wafers are fabricated in 76-mm (3 inch)- and 100-mm (4 inch)-diameter substrates. Since 2012, 152-mm (6 inch)-diameter substrates have been on the market [7,8]. Recently, the enlargement of SiC crystal size and decrease in the manufacturing cost has become a hot research topic.

### 1.2.2 Structure of SiC

SiC is a wide-gap semiconductor material of group IV-IV binary compound and the only solid compound in group IV of the periodic table. All SiC crystals are composed of exactly the same layers, which are perpendicular to the *c* axis. However, due to the different stacking sequence of the same layer, each structure has its own repetition period in the *c* axial direction. The most basic structural unit of SiC polymorphs is the Si-C or C-Si tetrahedron. Namely, in a SiC polymorphism the basic structural unit includes a tetrahedron formed by four Si atoms surrounding a C atom and a Si atom also surrounded by a tetrahedron formed by four C atoms, as shown in Fig. 1.1(a). The distance ratio from the C plane to the upper and lower Si planes is 1:3 and the distance ratio from each Si plane to the adjacent C plane is also 1:3. The tetrahedron is connected by covalent bonds (88% covalent bonds and 12% ionic bonds). The distance between Si-Si or C-C atoms is about 3.08 Å while the length of the Si-C bond is about 1.89 Å. The SiC crystal is formed by connecting these tetrahedrons to each other at the corners. The difference between cubic and hexagonal structures of SiC variants is formally due to the different docking of tetrahedrons. A SiC tetrahedron projection picture, which is obtained by expanding the upper and lower Si planes of the tetrahedron and the middle C plane along space, then projecting the structure, is shown in Fig. 1.1(b). In this figure, the positions of the Si plane atoms in the second layer and the C atoms in the C plane of the first layer overlap in the projection direction [9].

There are more than 250 kinds of SiC polytypes with different stacking orders of the C/Si diatomic layer [10,11]. In single-crystal SiC, the Si atomic layer and the C atomic layer constitute the basic diatomic layer. Si-C diatomic layers are alternately stacked in a certain sequence to form SiC crystals and the difference in the stacking sequence of the diatomic layers will lead to different crystal structures, such as sphalerite, wurtzite, and rhombus structures. There are three different stacking positions of the C-Si diatomic layer on the close packed surface, designated layers A, B, and C. Commonly, SiC materials include 3C-SiC with cubic sphalerite structure and 4H-SiC and 6H-SiC with hexagonal wurtzite structure. These crystal structures are shown in Fig.

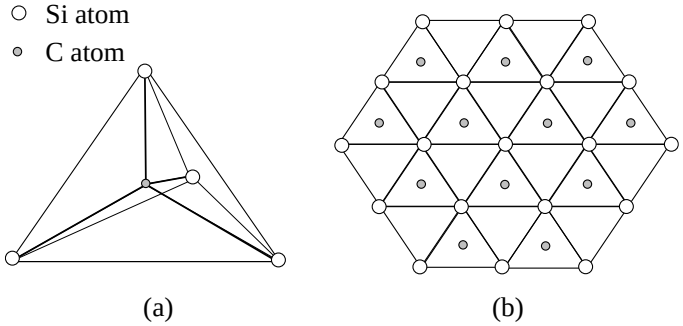



**Fig. 1.1** (a) SiC tetrahedron and (b) projection of the tetrahedral layer.

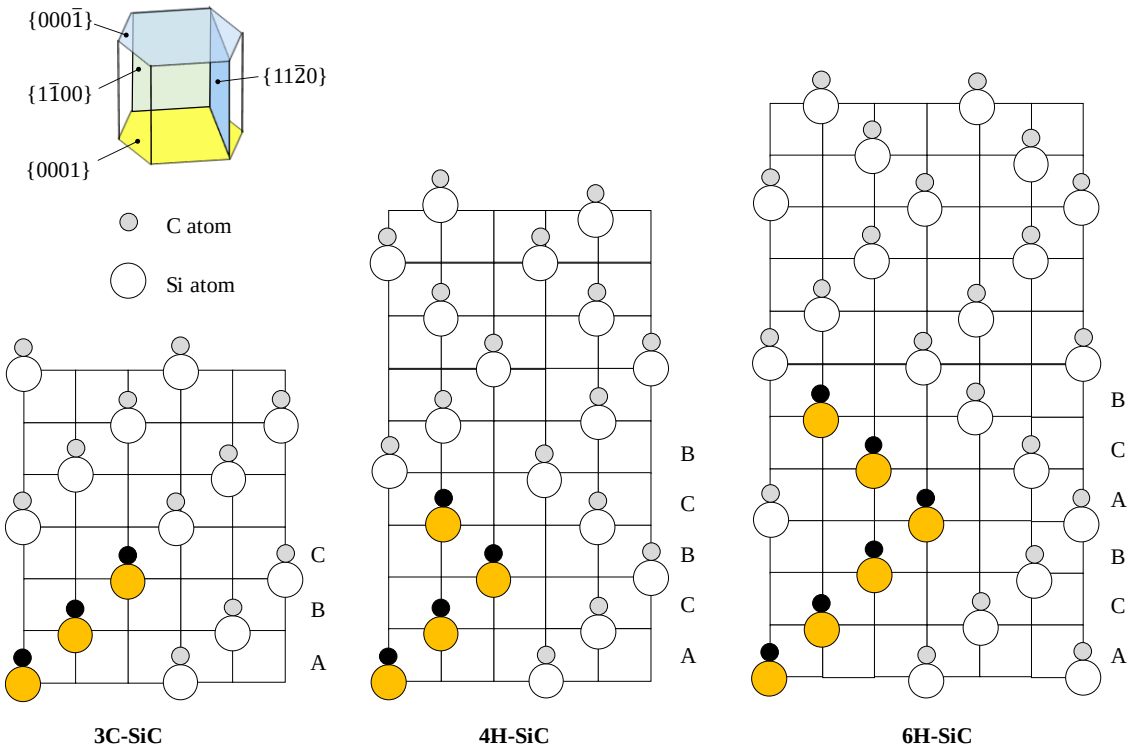



**Fig. 1.2** Crystal structure of 3C-, 4H-, and 6H-SiC.

1.2, the stacking sequence of 3C-SiC is ABCABC……; the stacking sequence of 4H-SiC is ABCBABCB……; and the stacking sequence of 6H-SiC is ABCACBABCACB……[12,13].

### 1.2.3 Advantages of SiC

The most common polytypes in SiC are cubic 3C-SiC and hexagonal 4H- and 6H-SiC [14]. 3C-SiC is the only SiC polytype with a sphalerite structure and it has excellent physical and electrical properties, such as a high melting point, high thermal conductivity, high critical breakdown electric field, and high saturation drift speed. Its electron mobility is the highest of all SiC polytypes and its high thermal conductivity and high critical breakdown electric field allow high device density. Thus, 3C-SiC is a promising material for high-temperature, high-frequency, and high-power devices. 6H-SiC has a wide bandgap and can be applied in optoelectronics, high-temperature electronics, anti-radiation electronics, and high-frequency high-power devices. High-frequency and high-power 6H-SiC devices can increase the power density of solid-state circuits by at least four orders of magnitude while increasing device operating temperature. In semiconductor applications, 4H- and 6H-SiC are widely used in electronic devices due to the maturity and good repeatability of the single-crystal growth process. Among them, 4H-SiC has a wider bandgap than 6H-SiC and its electron mobility is close to that of 3C-SiC, which makes it the most widely used in electronic devices. With the breakthrough in growth technology of high-

quality 4H-SiC single-crystal material, it is considered to be the most promising material for high-power electronic devices.

Table 1.1 shows the basic physical and electrical properties of typical first-generation semiconductor Si, second-generation semiconductor GaAs, and SiC. Compared with the traditional semiconductor materials Si and GaAs, SiC materials have the following characteristics and advantages.

(1) The bandgap determines many performance traits of an electronic device, including spectral response characteristics, radiation resistance, and operating temperature. Compared with Si and GaAs, SiC has a larger bandgap. Thus, unipolar metal-oxide-semiconductor field-effect transistors (MOSFETs) and Schottky barrier diodes (SBDs) can be realized using SiC. As a result, switching loss can be reduced compared to Si bipolar devices. Since a SiC device is a unipolar device, the overshoot and tail currents that exist during switching of Si devices do not exist in the switching of SiC devices; there is no loss caused by overshoot and tail currents and low-loss switching is possible with SiC [15,16]. This property also allows SiC transistors to be turned on or off in nanoseconds and to be applied under high-frequency conditions [17,18]. Additionally, a detector made of SiC has good ultraviolet spectral response characteristics but does not respond to infrared radiation; it has good radiation resistance and can be used to detect weak ultraviolet signal under infrared background signal. Furthermore, dark current of SiC detector is very low and its working temperature is high, so it can also be used to detect ultraviolet signals in high temperature environments [19,20]. Moreover, the increase in leakage current is very small, even at high temperature, owing to the wide

**Table 1.1** Comparison of properties of Si, GaAs, and SiC [21-23].

| | Si | GaAs | SiC | | |
|---|---|---|---|---|---|
| | | | 3C-SiC | 4H-SiC | 6H-SiC |
| Bandgap (eV) | 1.2 | 1.4 | 2.2 | 3.26 | 3.02 |
| Transition type | Indirect | Direct | Indirect | Indirect | Indirect |
| Electron mobility ($cm^2/Vs$) | 1350 | 8500 | 1000 | 947 | 380 |
| Horn mobility ($cm^2/Vs$) | 600 | 400 | 100 | 120 | 100 |
| Breakdown field (MV/cm) | 0.3 | 0.4 | 3 | 3.5 | 3 |
| Saturation velocity (cm/s) | $1 \times 10^7$ | $2.7 \times 10^7$ | $2.5 \times 10^7$ | $2.7 \times 10^7$ | $2 \times 10^7$ |
| Thermal conductivity (W/cm·K) | 1.5 | 0.55 | 4.9 | 5 | 5 |
| Young's modulus (GPa) | 160 | | 85.5 | 441–500 | |
| Density ($10^3$ $kg/m^3$) | 2.3 | 5.32 | 3.2 | 3.2 | 3.2 |
| Melting point (°C) | 1420 | 1240 | 2830 | 2830 | 2830 |
| Dielectric constant | 11.7 | 12.9 | 9.72 | 9.66 | 9.72 |

bandgap of SiC. Therefore, stable high-temperature operation can be realized. The maximum operation temperature of SiC devices, in theory, is very high (> 700 °C) and is much higher than that of Si devices. Small-signal MOSFETs from SiC have shown to be functional at 650 °C and an integrated operational amplifier working at 300 °C was presented based on negative-channel metal oxide semiconductor (NMOS) devices [24].

(2) The breakdown electric field of SiC is much larger than that of Si and GaAs. This means that devices made of SiC materials can withstand large applied voltages and have excellent high voltage resistance characteristics. Because of its high breakdown voltage, SiC is an ideal semiconductor material for high-power microwave devices with a frequency in the range of 1–100 GHz [25-27]. The higher electron saturation drift speed of SiC also determines its application potential in the preparation of high-frequency devices. With the continuous improvement of lattice integrity and the gradual reduction of material prices, SiC materials will continue to receive increased attention for the research and preparation of microwave devices.

(3) SiC has good thermal stability. It is impossible to melt under normal pressure and it sublimates and decomposes to carbon and silicon-containing vapor at high temperature; the remaining graphite exists in the form of the original crystal. The excellent thermal stability guarantees its high reliability when working at high temperatures. Thermal conductivity is one of the thermophysical properties of materials that determines the rate of energy transfer in the thermal diffusion process. SiC has a high thermal conductivity, it is three times higher than Si and nine times higher than GaAs [28,29]. The heat generated by a SiC device can be quickly dissipated, which is very important for the design of high-power high-density devices. In order to maintain the normal operating temperature of a device, a large cooling device is usually required for spaceborne devices. By applying SiC, these devices can be made smaller due to its higher power density and stability at high temperatures, which saves on huge auxiliary cooling facilities and is very beneficial for reducing the launch weight of a vehicle. In addition, the thermal conductivity of SiC materials at room temperature is the same as that of many metals. Therefore, SiC is suitable for high-temperature and high-power devices and circuits.

(4) The dielectric constant is a measure of the capacitive load of an electronic device. If the dielectric constant is low, the impedance of the device is small. From another point of view, for the same limit in device impedance, a material with a small dielectric constant uses a larger device area, which allows the development of higher radio frequency (RF) power levels. The dielectric constant of SiC is smaller than that of Si and GaAs. With the same performance, the size of a SiC monolithic circuit can be much smaller than that of Si-based devices [30].

(5) SiC is the only compound semiconductor that can form high-quality primary oxide $SiO_2$ through thermal oxidation. This is very useful for making MOSFETs, insulated gate bipolar transistors (IGBTs), and MOS controlled thyristors (MCTs) [31].

(6) SiC has a high hardness and can be used as an abrasive. Its Mohs hardness is 9.2–9.3, which is between that of diamond and topaz [32].

(7) A SiC substrate, compared to standard sapphire substrates, effectively decreases lattice mismatch between the substrate material and GaN, reducing defects and dislocations generated during the growth of GaN epitaxial films. The electrical-optical conversion efficiency of SiC fundamentally improves light emission and heat dissipation problems in semiconductor lighting. In addition, SiC materials have the characteristics of blue light-emitting materials. High-brightness blue light-emitting diodes (LEDs) can be made by utilizing the large bandgap of SiC to realize full-color large-area LED displays. The excellent performance of SiC allows it to occupy a new strategic high ground for the high-brightness LED industry, breaking the dominance of sapphire substrates in this field [33].

(8) SiC has excellent properties in terms of pressure sensitivity and piezoelectricity, which allows it to provide the possibility of pressure sensor miniaturization [34].

In short, SiC has a wide bandgap, high critical breakdown electric field, high thermal conductivity, and high carrier saturation drift velocity. It has huge application potential in high-temperature, high-frequency, high-power, and high-radiation conditions, and it is also a promising material for optoelectronics. Many countries have successively invested a large amount of funds to conduct extensive and in-depth research on SiC, making breakthroughs in crystal growth technology, key device technology, development of optoelectronic devices, integrated circuit manufacturing, etc. The application of SiC in various fields will become more and more extensive.

### 1.2.4 Requirements for SiC substrates in electronic applications

Although single crystal SiC has excellent material properties, if the surface quality is inadequate, its excellent performance as a next-generation semiconductor material will not be achieved and it could completely lose its advantageous material functions. Almost all fields of application have strict requirements on the surface quality of single crystal SiC. For example, surfaces of single-crystal SiC substrate material for high-brightness LEDs must be very smooth and reach atomic level surface roughness, without any defects or subsurface damage (SSD). This is because any SSD may cause a large number of dislocations and defects in the subsequent GaN epitaxial layer grown on the SiC surface, which will result in difficulties for subsequent device processing technology [34]. In the application of integrated circuit (IC) semiconductor devices, such as MOSFETs, IGBTs, etc., the epitaxial growth of an insulating oxide film is a key process. The quality of the insulating oxide film, which is severely affected by the SiC surface quality,

dominates the performance of the produced devices. Thus, the SiC surface is required to be ultra-smooth, defect-free, damage-free, and the surface roughness is required to reach $Ra \leq 0.3$ nm [35-37]. When single-crystal SiC is used as the substrate for large-scale ICs, the subsequent treatment process requires extremely high surface accuracy, low surface roughness, and an enlarged thermal contact area between the electronic component and its heat sink, which is beneficial to improve the heat dissipation efficiency [38]. Additionally, SiC-based microwave power devices are the core of detectors and their surface quality plays an important role in detection accuracy. In summary, if the surface quality of SiC is poor, it will be difficult for its excellent material properties to contribute to its performance.

Although, the growth technology of single-crystal SiC has gradually matured, SiC wafers are currently obtained by wire saw slicing of a SiC ingot. The as-sliced SiC surface is very rough, with a large number of wire saw slicing marks and surface damage. These wafers could not be used directly without processing. Therefore, the subsequent grinding and polishing processing technologies for single-crystal SiC occupy an increasingly important position in the device manufacturing process.

## 1.3 Motivation of this study

As mentioned in the previous sections, obtaining damage-free and atomically smooth surfaces is significantly important for difficult-to-machine next-generation semiconductor materials. Currently, existing manufacturing processes have several disadvantages, such as complicated processes, expensive equipment, expensive consumables, large manpower requirements, low efficiency, and environmental issues. The motivation of this study is to develop an environmentally friendly, low-cost, and high-efficiency ultra-precision processing technique for difficult-to-machine semiconductor materials.

In this study, a novel polishing technique called slurryless ultrasonic vibration-assisted electrochemical mechanical polishing (UAECMP) is proposed and developed. Surface modification of difficult-to-machine materials by ultrasonic vibration-assisted anodic oxidation and the removal of this modified layer by ultrasonic vibration-assisted fixed-soft-abrasive polishing are effectively combined in UAECMP. The three aims of this study are listed below.

1. To propose slurryless UAECMP and to test and verify its applicability by performing fundamental experiments.
2. To investigate the promotion mechanism of the material removal rate (MRR) of ultrasonic vibration in ECMP.
3. To develop a slurryless UAECMP machine for polishing SiC wafers and optimize the polishing process to obtain the highest MRR and lowest surface roughness.

## 1.4 Thesis organization

This thesis consists of seven chapters.

This chapter (Chapter 1), the background of this study, includes the properties and applications of the SiC substrates polished in this study, and the aims of this study are described.

In Chapter 2, slurryless UAECMP is proposed. The current manufacturing processes and existing ultra-precision polishing techniques for SiC wafers, as well as the development of electrochemical-assisted machining and ultrasonic vibration-assisted machining, are introduced. Slurryless UAECMP is proposed based on the advantages of electrochemical-assisted machining and ultrasonic vibration-assisted machining as a means of resolving problems facing conventional polishing techniques.

In Chapter 3, the effects of electrolyte type, electrolyte concentration, and electric current density on the anodic oxidation of SiC, as well as the accompanying action mechanism, are investigated. On the basis of the obtained results, an anodic oxidation system of SiC in NaCl aqueous solution is modeled and the anodic oxidation mechanism of SiC is clarified.

In Chapter 4, dominant material and processing factors, including temperature, doping concentration, damage, and strain, and their action mechanisms in the anodic oxidation and ECMP processes of the 4H-SiC (0001) surface are experimentally and theoretically investigated.

In Chapter 5, ultrasonic vibration-assisted anodic oxidation setups are developed and the effects of ultrasonic vibration on the anodic oxidation of the 4H-SiC (0001) surface, including the anodic oxidation rate, oxide layer structure, oxidation uniformity, etc., are investigated. Moreover, the difference between applying ultrasonic vibration to the electrolyte and to the SiC wafer is compared and discussed.

In Chapter 6, the developed slurryless UAECMP machine is introduced and slurryless UAECMP of 4H-SiC wafers is performed using the developed UAECMP machine. Moreover, a theoretical analysis of the slurryless UAECMP process is performed to evaluate its performance and clarify underlying processing mechanisms.

In Chapter 7, the thesis is summarized.

# References

1) J. H. An, G. S. Lee, W. J. Lee, B. C. Shin, J. D. Seo, K. R. Ku, H. D. Seo, H. D. Jeong, Mater. Sci. Forum 600 (2009) 831–834.

2) C. L. Lai, S. H. Lin, Chem. Eng. J. 95(1–3) (2003) 205–211.

3) Y. M. Tairov, V. F. Tsvetkov, J. Cryst. Growth 52 (1981)146–150.

4) D. Nakamura, I. Gunjishima, S. Yamaguchi, T. Ito, A. Okamoto, H. Kondo, K. Takatori, Nature 430(7003) (2004) 1009–1012.
5) J. A. Lely, Ber. Dtsch. Keram. Ges. 32 (1955) 229.
6) Y. M. Tairov, V. F. Tsvetkov. J. Cryst. Growth 43.2 (1978) 209–212.
7) N. Schulze, J. Gajowski, K. Semmelroth, M. Laube, G. Pensl, Mater. Sci. Forum 353 (2001) 45–48.
8) M. Ogawa, K. Mine, S. Fuchiyama, Y. Tawa, T. Kato, Mater. Sci. Forum 778–780 (2014) 776–779.
9) T. Kimoto, J. A. Cooper, Fundamentals of silicon carbide technology: growth, characterization, devices and applications. John Wiley & Sons, 2014.
10) N. W. Jepps, T. F. Page, Prog. Cryst. Growth Charact. 7 (1983) 259–307.
11) P. T. B. Shaffer, Acta Cryst. B. 25(3) (1969) 477–488.
12) W. J. Schaffer, G. H. Negley, K. G. Irvine, J. W. Palmour, MRS Online Proceedings Library Archive. 339 (1994) 595–600.
13) W. J. Choyke, Mater. Res. Bull. 4 (1969) 141–152.
14) C. H. Park, B. H. Cheong, K. H. Lee, K. J. Chang, Phys. Rev. B 49(7) (1994) 4485–4493.
15) A. K. Agarwal, In 2010 International Conference on Power, Control and Embedded Systems, IEEE (2010) 1–4.
16) W. Wondrak, R. Held, E. Niemann, U. Schmid, IEEE Trans. Ind. Electron. 48(2) (2001) 307–308.
17) S. Round, M. Heldwein, J.W. Kolar, I. Hofsajer, and P. Friedrichs, In Conf. Rec. 40th IAS Annu. Meeting – Industry Applications Conf. (2005) 410–416.
18) T. Friedli, S. D. Round, D. Hassler, J. W. Kolar, IEEE Trans. Ind. Applicat. 45(5) (2009) 1868–1878.
19) N. Naderi, M. R. Hashim, J. Alloys Compd. 552 (2013) 356–362.
20) J. Kou, K. Tian, C. Chu, Y. Zhang, X. Zhou, Z. Feng, Z. H. Zhang, Nanoscale Res. Lett. 14 (1) (2019) 1–18.
21) G. L. Harris, Properties of silicon carbide, Let, 13 (1995).
22) M. Bhatnagar, B. J. Baliga, IEEE Trans. Electron Dev. 40 (3) (1993) 645–655.
23) L. Jiang, R. Cheung, Int. J. Nanomanuf. 2(3/4) (2009) 225–240.
24) D. M. Brown, M. Ghezzo, J. Kretchmer, V. Krishnamurthy, G. Michon, G. Gati, Trans. 2nd Int. High-Temperature Elec. Conf. (HiTEC) 1 (1994) XI-17–XI-22.
25) R. C. Clarke, J. W. Palmour, Proc. IEEE 90(6) (2002) 987–992.
26) S. Sriram, R. R. Siergiej, R. C. Clarke, A. K. Agarwal, C. D. Brandt, Phys. Status Solidi. 162(1) (1997) 441–457.
27) C. E. Weitzel, J. W. Palmour, C. H. Carter, K. Moore, K. K. Nordquist, S. Allen, M. Bhatnagar, IEEE Trans Electron Devices 43(10) (1996)1732–1741.
28) R. Wei, S. Song, K. Yang, Y. Cui, Y. Peng, X. Chen, X. Xu, J. Appl. Phys. 113(5) (2013)053503.
29) P. G. Neudeck, SiC Technology, The VLSI Handbook, Florida, 1999.
30) J. W. Palmour, S. T. Sheppard, R. P. Smith, S. T. Allen, W. L. Pribble, T. J. Smith, J. W. Milligan,

In International Electron Devices Meeting. Technical Digest (Cat. No. 01CH37224) (2001) 17–4.

31) A. Agarwal, R. Callanan, M. Das, B. Hull, J. Richmond, S. H. Ryu, J. Palmour, In 2009 13th European Conference on Power Electronics and Applications. (2009) 1–10.
32) G. Guo, Z. Liu, Q. An, M. Chen, Int. J. Adv. Manuf. Technol. 57(1) (2011)135–142.
33) L. Liu, J. H. Edgar, Mater. Sci. Eng. R Rep. 37(3) (2002) 61–127.
34) J. Bi, G. Wei, L. Wang, F. Gao, J. Zheng, B. Tang, W. Yang, J. Mater. Chem. C 1(30) (2013)4514–4517.
35) T. Kato, K. Wada, E. Hozomi, H. Taniguchi, T. Miura, S. I. Nishizawa, K. Arai, Mater. Sci. Forum 556 (2007) 753–756.
36) L. Zhou, V. Audurier, P. Pirouz, J. A. Powell, J. Electrochem. Soc. 144(6) (1997) L161–163.
37) G. Pan, Y. Zhou, G. Luo, X. Shi, C. Zou, H. Gong, J. Mater. Sci. Mater. Electron. 24(12) (2013) 5040–5047.
38) G. Lorenzini, E. X. Barreto, C. C. Beckel, P. S. Schneider, L. A. Isoldi, E. D. Dos Santos, L. A. O. Rocha, Int. J. Heat Mass Transf. 108 (2017)1884–1893.

# Chapter 2
# Proposal of slurryless ultrasonic vibration assisted electrochemical mechanical polishing

## 2.1 Introduction

As described in Chapter 1, third-generation semiconductors, represented by SiC and GaN, have tremendous potential to completely replace Si and GaAs and become the main raw materials for manufacturing electronic components. This could strongly reduce energy consumption and help realize a low-carbon society. However, it is difficult to get scratch-free, subsurface damage (SSD)-free, and atomically smooth surfaces on these materials by traditional machining processes owing to their high hardness, high brittleness, and chemical inertness. Currently, the most widely used manufacturing processes for these wafers are mechanical and chemical processes. In the mechanical process, hard abrasives, such as diamond, are used to rapidly remove the deep SSD and reduce surface roughness to nanometer order. However, small scratches and shallow SSD are inevitably simultaneously introduced to the surface by hard abrasives during this process, which makes it almost impossible to get a damage-free and atomically smooth surface. In the case of chemical processing, SSD and scratches on the surface can be completely modified and dissolved by chemical etching, without introducing any strain, and a surface with good local surface roughness can be obtained. However, it is difficult to control the flatness of the surface using pure chemical etching, which makes the surface undulate and deteriorates the performance of electronic components. Therefore, for these difficult-to-machine semiconductor materials, hybrid process methods that combine the flattening abilities and surface modification abilities of mechanical and chemical processing methods, respectively, are promising to obtain flat, atomically smooth, and damage-free surfaces.

## 2.2 Current SiC wafer manufacturing process

After crystal growth, the SiC crystal is processed into ingots and the ingots are cut into wafers by a slicing machine. Then, the wafers are processed by edge profiling or chamfering. Chamfering of the peripheral edge portion of the wafer reduces the risk of wafer damage in further processing steps. The surface roughness and main shape parameters of the wafer are improved by a grinding

and double-sided lapping process. Finally, the wafers are finished by rough polishing and ultra-precision polishing.

### 2.2.1 Slicing

Slicing is the first step of the wafer manufacturing process that significantly impacts the entire process. Frosch reported that the cost of slicing is 50% of the cost of the entire wafer manufacturing process [1]. Furthermore, slicing a SiC ingot into wafers with small warpage, uniform thickness, and low cut-loss is essential for subsequent grinding and polishing. If the surface roughness is low and the surface damage layer is thin after slicing, the subsequent lapping and polishing processes would take less time and remove less material to obtain a damage-free smooth surface, decreasing the cost of the entire manufacturing process.

In the 1990s, the free-abrasive wire saw, wherein the cutting action mainly relies on abrasives rolling between a wire and the ingot, began to be used to cut silicon wafers [2,3]. Fig. 2.1(a) and (b) show a schematic diagram of a wire saw and the removal mechanism of a free-abrasive wire saw, respectively. Compared with traditional outer and inner diameter cut-off grinding, multi-wire cutting has advantages of higher cutting speed, higher processing accuracy, and longer lifetime; thus it has been widely used for cutting various types of wafers. In recent years, fixed-abrasive wire saw technology has been rapidly developed and has good cutting performance for slicing brittle and hard materials, including sapphire and SiC. Instead of using slurry that includes super-hard abrasives as cutting agents, the cutting tool used in fixed-abrasive wire sawing is a stainless-steel wire with diamond abrasives fixed on its surface using the plating or resin bonding method. The material removal mechanism of this tool is shown in Fig. 2.1(c). Material removal of the fixed-abrasive wire saw mainly relies on two-body wear, which provides several advantages, such as a higher processing efficiency and a smaller cut kerf. In 2014, Chung *et al.* established a model to simulate the distribution of diamond abrasives. They demonstrated that a higher abrasive density decreases the material removal rate (MRR) because the load is shared by the abrasives,

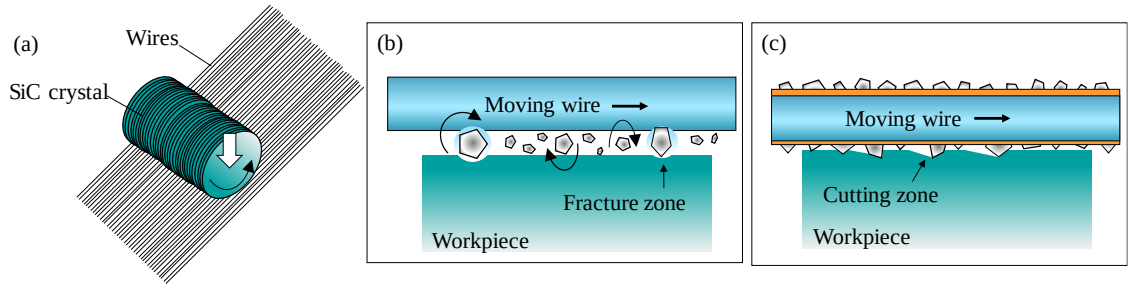



**Fig. 2.1** (a) Schematic diagram of a wire saw. Material removal process of (b) free-abrasive and (c) fixed-abrasive wire saws [6].

which prevents grains from penetrating deeply enough into the ingot to facilitate material removal [4]. Wurzner *et al.* studied the effect of wire speed on the surface damage of sliced wafers. They found that an increase in wire speed can decrease the depth of the damage layer [5].

### 2.2.2 Grinding

The purpose of grinding is to remove saw marks and the damage layer induced on the SiC surface in the slicing process. Due to the high hardness of SiC, high-hardness abrasives (such as boron carbide or diamond powder) have to be used to grind the sliced SiC crystal surface during the grinding process [7]. Grinding can be divided into rough and fine grinding according to the obtained surface roughness. Rough grinding is mainly applied to flat SiC surfaces to obtain wafers with minimum bow, warp, and total thickness variation (TTV). In addition, saw marks and the thick SSD layer induced in slicing are also removed in this step and abrasives with large diameters are used to obtain high processing efficiency. Fine grinding mainly removes the SSD damage layer left by rough grinding, improves the surface roughness, and controls the surface shape and thickness of the wafer to facilitate subsequent processing. Therefore, abrasives with smaller particle diameter are used to grind the wafer in fine grinding. Due to the low fracture toughness of SiC, it can easily crack during the grinding process, which makes SiC wafer grinding very difficult. Effective grinding requires appropriate grinding parameters to obtain the maximum MRR and to control surface integrity. Many researchers have studied a variety of grinding methods to improve the processing efficiency and surface quality of brittle materials. Studied methods include high-speed/ultra-high-speed grinding, ultrasonic vibration assisted grinding, and electrolytic in-process dressing grinding (ELID grinding) [8-10]. Churi *et al*. studied ultrasonic vibration assisted grinding of SiC and their results showed that ultrasonic vibration not only reduced the grinding force, but also improved the surface quality [8]. Lee *et al*. applied ELID grinding and chemical mechanical polishing (CMP) processes to SiC, sapphire, and GaN wafers. By using ELID grinding, the processing time was greatly reduced and a better surface quality was obtained [9]. These ultra-precision grinding methods can replace traditional rough and fine grinding to a large extent. However, mechanical damage, the residual stress layer, and large surface roughness induced during the grinding process require further elimination by the subsequent polishing process. Improving the shape accuracy and surface quality of the wafer also plays an important role in the performance of subsequently fabricated devices [10].

### 2.2.3 Lapping

Lapping is an important process in SiC wafer manufacturing, which mainly adopts the double-sided lapping method [11]. This process has the following effects: (1) makes the processing-induced damage on the wafer surface consistent; (2) adjusts the geometric thickness of the wafer to reduce

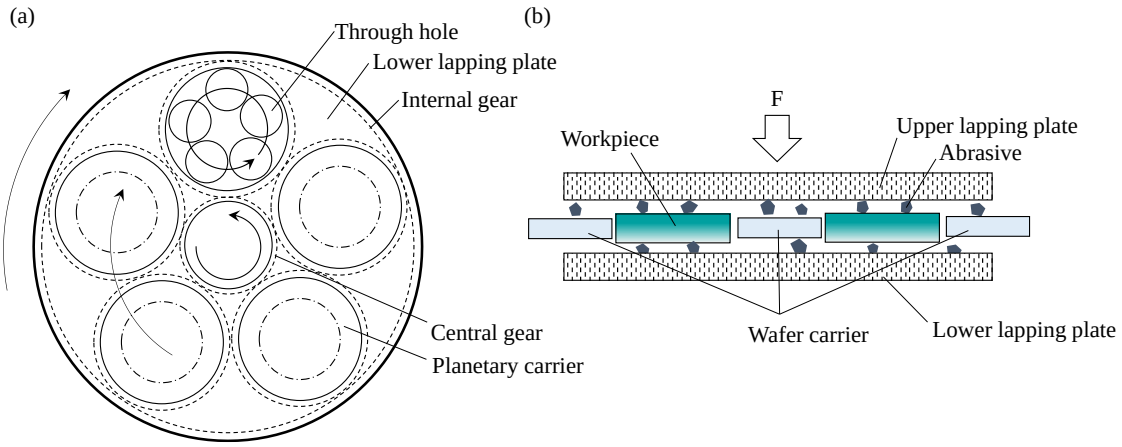



**Fig. 2.2** Schematic diagram of double-sided lapping [11].

the thickness difference between wafers; (3) further adjusts bow, warp, and TTV of wafers. A schematic diagram of the double-sided lapping process is shown in Fig. 2.2. The double-sided lapping process uses a double-sided grinding disc to simultaneously process the upper and lower surfaces of a single-crystal SiC wafer. During the lapping process, hard and loose abrasives are injected between relatively soft grinding discs with the rotation of the grinding disc, relative sliding occurs between the wafer and the grinding disc. Under a certain pressure, the wafer is processed by rolling and micro-cutting of the loose abrasives. Due to the action of the abrasives, a large number of micro-cracks can form on the surface of the wafer and extend below the surface, forming SSD. During the entire process, damage lines will continue to extend and cross each other until the single-crystal SiC material in the enclosed area falls off, forming tiny pits and grooves to achieve material removal. The lapping time ranges from 20 min to 2 h and depends on the wafer diameter and the required surface roughness. Yamaguchi *et al*. used a diamond grinding stone to conduct a constant lapping process on a SiC wafer. Their results showed that during the lapping process, the removal of the wafer mainly relies on brittle microcracks at the sub-microscopic scale. There were several residual scratches and grinding marks on the processed surface. The lowest surface roughness *R*a they achieved was 65 nm, the MRR reached 1.8 μm/min, and the flatness was decreased to 5.3 μm [12].

### 2.2.4 Rough polishing

Rough polishing mainly relies on the mechanical polishing method, which uses small-size hard abrasives, such as $B_4C$, diamond, etc., to trim the wafer surface and remove residual strain and mechanical damage layers induced during the grinding process. The goal of this step is to improve the surface flatness and quality at a high efficiency, laying the foundation for subsequent ultra-precision polishing.

Chen *et al*. conducted a two-step rough mechanical polishing process on 6H-SiC. Diamond abrasives with diameters of 3 and 0.05 μm were used in the slurry during the first and second polishing steps, respectively. Their results showed that the removal of the material mainly relied on brittle fracture and microcracking at the sub-microscopic scale. Several scratches remained on the surface and the surface roughness *R*a was ~2–3 nm [13]. Zhou *et al*. applied rough polishing to 4H-SiC using diamond abrasives with a diameter of 1 μm. They obtained an MRR of ~2–2.25 μm/h and the remaining damage layer on the polished surface was less than 50 nm in thickness. In addition, $Cr_2O_3$ abrasives with a diameter of 1 μm were used in rough polishing of the Si and C faces of 4H-SiC. It was found that the MRR of the Si face was extremely low and the surface scratches were severe, while the MRR of the C face was ~3–3.6 μm/h with a surface roughness lower than that of the Si face [14].

In the rough polishing process, the use of fine-grained diamond or $B_4C$ slurry has greatly improved the flatness and surface roughness of wafers, but many scratches and a shallow mechanical processing-induced damage layer still remain on the processed surface. In order to completely remove the remaining damage layer and improve the surface roughness and flatness to meet application accuracy requirements, subsequent ultra-precision polishing is very critical for the SiC wafer manufacturing process.

## 2.3 Current fine polishing techniques for SiC wafers

With the development of ultra-precision polishing technology, ultra-precision polishing processing methods currently suitable for single-crystal SiC wafers mainly include CMP [14,15], plasma-assisted polishing (PAP) [16,17], tribochemical polishing (TCP) [18-21], catalyst-referred etching (CARE) [22-24], and ultraviolet-assisted polishing [25-28].

### 2.3.1 Chemical mechanical polishing (CMP)

CMP technology is an ultra-precision polishing technology based on a combination of the chemical and mechanical action of polishing slurry. Fig. 2.3 shows a schematic of a typical CMP machine for wafer polishing. An elastic polishing pad is adhered to the polishing disc and rotates at a certain angular velocity while the wafer is set on the end face of the wafer holder, which also rotates with a certain angular velocity. Slurry is continuously supplied to the polishing pad at a certain rate. Fig. 2.4 shows the material removal mechanism of CMP. With the assistance of the chemical action of the slurry, a soft oxidized layer is generated on the surface of the SiC wafer, which is subsequently removed by the mechanical action of the abrasive in the slurry, so as to realize the flattening of the wafer surface. At present, CMP has been widely used in surface polishing and planarization in the semiconductor industry. It is also considered to be the most

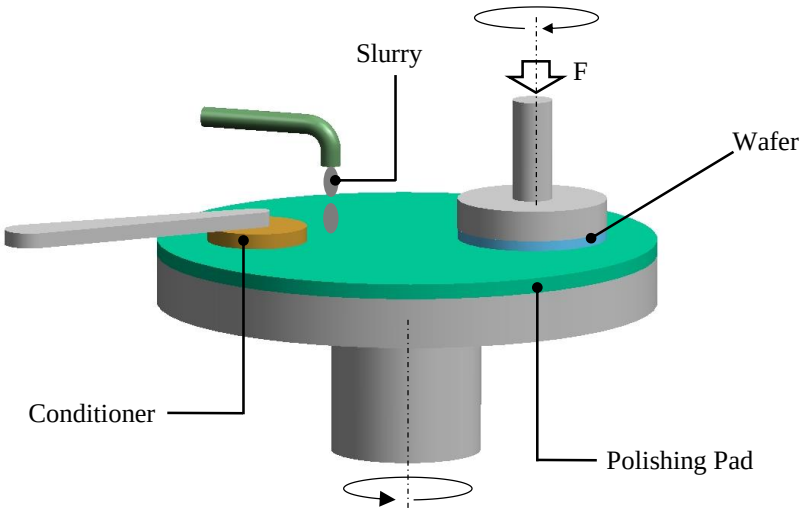



**Fig. 2.3** Schematic of conventional CMP for wafer polishing.

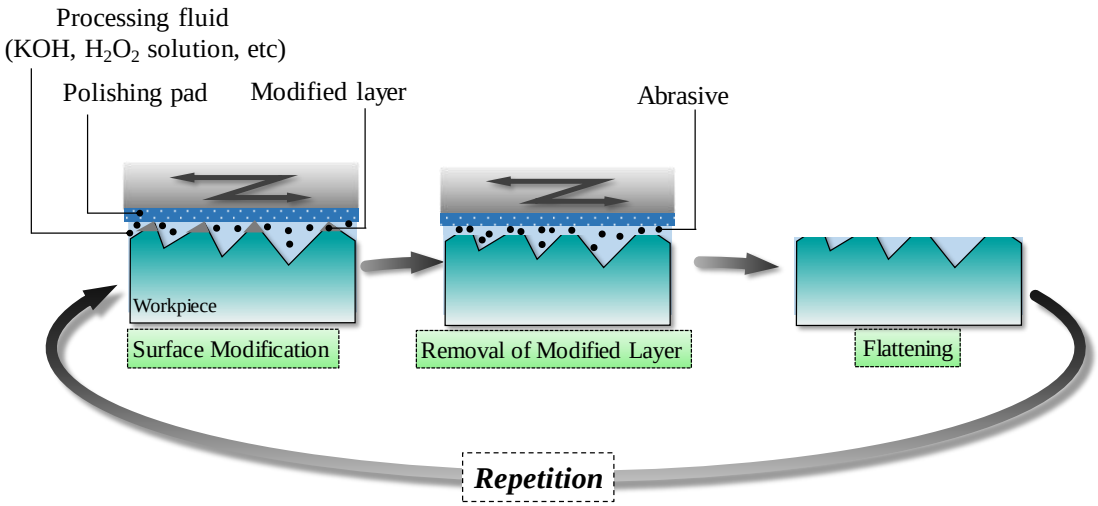



**Fig. 2.4** Polishing mechanism of CMP.

effective processing method to achieve global planarization and ultra-smooth damage-free SiC surfaces.

However, due to the extremely high hardness and chemical inertness of single-crystal SiC, CMP of a single-crystal SiC wafer is extremely difficult and has a very low MRR. Therefore, in recent years researchers have made several efforts in the development of polishing slurry for SiC wafers, aiming to obtain a higher MRR and minimal surface damage by CMP. Early on, increasing the efficiency of CMP for SiC wafers mainly relied on using high-concentration abrasives (such as adding 30 wt% $SiO_2$ abrasives), applying high polishing pressure (such as 6 psi), and increasing the polishing temperature (such as heating the wafer or the polishing slurry) to obtain strong mechanical action and thermal stress. Zhou *et al*. applied CMP to the Si face of 6H-SiC

usingcolloidal $SiO_2$ abrasives (average particle diameter of ~59–70 nm, concentration of 25 wt%, and temperature of ~55 °C). A maximum MRR (<200 nm/h) was obtained when the pH was greater than 11 and the temperature was 55 °C; the surface root mean square (RMS) roughness value was reduced from 2 nm to 0.5 nm. Furthermore, it has been proposed that a higher pH can increase the concentration of $OH^-$ groups in the solution; $OH^-$ groups can induce a dipole and weaken the Si-C bond, thereby increasing the chemical reaction activity of the atoms on the SiC surface so that $H_2O$ and dissolved oxygen in the polishing solution can attack the Si-C bonds and generate an oxide ($SiO_2$) layer. This oxidized layer is softer than the original SiC surface and is more easily removed by abrasives. Since the chemical reaction is a thermally activated process, it follows the Arrhenius model (chemical reaction rate constant formula), thus, increasing the polishing liquid temperature or polishing pad temperature is also an effective way to increase the chemical corrosion rate [14]. In addition, a combination of mechanical polishing (MP) and CMP has also been studied. Chen *et al.* applied MP and CMP to a 6H-SiC wafer in a KOH alkaline solution using colloidal $SiO_2$ abrasive with a diameter of ~50–60 nm. The MRR and surface roughness of the Si face (0001) and C face (000-1) were compared. The MRRs in CMP of the Si and C faces were 153 nm/h and 6 nm/h, respectively, and the RMS surface roughness was 0.096 nm and 1.66 nm, respectively. They also polished the 6H-SiC wafer using a two-step polishing process method that combined MP and CMP to improve the surface quality, obtaining a surface roughness *R*a of 0.18 nm [15].

## 2.3.2 Plasma-assisted polishing (PAP)

In 2010, Yamamura *et al*. first proposed a new compound ultra-precision polishing technique called plasma-assisted polishing (PAP), which combines plasma surface modification and mechanical polishing [16]. In this method, the high reactivity of radicals in plasma is used to soften difficult-to-machine materials, making them polishable by softer abrasives. Fig. 2.5 shows the material removal mechanism of PAP for wafer polishing. At first, the wafer surface is irradiated by plasma and chemical reactions occur between radicals in the plasma and the wafer surface. A modified layer with a hardness significantly lower than the wafer is formed on the wafer surface. Then, soft abrasives are used to remove the modified layer without introducing any damage to the base material. After multiple repeats of the surface modification and removal of the modified layer, an ultra-smooth and damage-free surface can be obtained.

Yamamura *et al*. demonstrated that the hardness of the 4H-SiC surface can be decreased from 37.4 to 4.5 GPa after irradiation with helium-based water vapor plasma. A surface with RMS roughness of 0.11 nm was obtained after the oxide layer was removed by slurry polishing. In addition, a much smoother surface with RMS roughness of 0.06 nm was obtained by simultaneously conducting plasma assisted oxidation and mechanical polishing with a $CeO_2$

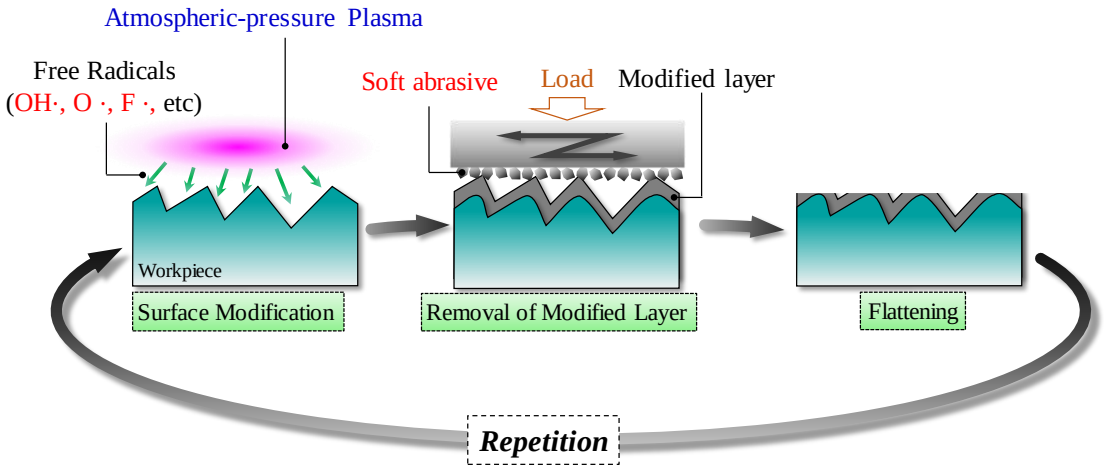



**Fig. 2.5** Polishing mechanism of PAP.

polishing film [16,17]. PAP can be conducted at room temperature and atmospheric pressure; it does not require a specific vacuum environment and the material removal process does not cause mechanical damage to the surface and subsurface of the SiC substrate. In terms of surface quality, PAP processed surfaces are atomically smooth and damage-free. However, the current MRR of 4H-SiC by PAP is lower than 1 μm/h, which is too low to satisfy the needs of industrial production. In addition, the composition of the PAP system is complicated and the equipment is expensive.

### 2.3.3 Tribochemical polishing (TCP)

TCP is a type of non-abrasive polishing technique. Fig. 2.6 shows the material removal mechanism of TCP. This method is based on friction between the workpiece surface and a hard polishing disc without abrasives. This friction causes chemical reactions to occur on the workpiece surface that then dissolve the material in the processing solution or modify the workpiece surface, achieving material removal. Friction accelerates the chemical reaction rate and the material removal only occurs in the friction regions [18,19]. Zhu *et al.* applied TCP to polycrystalline SiC and compared the effects of oxidation solutions of $Cr_2O_3$, $H_2O_2$, and $KMnO_4$ on polishing performance. Their results showed that when the SiC (5 mm × 5 mm) was polished by a $Si_3N_4$ polishing tool, the largest friction coefficient and MRR were obtained with the $Cr_2O_3$ oxidation solution. When they applied a cast-iron polishing disk to large polycrystalline SiC workpieces (20 mm × 20 mm), the MRR in the $Cr_2O_3$ oxidation solution was ~200–400 nm/h and the surface roughness *R*a of the polished surface was less than 1 nm. The use of oxidants ($Cr_2O_3$, $H_2O_2$, and $KMnO_4$) improved the MRR, but the reactivity of $KMnO_4$ was too strong and not suitable for TCP, resulting in a significant etching effect in SiC [20]. Lin *et al.* applied different metal polishing discs (cast iron, AISI304 stainless steel, S45C medium carbon steel plated

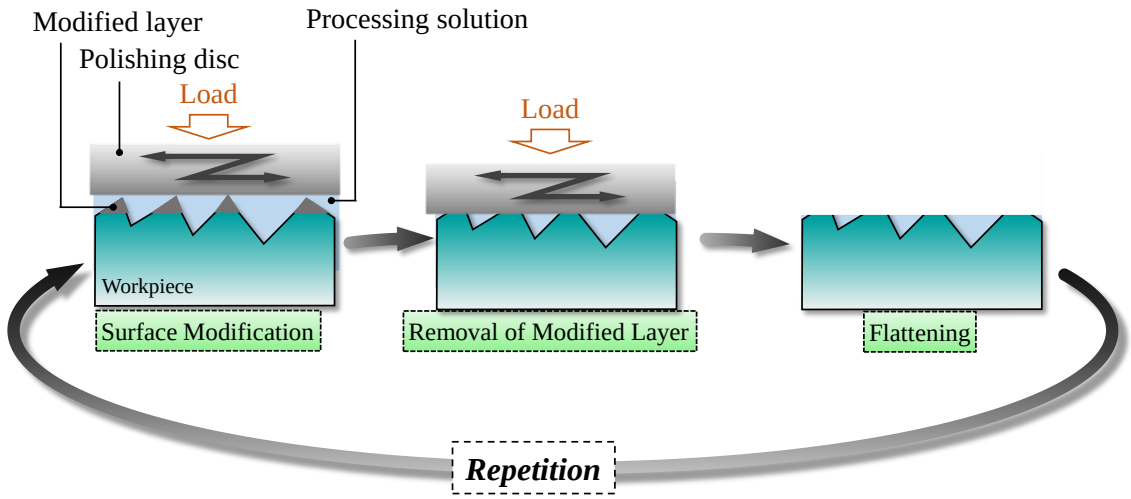



**Fig. 2.6** Polishing mechanism of TCP.

chromium, brass, and copper) to polish α-SiC (20 mm × 20 mm × 5 mm) by TCP in water and acetone solution, respectively. Their results showed that the iron metal disc can effectively polish SiC in water. The chemical analysis of polishing debris using X-ray photoelectron spectroscopy (XPS) showed that iron oxide plays an important role in catalytic assistance during the tribochemical removal process of the SiC surface. Iron oxide may reduce the activation energy and threshold temperature of the tribochemical reaction. By applying an iron metal disc, a maximum MRR of 60 nm/h and a *R*a surface roughness of 3.51 nm were obtained. The TCP had no polishing effect in the acetone solution. Furthermore, because TCP is a non-abrasive polishing process, the polishing disc plays a very important role in polishing performance. The hardness of the polishing disc needs to meet two requirements: a hardness lower than the material being processed, to avoid introducing mechanical damage to the workpiece surface, and a sufficiently high hardness to provide the required contact stress intensity. Comparing soft (made from polyurethane, aluminum, and copper) and hard (alumina and SiC) polishing pads, silicon nitride and cast-iron polishing pads exhibited better polishing performance. In addition, TCP must be applied in an aqueous solution, which provides a good polishing effect [21].

## 2.3.4 Catalyst-referred etching (CARE)

Catalyst-referred etching (CARE) is also called catalyst-referred polishing, which uses precious metal catalysts to accelerate chemical dissolution of the wafer surface without abrasives. At the same time, the precious metal is also used as a polishing disc to smooth the workpiece surface. The polishing mechanism of CARE is shown in Fig. 2.7. The polishing disc is made of a precious metal with a catalytic effect, thus there is a very thin catalyst layer on the surface. Since the polishing disc is very flat, the catalyst layer will preferentially etch and remove the protruding

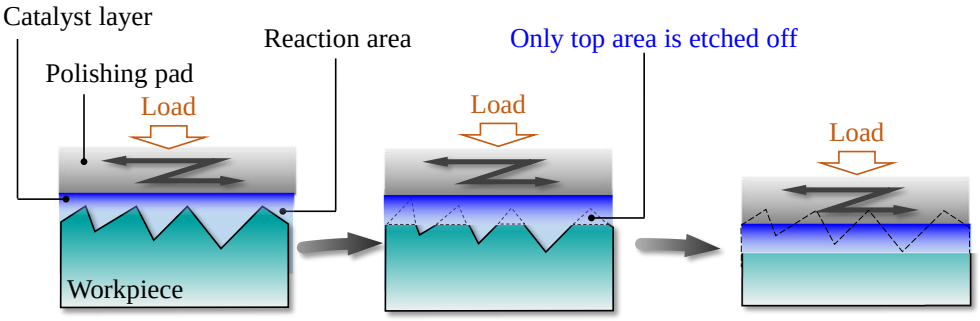



**Fig. 2.7** Polishing mechanism of CARE.

parts of the workpiece surface and recessed parts that are not in contact with the catalyst layer will not be processed. Finally, a smooth and damage-free surface can be obtained. In 2006, Hara *et al*. first proposed this kind of abrasive-free planarization method to process 4H-SiC (0001). Platinum (Pt) was used as the polishing disc and hydrofluoric acid (HF) was used as the corrosion reagent. At first, the SiC surface in contact with the catalyst Pt surface was activated in the HF solution to generate $SiO_2$, then the generated $SiO_2$ was dissolved by the HF. During polishing, these two processes are repeated continuously and the surface of SiC surface is polished. Their results showed that the surface roughness was significantly reduced, the surface lattice shape was not destroyed, and a MRR of about 0.1–0.2 μm/h was obtained. A step-terrace structure on the SiC surface was observed after CARE using atomic force microscopy (AFM). The height of the step was about 0.3 nm, which is the height of a diatomic layer of SiC. However, HF is volatile and highly corrosive, putting great pressure on the equipment and environment [22)]. Therefore, in 2008, Hara *et al*. tried a new reagent and 4H-SiC was first processed in a solution of ferrous sulfate ($FeSO_4$) and hydrogen peroxide ($H_2O_2$). Then, the processed workpiece was put into KOH solution. The material removal mechanism is the reaction between the hydroxyl groups in $H_2O_2$ (produced by the reaction with $Fe^{2+}$, that is, the Fenton reaction), SiC, and oxygen to generate $SiO_2$. The generated $SiO_2$ then reacts with hydroxide ions in KOH. Their experimental results showed that the MRR of CARE is related to the crystal plane. The MRR of the C plane was larger than that of the Si plane; a step-and-terrace structure was observed on the Si plane but not on the C plane [23)]. Isohashi *et al*. found that CARE can be used to process 4H-SiC in pure water and they obtained an ultra-smooth surface with a straight step-and-terrace structure. The use of pure water makes CARE an environmentally friendly and sustainable technology for the planarization of semiconductor wafers [24)].

### 2.3.5 Ultraviolet-assisted polishing

Touge *et al*. first developed an ultraviolet-assisted polishing (UV-assisted polishing) technique for SiC wafers, which combines ultraviolet chemical modification and mechanical polishing. Fig.

2.8 shows a schematic diagram of UV-assisted polishing. When SiC is irradiated using UV light (wavelength < 380 nm), the SiC surface is excited and electrons and holes are generated (chemical equation 2.1).

$$SiC \xrightarrow{h\nu} SiC + e^{-} + h^{+} \quad (2.1)$$

Electrons and holes briefly generated in this way normally do not participate in the chemical reaction but recombine and emit the received energy in the form of heat. However, in the case of continuous light irradiation, these electrons and holes are continuously generated on the wafer and increase the probability of participating in the chemical reaction. When UV is irradiated in an environment where materials are rubbing at high speed, the activation energy of the chemical reaction becomes small and occurs in an avalanche manner. When these electrons and holes participate in the chemical reaction, the electrons react with oxygen and the holes react with water molecules in the atmosphere. Hydroxyl radical (OH·) and atomic oxygen are generated; OH· has an extremely short lifetime but very strong oxidizing power. An oxide film softer than the base SiC material is formed on the surface and C in SiC is released as CO gas. The formed oxide film ($SiO_2$) is chemically and mechanically removed by $CeO_2$ abrasive grains or a synthetic quartz tool ($SiO_2$), thus a damage-free and ultra-smooth surface can be obtained [25,26]. Sakamoto *et al*. developed a UV-assisted polishing device with a tubular synthetic quartz polishing tool for large-diameter SiC wafers. Their device was used to polish 4-inch SiC wafers and ultra-smooth surfaces with *R*a = 0.2–0.4 nm and *R*z = 3–7 nm were obtained. In addition, they found that the MRR of UV-assisted polishing in an $O_2$-rich atmosphere is 1.73 times the MRR obtained in a normal atmosphere. The reason for this observation could be that the $O_2$-rich polishing atmosphere promoted the oxidizing action under UV light irradiation or promoted chemical and mechanical polishing action between SiC and the synthetic quartz tool ($SiO_2$) [27]. UV-assisted polishing is also an effective polishing method for GaN substrates. GaN has been excited by UV

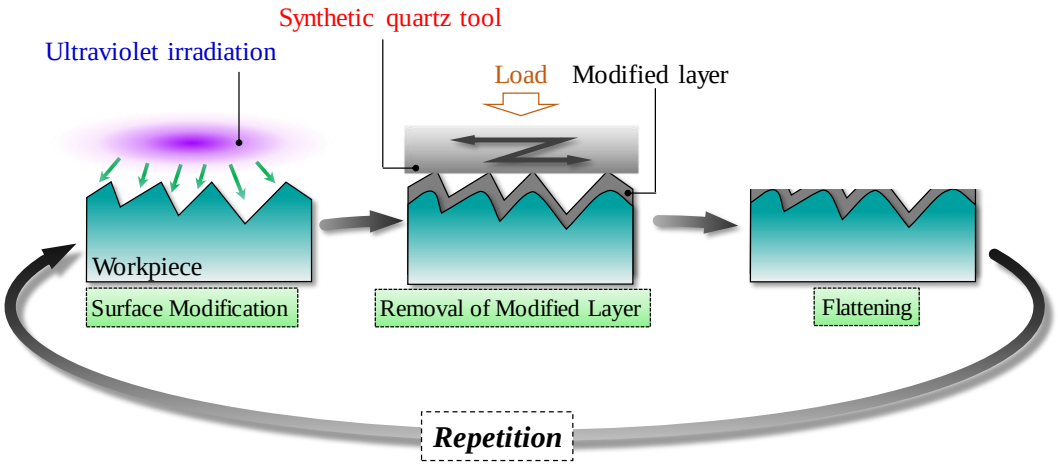



**Fig. 2.8** Polishing mechanism of UV-assisted polishing.

irradiation and the generated oxide layer was simultaneously removed by a synthetic quartz polishing tool. An atomically smooth surface with surface roughness of 0.18 nm RMS and 1.06 nm *Rz* was obtained. In addition, the MRR with UV was 16 times higher than that without UV, which confirmed that UV has a significant promotional effect on the MRR of GaN [28].

## 2.4 Electrochemical machining

Although ultra-precision polishing of SiC can be realized with the above discussed polishing techniques, there are still a series of problems, such as a low efficiency, high cost, relatively high surface roughness, etc., associated with these polishing processes. In addition, some of these techniques are still immature, making them currently inapplicable for industrial mass production. Furthermore, the current SiC wafer manufacturing process after slicing includes grinding, lapping, mechanical polishing, and CMP, which involves a series of expensive tools. Additionally, multiple disassembling and clamping of SiC wafers between these different tools at different processing steps causes low efficiency, waste of manpower, and increase in workpiece loss. The above discussed methods also can only be used at the final step in the SiC wafer manufacturing process owing to their extremely low MRR. Therefore, these methods do not simplify the current complicated SiC wafer manufacturing process.

SiC is a typical semiconductor material wherein holes and electrons are generated in the bulk due to p- or n-type doping, providing SiC with certain electrical conductivity. When applying a positive voltage to the SiC surface in an electrolyte, electron transfer between SiC and reactants in the electrolyte enhanced and the chemical reaction rate can be greatly increased. Therefore, the modification rate of SiC using electrochemical methods is promising to obtain a high MRR.

### 2.4.1 Electrochemical polishing

Electrochemical polishing (ECP) is a non-traditional machining process with a long history. Jacquet is the first person who applied an electrochemical reaction to an industrial surface treatment process in 1930, obtaining a patent [29]. As shown in Fig. 2.9, the workpiece is connected to a positive terminal of the power supply and a voltage (10–25 V) is applied across the interelectrode gap between a pre-shaped cathode and anode (workpiece). The rough surface of the workpiece is removed by the mechanism of anodic dissolution, without causing mechanical deformation during ECP. The anodic dissolution rate, which is governed by Faraday's law of electrolysis, depends on the electrochemical properties of the workpiece, electrolyte properties, and the supplied electric current/voltage. Compared with other traditional MP methods, ECP can be applied to any conductive material without being limited by the material hardness and workpiece geometry. In addition, ECP has a relatively high MRR and can obtain a smooth surface

without residual stress and cracks since it is a non-contact process [30]. Initially, ECP was mainly used to polish metals and alloys. In general, ECP includes two processes: macro- and micro-smoothing [31]. The aim of macro-smoothing is to remove surface roughness greater than 1 μm by eliminating the dissolution rate difference of "peaks" and "valleys" presented on a rough metal surface [32-34] . Micro-smoothing removes surface roughness lower than 1 μm by suppressing the effect of microstructure, defects, and crystallographic factors on the electrochemical process, realizing a mirror-like surface [35-38] . In general, during ECP, metal materials are anodized to the oxides that can directly dissolve in the water, thus realizing material removal. However, SiC is oxidized to $SiO_2$ during ECP, which cannot dissolve in water, and the generated oxide layer on the SiC surface hinders further progress of SiC anodization. In order to solve this problem, Rysy *et al*. first proposed ECP of SiC in an HF electrolyte with a pH of 3. Their ECP process for SiC consisted of two steps: an anodic oxidation step of the SiC to $SiO_2$ and a removal step of the $SiO_2$ layer by HF [39]. ECP of Si and C faces of p-type 4H-SiC has been performed in constant-current density mode and the polished Si face was smoother compared with the C face. By optimizing the current density and the concentration of the HF solution, a surface roughness of $Sq$ = 1.9 nm was obtained with a high etching rate of 40 μm/h on the Si face [40]. Ballarin *et al*. applied ECP to n-type 3C-polycrystalline SiC and reduced the roughness by more than one half compared to the initial surface. In addition, etching conditions, such as HF concentration, current density, and etching time, were optimized in order to assess the best values for polishing [41].

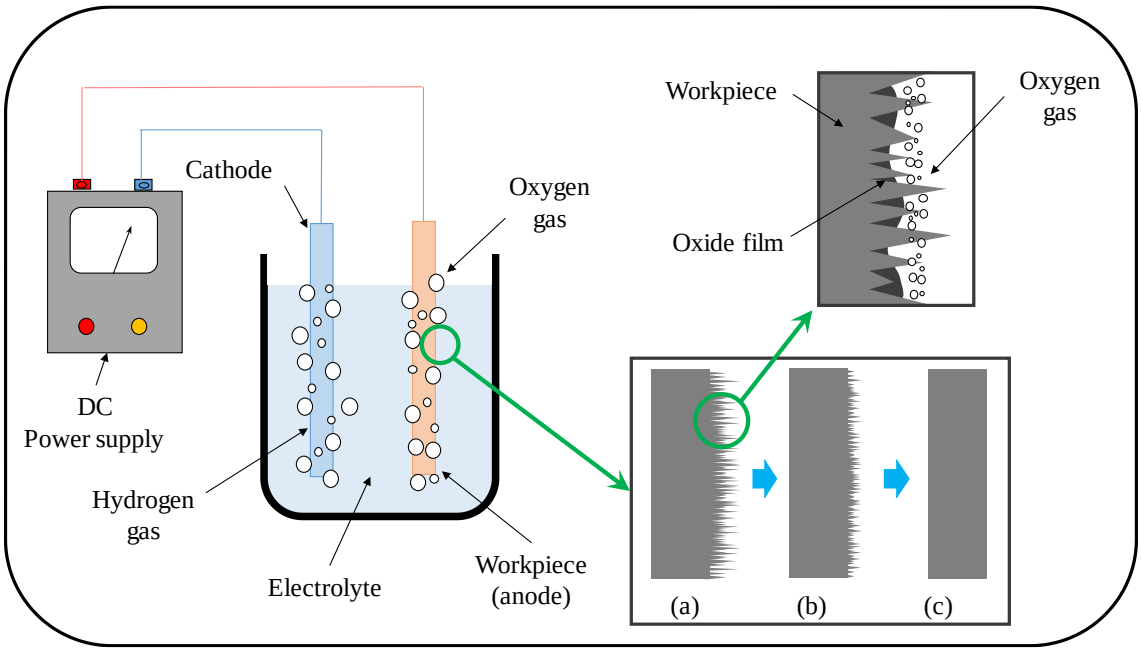



**Fig. 2.9** Polishing mechanism of ECP. (a) Initial surface, (b) surface during polishing, and (c) polished surface.

### 2.4.2 Electrochemical mechanical polishing

In ECP, Lin *et al*. reported that the material removal amount slightly increases with increasing time but is not consistent with Faraday's law after 400 s during the ECP of tungsten carbides. They attributed this phenomenon to the barrier effect of the oxide layer. Anodizing produces a passive film that covers the surface of the processed material and prevents the anodic reaction from proceeding smoothly. In addition, because the anodizing process is carried out under a static condition, without forced stirring, the reaction products continuously grow on the anode surface, which will also have certain inhibitory effects on the reaction rate [42].

To address this problem, electrochemical mechanical polishing (ECMP) was developed. ECMP is a composite polishing technology that combines electrochemical anodic oxidation and mechanical polishing. A passive film is formed on the workpiece surface after a positive potential is applied to the workpiece, then the passive film at the higher area of the surface is removed selectively by mechanical polishing. After removing the barrier effect of the passive film, the anodic oxidation rate at the higher region is again increased. Finally, the height of the entire surface tends to be uniform [43]. In ECMP, material removal mainly relies on anodic oxidation and only a small amount of material is removed by mechanical action. This greatly reduces the wear of the tool, increasing the polishing tool lifetime to fourteen times that of traditional mechanical machining [44-46]. Deng *et al*. reported that the hardness of the SiC surface decreased, from 34.5 to 1.9 GPa, after anodic oxidation, which is much softer than that of synthetic quartz glass (although they are both made of $SiO_2$). This characteristic of the oxide layer significantly reduces the processing difficulty of SiC. In addition, they successfully applied slurry ECMP to a 4H-SiC surface, using $CeO_2$ slurry as an electrolyte and polishing medium, and obtained an MRR of 3.62 μm/h [47]. Murata *et al.* and Gao *et al.* applied $CeO_2$ core/shell abrasives instead of traditional slurry to remove the oxide layer in ECMP. Murata *et al.* obtained a surface with *R*a surface roughness of 0.52 nm and Gao *et al.* obtained a surface with *R*a surface roughness of 3 nm. They both achieved MRRs of 3–4 μm/h [48,49].

In general, the maximum advantage of slurry polishing is that a constant MRR can be obtained by supplying abrasive particles in the slurry with a certain diameter and shape. In addition, the MRR can also be controlled by controlling the concentration of abrasive particles in the slurry, the material and hardness of the polishing pad, and even the metal disk, as well as other parameters related to the polishing motion. Because of the use of loose abrasive particles, abrasive particles are not forced to mechanically remove the wafer surface and would induce almost no mechanical damage. There are almost no defects, such as microcracks, remaining on the surface and it is easier to obtain a good surface compared with polishing methods using fixed abrasives. However, although abrasives used in slurry polishing have uniform particle size, the application of an elastic polishing pad makes the processed surface only follow the shape accuracy of the previous

processing step; shape correction cannot be performed. In addition, due to the discontinuity of the polishing pressure distribution, the shape accuracy of the processed surface also easily deteriorates. At the same time, slurry must be supplied to the wafer surface all time and the filtration and recovery of slurry is very difficult. Therefore, this method faces expensive waste treatment costs and an environmental pollution problem. In contrast, the shape of the processed surface is determined by the tool shape and the moving trajectory of the abrasives in fixed-abrasive polishing. Thus, the greatest merit of using fixed abrasive is that it can easily establish shape accuracy of the wafer surface. In addition, the application of a fixed abrasive can minimize waste treatment and environmental pollution.

Fig. 2.10 shows a comparison of slurry ECMP and fixed-abrasive ECMP. ECMP for SiC wafers contains two processes: anodic oxidation of the SiC surface and removal of the oxide layer. The hardness of the abrasives is higher than the oxide layer but softer than SiC, thus the application of soft fixed abrasives not only increases the shape accuracy of the processed surface but also does not introduce any damage to the wafer surface. The MRR mainly depends on the anodic oxidation rate. In slurry ECMP, the abrasives are separated from the polishing tool and mix with

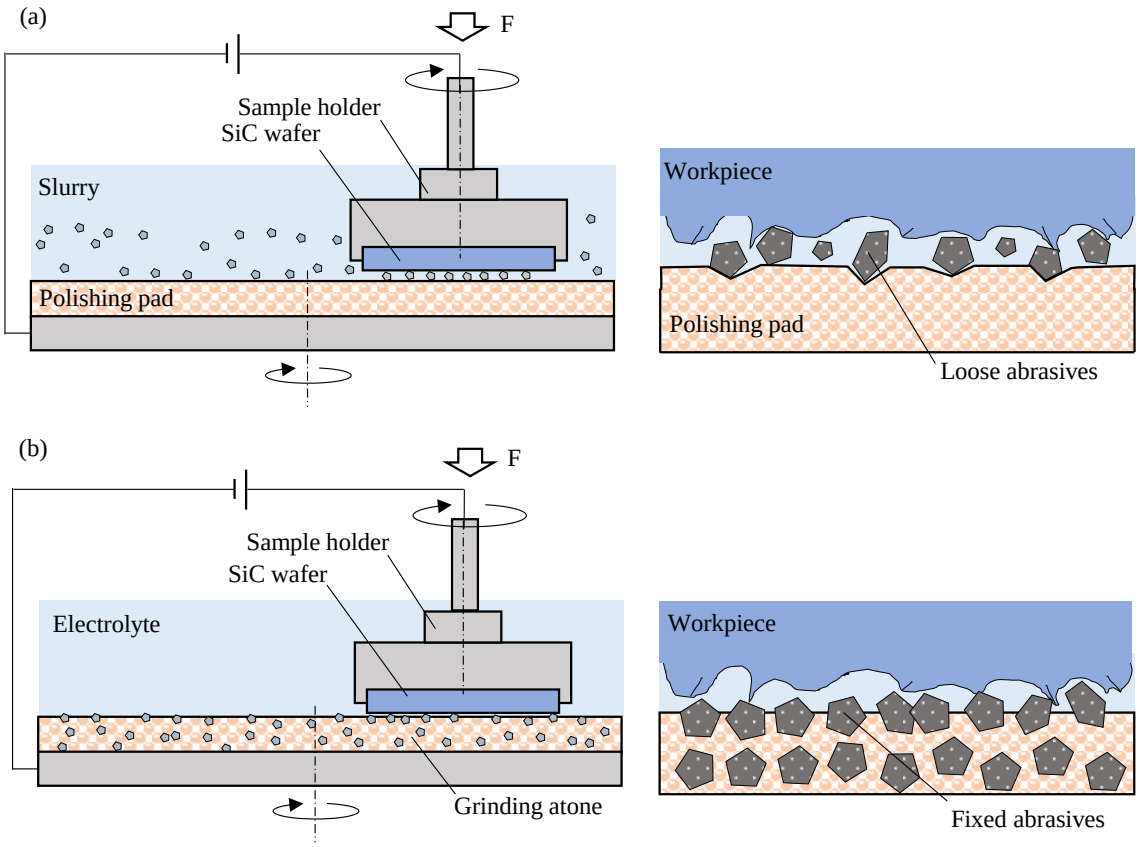



**Fig. 2.10** Comparison of loose-abrasive and fixed-abrasive ECMP. (a) Loose-abrasive and (b) fixed-abrasive ECMP.

the electrolyte; the slurry parameters, such as pH, abrasive concentration, abrasive diameter, and additive type, not only have an influence on the removal rate of the oxide layer, but also affect the anodic oxidation rate. In contrast, the application of a fixed abrasive can separate these two processes and eliminate the mutual influence of anodic oxidation and oxide layer removal in ECMP. The anodic oxidation and oxide layer removal rates can be adjusted separately to obtain a better balance. Thus, we propose slurryless ECMP, which uses fixed abrasives instead of slurry to remove the oxide layer. By using ceria fixed abrasives, MRRs of about 10 μm/h for a diamond-lapped SiC surface and 23 μm/h for a sliced SiC surface were obtained while a surface roughness of less than 1-nm *S*q was realized [50,51].

## 2.5 Sonochemistry

Acoustic frequency ranges are shown in Fig. 2.11. Sound with frequency above 20 kHz is defined as “ultrasound” or “ultrasonic” and cannot be heard by humans. In 1917, Langevin sandwiched a quartz oscillator between two pieces of thick iron plates, creating a transducer now known as a Langevin transducer [52]. The Langevin transducer can generate artificial ultrasound with high output power. This excellent achievement promoted vigorous development of ultrasound research and extended the application of ultrasound to many fields, such as chemistry, physics, biological engineering, medical science, waste treatment, etc. In these applications, high-power ultrasounds with frequencies ranging from 20 kHz to 1 MHz are used in industry, nanotechnology, ultrasonic therapy, etc. Low-power ultrasonic waves with frequencies ranging from 2 to 10 MHz are applied in medical imaging, nondestructive testing, etc.

In 1927, Wood and Loomis created the concept of “sonochemistry” and published an article about the physical and biological effects of ultrasound [53]. “Sonochemistry” is a formal term widely used in chemical, physical, and biological research fields that deal with the short-lived localized high pressure and high temperature produced during ultrasonic cavitation.

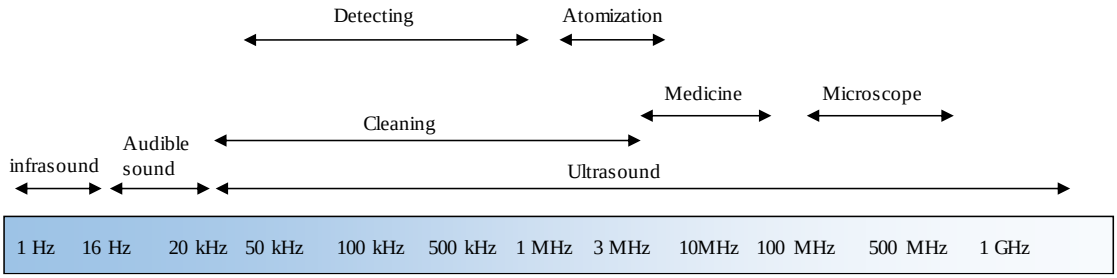



**Fig. 2.11** Frequency range of sound wave and the application of ultrasound with different ultrasonic frequencies.

When a high-power ultrasonic vibration is applied to water or other liquids, ultrasonic cavitation can be generated. All ultrasonic vibrators with a frequency from 20 kHz to several MHz can be used to produce ultrasonic cavitation. Fig. 2.12 shows the growth and implosion process of small bubbles induced by ultrasonic vibration during the formation of ultrasonic cavitation. Small bubbles (cavitation nuclei) in liquid grow and continuously accumulate the energy of the ultrasonic field. After a few acoustic cycles, the radius of these bubbles reaches a critical size and rapidly implodes, the surrounding liquid then suddenly rushes into the bubbles when these bubbles rapidly collapse. Assuming the compression process is adiabatic, the internal temperature and pressure of a bubble can reach 5000 K and hundreds of atmospheres, while cooling rates can reach $10^9$ K/s owing to the short lifetime of the velocity field in liquid. The core of the high temperature and pressure is called “hot spots”, which are the source of chemical and physical effects caused by acoustic cavitation [54]. In addition, bubbles can release a large amount of energy when they collapse sharply and produce a microjet with an extremely high speed and powerful impact energy. Under conditions of extreme temperature and pressure, water decompose and generates highly active radicals of H· and OH· [55,56].

In 1929, Schmitt published a report on the promotional effects of ultrasound in chemical oxidation. In general, oxidation of halide ions in neutral solutions by atmospheric oxygen in the dark is extremely slow. However, after an aqueous solution of potassium iodide was processed by ultrasonic radiation, iodine was quickly liberated under atmospheric pressure [57]. In 1934, Frenzel’s research group observed the phenomenon of sonoluminescence. An ultrasonic transducer was placed in a water tank filled with developer and afterwards tiny bright spots were observed on the film. At the same time, the bubbles in the liquid emitted light when the ultrasound

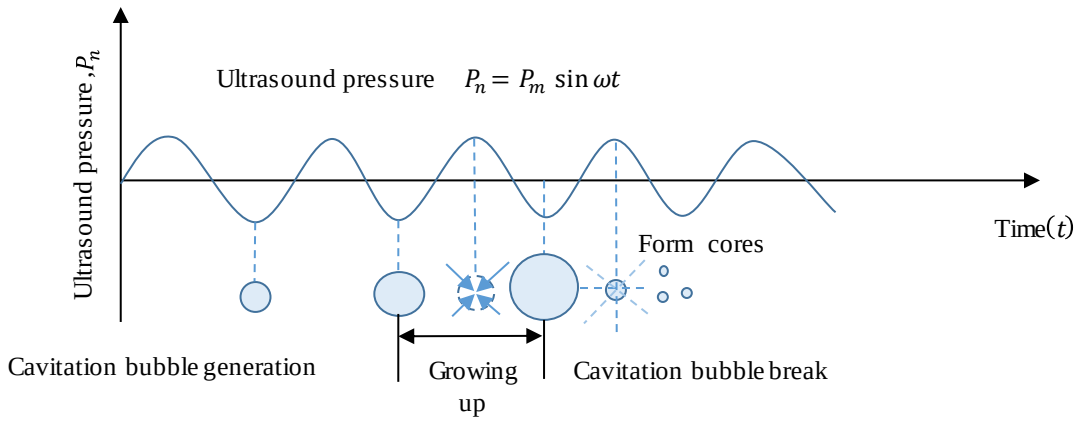



**Fig. 2.12** Growth and collapse of a bubble in the acoustic cavitation process.

was turned on [58]. In 1935, Claus and Hall introduced ultrasound to the field of electrochemistry. They found that ultrasonic irradiation applied to an electrode reaction can synthesize finer silver and mercury particles, improving their dispersion [59]. In 1938, Porter and Young investigated the effect of ultrasonic vibration on the rearrangement rates of benzazide ($C_6H_5CON_3$) in benzene and in aniline at the same temperature. They found that the rearrangement rate is greatly accelerated by the application of ultrasonic vibration. This was the first ultrasonic vibration applied to the field of organic chemistry [60]. In 2005, Flannigan *et al*. measured the temperature of a collapsed bubble under ultrasonic vibration to be up to 17000 K by spectral analysis; this ultra-high temperature indicated that there is plasma inside the bubble [61,62]. These studies have far-reaching implications for the study of more powerful energy sources. In 2018, Hu *et al*. compared the oxidation rate of SiC in CMP slurry with and without ultrasonic vibration assistance. In the XPS results of the oxidized surfaces, peaks corresponding to Si-O and Si-C-O were observed on the SiC surface processed in slurry with the assistance of ultrasonic vibration while no oxide was observed without ultrasonic vibration. It is obvious that ultrasonic vibration has a promotional effect on the oxidation of SiC in slurry. In addition, during the ultrasonic-assisted process, bubbles were generated under ultrasonic vibration and the slurry temperature significantly increased [63].

In recent years, more and more fields of research have begun to pay attention to the study of sonochemistry, including organic synthetic chemistry [64], nanomaterial preparation [65], biochemistry [66], analytical chemistry [67], polymer materials [68], surface processing [69], biotechnology and environmental protection [70], and medicine. Compared with conventional chemical reactions, sonochemistry has several advantages that include decreasing reaction time, lowering reaction temperature, changing reaction pathways, increasing reactivity of reagents and catalysts, and increasing reaction rate [72].

## 2.6 Ultrasonic vibration assisted machining

In addition to chemical and physical fields, ultrasonic vibration has been widely applied in the field of machining. Ultrasonic vibration-assisted machining (UVAM) is a non-traditional processing technique. In general, a UVAM system is composed of an ultrasonic generator, transducer, horn, and tool. The transducer (piezoelectric ceramic/magnetostriction) converts high-frequency electrical energy into high-frequency mechanical vibration energy. The amplitude of the ultrasonic vibration is enlarged by the horn and finally drives the tool, which is mounted on the horn and vibrates at a high-frequency during the machining process, thereby realizing ultrasonic vibration assisted removal of material [73-75].

### 2.6.1 Ultrasonic machining (USM)

USM is quite capable of processing hard and brittle materials irrespective of their electrical and chemical properties, which are generally a limitation for other machining techniques [76-78]. The history of USM can be traced back to 1927 [79,80]. In 1950, more and more researchers begun to study USM and some researchers provided USM with a name that is more representative of its material removal characteristics: ultrasonic impact grinding [81-85]. Fig. 2.13 shows a typical USM system, which is composed of an ultrasonic vibration tool, slurry supply unit, and a workpiece. During USM, the tool, which is also called a sonotrode, is kept a certain distance from the workpiece surface and the gap between the end face of the tool and the workpiece is continuously filled with slurry by the slurry supply system. The transducer transmits high-frequency mechanical vibration, with a frequency above 20 kHz, to the tool and then the slurry and the abrasives also vibrate with high frequency under the tool excitation. Abrasives continuously hammer against the hard workpiece surface, resulting in indentations, microcracks, and ultimately material removal. At the same time, with the assistance of ultrasonic vibration radiation from the end face of the tool, the slurry produces alternating hydraulic positive and negative shock waves and cavitation, which promotes abrasives in the slurry to penetrate into the micro-cracks of the processed material, promoting mechanical removal. Another role of cavitation is to force slurry circulation so that the abrasives are constantly updated. In addition, chemical reaction between the workpiece and slurry also could not be neglected [77]. The major parameters in USM that affect the MRR and surface roughness are abrasive size and ultrasonic power of the tool. As power and particle size increase, MRR increases proportionally and surface roughness is decreased [86-88]. Since USM is a method that completely relies on the movement of abrasives in the slurry, the MRR is too low to satisfy industrial applications [89-91]. Furthermore, the cost of slurry is very expensive. With the advent of rotary ultrasonic machining (RUM), USM gradually faded out of the researcher's field of vision.

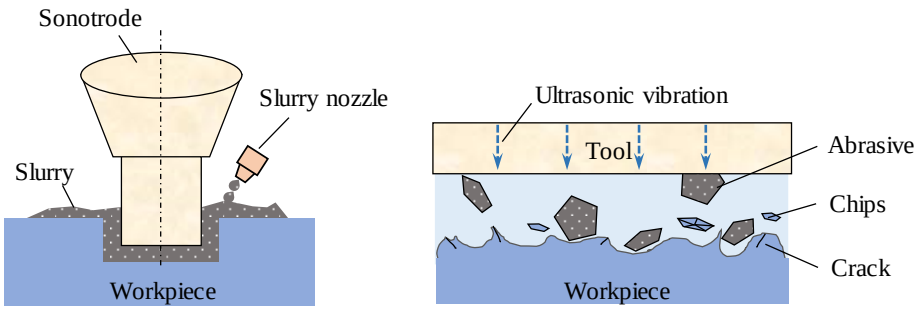



**Fig. 2.13** Material removal mechanism of USM.

### 2.6.2 Rotary ultrasonic machining (RUM)

The invention of rotary ultrasonic machining (RUM) originated from the up-scaling of static USM in order to overcome disadvantages of USM. RUM can be considered a hybrid process technique that consists of two manufacturing methods: conventional diamond grinding and static USM. The MRR in RUM is higher than that attained by either diamond grinding or USM [92,93]. In early USM, fixed diamond abrasives were used to replace the slurry and the workpiece was fixed in a four-jaw chuck, which was rotated. Although RUM is realized by this method, only a small or circular workpiece could be processed. Legge combined the rotating ultrasonic transducer with the RUM machine tool and a new era of RUM began [94]. This developed rotating transducer head enables the tool to produce high-frequency vibration while rotating, making it feasible to process the non-rotating workpiece using RUM and with quite fine dimensional accuracies. In addition, a variety of tool types can be attached to the rotating transducer to realize several kinds of machining. Therefore, RUM has also been used for drilling [95] and further extended to side/face milling [96-98], face grinding [99], surface texturing [100], and polishing.

The material removal mechanism of RUM is shown in Fig. 2.14. The abrasives fixed on the sonotrode indent to and separate from the workpiece periodically with ultrasonic frequency. During this indentation with diamond abrasives, lateral cracks and radial cracks are generated [101,102]. The lateral cracks propagate and interact with each other, leading to material removal in the brittle fracture mode. Furthermore, the diamond abrasive cutting motion accelerates the propagation of lateral cracks, consequently proving beneficial to the improvement of MRR of RUM. RUM has a wide range of applications, especially for processing hard and brittle materials, such as optical glasses, ceramics, semiconductors, and ceramic matrix composites represented by C/SiC and SiC/SiC [103]. The MRR of ultrasonic assisted grinding (UAG) is 6–10 times that of conventional grinding (CG) [104] and four times that of USM [105]. In RUM, thermal burns and physical and chemical property changes of the workpiece surface can be avoided [106]. Furthermore, a smaller surface roughness can be obtained and the surface integrity is improved [107].

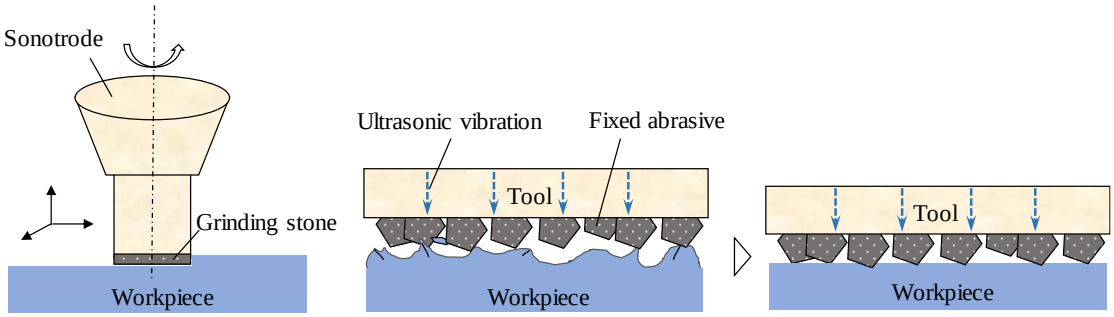



**Fig. 2.14** Material removal mechanism of RUM.

### 2.6.3 Ultrasonic vibration assisted CMP

At present, there is a trend in applying ultrasonic vibration to CMP. In ultrasonic vibration assisted CMP, ultrasonic vibration is applied to the workpiece or the polishing tool. Fig. 2.15 shows the polishing mechanism of ultrasonic vibration assisted CMP. During polishing, cavitation occurs in the slurry, which can arouse abrasives deposited in the voids of the polishing pad, making them participate in the polishing and increasing the number of effective abrasives, thereby increasing the MRR. Moreover, the local high temperature generated by ultrasonic cavitation can also promote chemical reactions on the workpiece surface, further increasing the MRR. At the same time, the micro-jet generated by cavitation can also effectively prevent the agglomeration of abrasives, avoid surface scratches caused by the agglomeration of abrasives, and thereby decrease surface roughness and SSD.

Ultrasonic vibration assisted CMP has been applied in the polishing of semiconductor wafers and the promotional effects of ultrasonic vibration on the MRR of CMP have been reported. For example, Ke, *et al*. [108] developed a novel method that combined megasonic vibration with CMP and applied it to the polishing of Si wafers. The MRR was increased by approximately 15–25% compared with traditional CMP in coarse polishing, and the average surface roughness value *R*a was reduced from 0.509 nm to 0.387 nm in precision polishing. Xu, *et al.* [109] proposed ultrasonic flexural vibration (UFV)-assisted CMP (UFV–CMP). The MRR of UFV–CMP increased by more than two times with the assistance of an ultrasonic flexural vibration and the RMS surface roughness and surface flatness obtained by UFV–CMP were 0.083 nm and 0.12 μm, respectively, which are much better than that obtained by traditional CMP: 0.212 nm and 0.23 μm, respectively. Hu, *et al*. [63] reported that ultrasonic vibration enhanced the oxidation of the SiC surface during CMP, increasing the MRR of a 2-inch SiC wafer from 0.574 μm/h to 1.057 μm/h while significantly decreasing the peak-to-valley roughness. By applying ultrasonic vibration to CMP, Zhai, *et al.* [110] increased the MRR of a SiC wafer, from 0.32 μm/h to 0.68 μm/h, and obtained a better surface compared with that of traditional CMP.

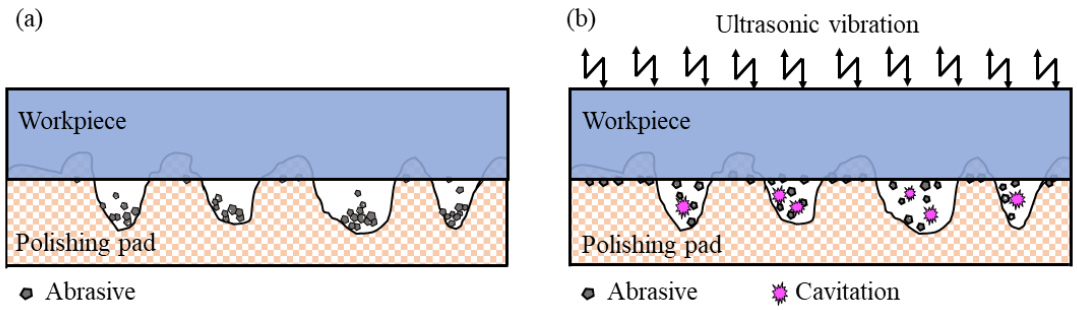



**Fig. 2.15** Mechanism of ultrasonic vibration assisted CMP. (a) Traditional CMP and (b) ultrasonic vibration assisted CMP.

## 2.7 Proposal of slurryless ultrasonic vibration assisted electrochemical mechanical polishing (UAECMP)

Currently, the SiC wafer manufacturing process is very complicated because it includes slicing, grinding, lapping, and CMP. The process involves many expensive pieces of equipment and requires an excessive amount of manpower and time. These disadvantages severely restrict the production of SiC wafers. Although slurryless ECMP can achieve a much higher MRR compared with CMP, it is still not high enough to replace grinding and lapping in the SiC wafer manufacturing process. Therefore, a further increase of the MRR of slurryless ECMP is necessary. Because the soft fixed-abrasive applied in ECMP can only remove the oxide layer, the MRR of slurryless ECMP strongly depends on the anodic oxidation rate of SiC. Based on the above analysis, it is obvious that ultrasonic vibration is a promising method to increase the anodic oxidation rate of SiC and the mechanical polishing rate of the oxide layer.

Therefore, slurryless UAECMP, which combines the advantages of ultrasonic vibration assisted electrochemical surface modification and ultrasonic vibration assisted fixed abrasive mechanical polishing, is proposed. Generally, when the diameter of the vibrator is too large, it is difficult to ensure uniform vibration of the end face of the vibrator. If applying ultrasonic vibration to SiC wafers, UAECMP cannot be applied to large-size SiC wafers. On the other hand, ultrasonic vibration can be applied to a grinding stone. First, large SiC wafers can be polished using a relatively small grinding stone by adjusting the grinding stone motion. Second, a large polishing disc can be formed by increasing the number of ultrasonic vibrator-grinding stone combinations. This design ensures the uniform vibration of the grinding stone and is more universal. With the development of SiC wafers, it is then only necessary to increase the number of vibrator-grinding stone combinations to process SiC wafers with much larger diameters, such as six and eight inches. Therefore, the proposed UAECMP is shown in Fig. 2.16. A SiC wafer is fixed on a rotating table by a vacuum chuck. The center of the vacuum chuck is made of a porous metal material and is connected to the work electrode (WE) terminal of a potentiostat. The ultrasonic vibrator is fixed opposite to the SiC wafer on a rotating spindle that can move with a uniaxial stage and the grinding stone is fixed on the end face of the ultrasonic vibrator. Thus, the grinding stone can vibrate with the ultrasonic vibrator while rotating with the spindle and oscillating along the moving table. In addition, a metal plate is set around the grinding stone and connected to the counter electrode (CE) terminal of the potentiostat. During UAECMP, the surface of the SiC wafer, the grinding stone, and the metal plate are all immersed in electrolyte and the grinding stone is in contact with the SiC surface with a set polishing pressure. Therefore, the potentiostat, SiC wafer, electrolyte, and metal plate form an electric circuit, and the anodic oxidation

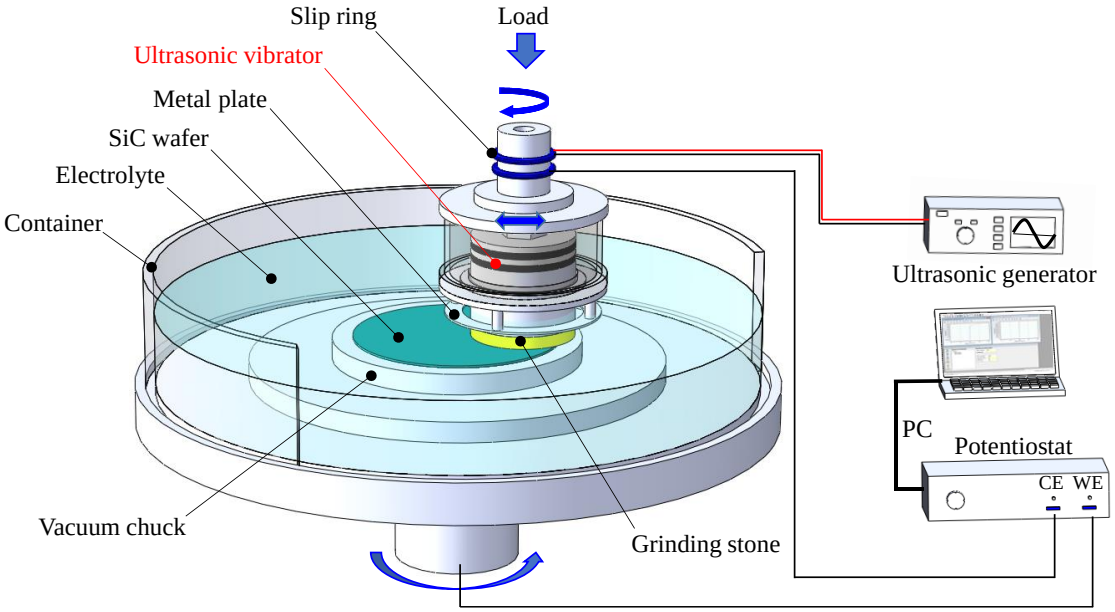



**Fig. 2.16** Schematic diagram of slurryless UAECMP.

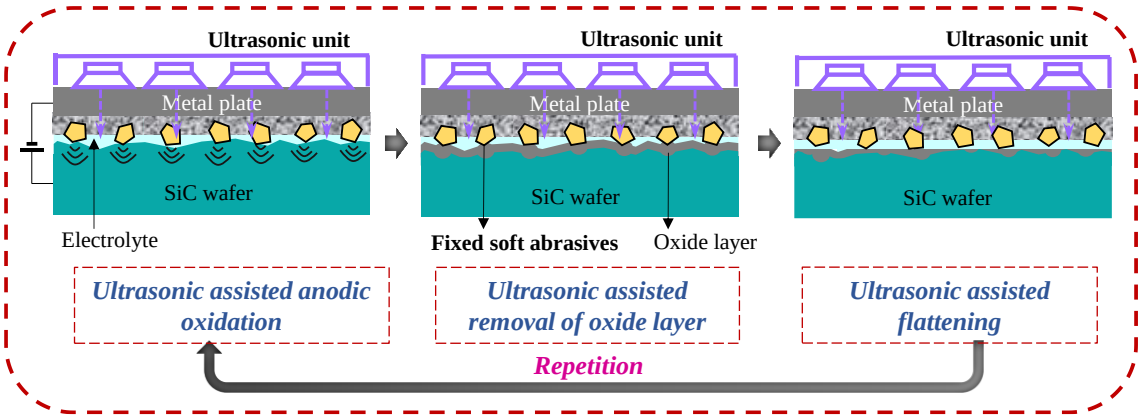



**Fig. 2.17** Polishing mechanism of slurryless UAECMP.

parameters of the SiC surface can be controlled by the potentiostat. With the rotation of the SiC wafer and the rotation and oscillation of the grinding stone, UAECMP of the SiC surface can be realized.

The polishing mechanism of slurryless UAECMP is shown in Fig. 2.17. The ultrasonic vibration unit is connected to the grinding stone, which makes the relative impacts at ultrasonic frequency occur between the grinding stone and the SiC wafer during anodic oxidation and polishing. The SiC wafer can be quickly softened by anodic oxidation with the assistance of ultrasonic vibration by applying a positive potential to the SiC wafer in the electrolyte. The

formed oxide layer is immediately removed by MP with fixed soft abrasives under the assistance of ultrasonic vibration. The hardness of the formed oxide layer and the fixed soft abrasive are much lower than that of SiC, thus, only the oxide layer is removed. By simultaneously conducting anodic oxidation and polishing with ultrasonic vibration, an ultra-smooth surface can be quickly obtained without forming scratches and SSD. Thus, highly efficient damage-free polishing of SiC can be expected via slurryless UAECMP. Compared with current polishing techniques, such as MP, CMP, and slurryless ECMP, slurryless UAECMP has the follow advantages.

First, a higher polishing efficiency is expected. In slurryless ECMP, MRRs of about 10 μm/h for a lapped surface and 23 μm/h for a sliced surface were obtained, which is significantly higher than other polishing methods. In ECMP, only the oxide layer is removed by the soft abrasives, which make the MRR mainly rely on anodic oxidation. The application of ultrasonic vibration has potential to increase the anodic oxidation rate of SiC and improvement of MRR can be expected. In addition, the resistance of the oxide layer is very high, which has a hindering effect on further oxidation of the SiC surface. In the ECMP process, incomplete removal of the oxide film will seriously decrease the anodic oxidation rate of SiC and then decrease the MRR. The application of ultrasonic vibration is expected to increase the mechanical removal rate of the oxide layer, which can decrease the hindrance of the oxide layer and increase the anodic oxidation rate of SiC.

Second, a damage-free and much smoother surface is expected in slurryless UAECMP. Slurryless UAECMP mainly uses ceria grindstone. The hardness of ceria is lower than that of SiC and thus only the oxide layer is removed during polishing and no damage is introduced to the SiC surface. In addition, the surface roughness is significantly affected by the balance of anodic oxidation rate and oxide layer removal rate in ECMP. The application of ultrasonic vibration is expected to increase the mechanical removal rate of the oxide layer, which can better control the balance between the anodic oxidation and oxide layer removal rates, decreasing the surface roughness of the processed surface.

Third, a low-cost and environmentally friendly process are expected. Slurryless UAECMP mainly uses fixed abrasives, the cost of which is significantly lower than that of CMP slurry and other loose abrasive polishing methods. Furthermore, a neutral electrolyte is used in slurryless UAECMP, which not only has less environmental pollution than acid and alkali solutions and convenient waste disposal, but also has lower requirements for equipment corrosion resistance. In addition, the high MRR of slurryless UAECMP makes this process likely to replace current post-slicing SiC manufacturing processes without the need to change equipment and grinding stones. This can greatly reduce equipment, manpower, and time costs.

## 2.8 Summary

To realize high-efficiency, high-quality, low-cost manufacturing of single crystal SiC wafers, the current SiC wafer manufacturing process was described and its characteristics were analyzed. Polishing techniques that are applied in the final processing step of SiC wafers were summarized and their advantages and disadvantages were discussed. Furthermore, the application of ultrasonic vibration in the fields of chemical, physical, and machining applications were introduced and the performance of ultrasonic vibration in these applications was reviewed. On the basis of these results, slurryless UAECMP was proposed. The obtained results in this chapter are summarized as follows.

(1) At present, the manufacturing of SiC wafers includes a series of processing steps after slicing: grinding, lapping, rough mechanical polishing, and CMP. This complex process involves the use of a variety of expensive equipment and a lot of manpower, which results in high cost and low efficiency.

(2) Although there are many polishing methods for the final finishing step of SiC wafers, some of these methods are low in efficiency, costly, and cannot obtain high surface quality. Therefore, these methods cannot be used for mass industrial production of SiC wafers. Slurryless ECMP can achieve damage-free and ultra-smooth surfaces with a relatively high MRR compared to other polishing techniques. However, it is necessary to further increase this MRR to replace the entire post-slicing SiC wafer manufacturing process and to simplify the SiC wafer manufacturing process.

(3) Cavitation induced by ultrasonic vibration, which is accompanied by high-energy output phenomenon and different physical mechanisms, such as acoustic streaming, micro-jetting, and shock waves, can enhance the mass transfer and activation (de-passivation) of the surface of an electrode, enhancing chemical and electrochemical processes. Additionally, in fixed-abrasive machining, the application of ultrasonic vibration introduces strong local impact between the tool and the workpiece, which significantly promotes the mechanical removal of the workpiece. In loose-abrasive polishing, the application of ultrasonic vibration can increase the effective number of abrasives and prevent abrasive agglomeration, which can improve the MRR and decrease surface roughness and SSD.

(4) Slurryless UAECMP, which combines ultrasonic vibration assisted anodic oxidation and ultrasonic vibration assisted mechanical polishing, was proposed. In this method, both the

anodic oxidation rate of SiC and the removal rate of the oxide layer are promoted by ultrasonic vibration. High-efficiency ultra-precision polishing of SiC wafers is expected with this method. In addition, slurryless UAECMP is expected to replace processing steps after slicing in the current SiC wafer manufacturing process and significantly improve efficiency while decreasing cost.

# References


1) H. Frosch, H. Buttner, J. Phys. D. 18(34) (1989) 6303–6310.
2) F. Yang, I. Kao, J. Electron. Packag. 123(3) (2001) 254–259.
3) M. Bhagavat, V. Prasad, I. Kao, J. Trib. 122(2) (2000) 394–404.
4) C. Chung, G. D. Tsay, M. H. Tsai, Int. J. Adv. Manuf. Technol. 73(9–12) (2014) 1485–1494.
5) S. Würzner, A. Falke, R. Buchwald, H. J. Möller, Energy Procedia. 77 (2015) 881–890.
6) Y. Gao, P. Ge, T. Liu, Mater. Sci. Semicond. Process 56 (2016) 106–114.
7) F. W. Huo, D. M. Guo, R. K. Kang, F. E. N. G. Guang, T. Nonferr. Metal Soc. 22(12) (2012) 3027–3033.
8) N. J. Churi, Z. J. Pei, D. C. Shorter, C. Treadwell, Int. J. Manuf. Technol. Manag. 12(1–3) (2007) 284–298.
9) H. Lee, H. Kasuga, H. Ohmori, H. Lee, H. Jeong, J. Cryst. Growth, 326(1) (2011) 140–146.
10) H. Kasuga, H. Ohmori, W. M. Lin, Y. Watanabe, T. Mishima, Key Eng. Mater. 404 (2009) 137–141.
11) K. Y. Ng, T. Dumm, D. Innovations, In CS Mantech Conference (2012).
12) K. Yamaguchi, M. Touge, T. Nakano, J. Watanabe, Adv Mat Res. 76 (2009) 282–287.
13) Q. F. Luo, J. Lu, X. P. Xu, Wear. 350 (2016) 99–106.
14) L. Zhou, V. Audurier, P. Pirouz, J. A. Powell, J. Electrochem. Soc. 144(6) (1997) L161–L163.
15) X. F. Chen, X. G. Xu, X. B. Hu, J. Li, S. Z. Jiang, L. N. Ning, M. H. Jiang, Mater. Sci. Eng. B 142(1) (2007) 28–30.
16) H. Deng, T. Takiguchi, M. Ueda, A. N. Hattori, N. Zettsu, K. Yamamura, Jpn. J. Appl. Phys. 50 (2011) 08JG05.
17) H. Deng, K. Yamamura, CIRP Ann. Manuf. Technol. 62 (2013) 575–578.
18) H. Tomizawa, T. E. Fischer, ASLE transactions, 30(1) (1987) 41–46.
19) S. R Hah, T. E. Fischer, J. Electrochem. Soc. 145(5) (1998) 1708–1714.
20) Z. Zhu, V. Muratov, T. E. Fischer, Wear 225 (1999) 848–856.
21) Y. C. Lin, C. H. Kao, Int. J. Adv. Manuf. Technol. 25(1–2) (2005) 33–40.
22) H. Hara, Y. Sano, H. Murata, K. Arima, A. Kubota, K. Yagi, J. Murata, K. Yamauchi, J. Electron. Mater. 35(8) (2006) L11–L14.

23) K. Yagi, J. Murata, A. Kubota, Y. Sano, H. Hara, T. Okamoto, K. Yamauchi, Surf. Interface Anal. 40(6–7) (2008) 998–1001.
24) A. Isohashi, P. V. Bui, D. Toh, S. Matsuyama, Y. Sano, K. Inagaki, K. Yamauchi, Appl. Phys. Lett. 110(20) (2017) 201601.
25) S. Hong, H. In Proc. International Conference on Micro/Nano Fabrication Technologies, (2006).
26) J. Watanabe, S. H. Hong, K. Yamaguchi, M. Touge, N. Kuroda, Advances in Abrasive Technology (ASAAT 2007), Michigan, USA (2007) 91–96.
27) T. Sakamoto, T. Tanaka, K. Oda, M. Touge, T. Fujita, J. Jpn. Soc. Abras. Technol. 58(4) (2014) 235–240.
28) T. Takita, H. Ando, A. Kubota, M. Touge, Key Eng. Mater. 656 (2015) 446–449.
29) H. Figoux, P.A. Jacquet, French Patent 707526, (1930).
30) Z. W. Fan, L. W. Hourng, Int. J. Mach. Tools Manuf. 49 (7–8) (2009) 659–666.
31) S.H abibzadeh, L. Li, D. Shum-Tim, E. C. Davis, S. Oma novic, Corros. Sci. 87 (2014) 89-100.
32) O. Piotrowski, C. Madore, D. Landolt, Electrochim. Acta. 44(19) (1999) 3389–3399.
33) R. D. Grimm, D. Landolt, Corros. Sci. 36(11) (1994) 1847–1868.
34) M. Bojinov, I. B etova, G. Fabricius, T. Laitinen, R. Raicheff, J. Electroanal. Chem. 475(1) (1999) 58–65.
35) C. Clerc, M. Datta, D. Landolt, Electrochim. Acta. 29(10) (1984) 1477–1486.
36) D. Landolt, Electrochim. Acta. 32(1) (1987) 1–11.
37) D. Landolt, P. F. Chauvy, O. Zinger, Electrochim. Acta. 48(20-22) (2003) 3185–3201.
38) F. Nazneen, P. Galvin, D. W. Arrigan, M. Thompson, P. Benvenuto, G. Herzog, J Solid State Electrochem. 16(4) (2012) 1389–1397.
39) S. Rysy, H. Sadowski, R. Helbig, J Solid State Electrochem, 3(7-8) (1999) 437–445.
40) Y. Ke, F. Yan, R. P. Devaty, W. J. Choyke, J. Appl. Phys. 106(6) (2009) 064901.
41) N. Ballarin, C. Carraro, R. Maboudian, L. Magagnin, Electrochem. Commun. 40 (2014) 17–19.
42) T. R. Lin, C. R. Su, Int. J. Adv. Manuf. Technol. 36(7–8) (2008) 715–723.
43) W. Xu, Z. Wei, J. Sun, L. Wei, Z. Yu, Int. J. Adv. Manuf. Technol. 63(1–4) (2012) 129–136.
44) A. K. Dubey, H.S. Shan, N.K. Jain, Int. J. Manuf. Technol. Manag. 17(4) (2009) 364–372.
45) P. S. Pa, Int. J. Adv. Manuf. Technol. 40(3) (2009) 277–285.
46) K. P. Rajurkar, G. Levy, A. Malshe, M. M. Sundaram, J. McGeough, X. Hu, A. DeSilva, CIRP Ann. 55(2) (2006) 643–666.
47) H. Deng, K, Hosoya, Y. Imanishi, K. Endo, K. Yamamura, Electrochem. Commun. 52 (2015) 5–8.
48) J. Murata, K. Yodogawa, K. Ban, Int. J. Mach. Tools Manu. 114 (2017) 1–7.
49) B. Gao, W. J. Zhai, Q. Zhai, Y. Q. Shi, ECS J. Solid State Sci. Technol. 9(4) (2020) 044005.
50) X. Yang, X. Yang, R. Sun, K. Kawai, K. Arima, K. Yamamura, Nanomanuf. Metrol. 2 (2019) 140–147.
51) N. Gabouze, A. Keffous, T. Kerdja, Y. Belaroussi, Appl. Surf. Sci. 255(15) (2009) 6751–6756.

52) S. Lin, Ultrasonics 33(6) (1995) 445–448.
53) W.T. Richards, A.L. Loomis, J. Am. Chem. Soc. 49 (1927) 3086–3100.
54) M. E. Fitzgerald, V. Griffing, J. Sullivan, J. Chem. Phys. 25(5) (1956) 926–933.
55) M. Ashokkumar, Ultrason. Sonochem. 18(4) (2011) 864–872.
56) S. Muthukumaran, S. E. Kentish, G. W. Stevens, M. Ashokkumar, Rev. Chem. Eng. 22(3) (2006) 155–194.
57) F. O. Schmitt, C. H. Johnson, A. R. Olson, J. Am. Chem. Soc. 51(2) (1929) 370–375.
58) H. Frenzel, H. Schultes, Zeitschrift für Physikalische Chemie 27(1) (1934) 421–424.
59) V. B. Claus, A. D. S. Hall, Z. Tech. Phys. 16(3) (1935) 80–82.
60) C. W. Porter, L. Young, J. Am. Chem. Soc. 60(6) (1938) 1497–1500.
61) D. J. Flannigan, K. S. Suslick, Nature, 434(7029) (2005) 52–55.
62) D. J. Flannigan, K. S. Suslick, Nat. Phys. 6(8) (2010) 598–601.
63) Y. Hu, D. Shi, Y. Hu, H. Zhao, X. Sun, Mater. 11(10) (2018) 2022.
64) J. L. Luche, Synthetic organic sonochemistry. Springer Science & Business Media. (2013)
65) A. Gedanken, Ultrason. Sonochem. 11(2) (2004) 47–55.
66) P. Riesz, T. Kondo. Free Radic. Biol. Med. 13(3) (1992) 247–270.
67) P. Linares, F. Lazaro, M. D. de Castro, M. Valcarcel, J. Autom. Chem. 10(2) (1988) 88–94.
68) J. Lindley, T. J. Mason, Chem. Soc. Rev. 16 (1987)275–311.
69) A. Cobley, T. Mason, Circuit World 33(3) (2007) 29–34.
70) C. Suresh, H. Nagabhushana, G. P. Darshan, R. B. Basavaraj, B. D. Prasad, S. C. Sharma, J. S. Begum, Arab. J. Chem. 11(2) (2018) 196–213.
71) M. Postema, G. Schmitz, Ultrason. Sonochem. 14(4) (2007) 438–444.
72) T. J. Mason, T. J. Mason, New York: Oxford University Press 2 (1999).
73) E. Shamoto, T. Moriwaki, CIRP Ann. Manuf. Technol. 43 (1994) 35–38.
74) J. Gan, X. Wang, M. Zhou, B. Ngoi, Z. Zhong, Int. J. Adv. Manuf. Technol. 21 (2003) 952–955.
75) B. Azarhoushang, T. Tawakoli, Int. J. Adv. Manuf. Technol. 57 (2011) 945–955.
76) J. Deng, T. Lee, J. Eur. Ceram. Soc. 22(8) (2002) 1235–1241.
77) D. K. Baek, J. T. Ko, H. Y. Seung, J. Mater. Process Technol. 213(2013) 553–569.
78) R. Halm, P. Schulz, In Ceram. Forum Int./Ber. DKG 70(7) (1993) 336–342.
79) G. Nishimura, Ultrasonic machining – Part I J. Fac. Eng. Tokyo Univ. 24 (3) (1954) 65–100.
80) E. A. Neppiras, Metalworking Prod. 100 (1956) 1283–1288, 1333–1336, 1377–1382, 1420–1424, 1464–1468, 1554–1560, 1599–1604.
81) J. B. Kohls, Carbide Tool J. 16(5) (1984) 12–15.
82) M.A. Moreland, D. O. Moore, Am. Ceram. Soc. Bull. 67(6) (1988) 1045–1047.
83) K. H. W. Scab, SME Tech. Paper. 11 (1990) 90–294.
84) E.V. Nair, A. Ghosh, Int. J. Prod. Res. 23 (1985) 731–753.

85) M. Ramulu, Int. J. Manuf. Technol. Manag. 7(2–4) (2005) 107–126.
86) T.L. Smith, Ultrasonics, 11(5) (1973) 196–198.
87) S. R. Ghabrial, S. M. Saleh, A. Moisan, D. Kremer, SME Manufacturing Engineering Transactions and 12th NAMRC North American Manufacturing Research, (1984) 227–232.
88) R. Singh, J. S. Khamba, In Proceedings of the 21st AIMTDR Conference (2004) 20–22.
89) V. K. Jain, Advanced Machining Processes. Allied Publishers, New Delhi, India, 2009.
90) R. Kataria, J. Kumar, B. S. Pabla, Mater. Manuf. Process 31(5) (2016) 685–693.
91) J. Kumar, Mach. Sci. Technol. 17(3) (2013)325–379.
92) N. Churi, Doctoral dissertation, Kansas State University, USA, (2010).
93) P. Legge, Ultrasonics. 4(3) (1966) 157–162.
94) P. Legge, Ind. Diam. Rev. 24(278) (1964) 20–24.
95) H. Hocheng, N. H. Tai, C. S. Liu. Compos. Part A Appl. Sci. Manuf. 31(2) (2000) 133–142.
96) C. Zhang, P. Feng, S. Zheng, Z. Wu, D. Yu, Adv. Mat. Res. 230–232 (2011) 644–648.
97) H. Gong, F. Z. Fang, X. T. Hu, Int. J. Mach. Tools Manuf. 50 (2010) 303–307.
98) Z. J. Pei, P. M. Ferreira, S. G. Kapoor, M. Haselkorn, Int. J. Mach. Tools Manuf. 35(7) (1995) 1033–1046.
99) M. Zhou, M. Wang, G. Dong, Mater. Manuf. Process 31(5) (2016) 673–678.
100) S. Xu, K. Shimada, M. Mizutani, T. Kuriyagawa, Int. J. Mach. Tools Manuf. 86 (2014) 12–17.
101) D. B. Marsgall, H. S. Abdalla, J. Am. Ceram. Soc. 65 (1982) 561–566.
102) B. R. Lawn, A. G. Evans, D. B. Marshall, J. Am. Ceram. Soc. 63(9–10) (1980) 574–581.
103) V. Gupta, P. M. Pandey, Proc. Inst. Mech. Eng. B. J. Eng. Manuf. 232(9) (2016) 1549–1560.
104) G. Spur, S. E. Holl, J. Mater. Process Technol. 62(4) (1996) 287–293.
105) M. Komaraiah, P. Narasimha Reddy, Int. J. Prod. Res. 29(11) (1991) 2177–2187.
106) E. Uhlmann, G. Spur, CIRP Annals, 47(1) (1998) 249–252.
107) S. Agarwal, P. V. Rao, Int. J. Mach. Tools Manuf. 50(12) (2010)1065–1076.
108) Z. Ke, H. Qing, L. Liang, R. Yi, Ultrasonics 80 (2017) 9–14.
109) W. Xu, X. Lu, G. Pan, Y. Lei, J. Luo, Appl. Surf. Sci. 256 (2010) 3936–3940.
110) W. Zhai, B. Gao, J. Chang, H. Wang, Nanomanuf. Metrol. 2 (2019) 36–44.

# Chapter 3
# Anodic oxidation mechanism of 4H-SiC (0001)

## 3.1 Introduction

In electrochemical mechanical polishing (ECMP) and ultrasonic vibration assisted ECMP (UAECMP), 4H-SiC is softened by anodic oxidation and then the generated oxidized layer is removed by fixed soft abrasives. The hardness of the fixed soft abrasive is much lower than that of SiC and only the oxidized layer is removed with no damage induced to the bulk SiC material. Therefore, the MRR of ECMP and UAECMP and the obtained surface roughness mainly depend on the anodic oxidation rate of SiC. Thus, it is necessary to clarify the anodic oxidation mechanism of 4H-SiC (0001) to achieve high efficiency and good surface quality. This chapter investigates the relationship between the anodizing parameters and the anodic oxidation of SiC and the accompanying mechanism.

## 3.2 Anodic oxidation and ECMP setup

### 3.2.1 Anodic oxidation setup

Fig. 3.1(a) shows a schematic of the anodic oxidation setup, which is a three-electrode anodic oxidation system. In the three-electrode anodic oxidation system, a SiC substrate is the working electrode (WE), a platinum mesh is set face-to-face with the substrate and serves as a counter electrode (CE), and an Ag|AgCl reference electrode is installed close to the substrate. The oxidation parameters are controlled using a potentiostat, which also monitors the current and potential during the anodic oxidation process.

The n-type 4°-off 4H-SiC wafers used in this study were supplied by TankeBlue Semiconductor Co., Ltd. The wafers had a thickness of 350 μm and a specific resistance in the range of 0.015–0.028 Ω·cm. They were cleaned before anodic oxidation using the wet chemical method. First, the wafers were dipped in a solution of $H_2SO_4$ (97 wt%) and $H_2O_2$ (34 wt%) with a volume ratio of 4:1 to remove contamination. They remained in the solution for 10 min and were then rinsed with deionized water for another 10 min. Next, the wafers were dipped in a concentrated hydrofluoric acid (HF) solution (50 wt%) for 10 min to remove native oxides. This was also followed by rinsing with deionized water for 10 min. Finally, the wafers were dried using $N_2$ gas. All of the experiments were conducted on the most commonly used 4H-SiC (0001) face and the

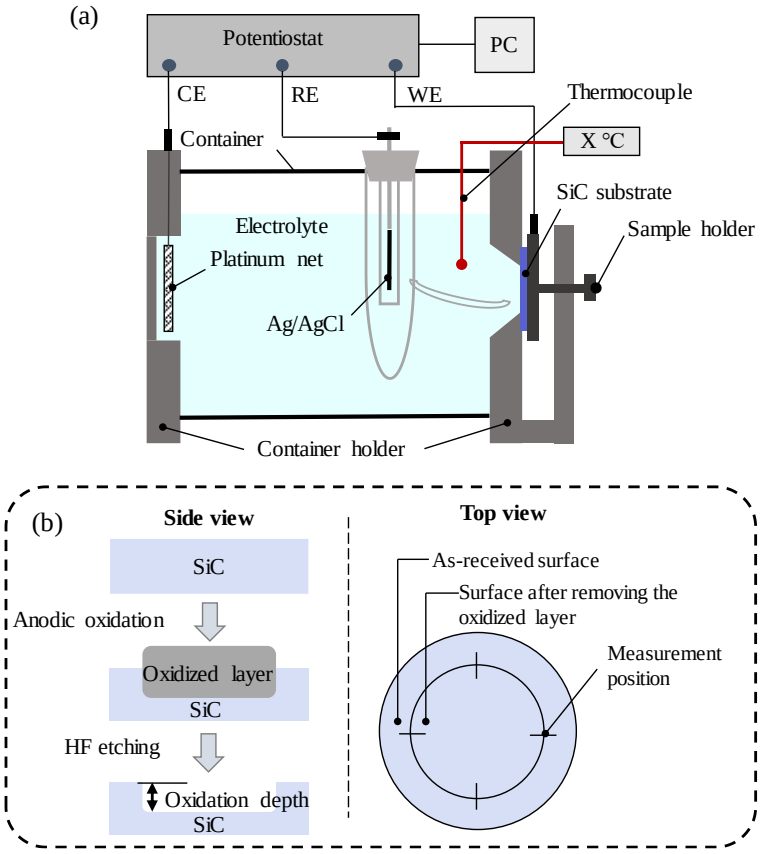



**Fig. 3.1** (a) Anodic oxidation setup; the oxidation area is a circle with an area of 1 $cm^2$. (b) Definition and measurement position of oxidation depth.

anodic oxidation area was 1 $cm^2$. The oxidized wafers were immersed in an HF solution to remove the generated oxidized layer and the anodic oxidation depth could be measured, as shown in Fig. 3.1(b), using a scanning white light interferometer (SWLI) (NewView 8300, Zygo). For each anodic oxidation experiment, the average oxidation depth of four locations evenly distributed along the edge of the circular oxidation area was taken as the oxidation depth, as shown in Fig. 3.1(b). The anodic oxidation rate was evaluated based on the change in oxidation depth per minute.

### 3.2.2 ECMP setup

Fig. 3.2(a) shows a schematic diagram of the ECMP machine, which consisted of an anodic oxidation system and a polishing unit. A SiC wafer was the WE and mounted on a metal plate while a ring grinding stone with an outer and inner diameter of 11 and 6 mm, respectively, was fixed on the end face of the spindle. The grinding stone was in contact with the SiC surface at a certain polishing pressure and an elastic resin was set between the grinding stone and spindle to adjust the parallelism between the grinding stone and the SiC surface. The CE was the tip of the spindle, which was made of stainless steel. The surface of the SiC wafer, grinding stone, and the

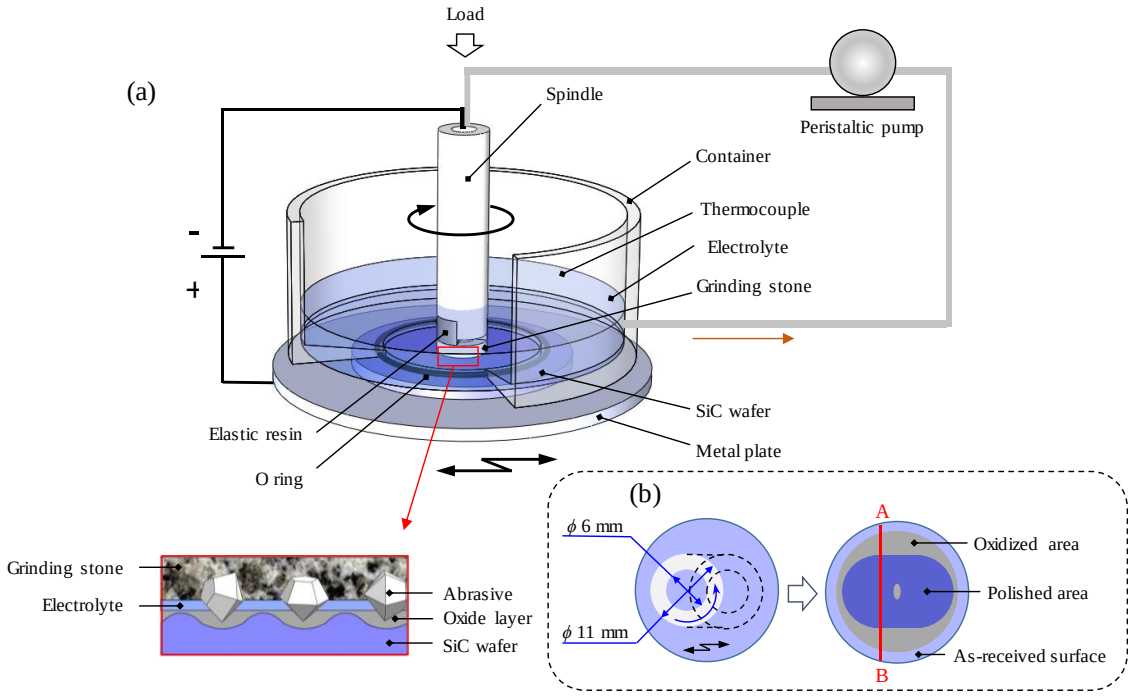



**Fig. 3.2** ECMP setup.

tip of the spindle were immersed in electrolyte and a potentiostat was applied to control the anodic oxidation condition.

During ECMP, the grinding stone was rotated with the spindle and the SiC wafer was reciprocated in the x-direction. The electrolyte was circulated by a peristaltic pump and supplied from the center of the spindle to prevent ejection from the polishing area owing to the centrifugal force of the spindle. Thus, the polishing area shown in Fig. 3.2(b) was defined. The removal depth was measured using a stylus profiler (Surfcom 1400D, Tokyo Seimitsu) along the line of A–B shown in Fig. 3.2(b). The removal depth was calculated by aligning the height of the as-received surface (unpolished area) to zero with consideration of wafer warp. The surface roughness after ECMP was measured using a SWLI and the residual strain on the ECMP-processed surface was evaluated using a confocal Raman microscope (RAMANtouch, Nanophoton).

## 3.3 Effects of electrolyte type and concentration

Three types of electrolytes, NaOH, NaCl, and $NaNO_3$, with concentrations of 0.01, 0.02, 0.05, 0.1, 0.2, 0.5, 1, 2, and 5 wt% were used in the anodic oxidation of 4H-SiC. The potential was set at 25 V and the oxidation time was 20 min. Fig. 3.3(a) shows the relationship between NaOH, NaCl, and $NaNO_3$ concentration and anodic oxidation rate. It is clear that anodic oxidation rate has the same trend with the change in concentration of the three electrolytes; as the electrolyte

concentration increases, the oxidation rate first increased and then decreased. However, the concentrations of different electrolytes were different when the anodic oxidation rate reached its maximum. These maximum anodic oxidation rates were reached at concentrations of 0.02, 0.05, and 0.05 wt% for NaOH, NaCl, and $NaNO_3$, respectively. Fig. 3.3(b) shows the electrical conductivity of these three electrolytes with increasing concentration. The electrical conductivity linearly increased with the increase in electrolyte concentration. However, at the same concentration, NaOH had the largest electrical conductivity, followed by NaCl, and the conductivity of $NaNO_3$ was the smallest while close to that of NaCl. Since the anodic oxidation rate was the first to reach a maximum in NaOH, as shown in Fig. 3.3(a), it seems that the maximum anodic oxidation rate is related to the electrical conductivity of the electrolyte. In order to verify the relationship between anodic oxidation rate and electrolyte conductivity, the conductivities of NaOH, NaCl, and $NaNO_3$ with different concentrations are taken as the horizontal axis and the anodic oxidation rate is taken as the vertical axis in Fig. 3.3(c). It is clear that the changes of anodic oxidation rate are mainly related to conductivity but not the type of electrolyte; as the electrolyte conductivity increases, the anodic oxidation rate first increased and then decreased. The anodic oxidation rate reached the maximum when the electrolyte conductivity was about 0.097 S/m.

Fig. 3.4(a) shows the current changes during anodic oxidation with NaCl electrolytes at different concentrations and Fig. 3.4(b) shows the relationship between the initial current in Fig. 3.4(a) and the electrolyte concentration. The initial current of anodic oxidation increases with the increase in electrolyte concentration. As the anodic oxidation progresses, the oxidation currents dropped significantly. This is considered to be caused by the hindrance of the oxide layer on the SiC surface. For 20-min anodic oxidation, the oxidation time was too long and the oxide layer may have too much of a hindrance effect on the anodic oxidation rate. Therefore, it is necessary

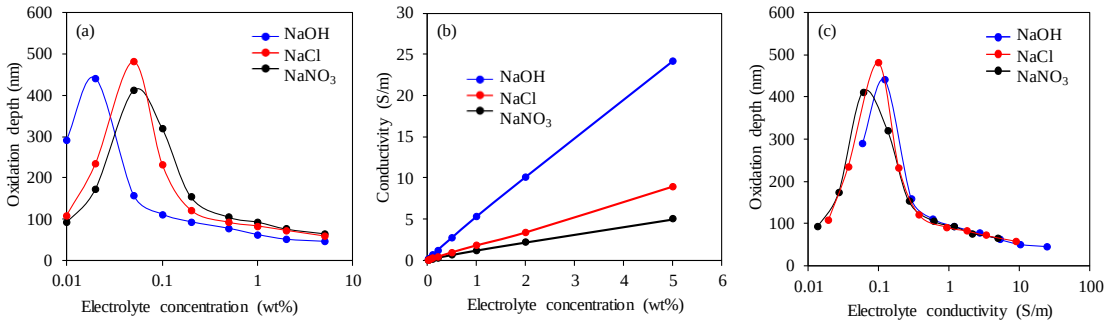



**Fig. 3.3** Relationships between (a) electrolyte concentration of NaOH, NaCl, and $NaNO_3$ and anodic oxidation rate; (b) electrical conductivity and electrolyte concentration of NaOH, NaCl, and $NaNO_3$; (c) anodic oxidation rate and electrical conductivity of NaOH, NaCl, and $NaNO_3$.

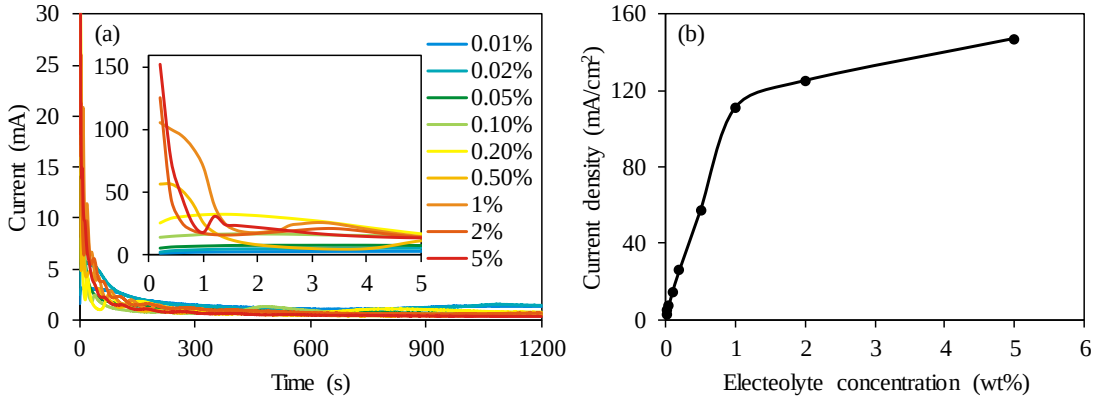



**Fig. 3.4** (a) Current changes in anodic oxidation with different NaCl concentrations; (b) relationship between the initial current in Fig. 3.4(a) and the electrolyte concentration.

to shorten the oxidation time to precisely investigate the relationship between oxidation rate and electrolyte concentration.

Fig. 3.5 shows the change of anodic oxidation rate under different NaCl electrolyte concentrations with different anodic oxidation times. Overall, the anodic oxidation rate increased with decreasing oxidation time. The relationship between anodic oxidation rate and electrolyte concentration were almost the same for these three different anodic oxidation times; they all first increased, then decreased, and finally maintained a certain level after an electrolyte concentration larger than 2 wt%. However, the time required to reach the maximum anodic oxidation rate differed. When the oxidation time was 20 min, the oxidation rate reached the maximum at an electrolyte concentration of 0.05 wt% and the maximum anodic oxidation rate was ~6.85 times than that of 2 wt% concentration. When the oxidation time was 30 s, the maximum anodic oxidation rate was obtained at an electrolyte concentration of 0.1 wt%, but the maximum anodic oxidation rate was ~2.21 times than that at the electrolyte concentration of 2 wt%. When the oxidation time was decreased to 5 s, the oxidation rate reached its maximum at an electrolyte concentration of 0.5 wt%, which was only 1.84 times that at an electrolyte concentration of 2 wt%. In other words, the electrolyte concentration at the maximum oxidation rate increases as the oxidation time decreases. Considering that the initial anodic oxidation current increased with an increase in electrolyte concentration, as shown in Fig. 3.4(b), these results indicate that the shorter the oxidation time, the stronger the effect of the initial current on the anodic oxidation rate. For long anodic oxidation, the decrease in anodic oxidation rate may be caused by the hindrance of the oxide layer. From Fig. 3.4(a), it can be seen that the higher the initial current, the faster the current decreases, which suggests that the hindrance of the oxide layer is greater when the current is higher. It has been reported that the oxide layer generated by anodic oxidation has a porous structure [1]. These results indicate that the oxide layer generated at a higher current

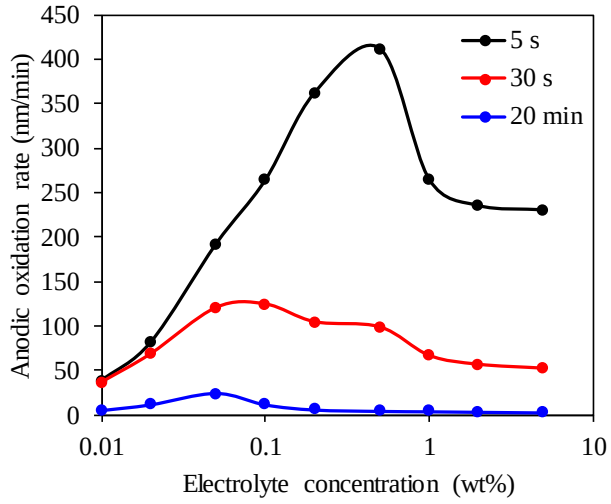



**Fig. 3.5** Relationship between the anodic oxidation rate and the concentration of NaCl electrolyte with oxidation times of 5 s, 30 s, and 20 min.

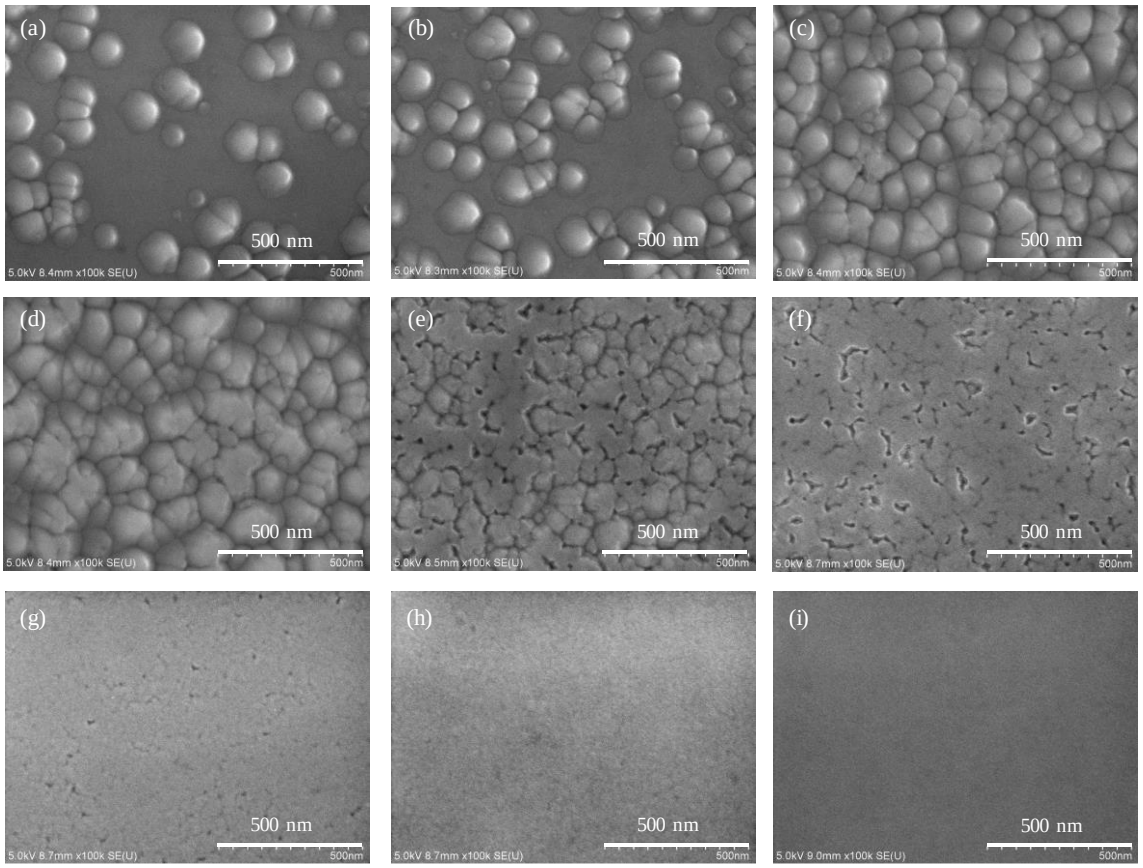



**Fig. 3.6** SEM images of the SiC surface after anodic oxidation at 25 V for 30 s with NaCl electrolyte concentrations of (a) 0.01, (b) 0.02, (c) 0.05, (d) 0.1, (e) 0.2, (f) 0.5, (g) 1, (h) 2, and (i) 5 wt%.

had a denser structure and a greater hindrance on the anodic oxidation rate than that generated at a lower current.

Fig. 3.6 shows the topographies of SiC surfaces after anodic oxidation at 25 V for 30 s in NaCl electrolytes with concentrations of 0.01, 0.02, 0.05, 0.1, 0.2, 0.5, 1, 2, and 5 wt%. After anodic oxidation with an electrolyte concentration of 0.01 wt%, oxide protrusions were randomly generated on the oxidized SiC surface, which shows that the anodic oxidation was not uniform. With the increase of electrolyte concentration, the number of generated oxide protrusions increased. Until the electrolyte concentration was increased to 0.1%, the entire SiC surface was covered by oxide protrusions after anodic oxidation. As the electrolyte concentration was further increased, the generated oxide protrusions became connected, merging into each other. It is clear that the oxidized surface became flat and smooth after the electrolyte concentration was increased to 5 wt%. It can be considered that with the increase in electrolyte concentration, the initial current in the anodic oxidation increased and the anodic oxidation of the SiC surface changed from random and non-uniform oxidation to uniform oxidation, forming a dense oxide layer.

To clearly observe the structure of the oxide layer generated at different electrolyte concentrations, SiC surfaces were anodically oxidized at 25 V for 30 min in NaCl electrolytes with concentrations of 0.01, 0.1, and 5 wt% to generate thick oxide layers. The structure of the oxide layers was observed using cross-sectional scanning electron microscope (SEM). Fig. 3.7 shows cross-sectional SEM images of the oxide layers. Fig. 3.7(b) shows a cross-sectional SEM image of the as-received SiC substrate where no oxide layer was observed. Fig. 3.7(c) shows a cross-sectional SEM image of the SiC substrate after anodic oxidation in 0.01 wt% NaCl electrolyte; an oxide layer with a thickness of about 670 nm was observed with several pores inside, indicating that the oxide layer had a certain porosity. In addition, the interface between the oxide layer and the bulk SiC was very rough, which showed that the anodic oxidation in 0.01 wt% NaCl electrolyte was uneven. When the electrolyte concentration was increased to 0.1 wt%, the number and size of pores in the oxide layer decreased and the interface between the oxide layer and bulk SiC became smoother, as shown in Fig. 3.7(d). After the electrolyte concentration was increased to 5 wt%, pores in the oxide layer were not observed and the interface between the oxide layer and bulk SiC was considerably smooth, as shown in Fig. 3.7(e). It could be considered that with the increase in electrolyte concentration, the anodic oxidation of the SiC surface becomes uniform and the generated oxide layer becomes dense.

In addition, nanoindentation tests were conducted on the SiC surfaces after anodic oxidation at 25 V for 30 min with different electrolyte concentrations to compare the hardness of the generated oxide layers. A load of 2 mN was applied to these surfaces by a Berkovich-type indenter made of diamond and the surface hardness was calculated by the Oliver–Pharr method. Fig. 3.8(a) shows typical load–displacement curves of these surfaces and Fig. 3.8(b) shows the hardness calculated

from the load–displacement curves. It is obvious that the hardness of the oxide layer increased as the electrolyte concentration increased. This confirmed that electrolyte concentration has a significant effect on the structure of the anodic oxide layer; the higher the electrolyte concentration, the denser the oxide layer.

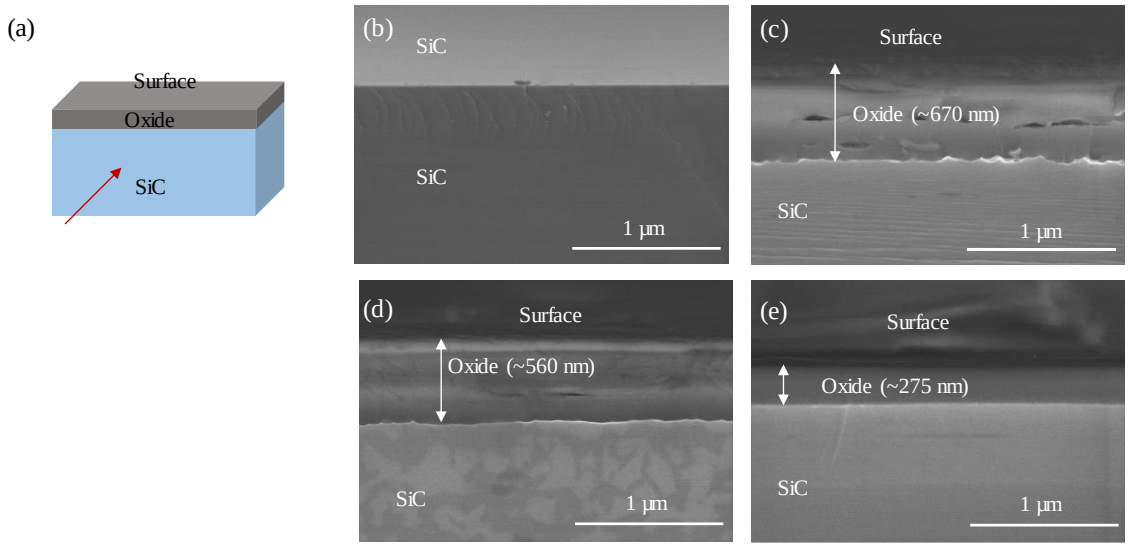



**Fig. 3.7** Observation of the oxide layer by cross-sectional SEM. (a) Schematic diagram of the observation. Cross-sectional SEM images of (b) as-received SiC substrate and SiC substrate after anodic oxidation at 25 V for 30 min with NaCl electrolyte concentrations of (c) 0.01, (d) 0.1, and (e) 5 wt%.

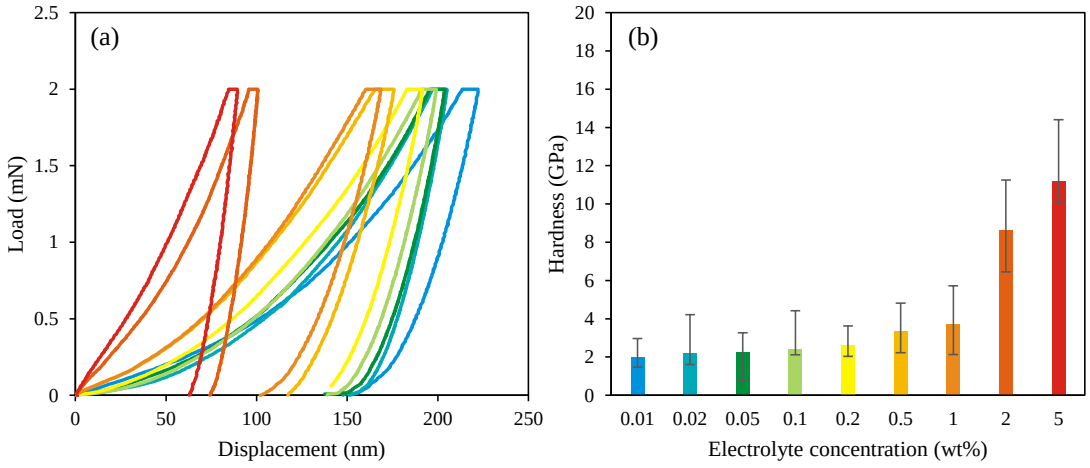



**Fig. 3.8** Hardness of SiC surface and anodic oxidized SiC surface at 25 V for 30 min with electrolyte concentrations of 0.01, 0.02, 0.05, 0.1 ,0.2, 0.5, 1, 2, and 5 wt%. (a) Load-displacement curves.

Fig. 3.9 shows SWLI images of the oxidized SiC surfaces in Fig. 3.6 after removing the oxide layer by HF etching. On the surface processed by 0.01 wt% NaCl electrolyte, many pits were observed, as shown in Fig. 3.9(a). With the increase in electrolyte concentration, the depth of pits on the surface became shallow and almost disappeared completely when the electrolyte concentration was 5 wt%. The *S*q and *S*z surface roughness decreased significantly with increasing electrolyte concentration and, finally, a smooth surface was obtained at an electrolyte concentration of 5 wt%. In the anodic oxidation of SiC, it has been reported that oxide protrusions on the oxidized surface changed with oxidation current density; the size of the oxide protrusions decreased and the density of the oxide protrusions increased with increasing current density [2)]. In Fig. 3.4, it can be seen that the initial oxidation current increased with the increase in electrolyte concentration. Therefore, the effect of electrolyte concentration on the anodic oxidation of SiC can be attributed to the oxidation current flowing during anodic oxidation. At the same potential

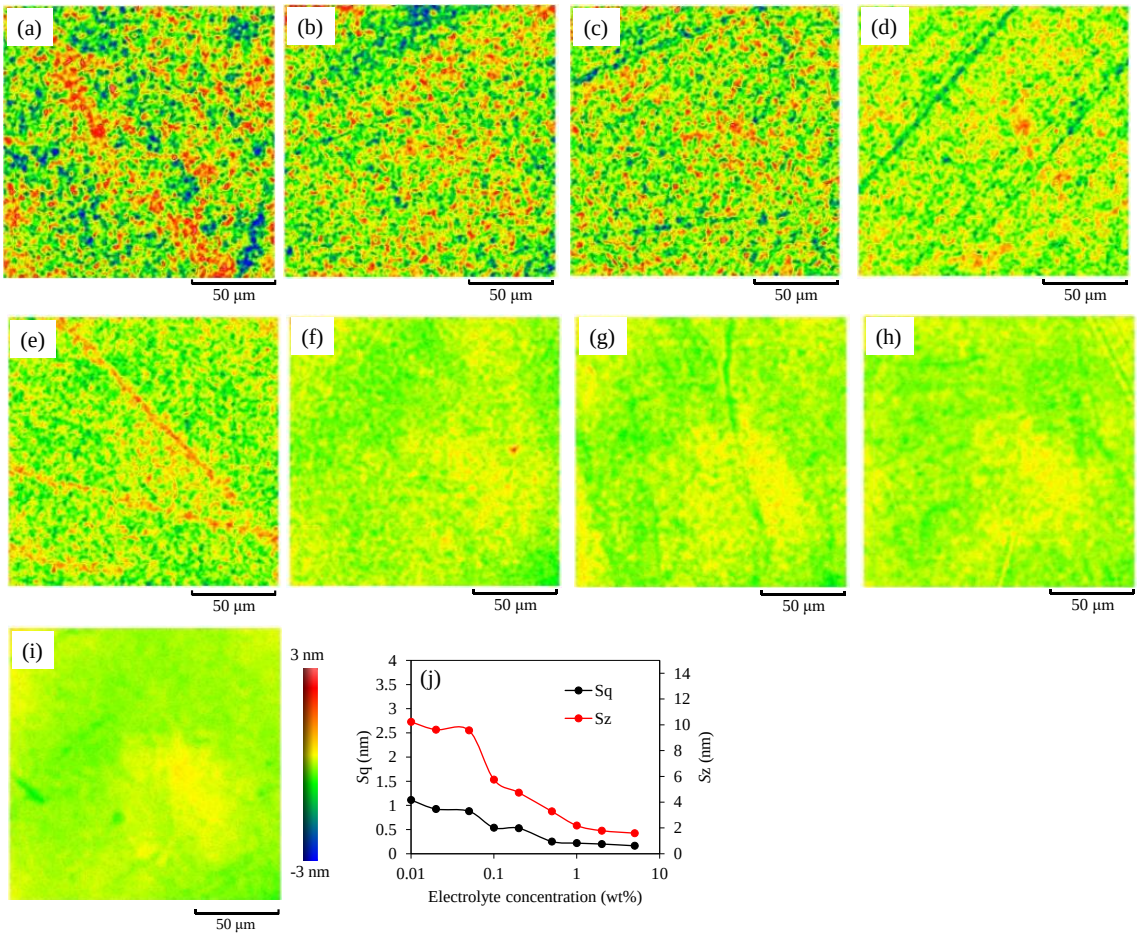



**Fig. 3.9** SWLI images of 4H-SiC surfaces oxidized with different electrolyte concentrations after removing the oxide layer by HF etching. (a) 0.01, (b) 0.02, (c) 0.05, (d) 0.1, (e) 0.2, (f) 0.5, (g) 1, (h) 2, and (i) 5 wt%; (j) changes of surface roughness with electrolyte concentration.

and with an increase in electrolyte concentration, the resistance of the electrolyte decreased and the oxidation current increased, which made the anodic oxidation even and the generated oxide layer dense.

In order to confirm the above hypothesis, anodic oxidation at current densities of 3 and 10 mA/cm$^2$ for 30 s with different electrolyte concentrations were applied to SiC surfaces. Then, oxidized SiC surfaces were dipped in HF to remove the oxide layer and the surface roughness and oxidation depth of the oxidized/etched surfaces were measured. Fig. 3.10 (a) and (b) show SWLI images after removing the oxide layer of 4H-SiC (0001) surfaces oxidized at current densities of 3 and 10 mA/cm$^2$, respectively, with an electrolyte concentration of 5 wt%. Several

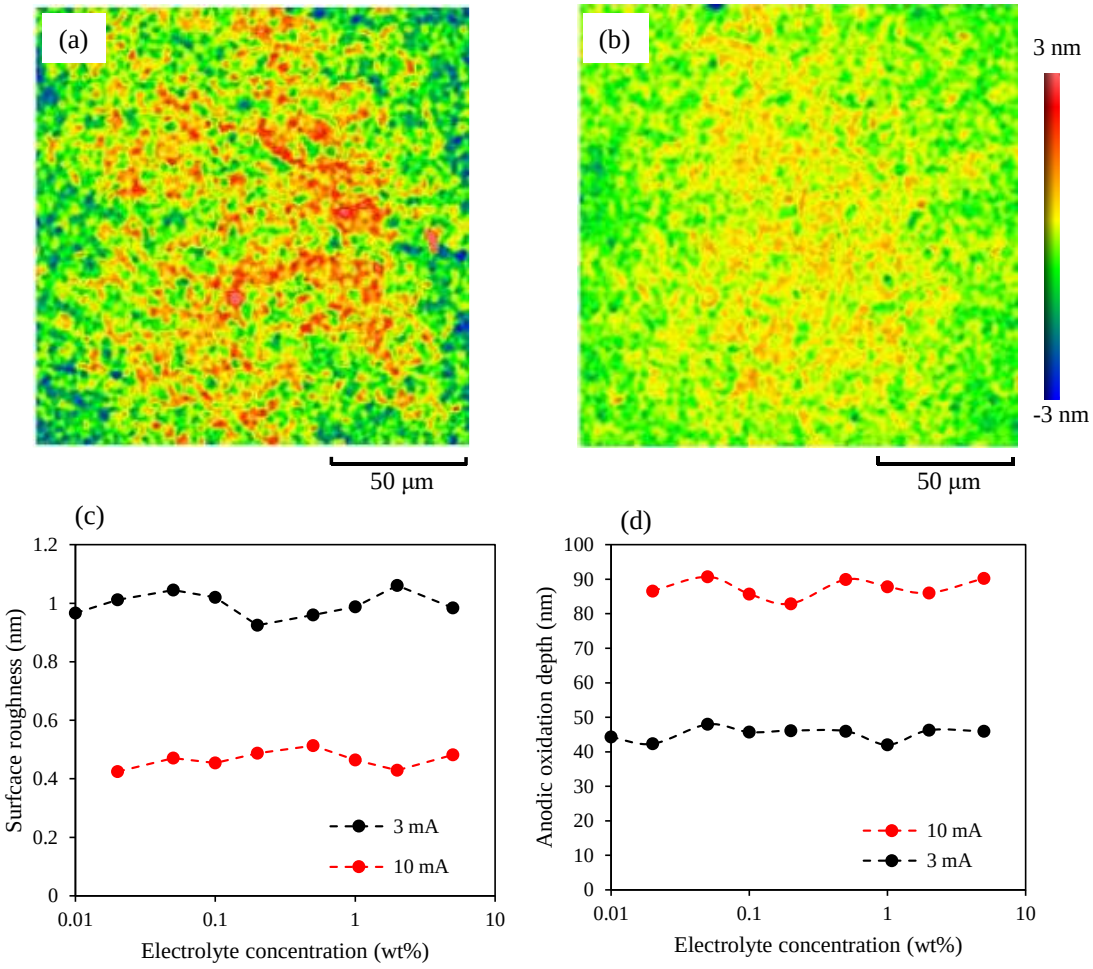



**Fig. 3.10** SWLI images of 4H-SiC (0001) surfaces oxidized in NaCl electrolyte with concentration of 5 wt% at (a) 3 mA/cm$^2$ (*Sq* = 0.966 nm; *Sz* = 14.864 nm) and (b)10 mA/cm$^2$ (*Sq* = 0.482 nm; *Sz* = 10.710 nm) after removing the oxide layer. (c) Anodic oxidation depths and (d) surface roughness of SiC surface after anodic oxidation at 3 and 10 mA/cm$^2$ for 30 s with electrolyte concentrations of 0.01, 0.02, 0.05, 0.1, 0.2, 0.5, 1, 2, and 5 wt%.

pits, which were caused by non-uniform anodic oxidation, were observed on both surfaces while the depth of the pits obtained at 3 mA/cm$^2$ was obviously larger than that obtained at 10 mA/cm$^2$. Fig. 3.10 (c) and (d) show the changes of *S*q surface roughness and anodic oxidation depth at current densities of 3 and 10 mA/cm$^2$, respectively, with different electrolyte concentrations. All the *S*q surface roughness values obtained with different electrolyte concentrations at 3 and 10 mA/cm$^2$ were maintained at about 1 and 0.45 nm, respectively, and the anodic oxidation depths were maintained at 45 and 90 nm, respectively. It is confirmed that when the electric current densities were the same, electrolyte concentration does not affect the surface roughness or the anodic oxidation rate of the SiC surface. The surface roughness after anodic oxidation and the anodic oxidation depth mainly depend on the electric current density. The surface roughness decreased, and the anodic oxidation rate increased when the electric current density was increased from 3 to 10 mA/cm$^2$. It is confirmed that the electric current plays an important role in the anodic oxidation of SiC.

## 3.4 Charge utilization efficiency in the anodic oxidation of SiC

### 3.4.1 Relationship between current density and charge utilization efficiency

Anodic oxidation experiments were conducted to investigate the effect of current density on the anodic oxidation of SiC. In the 1-wt% NaCl electrolyte, CMP-processed SiC surfaces were anodically oxidized using different current densities, ranging from 1 to 30 mA/cm$^2$, with the same charge amount of 300 mC in the first group while the same oxidation time of 10 s was used in the second group. Then, the oxide layers were removed by HF etching and the oxidation depths of the SiC surfaces were measured by SWLI. On the basis of Faraday's laws of electrolysis, the anodic oxidation depths would be the same in the first group owing to the samples in this group experiencing the same charge, while that of the second group would be linearly increased with current density. Figs. 3.11 and 3.12 show anodic oxidation depths obtained with different current densities. In Fig. 3.11, it can be seen that the anodic oxidation depth decreased with increasing current density regardless of having the same charge amount. In the case of the same oxidation time, as shown in Fig. 3.12, the oxidation depth linearly increased with current density below 15 mA/cm$^2$, then the increasing amount decreased when the current density increased to greater than 20 mA/cm$^2$. These results indicate that the charge utilization efficiency in the anodic oxidation of SiC decreased with increasing current density.

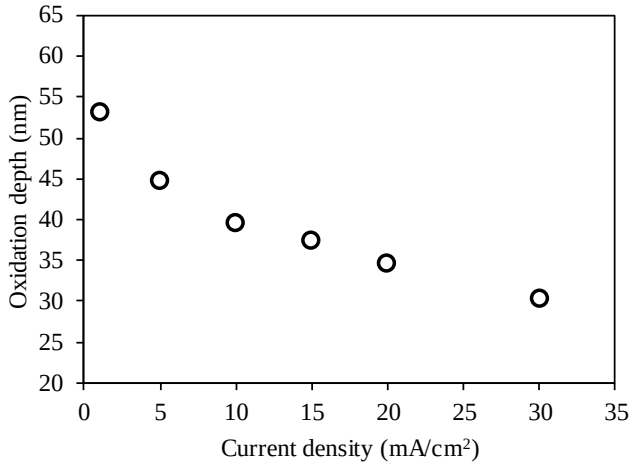



**Fig. 3.11** Anodic oxidation depths obtained at different electronic current densities with the same charge amount (300 mC).

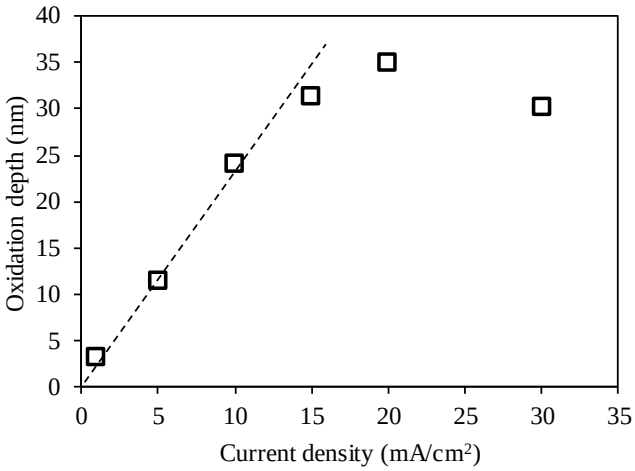



**Fig. 3.12** Anodic oxidation depths obtained at different current densities with the same oxidation time (10 s).

The results in Figs. 3.11 and 3.12 are obtained at purely anodic oxidation conditions, thus the generated oxide layer might have a hindrance effect on the anodic oxidation rate, especially under large current densities, due to the dense structure of the generated oxide layer. To remove the effect of the oxide layer, ECMP with a #8000 diamond grinding stone at different electronic current densities was conducted on the as-sliced SiC surfaces for 20 min. The grinding stone was rotated by the spindle at a speed of 1500 rpm, under a set polishing pressure (70 kPa), and a sodium chloride aqueous solution (NaCl *aq*.) (1 wt%) was used as the electrolyte. Fig. 3.13 shows the relationship between the MRR and current density obtained in these ECMP experiments. It

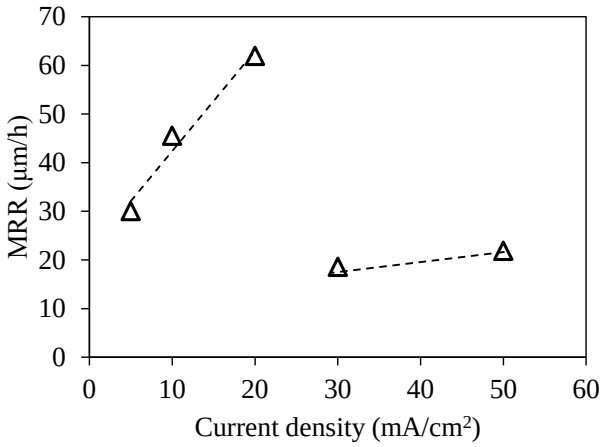



**Fig. 3.13** Relationship between MRR and electronic current density in ECMP.

can be seen that below 20 mA/cm$^2$, the MRR linearly increased with increasing current density. An MRR of 62 μm/h was reached at a current density of 20 mA/cm$^2$. However, when the current density was greater than 30 mA/cm$^2$, the MRR decreased to about 20 μm/h and slightly increased with increasing current density. This indicates that the anodic oxidation of the SiC surface was reduced when the current density was greater than 30 mA/cm$^2$, which is similar to that obtained in the anodic oxidation experiment shown in Fig. 3.12. Therefore, it is confirmed that the current utilization efficiency decreased after the electric current density increased beyond a certain value. In this case, it can be inferred that a part of the electric current was distributed among other chemical reactions, which hindered the anodic oxidation of the SiC surface.

## 3.4.2 Modeling of the anodic oxidation system of SiC

In general, the Fermi level of n-type SiC is higher than that of the redox couple in the electrolyte ($E_F > E^0_{F(O/R)}$) in the SiC-aqueous solution system. Therefore, when a SiC surface is in contact with the electrolyte, electrons ($e^-$) flow from the SiC to the redox pair in the electrolyte and the Fermi level of SiC will decrease and result in band bending at the SiC surface. Simultaneously, an electric field is established at the interface between SiC and the electrolyte that will prevent the transfer of electrons from SiC to the electrolyte. Thus, the transfer of electrons at the interface will reach a dynamic equilibrium after a period of time. After reaching the dynamic equilibrium, $E^0_{F(O/R)}$ becomes equal to $E_F$. When an external positive potential, $\eta$, is applied to the SiC, the Fermi level of SiC will decrease by $e\eta$, which will increase the degree of band bending near the SiC surface. Thus, more electrons will move from the SiC surface to the bulk SiC, causing a large number of holes ($h^+$) to gather on the surface. At the same time, electrons more easily transfer from substances in the electrolyte to the SiC, which results in oxidation reactions. In the SiC-NaCl aqueous solution system, oxidation of SiC, $H_2O$, and $Cl^-$ may occur at the interface between

the SiC and the electrolyte.

There are two reaction paths widely considered in the anodic oxidation of SiC, namely, SiC reacts with $H_2O$ [3-5] and SiC reacts with $OH^-$ [6-9]. In Section 3.3, the electrolyte type had no effect on the anodic oxidation of SiC; the anodic oxidation rate of SiC did not increase in the NaOH electrolyte compared with that in NaCl and $NaNO_3$ electrolytes. During SiC anodic oxidation with NaCl electrolyte, oxygen only exists in $H_2O$ and the amount of $OH^-$ generated by water ionization is much smaller. Therefore, it is considered that the SiC directly reacts with $H_2O$ in the anodic oxidation of SiC. Thus, the reactions that may occur on the SiC surface during the anodic oxidation are expressed as follows.

$$SiC + 3H_2O + 6h^+ \rightarrow SiO_2 + CO(g) + 6H^+, \tag{3.1}$$

$$SiC + 4H_2O + 8h^+ \rightarrow SiO_2 + CO_2(g) + 8H^+, \tag{3.2}$$

$$2H_2O \rightarrow O_2(g) + 4H^+ + 4e^-, \tag{3.3}$$

$$2Cl^- \rightarrow Cl_2(g) + 2e^-. \tag{3.4}$$

The chemical reaction that occurs on the cathode is as follows:

$$2H_2O + 2e^- \rightarrow 2OH^- + H_2(g). \tag{3.5}$$

In general, the priority of the reaction at the electrode interface depends on the equilibrium potential of the reaction. The lower the equilibrium potential, the easier it is for the reaction to occur. Generally, the following formula can be used to express an electrode reaction:

$$a\mathrm{O} + n\mathrm{e}^- \leftrightarrow b\mathrm{R}, \tag{3.6}$$

where $a$ and $b$ are the stoichiometric coefficients, O is the oxidation state substance, R is the reduced state substance, and $n$ is the number of electrons required for the reaction.

The actual equilibrium potential of each reaction can be calculated using the Nernst equation [10]:

$$\varphi = \varphi^0 + \frac{RT}{nF}\ln\frac{C_{\mathrm{O}}^a}{C_{\mathrm{R}}^b}, \tag{3.7}$$

where $\varphi^0$ is the equilibrium potential at standard conditions (temperature is 25 °C, pressure is 1 atm, and the molar concentration of reactants is 1 mol/L) and is also called the standard electrode potential; $R$ is the gas constant, $T$ is the absolute temperature, $F$ is the Faraday constant (96500 C/mol), and $C_{\mathrm{O}}$ and $C_{\mathrm{R}}$ are the activity of the oxidation state and reduced state substances, respectively. In general, $C_{\mathrm{O}}$ and $C_{\mathrm{R}}$ are equal to the molar concentration of the oxidation state and reduced state substances, respectively. When O or R is pure solid and pure liquid, $C_{\mathrm{O}}$ or $C_{\mathrm{R}}$ is treated as one; when O or R is gas, $C_{\mathrm{O}}$ or $C_{\mathrm{R}}$ is expressed by partial pressure ($P/P_0$) [11].

For an electrochemical reaction:

$$\sum \nu M + n\mathrm{e}^- = 0. \tag{3.8}$$

The standard equilibrium potential can be expressed as [12]

$$\varphi^0 = \frac{\sum \nu\mu_0}{nF}, \tag{3.9}$$

where $v$ are the stoichiometric coefficients, $M$ is the reaction substance, and $\mu_0$ is the standard chemical potential of substance $M$. For the reaction in Eq. (3.6), the equilibrium potential can be expressed as

$$\varphi^0 = \frac{\sum a\mu_{O0} - \sum b\mu_{R0}}{nF}, \tag{3.10}$$

where $\mu_{O0}$ and $\mu_{R0}$ are the standard chemical potential of substances O and R, respectively.

The standard chemical potentials of the substances in Eqs. (3.1)–(3.5) are shown in Table 3.1. On the basis of Eq. (3.10), the standard equilibrium potentials of Eqs. (3.1), (3.2), (3.3), (3.4), and (3.5) can be calculated to be −0.18 V, −0.16 V, 1.23 V, 1.40 V, and −0.83 V, respectively [13]. Therefore, the relationships between the actual equilibrium potential, $\varphi$, and the pH in every reaction can be calculated using Eq. (3.7), as shown in Table 3.2. In the actual anodic oxidation system of SiC, the pH of 1 wt% NaCl is 6.02 and its molar concentration is 0.17 mol/L. Then, based on the result in Table 3.2, $\varphi$ of Eqs. (3.1), (3.2), (3.3), (3.4), and (3.5) in the SiC-1 wt% NaCl system are obtained to be −0.54 V, −0.51 V, 0.87 V, 1.45 V, and −1.30 V, respectively. Therefore, on the SiC surface, the order of reaction occurrence, from easy to difficult, is Eqs. (3.2), (3.1), (3.3), and, finally, (3.4), as shown in Fig. 3.14.

A linear sweep voltammetry (LSV) experiment was conducted on the CMP-processed SiC surface to confirm the potential at which each reaction occurs. The anodic oxidation setup is shown in Fig. 3.1. Here, the oxidation potential was accurately controlled by referring to the Ag|AlCl electrode. The potential of the SiC substrate was swept from 0 to 50 V at a speed of 50

**Table 3.1** Standard chemical potentials of substances in the anodic oxidation of SiC [14].

| State | Substance | Standard chemical potential (kJ/mol) |
|---|---|---|
| Solution | $H_2O$ | −237.3 |
| | $H^+$ | 0 |
| | $OH^-$ | −157.37 |
| | $Cl^-$ | −131.23 |
| Solid | SiC | −109.25 |
| | $SiO_2$ (amorphous) | −786.14 |
| Gas | $H_2$ | 0 |
| | $O_2$ | 0 |
| | CO | −137.34 |
| | $CO_2$ | −394.56 |
| | $Cl_2$ | 6.91 |

**Table 3.2** Equilibrium condition for reactions in anodic oxidation of SiC.

| Number | Reaction | Equilibrium condition (V) |
|---|---|---|
| 3.1 | $SiC + 3H_2O + 6h^+ \rightarrow SiO_2 + CO(g) + 6H^+$ | $\varphi = -0.18 - 0.0591pH$ |
| 3.2 | $SiC + 4H_2O + 8h^+ \rightarrow SiO_2 + CO_2(g) + 8H^+$ | $\varphi = -0.16 - 0.0591pH$ |
| 3.3 | $2H_2O \rightarrow O_2(g) + 4H^+ + 4e^-$ | $\varphi = 1.23 - 0.0591pH$ |
| 3.4 | $2Cl^- \rightarrow Cl_2(g) + 2e^-$ | $\varphi = 1.40 - 0.0591\log C_{Cl^-}$ |
| 3.5 | $2H_2O + 2e^- \rightarrow 2OH^- + H_2(g)$ | $\varphi = -0.83 - 0.0591(14 - pH)$ |

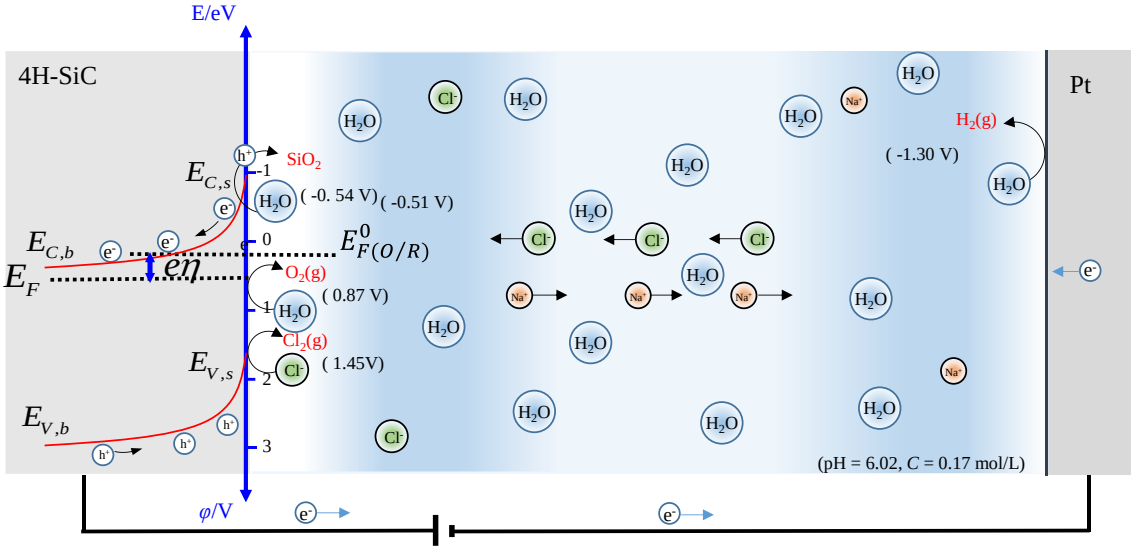



**Fig. 3.14** Model of SiC anodic oxidation in NaCl electrolyte.

mV/s using the potentiostat. To ensure the reliability of the experiment results, the two same LSV experiments were conducted on the CMP processed SiC surface. The LSV result is shown in Fig. 3.15(a). As the voltage was increased, the overall current showed an upward trend. From 0 to 3.7 V, no electric current flowed and the value of 0.2 mA was the noise of the potentiostat. The electric current started to flow at 3.7 V, wherein SiC was beginning to be oxidized, as shown in Fig. 3.15(b). With the increase in potential, the electric current reached a peak value at about 13 V and then the electric current decreased with increasing potential, which was considered to be caused by the hindrance effect of the generated oxide layer on the SiC surface. Then, the electric current increased again when the potential increased to about 25 V, which is considered to be when the anodic oxidation of $H_2O$ occurred (Eq. (3.3)). With the increase in potential, the increase in oxidation current gradually decreased until the potential reached about 28 V. At 28 V, the electric current rapidly increased again, which is considered to be when the anodic oxidation of $Cl^-$ occurred (Eq. (3.4)). In addition, the fluctuation of the electric current became strong when the applied potential was greater than 38 V. A possible reason for this is that the reactions of Eqs.

(3.3) and (3.4) occurred strongly at this time and a large amount of gas was generated, strongly changing the surface condition of the SiC and thus strongly fluctuating the current.

The difference between the potentials calculated by the Nernst equation in Eq. (3.7) and that obtained by LSV in Fig. 3.15 is attributed to the overpotential on the SiC surface. Overpotential is the potential difference between the theoretical potential of the thermodynamically obtained reaction (equilibrium electrode potential) and the potential of the electrode when the reaction actually occurs [15]. Overpotential mainly consists of the activation overpotential due to the consumption of extra energy to activate the reactants, the concentration overpotential caused by the difference between the concentration of the reactive species on the electrode surface and the concentration in the electrolyte, and the resistance overpotential resulting from the resistance on the electrode surface. In the anodic oxidation of SiC, the SiC surface was covered by the generated oxide layer, which has a very high resistance (hundreds of kΩ [16]). Thus, it is reasonable to suppose that the overpotentials of Eqs. (3.3) and (3.4) on the SiC electrode were much larger than that on the platinum electrode (with values of several volts [17]).

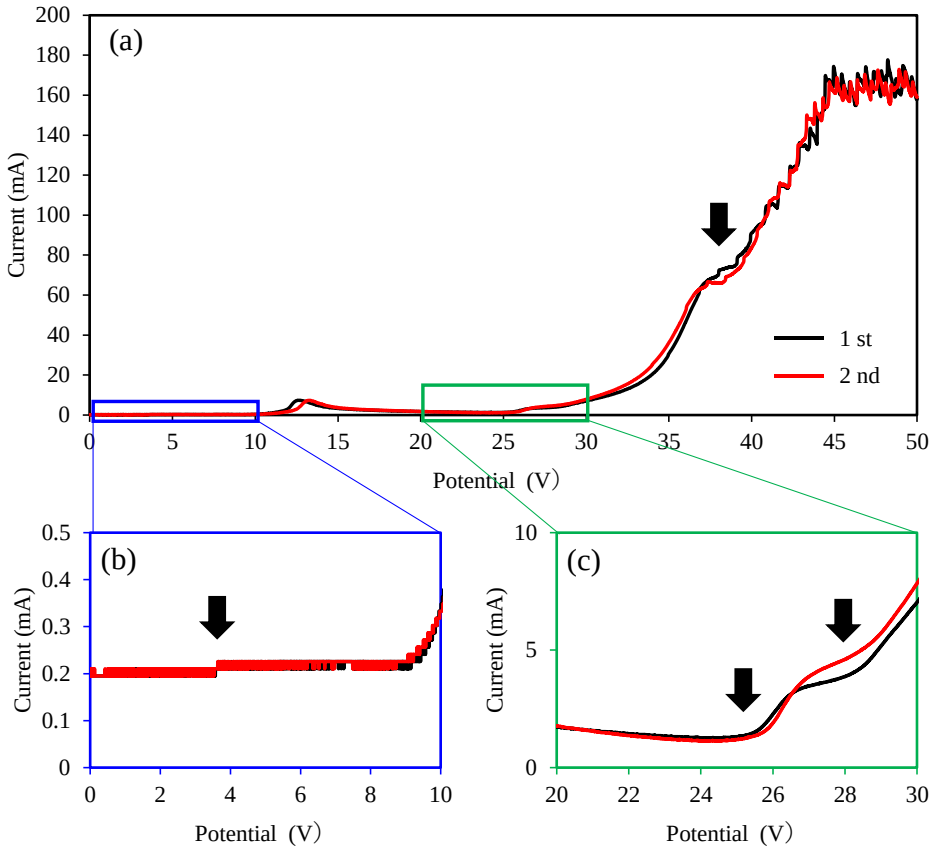



**Fig. 3.15** (a) Results of LSV measurements; magnified images of the current change at potential ranges of (b) 0–10 V and (c) 20–30 V.

To confirm these hypotheses, anodic oxidation experiments with different potentials were conducted on the CMP-processed SiC surfaces in 1 wt% NaCl electrolyte for 10 min and the relationship between potential and oxidation depth was investigated. In addition, to ensure the reproducibility of the experimental results, two experiments were conducted with the same experimental parameters. Fig. 3.16(a) shows the anodic oxidation depths for anodic oxidation of 4H-SiC (0001) surfaces with different potentials, the results of the two experiments were almost the same. As the potential was increased from 10 to 20 V, the oxidation depth increased. After the potential reached 30 V, the oxidation depth decreased significantly and was even less than that obtained at 10 V. As the potential was further increased from 30 to 50 V, the oxidation depth increased minimally. Fig. 3.16(b) shows the amount of charge that flowed during the anodic oxidation with these different potentials. It can be seen the charge increased with the increase in oxidation potential, except for 30 V, at which the charge decreased slightly compared with that at 20 V but more than that at 10 V. This is different from the relationship between the oxidation depth and the potential, as shown in Fig. 3.16(a).

During anodic oxidation of SiC, reactions with six and eight holes, as shown in Eqs. (3.1) and (3.2), may occur. The combination of these two reactions can be expressed as Eq. (3.11) and the value of the electrochemical valence, $z$, can be defined by the following Eq. (3.12), which represents the number of holes (electrons) needed for anodizing 1 mol of SiC during the actual anodic oxidation. If all the flowed charge was used for the anodic oxidation of SiC, $z$ should be greater than six and smaller than eight.

$$\mathrm{SiC} + \frac{z}{2}\mathrm{H_2O} + z\mathrm{h^+} \rightarrow \mathrm{SiO_2} + \varepsilon\mathrm{CO(g)} + (1-\varepsilon)\mathrm{CO_2(g)} + z\mathrm{H^+}, \tag{3.11}$$

$$z = \frac{Q/F}{\rho Sd/M}. \tag{3.12}$$

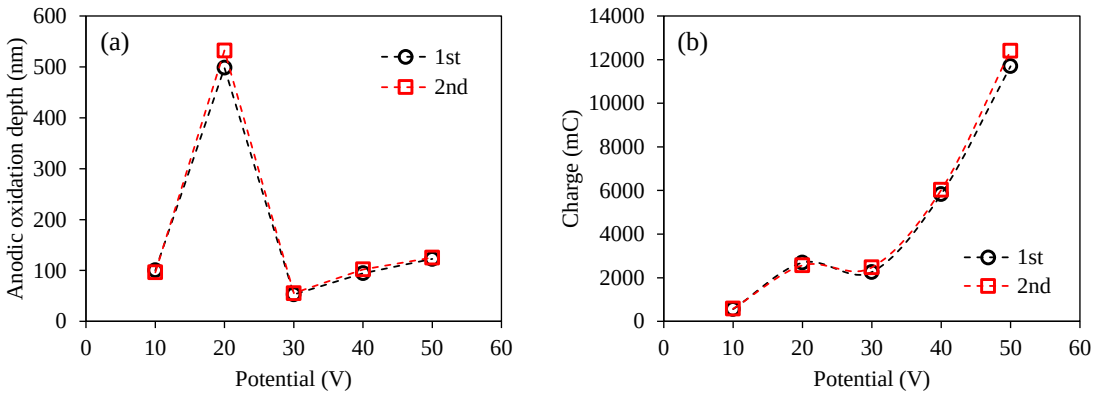



**Fig. 3.16** Relationship between (a) anodic oxidation depths and (b) charge and potential during the anodic oxidation of the 4H-SiC (0001) surface.

In Eq. (3.11), $\varepsilon$ is the proportion of Eq. (3.1) in the anodic oxidation of SiC and, in Eq. (3.12), $Q$ is the charge flowed during anodic oxidation, $F$ is the Faraday constant, $\rho$ is the density of SiC, $S$ is the oxidation area of the SiC surface, $d$ is the anodic oxidation depth, and $M$ is the molar mass of SiC. Combining the oxidation depth and charge flowed during anodic oxidation shown in Fig. 3.16, $z$ can be calculated using Eq. (3.12).

Fig. 3.17 shows the changes of $z$ in the anodic oxidation of 4H-SiC with different potentials. When the potential increased from 10 to 20 V, $z$ was maintained at around seven, which is between six and eight, indicating that the main reactions that occurred at the SiC surface were the anodic oxidation of SiC via Eqs. (3.1) and (3.2). After the potential was further increased from 30 to 50 V, $z$ increased significantly and was much larger than eight. This means that a large number of electrons were divided to participate in other chemical reactions during the anodic oxidation process, namely the oxidation of $H_2O$ and $Cl^-$, when the potential was larger than 30 V. This result is consistent with the LSV result shown in Fig. 3.15.

Fig. 3.18(a) shows the potential changes during the anodic oxidation of the SiC surface with different electric current densities and with the same charge of 300 mC; the corresponding oxidation depth is shown in Fig. 3.11. The potential increased with the increase in electric current density and the potential changes had the same trend with the oxidation time, namely, they first slowly increased and then rapidly increased with increase in anodic oxidation time. From the results of LSV in Fig. 3.15, oxidation of $H_2O$ and $Cl^-$ would occur when the potential is greater than 25 V and consume a large amount of charge flowed into the anodic oxidation system. Therefore, the number of flowed charges with different electric current densities below 25 V were counted, as shown in Fig. 3.18 (b). The larger the oxidation current density, the smaller the

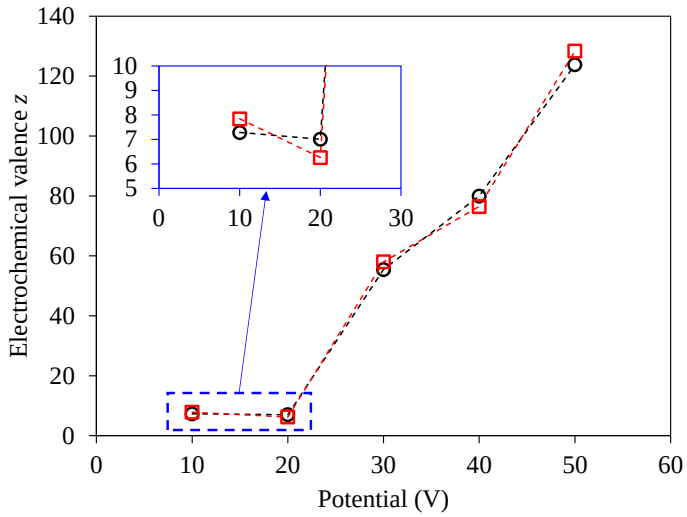
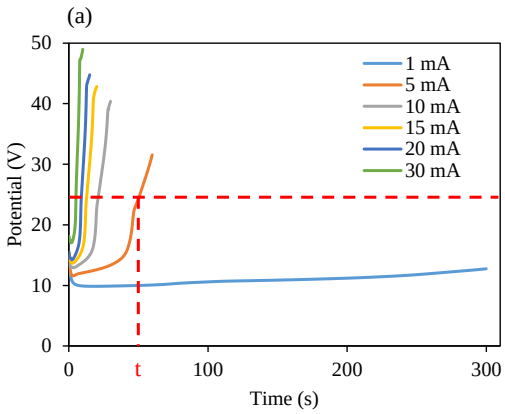



**Fig. 3.17** Change of electrochemical valence ($z$) with the increase in oxidation potential.

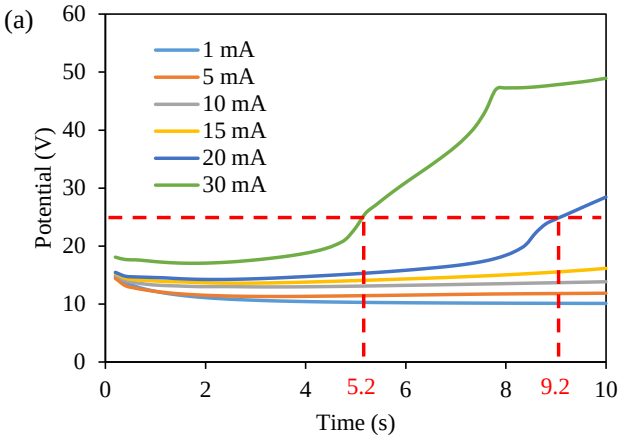



(b)

| Current density (mA/cm²) | Time *t* (s) | Charge *Q* (mC) | Anodic oxidation depth *d* (nm) | *z* |
|---|---|---|---|---|
| 1 | 300 | 300 | 53.16325 | 7.314132 |
| 5 | 51.2 | 256 | 44.68875 | 7.424895 |
| 10 | 21.4 | 214 | 39.52025 | 7.018557 |
| 15 | 13 | 195 | 37.36225 | 6.764808 |
| 20 | 9.2 | 184 | 34.5075 | 6.91159 |
| 30 | 5.2 | 156 | 30.246 | 6.685096 |

**Fig. 3.18** (a) Potential change in the anodic oxidation of 4H-SiC (0001) with different electric current densities at the same charge (300 mC). (b) Summary of anodic oxidation depths and charge with different electric current densities (below 25 V).

amount of charge that flowed when the potential was below 25 V. However, *z* was maintained around seven and the slight decrease in *z* as the current increases is attributed to a tiny amount of SiC oxidation after the potential is greater than 25 V, which is not included in the calculation of *z*. Based on this result, it can be concluded that the amount of charge that flowed below 25 V dominates the oxidation depth. Similar to the same-charge anodic oxidation, in the case of same-time anodic oxidation, the oxidation depth increased proportionally with the increase in current density below 15 mA/cm$^2$, as shown in Fig. 3.12, and the amount of charge that flowed below 25 V also changed proportionally, as shown in Fig. 3.19. However, after the electric current increased




(b)

| Current density (mA/cm²) | Time *t* (s) | Charge *Q* (mC) |
|---|---|---|
| 1 | 10 | 10 |
| 5 | 10 | 50 |
| 10 | 10 | 100 |
| 15 | 10 | 150 |
| 20 | 9.2 | 184 |
| 30 | 5.2 | 156 |

**Fig. 3.19** (a) Potential change in anodic oxidation of 4H-SiC (0001) with different electric current densities at the same anodic oxidation time (10 s). (b) Summary of anodic oxidation depths and charge with different electric current densities (below 25 V).

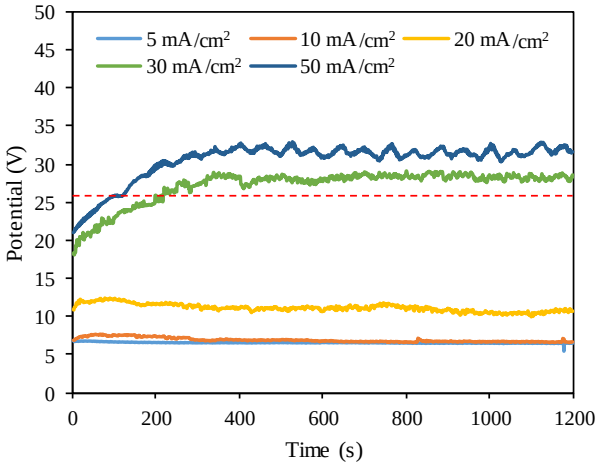



**Fig. 3.20** Potential change during ECMP with different electric current densities.

to 20 and 30 mA/cm$^2$, the potential increased to larger than 25 V with the increase in anodic oxidation time, as shown in Fig. 3.19(a). Since anodic oxidation of $H_2O$ and $Cl^-$ mainly occurred after the potential was greater than 25 V, the anodic oxidation depth was no longer proportional to the current density. The changes of anodic oxidation depth and the amount of charge are also consistent with the LSV results in Fig. 3.15.

The potential change during ECMP with different current densities is shown in Fig. 3.20 and the MRRs are shown in Fig. 3.13. The MRR increased as the electric current density increased from 5 to 20 mA/cm$^2$, and then decreased significantly after the electric current density increased to values larger than 30 mA/cm$^2$. From Fig. 3.20, it can be seen that the potentials were lower than 25 V during ECMP with 5, 10, and 20 mA/cm$^2$. After the electric current density increased to 30 and 50 mA/cm$^2$, the potential increased to larger than 25 V, which resulted in the oxidation of $H_2O$ and $Cl^-$ while the anodic oxidation of SiC significantly decreased, thus the MRR had a significant decrease at current densities of 30 and 50 mA/cm$^2$. These results verify the proposed model in Fig. 3.14.

In addition, potassium iodide starch paper test was conducted to confirm the oxidation order of $H_2O$ and $Cl^-$. It is known that $Cl_2$ will react with iodide ion ($I^-$) and generate iodine ($I_2$) and the color of the potassium iodide starch paper will change to blue when $I_2$ is combined with the starch. Therefore, the potential at which $Cl_2$ is generated can be confirmed by potassium iodide starch paper test. Anodic oxidations of a CMP-processed SiC surface were conducted at potentials of 20, 26, 30, 35, 40, and 45 V for 30 min using the anodic oxidation setup shown in Fig. 3.1. During each anodic oxidation, a potassium iodide starch paper was set in the container of the anodic oxidation setup and close to the SiC substrate. Its lower part was immersed in the electrolyte and the upper part was exposed to the air.

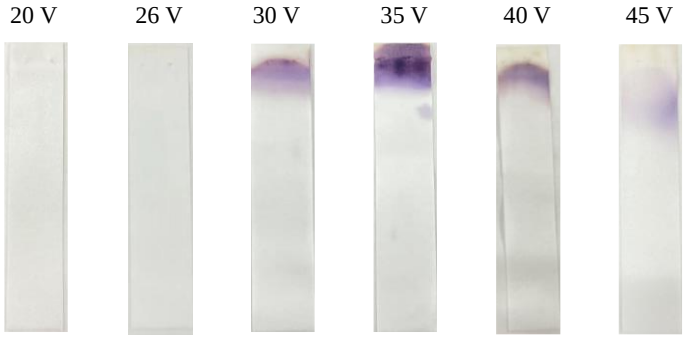



**Fig. 3.21** Changes of potassium iodide starch papers during anodic oxidation of SiC at different potentials.

Fig. 3.21 shows the results of potassium iodide starch paper test during SiC anodic oxidation at different potentials. The color of potassium iodide starch paper was not change when the potential was lower than 26 V, indicating $Cl_2$ was not generated, namely, anodic oxidation of $Cl^-$ was not occur. Upper parts of potassium iodide starch papers were changed to blue at potentials greater than 30 V, indicating anodic oxidation of $Cl^-$ occurred and $Cl_2$ was generated. Moreover, the blue color of the potassium iodide starch paper became darker when the potential increased from 30 to 35 V and became lighter when the potential further increased to 45 V, suggesting that oxidation of $Cl^-$ was strongest at 35 V. These results confirmed the LSV results in Fig. 3.15; the oxidation of $H_2O$ was prior to the oxidation of $Cl^-$ in the SiC-1 wt% NaCl aqueous solution and both oxidation of $H_2O$ and $Cl^-$ strongly occurred when the potential was greater than 38 V.

### 3.4.3 The role of $Cl^-$ and $Na^+$ in SiC anodic oxidation

When the potential is lower than 25 V, the main reaction that occurs on the WE is the anodic oxidation of SiC. After applying voltage between two electrodes, $Na^+$ ions move to the cathode and $Cl^-$ ions move to the anode, as shown in Fig. 3.14. $Na^+$ and $Cl^-$ ions do not participate in the reaction of SiC anodic oxidation and only play the role of electrical conduction. This would result in the gathering of $Cl^-$ and $Na^+$ on the anode and cathode, respectively. However, the accumulation of $Cl^-$ and $Na^+$ ions on the electrode surfaces is limited due to the following reasons.

First, diffusion of $Cl^-$ and $Na^+$ from the electrode surfaces to the bulk electrolyte would occur due to the concentration difference when the $Na^+$ and $Cl^-$ ions gather too much at the electrode surfaces.

Second, the amount of migrated $Na^+$ and $Cl^-$ ions in the electrolyte depends on the amount of charge that flowed through the electrodes during the anodic oxidation of SiC. Taking the anodic oxidation of SiC at 20 V for 10 min as an example, the amount of charge that flowed through the two electrodes was only 2569.982 mC. The total charge ($Q_E$) of $Na^+$ and $Cl^-$ ions in the electrolyte

can be calculated by the following formula:

$$Q_E = cVF, \quad (3.13)$$

where $c$ is the molar concentration of electrolyte (0.17 mol/L (1 wt%)), $V$ is the volume of the electrolyte (300 mL during the anodic oxidation), and $F$ is the Faraday constant. The charge of $Na^+$ and $Cl^-$ ions in the electrolyte is 4920.735 C, which is considerably larger than the amount of migrated $Na^+$ and $Cl^-$ ions during the anodic oxidation process. Therefore, only a very small amount of $Na^+$ and $Cl^-$ gathered near the electrode surfaces compared with their total amount in the electrolyte.

Third, the grinding stone is in contact with the SiC surface during ECMP and is rotating at high speed. This has a strong stirring effect on the electrolyte and prevents $Cl^-$ and $Na^+$ from accumulating on the electrode surfaces.

## 3.5 Summary

This chapter investigated the role of electrolyte type, electrolyte concentration, and electric current density in the anodic oxidation of SiC, as well as their underlying mechanisms. On the basis of the above results, the anodic oxidation system of SiC in NaCl aqueous solution was modeled and an anodic oxidation mechanism of SiC was proposed. The main results of the chapter are summarized as follows.

(1) NaOH, NaCl, and $NaNO_3$ with different concentrations were used for anodic oxidation of the 4H-SiC (0001) surface. It is found that the changes of anodic oxidation rate were mainly affected by the conductivity, but not by the type of electrolyte in constant-potential anodic oxidation, while the electrolyte conductivity affected the electric current at the beginning of the anodic oxidation. As the electrolyte conductivity increases, the electric current at the beginning of the anodic oxidation increased, but the anodic oxidation rate of SiC first increased and then decreased.

(2) Anodic oxidation at the same electric current densities with different electrolyte concentrations was applied to 4H-SiC surfaces. When the electric current densities were the same, electrolyte concentration did not affect the surface roughness or anodic oxidation of SiC. It was confirmed that the anodic oxidation of SiC is mainly affected by the flowed current.

(3) It was found that with the increase in electric current during anodic oxidation, pits on the oxidized/etched surface were reduced and gradually disappeared, the surface roughness decreased significantly, and a smooth and flat surface was obtained during anodic oxidation

in 5 wt% NaCl electrolyte. The anodic oxidation of the SiC surface changed from non-uniform oxidation to uniform oxidation with the increase in electric current density.

(4) With the increase in flowed electric current during anodic oxidation, the generated oxide layer changed from a porous to a dense structure; the size and number of pores in the oxide layer decreased and the interface between the oxide layer and bulk SiC became smooth. The dense oxide layer more greatly hindered the anodic oxidation of SiC and had higher hardness compared with the porous oxide layer.

(5) Anodic oxidation at the same charge with different electric current densities was applied to 4H-SiC surfaces. The anodic oxidation rate decreased with the increase in electric current density although the amount of charge was the same.

(6) Anodic oxidation for the same period of time and with different electric current densities was applied to 4H-SiC surfaces. The anodic oxidation depths increased linearly with the increase in electronic current densities, then slightly decreased. After the electronic current density increase to a certain degree, the charge utilization efficiency was reduced.

(7) ECMP with different electric current densities was conducted on 4H-SiC (0001) surfaces. The MRRs of the ECMP increased with increasing electric current density and then significantly decreased after the electric current density was increased to a certain level.

(8) The anodic oxidation system of SiC in NaCl electrolyte was modeled. The order of oxidation reactions that may occur on the SiC surface was evaluated from the equilibrium potentials of each reaction calculated by the Nernst equation. The results showed that the order of oxidation reactions, from easy to difficult, is the anodic oxidation of SiC, oxidation of $H_2O$, and, finally, the oxidation of $Cl^-$.

(9) LSV measurements were applied to CMP-processed SiC surfaces to confirm the potential at which the reaction occurs. The reaction occurring on the SiC surface is mainly the oxidation of SiC from 3.7 to 25 V; the oxidation reaction of $H_2O$ from 25 to 28 V, and the oxidation of $Cl^-$ when the potential is greater than 28 V. The LSV results were verified by the anodic oxidation and ECMP experiments.

(10) The number of holes (electrons) that are needed for anodizing 1 mol SiC was calculated through anodic oxidation experiments. It was found that about 7 mol of holes is required to

anodize 1 mol SiC and the reactions of six and eight holes are almost equal to each other in the anodic oxidation of SiC.

(11) The role of $Na^+$ and $Cl^-$ in the anodic oxidation of SiC with NaCl electrolyte was modeled. $Na^+$ and $Cl^-$ ions do not participate in the oxidation reaction of SiC, they only play a role in the transmission of electric current.

# References


1) D.H. van Dorp, E.S. Kooij, W.M Arnoldbik, J.J. Kelly, Chem. Mater. 21 (2009) 3297–3305.
2) X. Yang, R. Sun, Y. Ohkubo, K. Kawai, K. Arima, K. Endo, K. Yamamura, Electrochim. Acta, 271 (2018) 666–676.
3) I. Lauermann, R. Memming, D. Meissner, J. Electrochem. Soc. 144 (1) 73–80.
4) D.H. van Dorp, J.J.H.B. Sattler, J.H. den Otter, J.J. Kelly, Electrochim. Acta 54 (2009) 6269–6275.
5) W. S. Woon, S. D. Hutagalung, K. Y. Cheong, Thin Solid Films 517(8) (2009) 2808–2812.
6) C. Chen, S. Chen, M. Shang, F. Gao, Z. Yang, Q. Liu, W. Yang, J. Mater. Chem. C 4(23) (2016) 5195–5201.
7) H. Morisaki, H. Ono, K. Yazawa, J. Electrochem. Soc. 131(9) (1984) 2081–2086.
8) A. Takazawa, T. Tamura, M. Yamada, Jpn. J. Appl. Phys. 32 (1993) 3148–3149.
9) N. Liu, R. Yi, H. Deng, Electrochem. Commun. 89 (2018) 27–31.
10) F. J. Vidal-Iglesias, J. Solla-Gullón, A. Rodes, E. Herrero, A. Aldaz, J. Chem. Educ. 89(7) (2012) 936–939.
11) C. N. Chang, H. B. Cheng, A. C. Chao, Environ. Sci. Technol. 38(6) (2004) 1807–1812.
12) M. Pourbaix, Atlas of electrochemical equilibria in aqueous solutions, National Association of Corrosion Engineers, (1974).
13) P. Atkins, J. De Paula, R. Friedman, Physical Chemistry: Quanta, Matter, and Change. Oxford University Press, (2014).
14) J. A. Dean, Lange's handbook of chemistry, McGraw-Hill, (1999).
15) A. J. Bard, L. R. Faulkner, Electrochemical methods: fundamentals and applications, Wiley, (2000).
16) D.H. van Dorp, E.S. Kooij, W.M. Arnoldbik, J.J. Kelly, Chem. Mater. 21 (2009) 3297–3305.
17) D. M. Heard, A. J. J. Lennox, Angew. Chem. Int. Ed. 59 (2020) 18866–18884.

# Chapter 4
# Dominant factors and their action mechanisms on MRR in the ECMP of the 4H-SiC (0001) surface

## 4.1 Introduction

In Chapter 3 it was found that when sodium chloride aqueous solution was used as the electrolytic solution there exists a limit to the anodic oxidation rate with the increase in oxidation current density or potential. This limit was due to the occurrence of water electrolysis and the oxidation of chloride ions. Therefore, to further increase the anodic oxidation rate of SiC and thereby increase the material removal rate (MRR) of electrochemical mechanical polishing (ECMP) and ultrasonic vibration assisted ECMP (UAECMP), it is necessary to investigate the dominant factors that affect the anodic oxidation of SiC.

Until now, only a few researchers have investigated the effect of temperature on the chemical etching of SiC surfaces. Gabouze *et al.* studied effects of the chemical etching rates of polycrystalline p-type 6H-SiC in HF/$Na_2O_2$ solutions with various bath temperatures. They found that the etching rate first increased and then decreased with increasing bath temperature, and that the rate reached a maximum at 80 °C [1)]. Moreover, Van Dorp *et al.* found that the etching rate of SiC in a KOH solution also had a significant temperature dependence and that the etching rate increased exponentially with increasing solution temperature [2)]. Unlike SiC, the anodic oxidation rate of Si was found to increase, from around 225 to 325 nm/s, in a solution of HF:$H_2O$:ethanol = 35:35:30 at a current density of 333 mA/$cm^2$, as the temperature increased from −30 to 30 °C. The surface roughness was also found to decrease significantly at low temperatures [3)]. Although these results are not consistent with each other, they show that temperature has a strong influence on the etching/oxidation rate of SiC and Si surfaces. However, the mechanism is still not clear.

On the other hand, it has been reported that doping and damage can affect the chemical reactivity of SiC. Daas *et al.* found that the thermal oxidation rate of n-type 4H-SiC has a clear doping dependence. They obtained higher oxidation rates on SiC samples with higher doping concentrations [4)]. Jia *et al.* reported that the atomic bonds at defect sites are weaker than those at damage-free sites in 4H-SiC. Consequently, in plasma etching, the defect site always has a higher

etching rate than the defect-free area [5]. This phenomenon was also reported in the study of dry and wet thermal oxidation of 3C-SiC films by Eickhoff [6] and Severino [7]. Defects and damaged areas are also found to be preferentially oxidized during the anodic oxidation of 4H-SiC (0001) surfaces and had a higher anodic oxidation rate than damage-free areas [8]. However, the differences induced by doping and damage have not been quantitatively investigated and the mechanism is still unclear.

This chapter quantitatively studies the effects of temperature, doping concentration, damage, and strain on the anodic oxidation rate of the 4H-SiC (0001) surface. Their action mechanisms were studied using Raman spectroscopy, conductive atomic force microscopy (C-AFM), and anodic oxidation experiments. Furthermore, the promotional effects of these factors were applied to increase the MRR in the slurryless ECMP of SiC wafers.

## 4.2 Temperature-controllable anodic oxidation setup

Fig. 4.1 shows a schematic of the temperature-controllable anodic oxidation setup. This setup consisted of the three-electrode anodic oxidation system used in Chapter 3 and a temperature control system. The temperature control system consisted of a sink, a constant-temperature water bath, a magnetic stirrer, tubes, and a peristaltic pump. The electrolyte was maintained at the required temperature by circulating water at a certain temperature from the constant-temperature water bath. The stirring bar of the magnetic stirrer was placed in the anodic oxidation system container and was rotated at 500 rpm to ensure uniform temperature distribution of the electrolyte. During anodic oxidation, temperature changes were monitored using a K-type thermocouple.

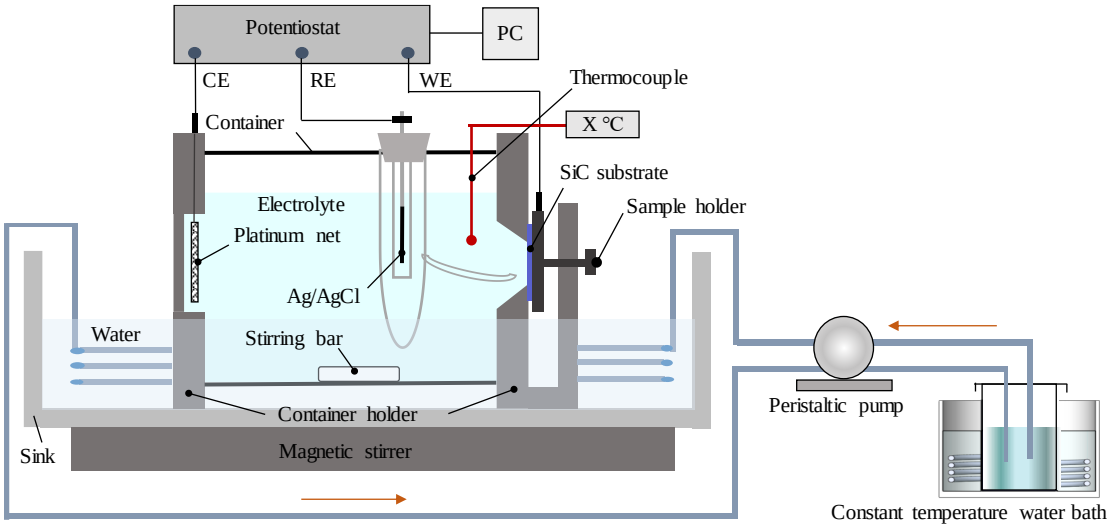



**Fig. 4.1** Temperature-controllable anodic oxidation setup.

N-type 4°-off 4H-SiC wafers used in this study were supplied by TankeBlue Semiconductor Co., Ltd. The wafers had a thickness of 350 μm and a specific resistance in the range of 0.015–0.028 Ω·cm. They were cleaned before anodic oxidation, using the wet chemical method. First, the wafers were dipped in a solution of $H_2SO_4$ (97 wt%) and $H_2O_2$ (34 wt%) with a volume ratio of 4:1 to remove contamination. They remained in the solution for 10 min and were then rinsed with deionized water for another 10 min. Next, they were dipped in a concentrated hydrofluoric acid (HF) solution (50 wt%) for 10 min to remove native oxides. This was also followed by rinsing with deionized water for 10 min. Finally, the wafers were dried with $N_2$ gas. All of the experiments were conducted on the most commonly used 4H-SiC (0001) face. A sodium chloride aqueous solution (NaCl *aq*.) (1 wt%) was used as the electrolyte. To study the relationship between the anodic oxidation rate and the electrolyte temperature, the SiC wafers were oxidized for 20 min at various temperatures and current densities. After anodic oxidation, the oxidized wafers were immersed in an HF solution to remove the generated oxidized layer and the anodic oxidation depth was measured using a scanning white light interferometer (SWLI). For each anodic oxidation experiment, the average oxidation depth of four positions, which were evenly distributed along the edge of the circular oxidation area, was taken as the oxidation depth. The definition and measurement position of the oxidation depth is shown in Fig. 3.1(b). The anodic oxidation rate was evaluated based on the change in oxidation depth per minute.

## 4.3 Temperature-controllable slurryless ECMP setup

Fig. 4.2 shows a schematic diagram of the temperature-controllable ECMP machine, which combined the ECMP setup used in Chapter 3 with a constant-temperature water bath. Electrolytes in the constant-temperature water bath and in the container of the ECMP machine were circulated through the center of the spindle using a peristaltic pump. This maintained the temperature of the electrolyte and prevented it from being ejected by the centrifugal force of the spindle.

A vitrified-bonded (#8000) ceria grinding stone (average particle size: 1 μm) with an inner diameter of 6 mm and an outer diameter of 11 mm (MIZUHO Co., Ltd.) was used to remove the oxide layer during ECMP. The grinding stone was rotated by the spindle at a speed of 1500 rpm under a set polishing pressure (70 kPa) and an elastic resin was set between the grinding stone and spindle to adjust the parallelism between the grinding stone and SiC surface. The SiC wafer was reciprocated in the x-direction with a feed rate of 10 mm/s and a reciprocation distance of 5 mm. The SiC wafers were polished by ECMP for 1 h under various conditions. The surface roughness after ECMP was measured using a SWLI and the residual strain on the ECMP-processed surface was evaluated using a confocal Raman microscope (RAMANtouch, Nanophoton). The removal depth at the polished area was measured using a stylus profiler (Surfcom 1400D, Tokyo Seimitsu).

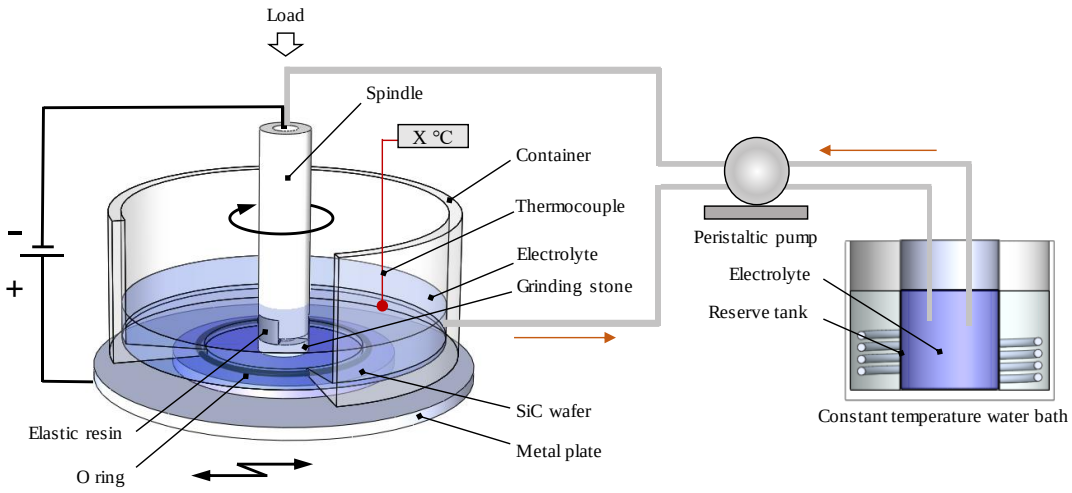



**Fig. 4.2** Temperature-controllable ECMP setup.

The removal depth was calculated by aligning the height of the as-received surface (unpolished area) at zero with consideration of wafer warp.

## 4.4 Effects of electrolyte temperature

### 4.4.1 Effects of electrolyte temperature on anodic oxidation of SiC

Fig. 4.3 shows the anodic oxidation rates of the 4H-SiC (0001) surface after anodic oxidation in 1 wt% NaCl *aq*. at various current densities and electrolyte temperatures. It can be seen from Fig. 4.3 that the anodic oxidation rate first increased and was then saturated as the current density increased. Fig. 4.3 also shows that the saturated oxidation rate increased with increasing electrolyte temperature. The saturated anodic oxidation rate was 5.2 nm/min at 25 °C, which increased to 12.5 nm/min at 40 °C and 57.1 nm/min at 60 °C. This means that a saturated oxidation rate existed at a certain electrolyte temperature and it increased as the electrolyte temperature increased. As mentioned in Chapter 3, in the anodic oxidation of SiC in NaCl *aq*., other electrochemical reactions, such as water electrolysis and oxidation of chloride ions, may occur at high current densities. These results indicate the current efficiency increased with the increase in electrolyte temperature.

Fig. 4.4(a) shows the dependence of the anodic oxidation rate of the 4H-SiC (0001) surface and the electrolyte temperature obtained by constant-voltage anodic oxidation at a voltage of 25 V for 20 min; an exponential increase in the anodic oxidation rate can be seen. As we know, the reaction rate, $k$, in a chemical reaction can be described by the Arrhenius equation

$$k = Ae^{(-E_a/RT)}, \tag{4.1}$$

or

$$\ln k = -\frac{E_a}{RT} + \ln A, \tag{4.2}$$

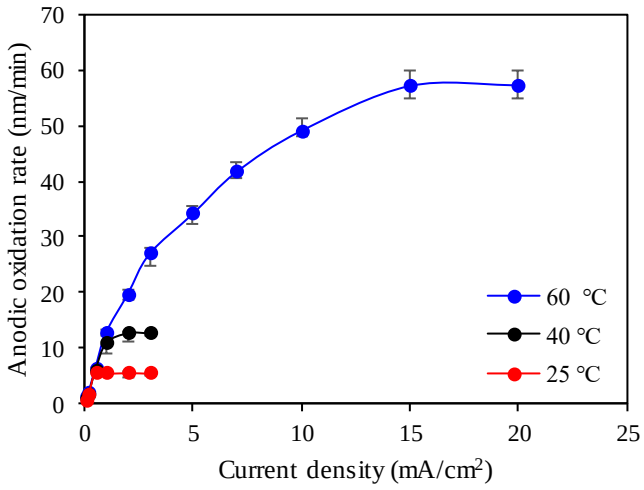



**Fig. 4.3** Relationship between anodic oxidation rate, electrolyte temperature, and current density.

where $E_a$ is the activation energy, $T$ is the absolute temperature, $R$ is the gas constant (8.31 J/(mol·K)), and $A$ is the pre-exponential factor, a constant for the chemical reaction. Eqs. (4.1) and (4.2) indicate a remarkable increase in the reaction rate with temperature. Using Eq. (4.2), we can obtain the average activation energy of 4H-SiC in anodic oxidation to be 62 kJ/mol from the fitted result, as shown in Fig. 4.4(b). The activation energy of SiC is reported to be 15–20 kcal/mol (62.8–83.7 kJ/mol) for molten KOH etching [9,10], 45.8 kJ/mol for electrochemical etching with 0.1 mol/L KOH solution [2], and 1.34–2.9 eV (129.3–279.8 kJ/mol) for thermal oxidation [11-13]. This indicates that the anodic oxidation of SiC is easier than thermal oxidation and molten KOH etching but slightly more difficult than electrochemical etching.

Fig. 4.5(a) shows the changes in the saturated anodic oxidation rate with the increase in electrolyte temperature during constant-current anodic oxidation. The applied current densities were 3, 3, 3, 20, and 20 mA/cm$^2$ at electrolyte temperatures of 25, 30, 40, 50, and 60 °C, respectively, according to the results obtained in Fig. 4.3. It is obvious that the anodic oxidation rate increased exponentially with the increase in electrolyte temperature. Fig. 4.5(b) shows the fitted result of the saturated anodic oxidation rate and electrolyte temperature using Eq. (4.2). It can be seen that the fitted result obtained for the saturated anodic oxidation rate during constant-current anodic oxidation was consistent with that obtained during constant-voltage anodic oxidation shown in Fig. 4.4(b). Therefore, it can be concluded that the changes in the saturated anodic oxidation rate obtained in constant-current anodic oxidation at various electrolyte temperatures were consistent with the Arrhenius equation.

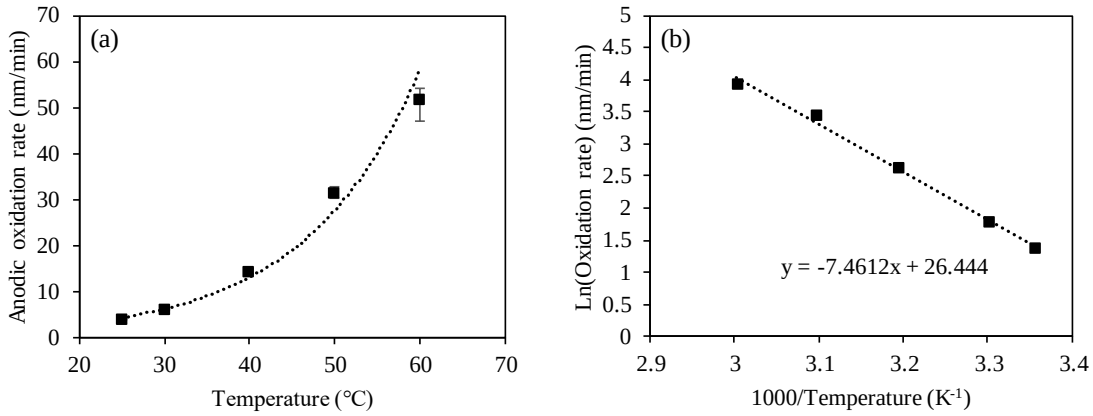



**Fig. 4.4** (a) Relationship between anodic oxidation rate and electrolyte temperature obtained in constant-voltage anodic oxidation at 25 V for 20 min. (b) Arrhenius plots of anodic oxidation rate as a function of electrolyte temperature during constant-voltage anodic oxidation.

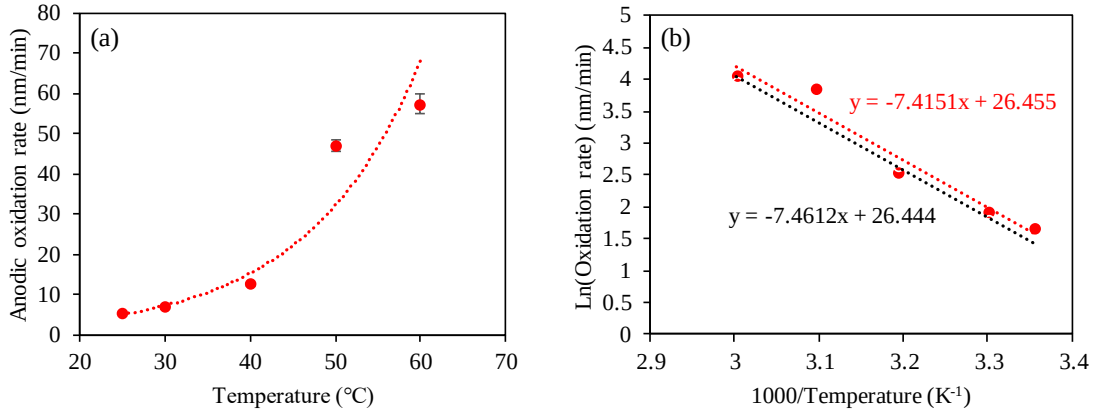



**Fig. 4.5** (a) Saturated anodic oxidation rate as a function of electrolyte temperature during constant-current anodic oxidation. The applied current densities were 3, 3, 3, 20, and 20 mA/cm$^2$ at electrolyte temperatures of 25, 30, 40, 50, and 60 °C, respectively. (b) Arrhenius plots of the saturated anodic oxidation rate as a function of electrolyte temperature (red dotted line). Black dotted line shows the fitted result for constant-voltage anodic oxidation.

## 4.4.2 Effects of electrolyte temperature on the ECMP of SiC

To verify that an increase in electrolyte temperature can increase the MRR of ECMP by increasing the saturated anodic oxidation rate of SiC, ECMP experiments were conducted on CMP-processed 4H-SiC (0001) surfaces for 1 h. The electrolyte temperature was controlled at 25, 40, and 60 °C. From Fig. 4.3, it can be seen that the anodic oxidation was saturated at 25, 40, and 60 °C when the current density increased to 20 mA/cm$^2$. Therefore, in order to investigate the relationship

between the saturated anodic oxidation rate and the MRR during ECMP at various temperatures, the current density was set at 20 mA/cm$^2$.

Fig. 4.6 shows the experimental results for ECMP conducted at various electrolyte temperatures. The depths of the polished areas were measured using a stylus profiler. Fig. 4.6(a) and (b) show that MRRs of 4.5, 5.5, and 9.5 μm/h were obtained at electrolyte temperatures of 25, 40, and 60 °C, respectively. The MRR increased exponentially with increasing electrolyte temperature, as shown in Fig. 4.6(b). The MRR increased from 4.5 to 9.5 μm/h (2.11 times) as the temperature increased from 25 to 60 °C. However, the anodic oxidation rate increased from 5.2 to 57.1 nm/min over the same temperature range. This is an increase of 11 times, which is much greater than that the increase in MRR. If we calculate the MRR using only the anodic oxidation rate in Fig. 4.5(a), there is a large difference between calculated and actual values; the result is shown as the "calculated value" in Fig. 4.6(b). During ECMP, the oxide layer was removed by the fixed abrasives at a certain polishing pressure. On the other hand, during anodic oxidation, there was no pressure and the oxide layer remained on the SiC surface. This difference is thought to be caused by the polishing pressure and the barrier effects of the oxide layer.

In addition, Fig. 4.6(c) shows the changes in potential during ECMP at various electrolyte temperatures. The potential decreased with increasing electrolyte temperature. The potential reflected the degree of difficulty in anodic oxidation of the SiC surfaces because a constant current was applied during ECMP. Therefore, this result indicates that the anodic oxidation of the SiC surfaces in ECMP became easier with increasing electrolyte temperature, which also increased the efficiency of the applied current.

SWLI images of 4H-SiC (0001) surfaces processed by ECMP at 20 mA/cm$^2$ and at various electrolyte temperatures are shown in Fig. 4.7. It is clear that on the surface obtained at 25 °C, there are many tool marks in the polishing direction. As the temperature of the electrolyte increases, the tool marks gradually become less obvious. Fig. 4.8 shows the relationship between the surface

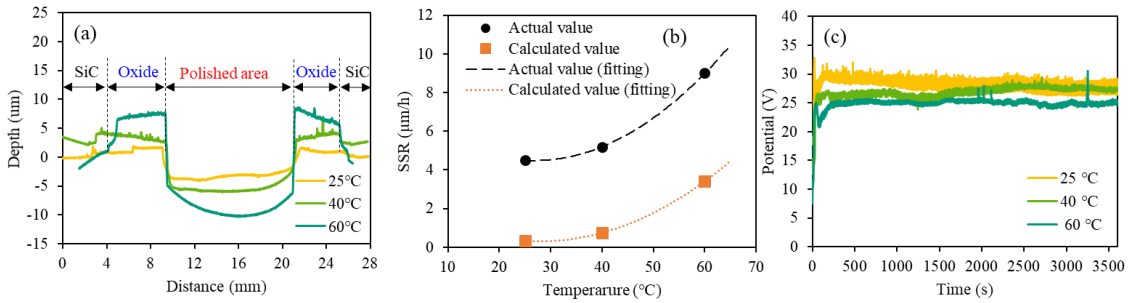



**Fig. 4.6** ECMP results for CMP-processed 4H-SiC (0001) surfaces at 20 mA/cm$^2$ with various electrolyte temperatures. (a) Cross-sectional views of the polished areas. (b) MRRs obtained at various electrolyte temperatures. (c) Changes in potential during ECMP.

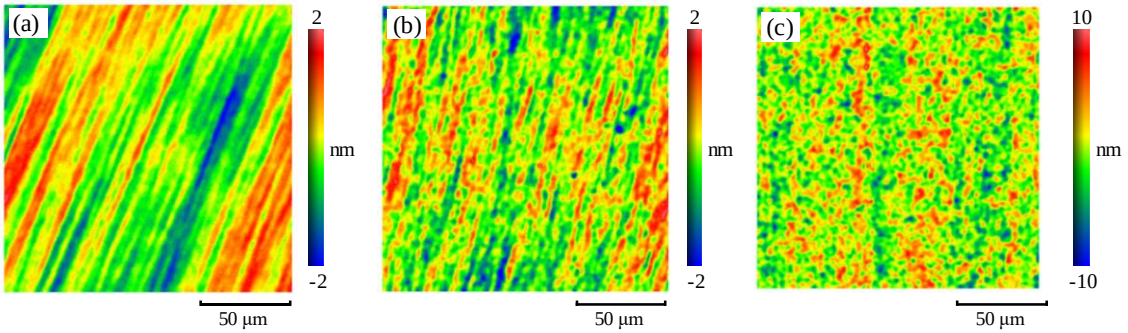



**Fig. 4.7** SWLI images of 4H-SiC surfaces processed by ECMP at 20 mA/cm$^2$ with electrolyte temperatures of (a) 25, (b) 40, and (c) 60 °C.

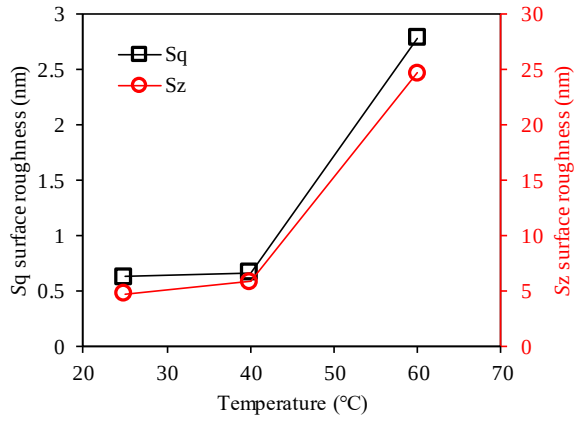



**Fig. 4.8** Relationship between surface roughness and electrolyte temperature in ECMP with a constant current of 20 mA/cm$^2$.

roughness and the electrolyte temperature. The *Sq* and *Sz* surface roughness of ECMP-processed surfaces obtained at electrolyte temperatures of 25 and 40 °C were almost the same but increased significantly once the temperature reached 60 °C. The X-ray photoelectron spectroscopy (XPS) measurement results for 4H-SiC surfaces processed at various electrolyte temperatures are shown in Fig. 4.9. Strong peaks corresponding to Si-C bonds and weak peaks corresponding to Si-O-C bonds can be seen on the surface polished at 25 and 40 °C, respectively. This indicates that a small amount of silicon oxycarbide remained on the polished surfaces at electrolyte temperatures of 25 and 40 °C. However, peaks corresponding to Si-O-C and Si-O bonds on the surface obtained at 60 °C are very strong, which indicates that a large amount of oxide remained on the polished surface.

The anodic oxidation of SiC is an anisotropic process and the interface between the oxide layer and bulk SiC becomes rougher with the thickening of the oxide layer. Therefore, to obtain a smooth surface with ECMP, the removal rate of the oxide layer should be greater than the anodic oxidation

rate [14]. Based on the Preston equation, the removal rate of the oxide film during ECMP is proportional to the polishing pressure and the relative velocity of the grinding stone and SiC wafer. Because these parameters were the same for the ECMP at various electrolyte temperatures, the removal rate of the oxide layer was the same in all three ECMP experiments. Therefore, the difference in the obtained SiC surfaces should be attributed to the difference in the electrolyte temperature, as modeled in Fig. 4.10. The anodic oxidation rate of SiC increased with increasing electrolyte temperature. As the anodic oxidation rate increased, the thickness of the oxide layer (prior to removal by the grinding stone) also increased when the temperature was high. In the case of low temperatures (25 or 40 °C), the anodic oxidation rate was low and the generated oxide layer was thin; it could be completely removed by the grinding stone with the applied polishing parameters and a smooth surface was obtained. After the temperature was increased to 60 °C, the anodic oxidation rate increased significantly while the removal rate of the oxide layer remained stable and could not catch up to the anodic oxidation rate. This resulted in residual oxide and a rougher surface.

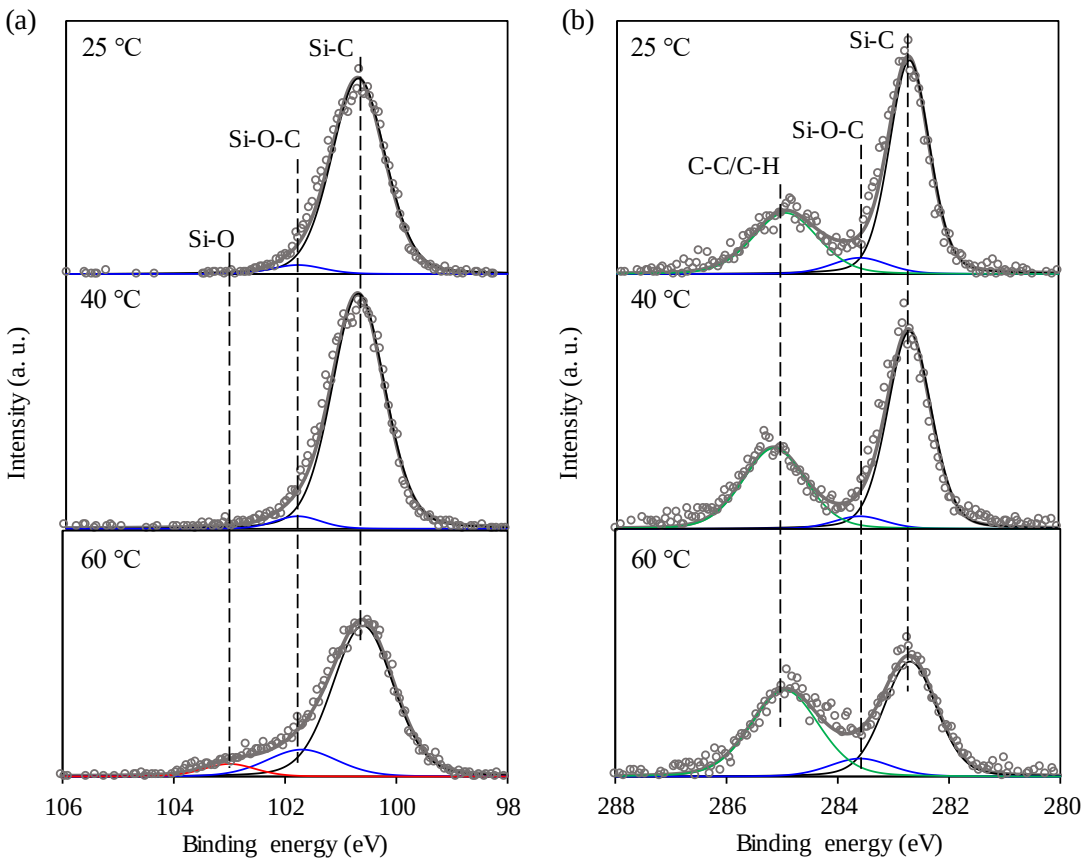



**Fig. 4.9** XPS spectra of 4H-SiC surfaces processed at various electrolyte temperatures measured with a take-off angle of 45º: (a) Si 2p spectra and (b) C 1s spectra.

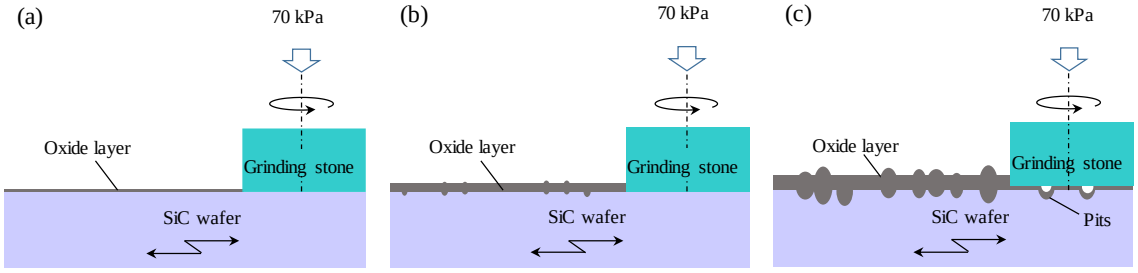



**Fig. 4.10** Modeling of the ECMP process at electrolyte temperatures of (a) 25, (b) 40, and (c) 60 °C.

## 4.5 Effects of doping concentration and damage on the anodic oxidation of SiC

To investigate the effects of nitrogen (N) doping concentration and surface damage on the anodic oxidation of SiC, anodic oxidation experiments were performed on 4H-SiC substrates with various doping concentrations and degrees of surface damage. Before anodic oxidation, the doping concentration of the SiC wafer was measured by secondary ion mass spectrometry (SIMS) (IMS-6F, CAMECA) with a measuring depth of 2 μm. The average value of N-doping concentration in the depth range of 0.1 to 2 μm was used as the doping concentration of the wafer. Anodic oxidation was conducted with various current densities for 20 min at 25 °C on CMP-processed surfaces with doping concentrations of $6.62 \times 10^{18}$ and $7.86 \times 10^{18}$ $cm^{-3}$ and a lapped surface with a doping

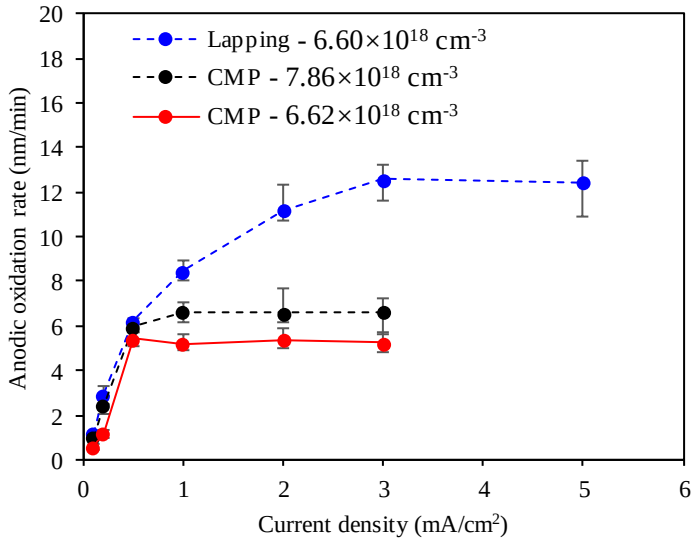



**Fig. 4.11** Relationship between anodic oxidation rates and current density for CMP-processed surfaces with different doping concentrations and a lapped surface.

concentration of $6.60 \times 10^{18}$ $cm^{-3}$. Fig. 4.11 shows the anodic oxidation rates of these different 4H-SiC surfaces, which show the same trend with increasing current density: The anodic oxidation rates all first increase with increasing current density and then reach saturation. Meanwhile, the saturated anodic oxidation rates are different. The saturated anodic oxidation rates of the CMP-processed surfaces with doping concentrations of $6.62 \times 10^{18}$ and $7.86 \times 10^{18}$ $cm^{-3}$, and the lapped surface with a doping concentration of $6.60 \times 10^{18}$ $cm^{-3}$ are 5.2, 6.6, and 12.4 nm/min, respectively. It is clear that doping and surface damage have a promotional effect on the anodic oxidation rates of the 4H-SiC surfaces and improved the current efficiency in anodic oxidation of SiC at high current densities.

To investigate why doping and damage can increase the anodic oxidation rate, anodic oxidation experiments at a constant potential were also conducted on CMP-processed surfaces with doping concentrations of $8.35 \times 10^{18}$ and $9.08 \times 10^{18}$ $cm^{-3}$ and a lapped surface with doping concentration of $6.60 \times 10^{18}$ $cm^{-3}$ to evaluate their activation energies. Fig. 4.12 shows the dependence of the anodic oxidation rates obtained at 25 V for 20 min on the electrolyte temperature. An exponential increase in the anodic oxidation rate was observed with increasing temperature. From the fitted value of the anodic oxidation rate curve by the Arrhenius equation in Fig. 4.12(b), average activation energy ($E_a$) of the CMP-processed surfaces with doping concentrations of $8.35 \times 10^{18}$ and $9.08 \times 10^{18}$ $cm^{-3}$ and the lapped surface with doping concentration of $6.60 \times 10^{18}$ $cm^{-3}$ were obtained to be 62.00, 58.97, and 33.37 kJ/mol, respectively. Therefore, it can be concluded that the relatively high anodic oxidation rate of the lapped surface and the CMP-processed surface with doping concentration of $9.08 \times 10^{18}$ $cm^{-3}$ compared with that of the CMP-processed surface with doping concentration of $8.35 \times 10^{18}$ $cm^{-3}$ was due to their lower activation energy in oxidization.

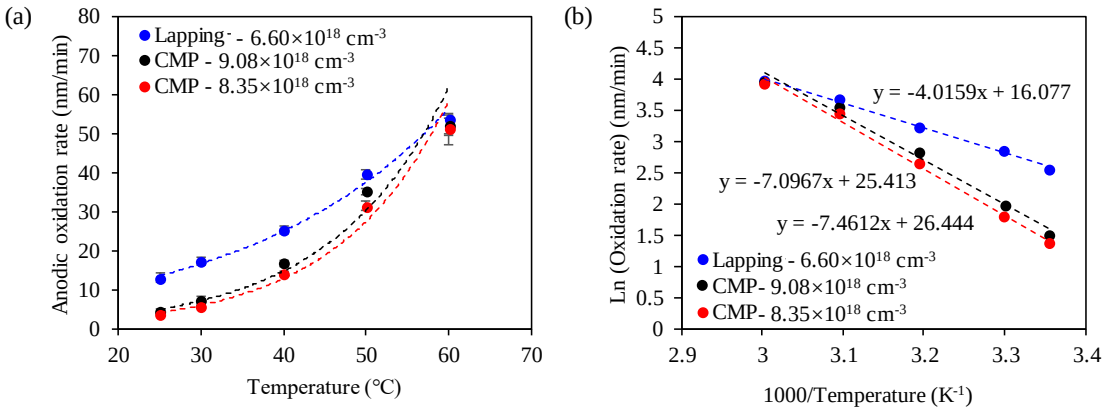



**Fig. 4.12** Results of anodic oxidation at 25 V for 20 min on CMP-processed surfaces with different doping concentrations and a lapped surface. (a) Relationship between anodic oxidation rate and electrolyte temperature. (b) Arrhenius plots of anodic oxidation rate as a function of electrolyte temperature.

Fig. 4.13(a) and (b) show the typical Raman spectra of CMP-processed surfaces with doping concentration of $6.62 \times 10^{18}$ and $7.86 \times 10^{18}$ $cm^{-3}$ and lapped surfaces with doping concentration of $6.60 \times 10^{18}$ and $8.82 \times 10^{18}$ $cm^{-3}$. The laser wavelength used in the Raman measurements was 532 nm and the grating was 2400 gr/mm. Raman spectroscopy measurements were conducted at any three points in each sample and their average full width at half maximum (FWHM) of the FTO(2/4)E2 peaks are shown in Fig. 4.13(c). It can be seen from Fig. 4.13 that both doping and damage increased the FWHM of the Raman peaks of the SiC surfaces. On the basis of the definition of the FWHM in the Raman spectra, these results indicate that the crystallinity of a SiC surface was worsened by doping and damage.

Generally, doping is accompanied by series lattice deformation, lattice mismatch, and dislocations [4,15]. The SiC structure can be considered an assembly of corner-sharing tetrahedrons composed of a carbon atom in a centroid position with four effectively tetrahedrally bonded silicon neighbors. The incorporation of a N atom takes place at the C atom sites, which gives a shift in the

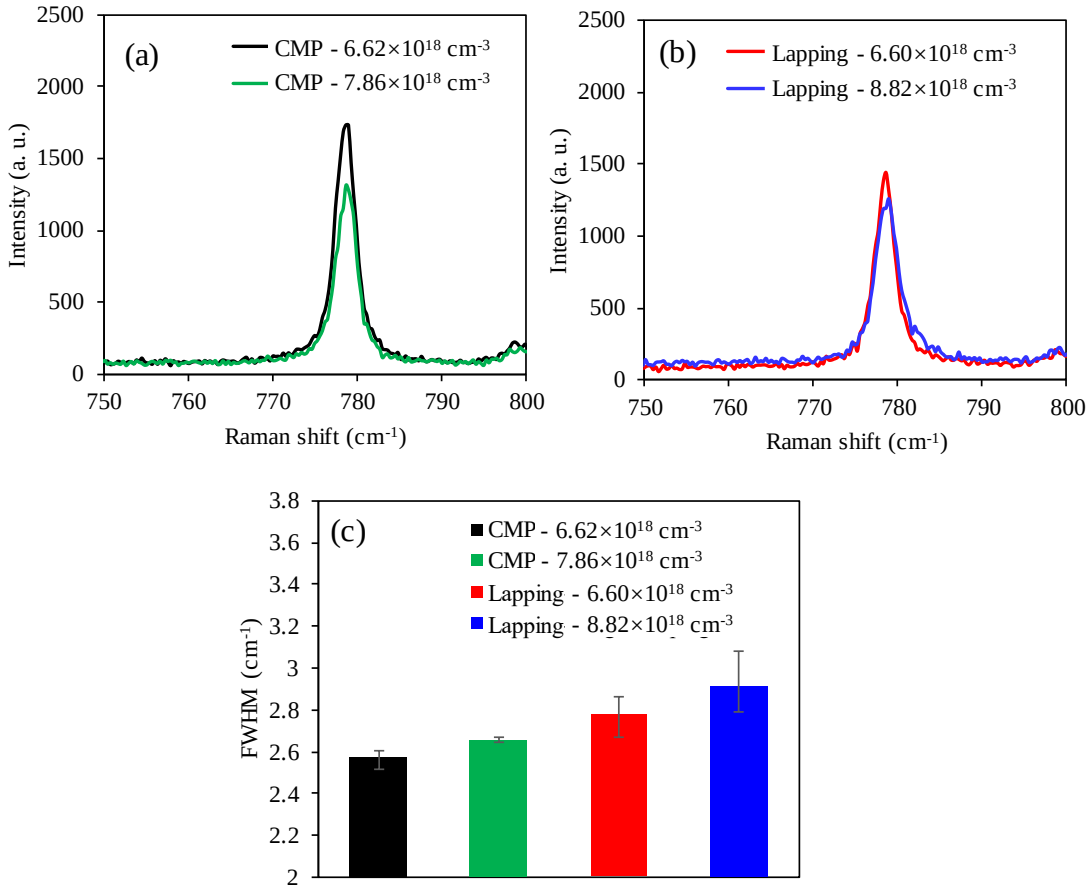



**Fig. 4.13** Raman spectroscopy results for (a) CMP-processed surfaces with different doping concentrations and (b) lapped surfaces with different doping concentrations. (c) FWHM of Raman spectra peaks of each surface.

interplanar spacing between the Si and C atoms caused by the difference in atomic radius. The N atom has a smaller radius than the C atom, which results in a decreased lattice constant and lattice misfit strain. Jacobson *et al.* reported that N-doping in 4H-SiC introduces isotropic lattice strain, which increases with N-doping concentration [16].

On the other hand, damage on the surface is always accompanied by a series of dislocations, deformations [17], microcracks [18], and stacking faults [19]. These defects introduce residual strain into the surface and change the material properties of SiC [5]. Fig. 4.14 shows the residual stress distribution obtained by Raman spectroscopy on a lapped surface and on a CMP-processed surface. A shift of the FTO(2/4)E2 (777.6 $cm^{-1}$) peak of 4H-SiC was investigated to evaluate the residual stress on the surface by multiplying by the proportional coefficient of −510 MPa/$cm^{-1}$ [20]. Tensile and compressive stresses can clearly be seen on the lapped surface in Fig. 4.14(a). The tensile stress, which reached a maximum of about 100 MPa, was mainly concentrated at the positions of the scratches and a few small compressive stresses were distributed among them. In contrast, no damage appeared on the CMP-processed surface, as shown in Fig. 4.14(b). Because residual strain existed on the doped and damaged surface, it can be assumed that the existence of residual strain on the highly doped surface and the damaged (lapped) surface resulted in low activation energy in the anodic oxidation of the SiC.

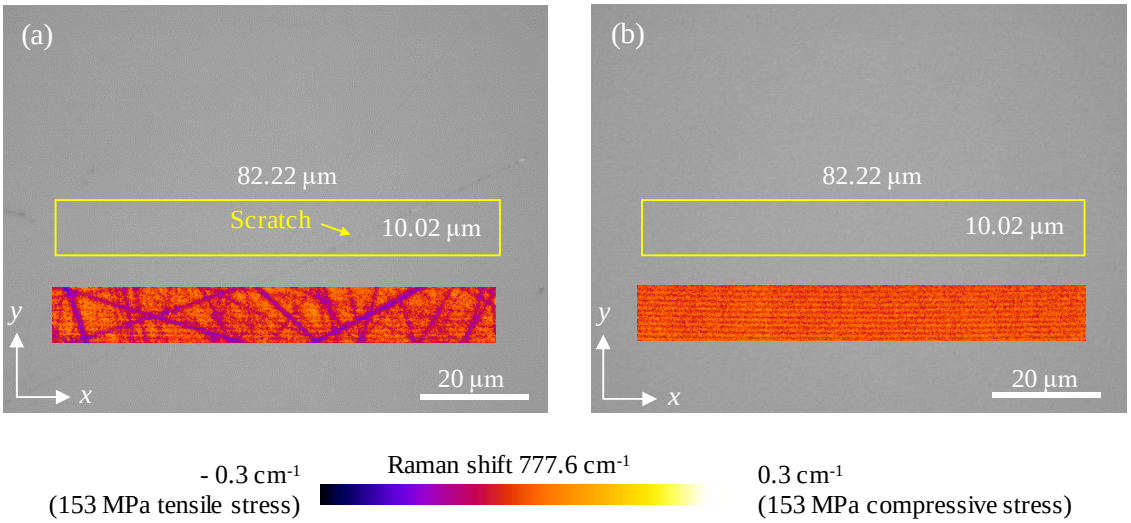



**Fig. 4.14** Optical microscope images of (a) lapped and (b) CMP-processed surfaces. Insets show the residual stress distributions (in yellow rectangle area) on the surfaces measured by confocal Raman microscope with an observation area of 82.22 × 10.02 $\mu m^2$.

## 4.6 Effects of strain

### 4.6.1 Effects of strain on the anodic oxidation of SiC

A strain-controllable, constant-temperature anodic oxidation setup was specially developed to investigate the effect of strain on the anodic oxidation of SiC, as shown in Fig. 4.15. This setup consisted of a four-point bending system and a coaxial nozzle anodic oxidation system. In the four-point-bending system, a SiC strip was placed among four metal bars and compression and tensile stresses could be applied to the Si face of a 4H-SiC strip by adjusting its relative position to the four metal bars. Because the strain on the Si face was equal but opposite to that on the C face, strain gauges were attached to the C face to monitor the changes in strain at various degrees of bending. During anodic oxidation, it was very important to avoid introducing any stress to the SiC surface other than what was applied by the four-point bending system. Therefore, we adopted a non-contact local anodization method. As shown in Fig. 4.15, non-contact local anodization was realized using the coaxial nozzle anodic oxidation system [21]. This system consisted of a double-pipe nozzle, an electrolyte circulation unit, and a two-electrode electrochemical unit. The double-pipe nozzle consisted of two metal pipes that were arranged coaxially. The outer diameters of the pipes were 2 and 4 mm, and the inner diameters were 1.6 and 3.6 mm, respectively. Electrolyte was supplied through the outer pipe and sucked through the inner pipe; thus, the electrolyte was confined to the tip of the nozzle without any contact of the nozzle with the SiC surface (i.e., without introducing additional stress). The two-electrode electrochemical unit consisted of a working electrode (WE), a counter electrode (CE), and a potentiostat. The WE was connected to the SiC strip through a metal bar, the CE was connected to the nozzle, and the potentiostat was used to control the electrical parameters for oxidation.

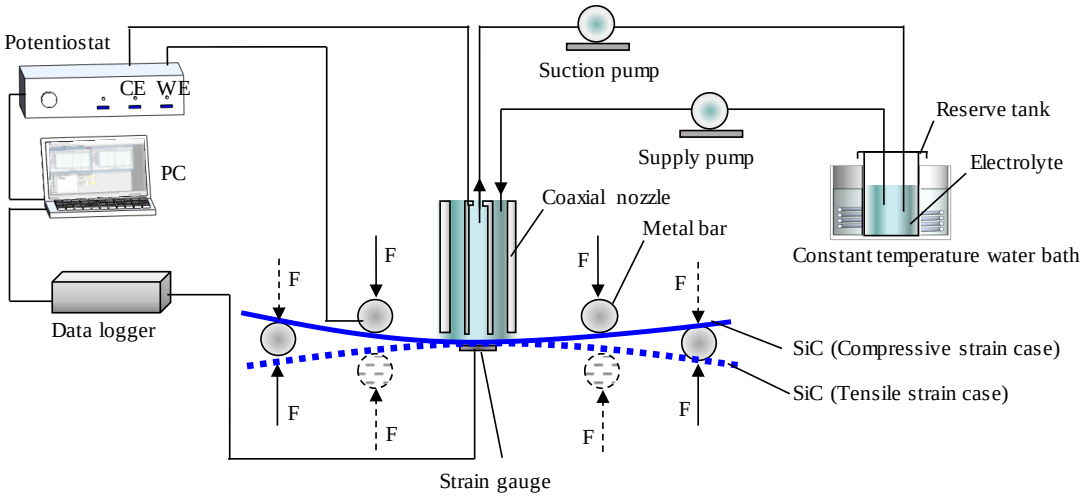
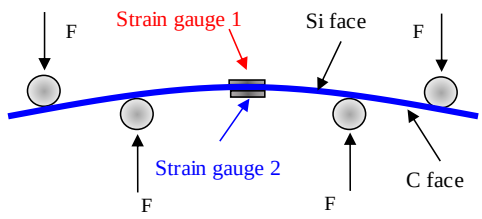



**Fig. 4.15** Strain-controllable constant-temperature anodic oxidation setup.

In the strain-controllable constant-temperature anodic oxidation setup, a strain gauge was attached to the C face of the SiC strip to control the strain on the Si face by controlling the bending degree of the SiC strip. In order to confirm that the strain on the Si face was equal but opposite to that on the C face, two strain gauges were simultaneously attached on Si and C faces of a SiC strip, and various degrees of bending were applied to the SiC strip, as shown in Fig. 4.16(a). The strains on the Si and C faces were then compared. The strains on Si face and C face at various bending degrees are shown in Fig. 4.16(b). It is clear that the strains on Si and C faces were almost the same but opposite to each other. Therefore, it is confirmed that the strain on the Si face of the SiC strip can be monitored by a strain gauge attached to the C face.

Strain represents the relative change in length, which is the ratio of deformation ($\Delta L$) to the original length (L) and is represented by $\delta$. That is, $\delta = \Delta L/L$. If $\delta$ is $10^{-6}$, it is denoted as 1 με. In this study, strains of −450, −350, −250, −150, −50, 0, 50, 150, 250, 350, and 450 με (a negative and positive values represent compressive and tensile strains, respectively) were applied to the Si face of the SiC strip (N-doping concentration of $8.25 \times 10^{18}$ $cm^{-3}$) through the four-point bending system and the SiC surfaces were anodically oxidized at 10 V for 15 min. Before each oxidation experiment, the strains on the SiC surface under bending were confirmed by a shift of the FTO(2/4)E2 peak of the 4H-SiC surface using Raman spectroscopy [20], as shown in Fig. 4.17(a). The positions of the FTO(2/4)E2 peak under various strains are shown in Fig. 4.17(c). It can be seen that the position of the FTO(2/4)E2 peak shifted to larger values under compressive stress and became smaller under tensile stress. Furthermore, the peak position shifted linearly, to a smaller value, with decreasing compressive strain and increasing tensile strain. These results indicate that the strain was precisely applied to the SiC surface by the four-point bending system. This experiment was conducted twice to evaluate its repeatability. The effect of the N-doping concentration was also investigated in the anodic oxidation experiment on a highly doped SiC strip ($1.25 \times 10^{19}$ $cm^{-3}$).

(a)




(b)

| Strain gauge 1 (με) | Strain gauge 2 (με) |
|---|---|
| +50 | -50 |
| +151 | -150 |
| +250 | -251 |
| +349 | -350 |
| +450 | -450 |

**Fig. 4.16** Comparison of strains on the Si and C faces during bending. (a) Installation diagram of strain gauges (strain gauges were simultaneously attached on the Si and C faces of the SiC strip). (b) Strains on the Si and C faces at various degrees of bending.

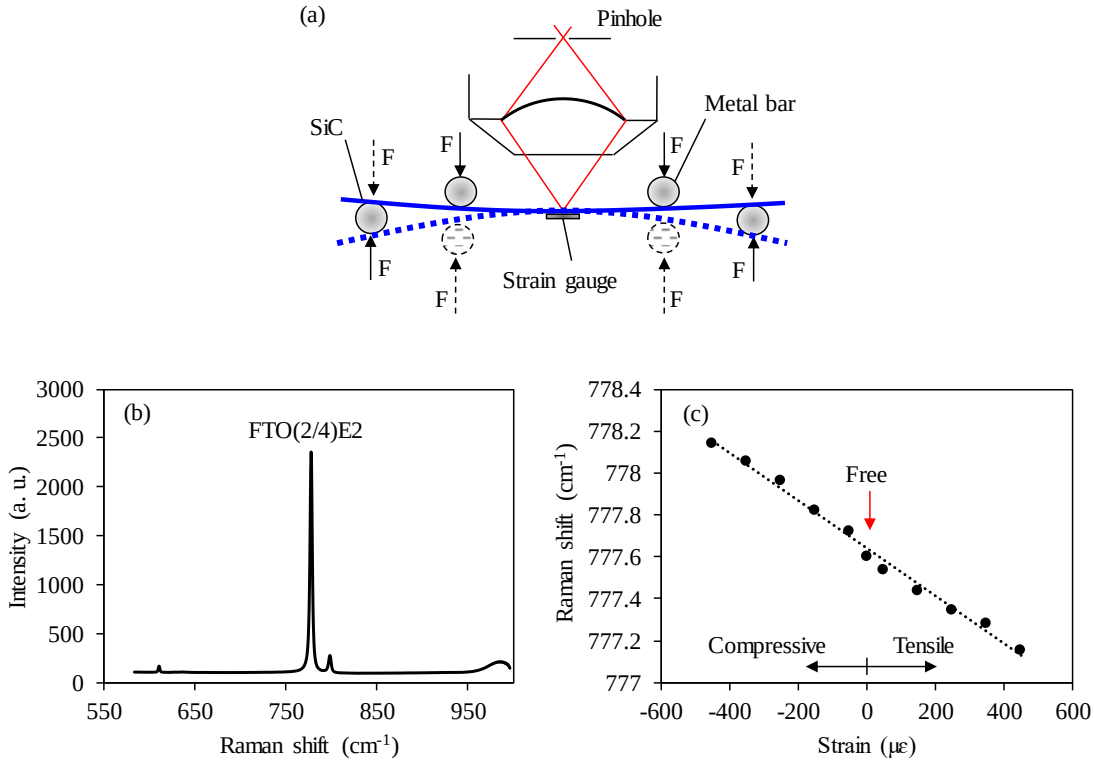



**Fig. 4.17** (a) Schematic diagram of Raman spectroscopy measurement of SiC strips under bending; (b) a typical Raman spectrum of 4H-SiC without bending; (c) relationship between Raman shift and applied strain on the SiC surface.

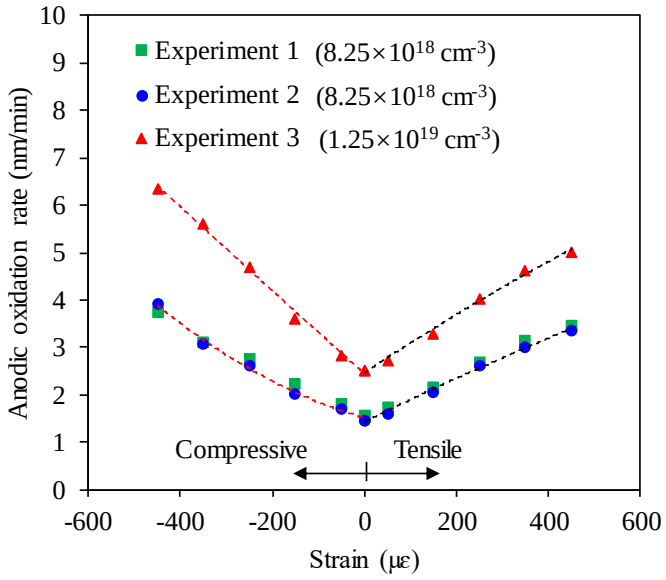



**Fig. 4.18** Anodic oxidation rate of the SiC surface with various strains; negative and positive values represent compressive and tensile strain, respectively.

Fig. 4.18 shows the relationship between the anodic oxidation rate and the applied strain on the SiC surface. The anodic oxidation rates obtained on SiC strips with the same N-doping concentration of $8.25 \times 10^{18}$ $cm^{-3}$ are almost the same, showing good reproducibility. However, the rate increased by about 1.6 times on the SiC strip with an N-doping concentration of $1.25 \times 10^{19}$ $cm^{-3}$, which can be attributed to a difference in the doping concentration. On the other hand, all of the anodic oxidation rates show the same trend with the change in surface strain. It is clear that anodic oxidation rate increased with the increase in both compressive and tensile strain (increased more than two times under ±450 με). Although the degree of increase was different, compressive strain clearly had a stronger effect on the anodic oxidation rate than tensile strain in total.

### 4.6.2 Effect of strain on the ECMP of SiC

On the basis of the above results, it was confirmed that a higher anodic oxidation rate could be achieved by applying strain to the SiC surface during the anodic oxidation process. Therefore, it was expected that the MRR of slurryless ECMP could be further increased by the introduction of strain on the SiC surface during the process. To confirm the effects of strain application, ECMP was conducted at various polishing pressures on CMP-processed SiC surfaces. There were two reasons to change the polishing pressure. First, changing the polishing pressure changed the compressive strain on the SiC surface along the <0001> direction. Second, changing the polishing pressure changed the friction between the SiC surface and the grinding stone, which changed the tensile strain on the SiC surface perpendicular to the <0001> direction. It is definite that both the compressive and tensile strains on the surface increased with increasing polishing pressure.

ECMP with pressures of 35, 70, 105, 140, and 175 kPa were conducted on CMP-processed 4H-SiC (0001) surfaces at 25 V for 1 h. Fig. 4.19(a) shows cross-sectional views of the polished areas obtained by ECMP with these different polishing pressures. It is clear that the MRR of ECMP increased with increasing polishing pressure. Fig. 4.19(b) shows the changes in MRR with polishing pressure. The MRR increased linearly with increasing polishing pressure, which is consistent with Fig. 4.18. Also, Fig. 19(c) shows the changes in current during ECMP with various polishing pressures and it was observed that the current increased with increasing polishing pressure. Because a constant potential of 25 V was applied during the ECMP, the changes in current reflected not only the degree of difficulty of anodic oxidation of the SiC surfaces but also the anodic oxidation rate. This suggests that anodic oxidation of the SiC surface in ECMP became easier and that the anodic oxidation rate increased with increasing polishing pressure, which corresponds to the changes in MRR in Fig. 4.19(b). Also, the changes in current became large (i.e., the current fluctuated between a few milliamps and tens of milliamps) with the increase in polishing pressure, as shown in Fig. 4.19(c). In the ECMP polishing process, anodic oxidation and removal of the oxide layer occurred continuously. The resistance of the SiC surface changes with the generation and removal of the

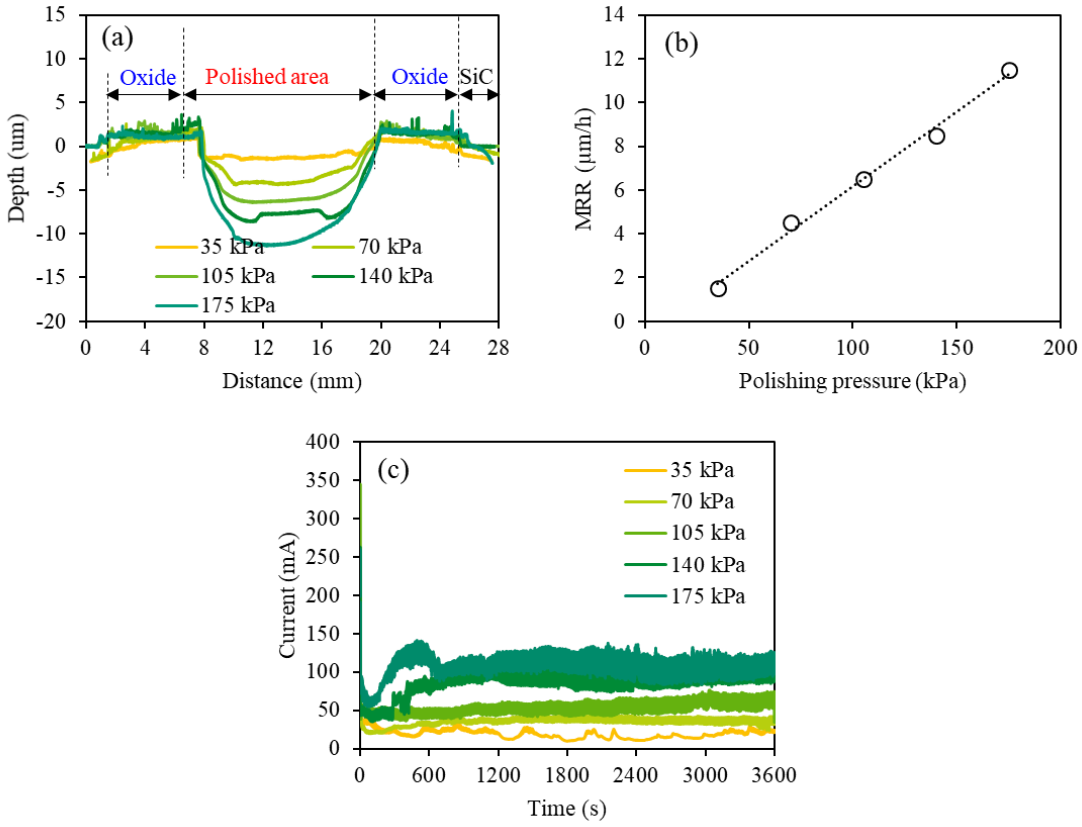



**Fig. 4.19** ECMP results for CMP-processed 4H-SiC (0001) surfaces at 25 V for 1 h with various polishing pressures. (a) Cross-sectional views of the polished areas. (b) Relationship between MRR and polishing pressure. (c) Changes of current during ECMP with different polishing pressures.

oxide layer from the surface. When the polishing pressure was low, the oxide layer growth rate was also low and it was removed in very small thicknesses. Therefore, the oxide film had little effect on the resistance of the SiC surface, which resulted in small current fluctuation during ECMP. However, under high polishing pressure, the oxidation rate of the SiC increased and the oxide layer become thicker before its removal; thus, the changes in the resistance of the SiC surface increased before and after the oxide layer was removed. This resulted in large current fluctuations during ECMP.

Fig. 4.20 shows the cross-sectional residual stress distributions, measured using the confocal Raman microscope, in surfaces polished by ECMP at various polishing pressures. The laser wavelength used for Raman spectroscopy was 532 nm. In Raman spectroscopy, the set detection depth of the SiC surface was 4 μm, whereas the actual observed depth was about 10.8 μm. This was according to the refraction index of 4H-SiC, which has a value of 2.7 under an applied laser wavelength of 532 nm [22,24]. From Fig. 4.20, it can be seen that no residual stress was observed on or below the polished surface, which indicates that the increase in polishing pressure during ECMP did not introduce damage to the SiC surfaces.

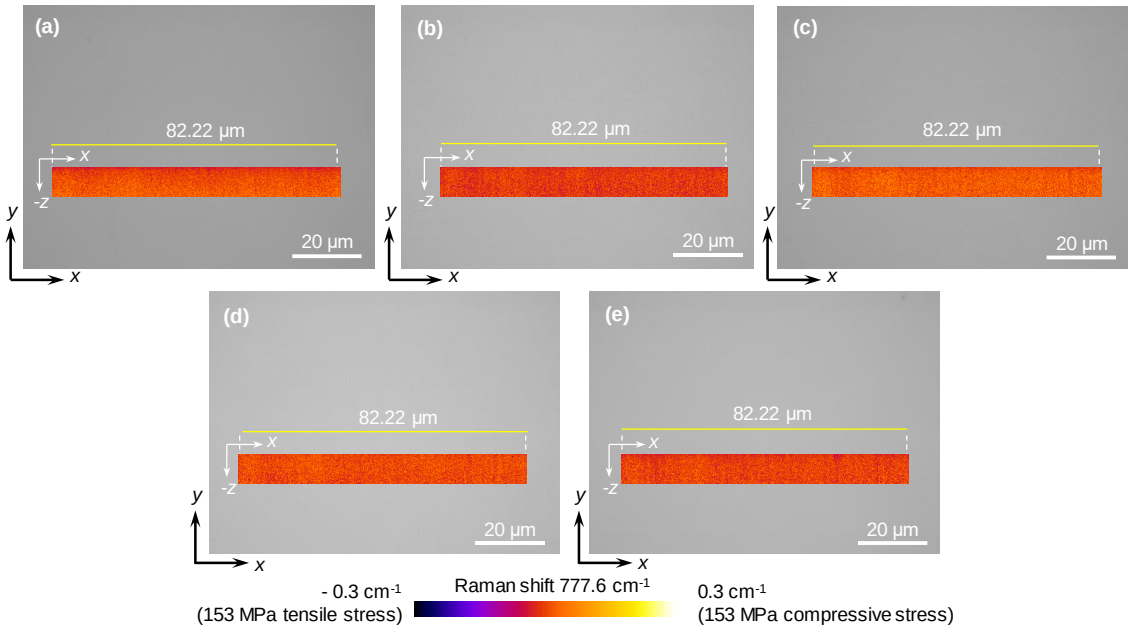



**Fig. 4.20** Microscope images and cross-sectional residual stress distribution images of 4H-SiC (0001) surfaces processed by ECMP at 25 V with polishing pressures of (a) 35, (b) 70, (c) 105, (d) 140, and (e) 175 kPa. The observation depth was ~10.8 μm.

Fig. 4.21 shows the relationship between the surface roughness and the polishing pressure during ECMP using the ceria grinding stone. The *S*q and *S*z surface roughness remained at about 0.6 and 4.5 nm, respectively, with increasing polishing pressure. Fig. 4.22 shows XPS spectra of 4H-SiC surfaces polished by ECMP at various polishing pressures. Peaks corresponding to Si-O bonds were not observed on all of the polished surfaces. Only strong peaks corresponding to Si-C bonds

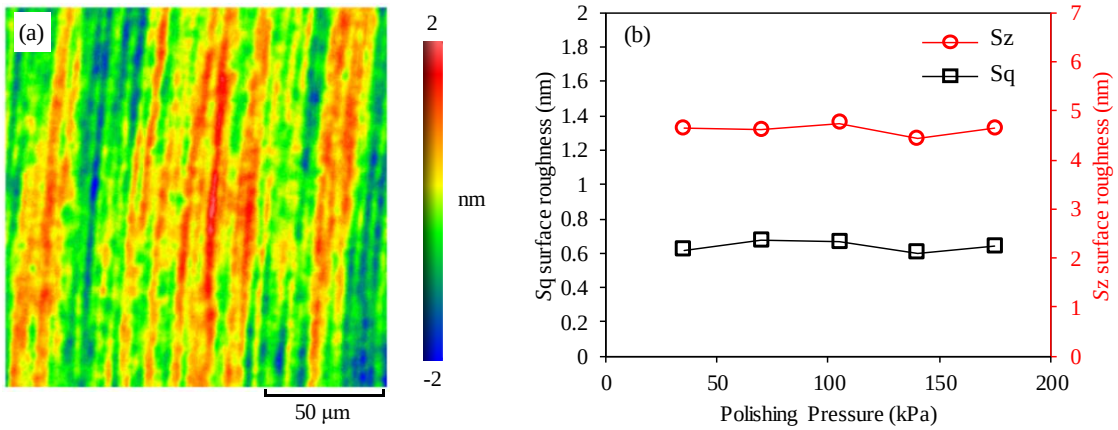



**Fig. 4.21** Relationship between surface roughness and polishing pressure in ECMP using a ceria grinding stone.

and weak peaks corresponding to Si-O-C bonds were observed, which indicates that no residual oxide remained on these surfaces. The removal rate of the oxide layer was always greater than the anodic oxidation rate in ECMP under various polishing pressures.

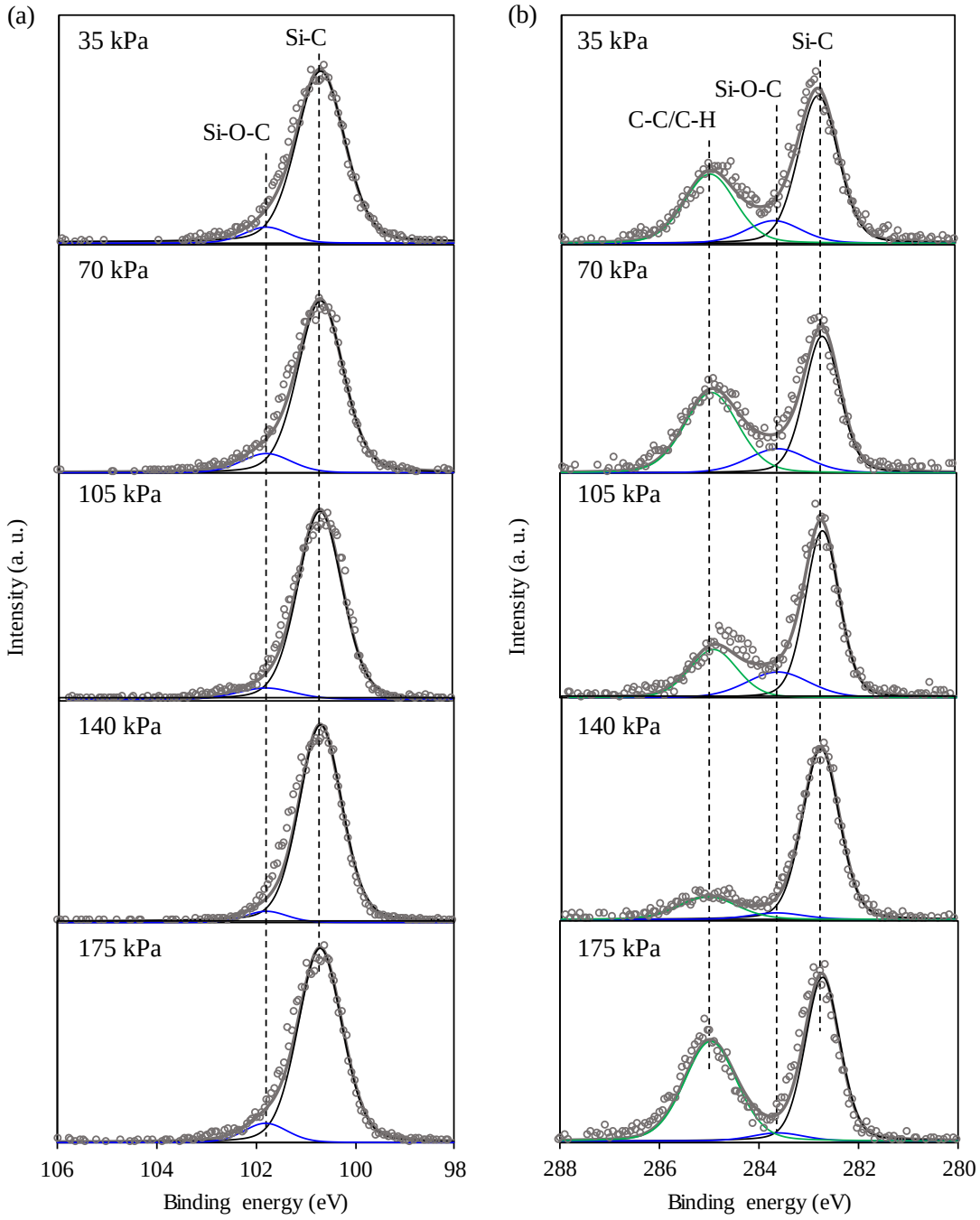



**Fig. 4.22** XPS spectra, measured with a take-off angle of 45°, for 4H-SiC surfaces polished by ECMP at various polishing pressures: (a) Si2p spectra, (b) C1s spectra.

According to Preston's law, the MRR increases with increasing polishing pressure during mechanical polishing (MP). Therefore, as the polishing pressure was increased, there is a possibility that the SiC was directly mechanically removed by the grinding stone, resulting in an increase in MRR during ECMP at higher polishing pressures. To investigate the effect of polishing pressure on the mechanical removal rate of SiC, MP at those higher polishing pressures was conducted on CMP-processed 4H-SiC (0001) surfaces. The parameters were the same as those in the ECMP experiments apart from electric potentials. Fig. 4.23 shows cross-sectional views of the polished areas obtained using MP at various polishing pressures; almost no material was removed with increasing pressure. This result indicates that the ceria grinding stone had difficulty removing SiC because its hardness was lower than that of SiC. Therefore, the mechanical removal of SiC by the ceria grinding stone in ECMP could be ignored.

Also, Fig. 4.24 shows cross-sectional residual stress distributions, measured using the confocal Raman microscope, on surfaces polished using MP at various polishing pressures. The observation parameters were the same as those in Fig. 4.20. No residual stress was observed on these surfaces and it was confirmed that even with the MP method, damage was unlikely to be introduced to the SiC surface by increasing the polishing pressure when applying the ceria grinding stone. This result indicates that an increase in polishing pressure only increased the compressive and tensile strains at the contact area between the SiC surface and the grinding stone. The MRR during ECMP was promoted by these strains and not by mechanical damage.

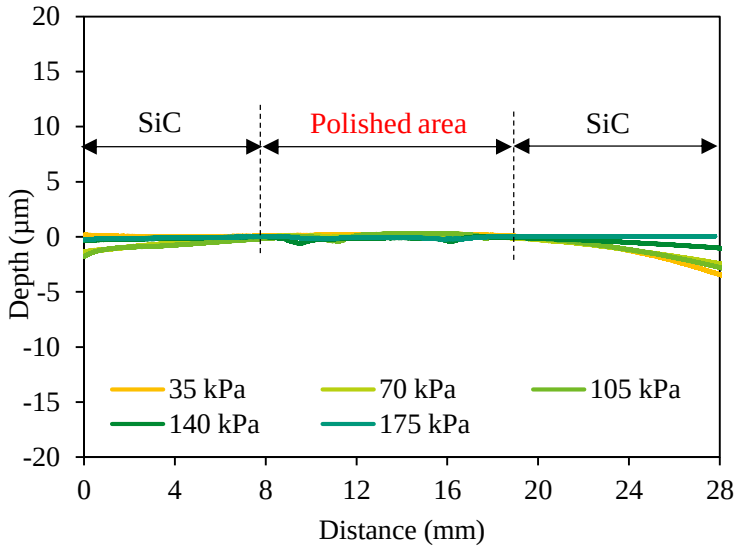



**Fig. 4.23.** Cross-sectional views of MP polished areas on 4H-SiC (0001) surfaces at various polishing pressures.

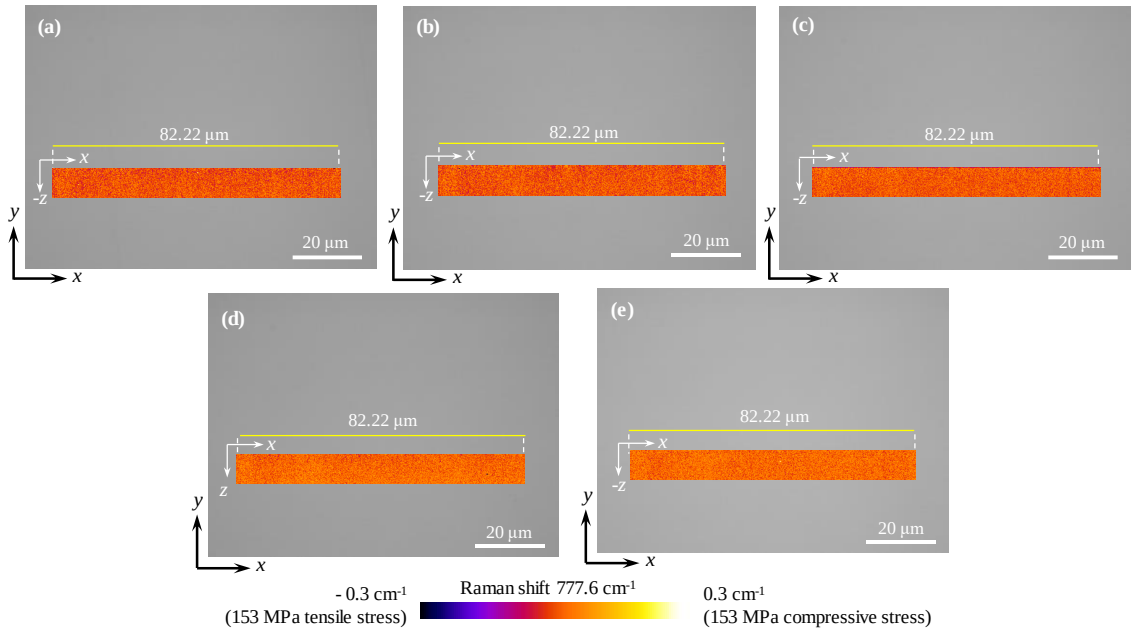



**Fig. 4.24** Microscope images and cross-sectional residual stress distribution images of MP-processed 4H-SiC (0001) surfaces with various polishing pressures of (a) 35, (b) 70, (c) 105, (d) 140, and (e) 175 kPa. The observation depth was ~10.8 μm.

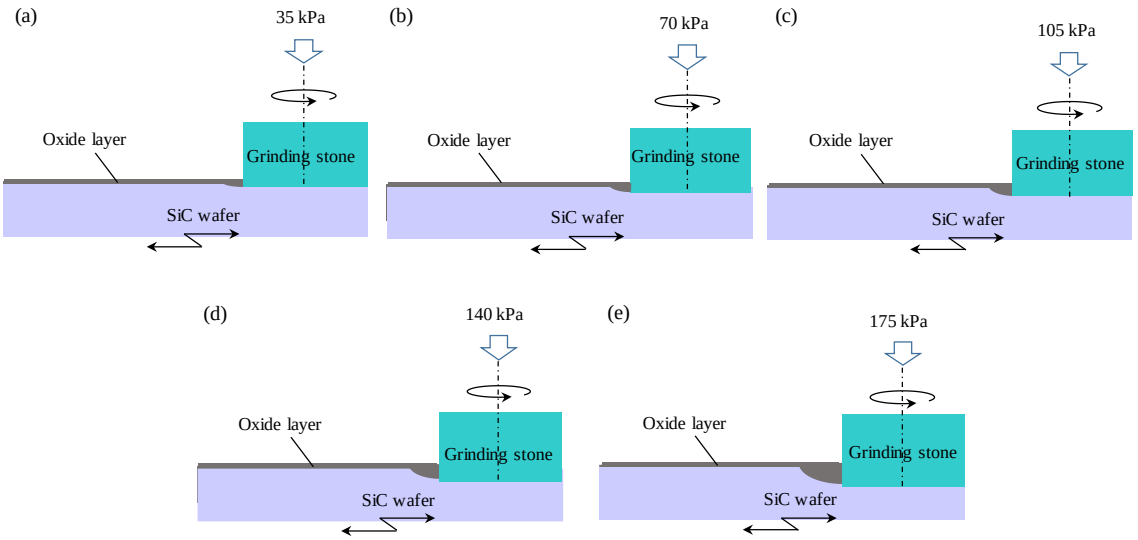



**Fig. 4.25** Modeling of the ECMP process at various polishing pressures.

Based on the above results, it can be concluded that the generation rate of oxide layer increased with increase in polishing pressure, which further increased the MRR of ECMP as shown in Fig. 4.19. Therefore, the ECMP of SiC surfaces at various polishing pressures can be modeled as shown in Fig. 4.25. During ECMP, the area under and adjacent to the grinding stone would be strained

owing to the polishing pressure; the farther away from the grinding stone, the smaller the strain. Additionally, both strains increase with an increase in polishing pressure. Based on the results in Section 4.6.1, the anodic oxidation rate is observed to increase with increase in strain. Therefore, the anodic oxidation rate below and adjacent to the grinding stone should increase with increase in polishing pressure. According to the Preston equation, the removal rate of the oxide layer also increases with high polishing pressure. Therefore, the balance between the anodic oxidation rate and the removal rate of the oxide layer was maintained as the polishing pressure increased, resulting in polished surfaces with almost the same surface roughness, although the MRR increased.

### 4.6.3 Action mechanism of strain in the anodic oxidation of SiC

The effects of strain in the thermal oxidation of Si have been investigated. Most studies have found that tensile stress promotes the oxidation of Si, whereas compressive stress had no effect [25-28]. The reason for this is thought to be changes in the distance between Si atoms. This distance becomes large under tensile stress, which promotes the inward penetration of O atoms on the Si surface, causing an increase in oxidation rate [27,28]. However, this does not explain the greater increase in anodic oxidation rate observed for SiC under compressive strain in our study. Because electricity is applied during anodic oxidation of SiC, it is believed that changes in the electrical properties of SiC have greater effects on its anodic oxidation.

In order to investigate the effects of residual strain on the electrical properties of SiC, C-AFM observations were conducted on CMP and diamond-lapped surfaces. To observe the same area on the SiC surface, 20 × 20 indents at distances of 5 μm were created using a nanoindentor with a pressure load of 100 mN. These indents were used as benchmarks, as shown in Fig. 4.26(a). The indents in the upper-right corner and two areas (1.5 × 1.5 μm on the CMP surface and 3 × 3 μm on the diamond-lapped surface) among the indents were observed using C-AFM, as shown in Fig.

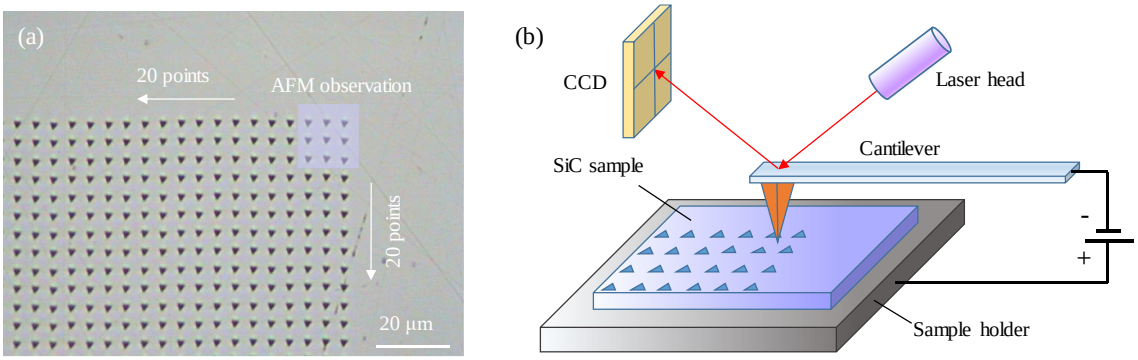



**Fig. 4.26** (a) Optical microscope image of an indented SiC surface. (b) Schematic of C-AFM observations of a SiC sample. When a positive potential was applied to the SiC sample, a negative current was observed in the C-AFM system.

4.26(b). A silicon cantilever, whose tip side and detector side were coated with conductive diamond and Al, respectively, was used for C-AFM observations. During the observation, a positive potential of 4 V was applied to the SiC wafer, which resulted in observation of a negative current by the C-AFM system; thus, the surface topography and current distribution were obtained simultaneously. After C-AFM observation, the CMP and diamond-lapped SiC surfaces were anodically oxidized for 1 s with potentials of 12 and 8 V, respectively. The same areas were also observed using AFM after anodic oxidation to evaluate the effects of residual strain on the anodic oxidation of SiC.

Fig. 4.27 shows C-AFM observation results for the CMP-processed surface. From Fig. 4.27(a) and (b), the current on the indented CMP surface is mainly concentrated at the indents, whereas the other areas have almost no current flow. Because the indents were mechanically formed by the indenter with a load of 100 mN, there is no doubt that the indents were accompanied by damage and residual strain. This means the damaged areas have a higher conductivity than the strain-free area. From Fig. 4.27(c) and (d), after anodic oxidation, the indents were covered by oxide and the depth of the indents was reduced from about 160 to 80 nm, whereas the other areas showed almost no oxidation. Fig. 4.27(a1) to (c1) and (a2) to (c2) show the detailed current distribution and anodic oxidation characteristics of areas 1 and 2, respectively, with sizes of 1.5 × 1.5 μm. In these two areas, the current flow was very small, with a random point distribution. On the other hand, the SiC surface was also point oxidized, with the generation of many oxide protrusions, as shown in Fig. 4.27(c1) and (c2). This suggests that the anodic oxidation of SiC is related to the current distribution obtained in C-AFM.

Fig. 4.28 shows C-AFM observation results for the diamond-lapped SiC surface. From Fig. 4.28(a) and (b), it can be seen that the current distribution of the indented diamond-lapped SiC was not uniform. All of the indents and most of the scratches had a much higher current compared with the other areas. Because the scratches and indents were accompanied by residual strains, as shown in Fig. 4.14, these results mean that the strained areas had higher electrical conductivity than the strain-free area. After anodic oxidation, as shown in Fig. 4.28(c) and (d), oxides were preferentially generated in areas that had high current in C-AFM observations. Their thickness reached tens of nanometers while the other areas showed almost no oxidation. These areas having high current in C-AFM observations clearly had a much higher anodic oxidation rate. Fig. 4.28(a1) to (d1) and (a2) to (d2) show the detailed current distribution and anodic oxidation of the diamond lapping-induced scratches. Deep scratches, like scratch L1, are observed to have high current flow; they were fully covered by oxide after anodic oxidation. Since deep scratches are accompanied by large strains, this result indicates that the value of the current flow reflects the degree of strain; the higher the current flow, the larger the strain and the greater the oxidation rate. Alternately, some shallow scratches, like scratch L2, also had high current flow; thick oxide was generated after anodic oxidation, indicating that the shallow scratch L2 was also accompanied by large strain and the anodic oxidation

rate was dominated by the degree of strain, not the depth of scratch. Fig. 4.28(f) shows an enlarged view of Fig. 4.28(d2) at scratches L1 and L2. The deep scratch L1 (position G) is observed to have a larger current flow than the shallow scratch L2 (position H). The height change of scratch L1 (*h*1) was also greater than that for scratch L2 (*h*2) after anodic oxidation. This result confirmed that the degree of strain can be reflected by the current flow value and the anodic oxidation rate is dominated by the strain on the SiC surface.

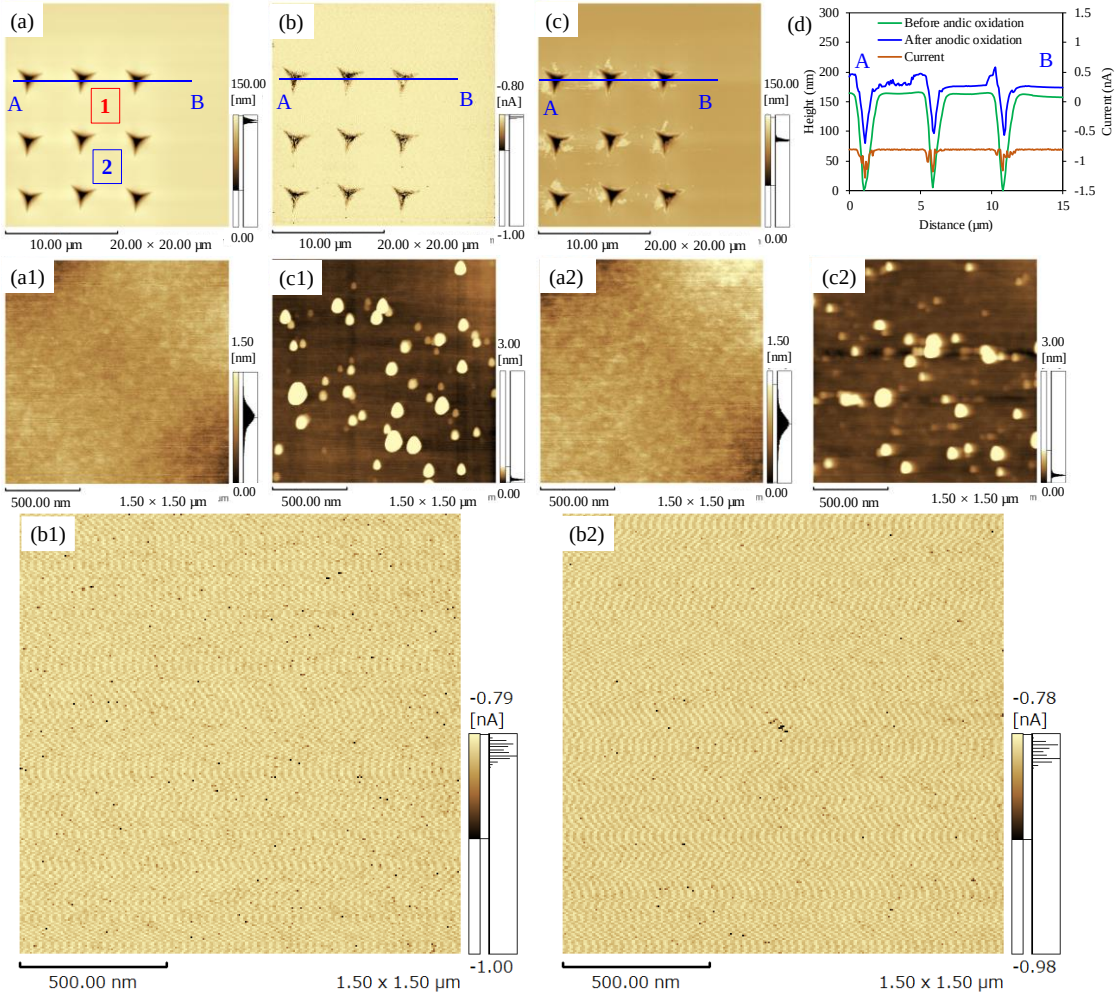



**Fig. 4.27** C-AFM observation results for a CMP-processed 4H-SiC (0001) surface. (a) to (c) surface topography, current distribution, and surface topography after anodic oxidation (observed on the upper-right corner of the indented area with a size of 20 × 20 µm) and (d) their cross-sectional views along A–B. (a1) to (c1) surface topography, current distribution, and surface topography after anodic oxidation of area 1 in (a). (a2) to (c2) surface topography, current distribution, and surface topography after anodic oxidation of area 2 in (a).

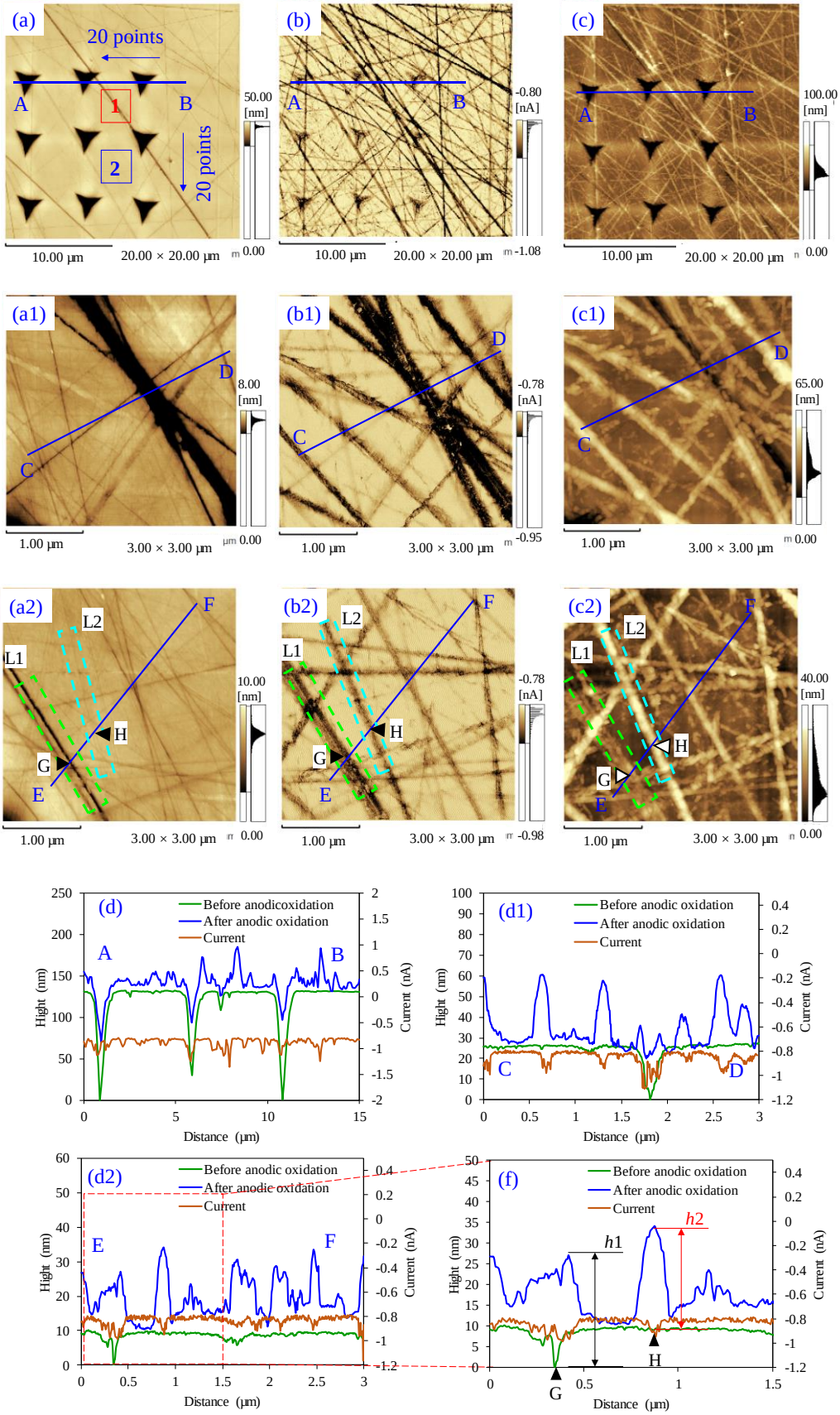

(a)
20 points
A
B
1
2
20 points
50.00 [nm]
0.00
10.00 μm
20.00 × 20.00 μm
(b)
A
B
-0.80 [nA]
-1.08
10.00 μm
20.00 × 20.00 μm
(c)
A
B
100.00 [nm]
0.00
10.00 μm
20.00 × 20.00 μm
(a1)
D
C
8.00 [nm]
0.00
1.00 μm
3.00 × 3.00 μm
(b1)
D
C
-0.78 [nA]
-0.95
1.00 μm
3.00 × 3.00 μm
(c1)
D
C
65.00 [nm]
0.00
1.00 μm
3.00 × 3.00 μm
(a2)
F
L2
L1
H
G
E
10.00 [nm]
0.00
1.00 μm
3.00 × 3.00 μm
(b2)
F
L2
L1
H
G
E
-0.78 [nA]
-0.98
1.00 μm
3.00 × 3.00 μm
(c2)
F
L2
L1
H
G
E
40.00 [nm]
0.00
1.00 μm
3.00 × 3.00 μm
(d)
Before anodicoxidation
After anodic oxidation
Current
A
B
Hight (nm)
Current (nA)
Distance (μm)
(d1)
Before anodic oxidation
After anodic oxidation
Current
C
D
Hight (nm)
Current (nA)
Distance (μm)
(d2)
Before anodic oxidation
After anodic oxidation
Current
E
F
Hight (nm)
Current (nA)
Distance (μm)
(f)
Before anodic oxidation
After anodic oxidation
Current
h2
h1
H
G
Hight (nm)
Current (nA)
Distance (μm)

**Fig. 4.28** C-AFM observation results for a diamond-lapped 4H-SiC (0001) surface. (a) to (c) surface topography, current distribution, and surface topography after anodic oxidation (observed on the upper-right corner of the indented area with a size of 20 × 20 μm) and (d) their cross-sectional views along A–B. (a1) to (c1) surface topography, current distribution, and surface topography after anodic oxidation of area 1 in (a) and (d1) their cross-sectional views along C–D. (a2) to (c2) surface topography, current distribution, and surface topography after anodic oxidation of area 2 in (a) and (d2) their cross-sectional views along E–F. (f) Partially enlarged view of (d2).

From the AFM observations for CMP and diamond-lapped SiC surfaces, it can be concluded that the strain on the SiC surface changed the electrical properties of the SiC, which resulted in higher electrical conductivity in strained areas. It has been reported that biaxial and uniaxial strain can affect the band gap of SiC. Compressive biaxial strain in the (0001) plane of 4H-SiC leads to a linear decrease of band gap. The band gap increases almost linearly with the strain, up to 0.4% tensile biaxial strain, and then begins to decrease [29,30]. However, both compressive and tensile uniaxial strain are reported to reduce the band gap of SiC [31,32]. This may be caused by the difference in the changes of SiC structure. Uniaxial stress may bring structural changes that reduce the symmetry of the system while biaxial stress provides no changes to the symmetry or shape of the material [33]. In the anodic oxidation experiment in Section 4.6.1, it is clear that uniaxial strain was applied to the SiC surface; therefore, it is believed that both compressive and tensile stresses decreased the band gap of the SiC during anodic oxidation. The reduction of the band gap leads to the generation of holes during anodic oxidation, which increases the anodic oxidation rate.

In the case of doping, it is known that carrier concentration in SiC increases with increasing doping concentration, changing the electrical conductivity of SiC. It has been reported that the electrical conductivity of SiC increases with increasing doping concentration; the resistivity of 4H-SiC decreased from 0.036 to 0.012 Ω·cm when the N concentration was increased from $4.02 \times 10^{18}$ to $1.59 \times 10^{19}$ $cm^{-3}$ [34,35] (decreased by three times). The resistance of the SiC anodic oxidation system consists of the resistances of bulk SiC, electrolyte, oxide layer, and the electrochemical reaction occurring at the interface between SiC and electrolyte, which is determined by the difficulty of the anodic oxidation reaction. In this study, the resistance of bulk SiC is at the $10^{-3}$ Ω level according to its resistivity and the oxidation area; the resistance of the electrolyte is at the level of $10^2$ Ω, according to its electrical conductivity; and the resistance of the oxide layer and the interface between SiC and electrolyte are generally at the level of $10^3$ Ω [36]. The resistance of the bulk SiC is negligibly small compared with the other resistances. Therefore, it is considered that the decrease in the resistance of SiC caused by doping has little effect on the total resistance of the anodic oxidation system and has a very small effect on the anodic oxidation rate of SiC. Moreover, the highly doped SiC has a high anodic oxidation rate, even under the same oxidation current density,

as shown in Fig. 4.11. This means the anodic oxidation of highly doped SiC is much easier than that of low doped SiC, which was not affected by the resistance of the bulk SiC. Therefore, the promotional effects of doping in anodic oxidation of SiC in this study is considered to be caused by doping-induced strain.

In N doped SiC, C atoms are generally known to be replaced by N atoms [37]. Since the atomic radius of N is smaller than that of C, the bond length and bond angle are changed in N-doped SiC. Reshanov *et al.* reported that N atom-nearest neighbor bond length contracts by 0.038 Å when a C atom is replaced by an N atom in SiC and contracted by 0.363 Å when a Si atom is replaced [38]. This resulted in both *c*- and *a*-axes lattice constants of 4H-SiC decreasing with an increase of N concentration [39] and lattice strain in doped SiC linearly increasing with increasing N-doping concentration (strain in the *a*-axis direction increased from ~3 to ~300 με when N-doping concentration increased from $1 \times 10^{17}$ to $1 \times 10^{19}$ $cm^{-3}$) [16]. From Fig. 4.18, the anodic oxidation rate of the SiC surface with a doping concentration of $1.25 \times 10^{19}$ $cm^{-3}$ is about 1.6 times that of the surface with a doping concentration of $8.25 \times 10^{18}$ $cm^{-3}$ under strain-free conditions. The anodic oxidation rate is almost linearly increased with doping concentration (doping concentration increased by 1.5 times). The anodic oxidation rate of the SiC surface with a doping concentration of $1.25 \times 10^{19}$ $cm^{-3}$ is equivalent to that when applying a uniaxial compressive/tensile strain of ~200 με to the surface with doping concentration of $8.25 \times 10^{18}$ $cm^{-3}$ based on the results in Fig. 4.18. According to Ref. 16), lattice strain along the *a*-axis at a doping concentration of $8.25 \times 10^{18}$ $cm^{-3}$ is about 250 με, which increases to about 380 με at a doping concentration of $1.25 \times 10^{19}$ $cm^{-3}$ (an increase of 130 με, slightly smaller than 200 με). This difference is caused by the difference in strain direction. Only doping-induced strain along the *a*-axis direction was calculated in Ref. 16), while strain also exists in other axis directions. Thus, the total changes in strain would be greater than 130 με when the doping concentration is increased from $8.25 \times 10^{18}$ to $1.25 \times 10^{19}$ $cm^{-3}$. Therefore, it can be concluded that doping-induced strain promoted the anodic oxidation rate of SiC.

## 4.7 Summary

Dominant factors, including temperature, doping concentration, damage, and strain, and their action mechanisms in anodic oxidation and ECMP of the 4H-SiC (0001) surface were investigated experimentally and theoretically. The following results were obtained.

(1) A constant-temperature anodic oxidation set up was developed. Anodic oxidation of 4H-SiC (0001) was performed with different electrolyte temperatures. In constant-current anodic oxidation, there existed a saturated anodic oxidation rate with increasing oxidation current density. This saturated anodic oxidation rate increased exponentially with increasing

electrolyte temperature and satisfied the Arrhenius equation.

(2) At the same current density of 20 mA/cm$^2$, the MRR of ECMP increased from 4.5 to 9.5 μm/h as the electrolyte temperature increased from 25 to 60 °C. The surface roughness was not affected by electrolyte temperature. It was mainly affected by the balance between anodic oxidation rate and the removal rate of the oxide layer.

(3) Both N-doping and surface damage increased the anodic oxidation rate of SiC and the current efficiency at high current densities. The activation energies of highly doped and diamond-lapped SiC were lower than those of low doped CMP-processed SiC; damage showed a greater promotional effect. These observations were attributed to the residual strain on the SiC surface.

(4) The effects of strain on the anodic oxidation rate of SiC were quantitatively investigated using a strain-controllable, constant-temperature anodic oxidation setup. The results showed that both compressive and tensile strains increase the anodic oxidation rate of SiC; the anodic oxidation rate of the SiC surface increased by more than two times when compressive and tensile strains were increased from 0 to 450 με. The promotional effect of compressive strain was stronger than that of tensile strain.

(5) MP with different polishing pressures was conducted on SiC surfaces; almost no material was removed with increasing polishing pressure. The surfaces obtained with different polishing pressures were measured by Raman spectroscopy and no residual stress was observed on these surfaces. It was confirmed that damage was unlikely to be introduced to the SiC surface by increasing the polishing pressure when applying a ceria grinding stone during MP.

(6) Increasing the polishing pressure was an effective method for introducing strain on the SiC surface during ECMP and resulted in an increase in anodic oxidation rate and MRR. The MRR of ECMP was increased from 1.5 to 11.5 μm/h by increasing the polishing pressure from 35 to 175 kPa and the same surface roughness of about 0.6 nm *S*q were obtained.

(7) The promotional mechanism of anodic oxidation by strain on SiC was investigated using C-AFM. The C-AFM results showed that the strained areas had a higher electrical conductivity than the strain-free areas, and the distribution of the anodic oxidation rate was perfectly consistent with the current distribution on the SiC surface. It is considered that the strain changed the electrical property of the SiC.

# References


1) N. Gabouze, A. Keffous, T. Kerdja, Y. Belaroussi, Appl. Surf. Sci. 255(15) (2009) 6751–6756.
2) D. H. Van Dorp, J. L. Weyher, J. J. Kelly, J. Micromech. Microeng. 17(4) (2007) S50–S55.
3) S. Setzu, G. Lérondel, R. Romestain, J. Appl. Phys. 84(6) (1998) 3129–3133.
4) B. K. Daas, M. M. Islam, I. A. Chowdhury, F. Zhao, T. S. Sudarshan, M. V. S. Chandrashekhar, Electron Devices 58(1) (2010) 115–121.
5) G. Jia, B. Li, J. Zhang, Mater. Sci. 146 (2018) 26–35.
6) M. Eickhoff, N. Vouroutzis, A. Nielsen, G.Krötz, J. Stoemenos, J. Electrochem. Soc. 148 (2001) G336–G343.
7) A. Severino, M. Camarda, S. Scalese, P. Fiorenza, S. Di Franco, C. Bongiorno, A. La Magna, F. La Via, Appl. Phys. Lett. 95 (2009) 111905.
8) X. Yang, R. Sun, K. Kawai, K. Arima, K. Yamamura, ACS Appl. Mater. Interfaces 11(2) (2018) 2535–2542.
9) M. Katsuno, N. Ohtani, J. Takahashi, H. Yashiro, M. Kanaya, Jpn. J. Appl. Phys. 38 (1999) 4661–4665.
10) R. Yakimova, A.-L. Hylén, M. Tuominen, M. Syväjärvi and E. Janzén, Diamond Relat. Mater. 6 (1997) 1456–1458.
11) V. Simonka, A. Hossinger, J. Weinbub, S. Selberherr, J. Appl. Phys. 120 (2016) 135705.
12) Y. Song, S. Dhar, L. C. Feldman, G. Chung, J. R. Williams, J. Appl. Phys. 95(9) (2004) 4953–4957.
13) T. Hosoi, D. Nagai, M. Sometani, Y. Katsu, H. Takeda, T. Shimura, M. Takei, H. Watanabe, Appl. Phys. Lett. 109(18) (2016) 182114.
14) X. Yang, X. Yang, R. Sun, K. Kawai, K. Arima, K. Yamamura, Nanomanuf. Metrol. 2 (2019) 140–147.
15) S. Sasaki, J. Suda, T. Kimoto, Mater. Sci. Forum 717 (2012) 481–484.
16) H. Jacobson, J. Birch, C. Hallin, A. Henry, R. Yakimova, T. Tuomi, E. Janzén, and U. Lindefelt, Appl. Phys. Lett. 82 (2003) 3689–3691.
17) E. K. Sanchez, S. Ha, J. Grim, M. Skowronski, W. M. Vetter, M. Dudley, R. Bertke, W. C. Mitchel, J. Electrochem. Soc. 149 (2002) 131–136.
18) J. Yan, X. Gai, H. Harada, J. Nanosci. Nanotechnol. 10 (2010) 7808–7811.
19) S. Nakashima, T. Mitani, M. Tomobe, T. Kato, H. Okumura, AIP Adv. 6 (2016) 015207.
20) N. Sugiyama, M. Yamada, Y. Urakami, M. Kobayashi, T. Masuda, K. Nishikawa, F. Hirose, S. Onda, MRS Proc. 1693 (2014).
21) G. Liu, Y. Zhang, W. Natsu, Int. J. Mach. Tools Manuf. 142 (2019) 66–75.
22) S. Hell, G. Reiner, C. Cremer, E.H. Stelzer, J. Microsc. 169(3) (1993) 391–405.
23) P.T. Shaffer, R.G. Naum, JOSA 59 (11) (1969) 1498–1498.
24) B. Pégourié, Optical properties of alpha silicon carbide, Astron. Astrophys. 194 (1988) 335–339.
25) A. Mihalyi, R. J. Jaccodine, and T. J. Delph, Appl. Phys. Lett. 74 (1999) 1981–1983.

26) J. Y. Yen and J. G. Hwu, J. Appl. Phys. 89 (2001) 3027–3032.
27) J. Y. Yen and J. G. Hwu, Appl. Phys. Lett. 76 (2000) 1834–1835.
28) Y. Sun, Y. Liu, X. Chen, Z. Zhai, and S. Izumi, J. Appl. Phys. 123 (2018) 135104.
29) Y. Kuroiwa, Y. Matsushita, K. Harada, and F. Oba, Appl. Phys. Lett. 115 (2019) 112102.
30) K. Chokawa, K. Shiraishi, Jpn. J. Appl. Phys. 57 (2018) 071301.
31) F. M. Steel, B. R. Tuttle, X. Shen, S. T. Pantelides, J. Appl. Phys. 114 (2013) 013702.
32) B. Gao, Q. Xu, S. Ke, N. Xu, G. Hu, Y. Wang, F. Liang, Y. Tang, S. Xiong, Phys. Lett. A 378 (2014) 565–569.
33) M.S. Manju, K.M. Ajith, M.C. Valsakumar, Mech. Mater. 120 (2018) 43–52.
34) E. Brinciotti, G.Gramse, S. Hommel, T. Schweinboeck, A. Altes, M. A. Fenner, F. Kienberger, Nanoscale 7(35) (2015) 14715–14722.
35) Y. Cui, X. Hu, K. Yang, X. Yang, X. Xie, L. Xiao, X. Xu, Cryst. Growth. Des. 15(7) (2015) 3131–3136.
36) D. H. van Dorp, E. S. Kooij, W. M. Arnoldbik, J. J. Kelly, Chem. Mater. 21 (2009) 3297–3305.
37) D. J. Larkin, P. G. Neudeck, J. A. Powell, L. G. Matus, Appl. Phys. Lett. 65 (1994) 1659–1661.
38) S. A. Reshanov, I. I. Parfenova, V. P. Rastegaev, Diamond Relat. Mater. 10 (2001) 1278–1282.
39) T. Matsumoto, S. I. Nishizawa, S. Yamasaki, Mater. Sci. Forum 645–648 (2010) 247–250.

# Chapter 5
# Ultrasonic vibration assisted anodic oxidation of the 4H-SiC (0001) surface

## 5.1 Introduction

Like that in slurryless electrochemical mechanical polishing (ECMP), in slurryless ultrasonic vibration assisted ECMP (UAECMP), the SiC surface is also first softened by anodic oxidation and then the oxide layer is removed by soft abrasives. The material removal rate (MRR) of UAECMP also depends on the anodic oxidation rate of the 4H-SiC surface. Therefore, it is necessary to investigate the effect of ultrasonic vibration on the anodic oxidation of SiC. This chapter investigates the effect of ultrasonic vibration on the anodic oxidation of SiC when ultrasonic vibration is applied to the electrolyte and to the SiC wafer, respectively. The promotional effects of these ultrasonic vibration applications were compared. In addition, the promotional mechanism of ultrasonic vibration on the anodic oxidation of SiC is also discussed.

## 5.2 Application of ultrasonic vibration to the electrolyte during anodic oxidation of the 4H-SiC (0001) surface

### 5.2.1 Anodic oxidation setup

Fig. 5.1 shows the ultrasonic vibration assisted anodic oxidation setup, which consists of an anodic oxidation system and an ultrasonic vibration system. The ultrasonic system was an ultrasonic cleaner (ASU-10M) supplied by AS ONE Corporation and the ultrasonic cleaner sink was made of 304 stainless steel. The anodic oxidation system was immersed in the sink. The anodic oxidation system container was specially developed for ultrasonic cleaning and was made of quartz glass. The power and frequency of the ultrasonic cleaner was 30 W and 40 kHz, respectively. The anodic oxidation system consisted of a potentiostat and three electrodes: a reference electrode (RE, Ag|AgCl), a work electrode (WE, SiC substrate), and a counter electrode (CE, platinum mesh). The potential of the WE was maintained at 3 V with reference to the RE using the potentiostat.

The 4H-SiC substrates (on-axis, n-type, thickness: 408 μm, specific resistance: 0.10 Ω·cm)

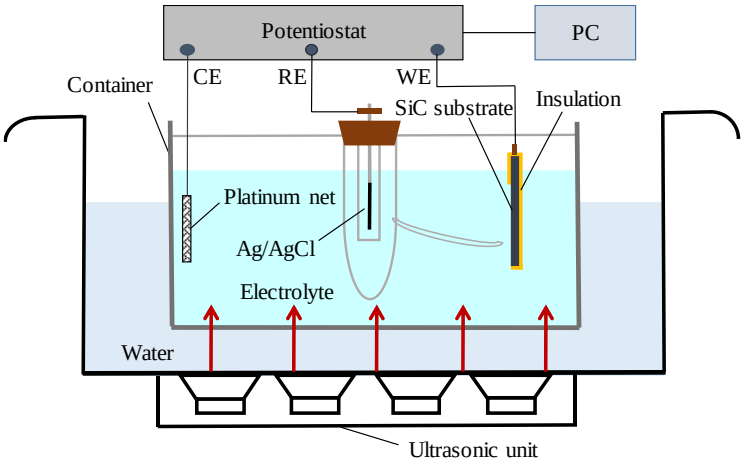



**Fig. 5.1** Anodic oxidation setup for applying ultrasonic vibration to the electrolyte.

used in this work were supplied by TankeBlue Semiconductor Co. Ltd. The substrates were processed by diamond lapping and cleaned by wet chemical cleaning before the experiments. All experiments were conducted on SiC (0001) surfaces and the (000-1) surfaces of the SiC substrates were covered with insulating glue to isolate them from the electrolyte during anodic oxidation. The electrolyte was 1 wt% aqueous sodium chloride solution with an electrical conductivity of 1.8 S/m. The morphologies of the SiC surfaces before and after anodic oxidation were observed by atomic force microscopy (AFM, Shimadzu SPM 9700) and scanning electron microscopy (SEM, Hitachi S-4800). The oxygen content of the SiC surface was measured by X-ray photoelectron spectroscopy (XPS, Quantum 2000, ULVAC-PHI).

### 5.2.2 Effects of ultrasonic vibration in electrolyte on the anodic oxidation rate of the SiC surface

Fig. 5.2(a) shows an AFM image of a diamond-lapped surface, on which many scratches formed by diamond lapping can be observed. After anodic oxidation without ultrasonic vibration assistance (UA) for 20 min, shown in Fig. 5.2(b), the scratched area on the surface was preferentially oxidized and many oxide lines were generated. In addition, the shallower scratches were fully covered by oxide, whereas the deeper scratches were only partially covered by oxide. Fig. 5.2(c) shows the SiC surface anodically oxidized with UA for 20 min; it is clearly observed that all scratches were completely covered by oxide.

From the cross-sectional view of the surface anodically oxidized without UA, shown in Fig. 5.2(e), the maximum height of the oxide lines was 20.98 nm, whereas that of the oxide lines anodically oxidized with UA was 80.37 nm, as shown in Fig. 5.2(f). Therefore, the degree of anodic oxidation of the SiC surface with UA is significantly greater than that of conventional anodic oxidation. This result indicates that UA can promote the anodic oxidation of SiC.

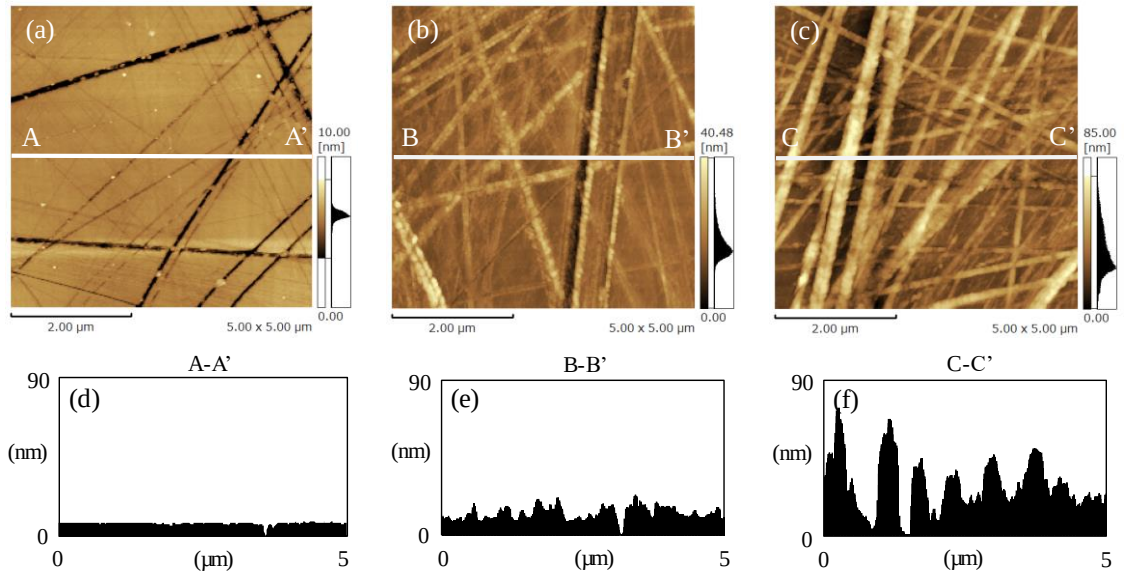



**Fig. 5.2** AFM images of (a) diamond-lapped surface and surfaces anodically oxidized at 3 V (b) without and (c) with UA for 20 min. Cross-sectional views along (d) A–A', (e) B–B', and (f) C–C' in (a), (b), and (c), respectively.

Fig. 5.3 shows the XPS measurement results of the diamond-lapped surface and the surfaces anodically oxidized without and with UA for 20 min. There was no oxide on the diamond-lapped surface because only peaks corresponding to Si-C bonds were observed, as shown in Fig. 5.3(a). Peaks corresponding to Si-O bonds were observed after anodic oxidation with and without UA, as shown in Fig. 5.3(b) and (c), and the intensity ratios of peaks corresponding to Si-O and Si-C bonds were calculated to be 0.845 and 1.369, respectively. Therefore, the XPS measurement results also indicate that ultrasonic vibration is effective for promoting the anodic oxidation of SiC.

Fig. 5.4 shows the changes in electric current during oxidation intermittently assisted by ultrasonic vibration at 3 V, where oxidation without UA (5 min) and oxidation with UA (5 min) were alternately conducted on a SiC (0001) surface. The current increased by 34.07% after first applying UA (position ① in Fig. 5.4), then by 11.05% and 14.05% at the second and third applications, respectively. The effect of ultrasonic vibration on promoting anodic oxidation weakened with increasing thickness of the oxide layer at the initial oxidation stage and gradually saturated to a constant value with the progress of oxidation. Moreover, current drops occurred at anodizing times of 600 and 1200 s, where the ultrasonic vibration was turned off. This is consistent with the results in Figs. 5.2 and 5.3, where UA can promote the anodic oxidation of SiC.

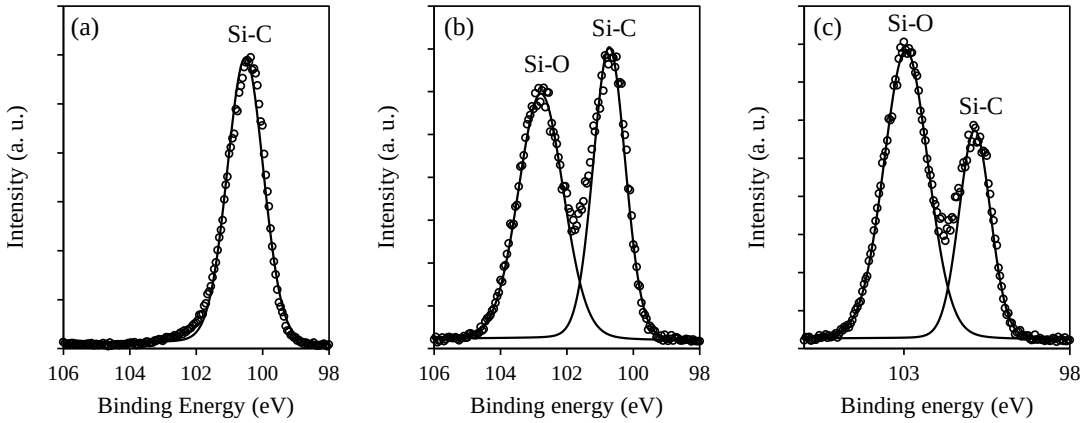



**Fig. 5.3** XPS results for (a) diamond lapped surface and surfaces anodically oxidized (b) without and (c) with UA for 20 min.

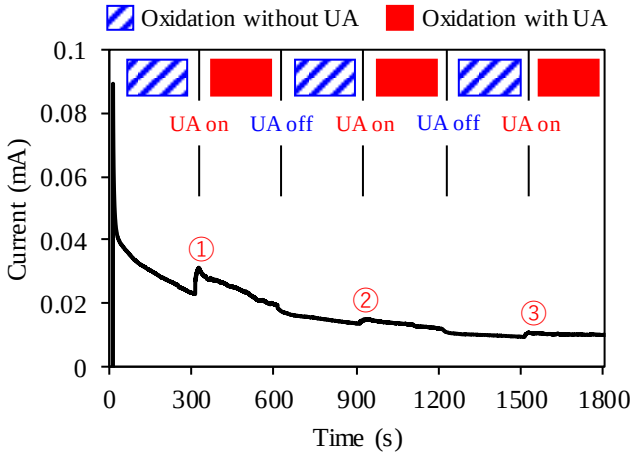



**Fig. 5.4** Changes in electric current during anodic oxidation intermittently assisted by ultrasonic vibration at 3 V.

### 5.2.3 Effects of ultrasonic vibration in electrolyte on the anodic oxidation state of the SiC surface

It has been reported that the SiC surface has different oxidation states under different applied potentials [1]. Linear sweep voltammetry (LSV) was employed to investigate the effect of ultrasonic vibration on the anodic oxidation state of SiC. The anodic oxidation setup was the same as shown in Fig. 5.1. Here, the oxidation potential was accurately controlled by referring to the Ag|AgCl electrode. The potential of the WE was swept from 0 to 9.8 V at a speed of 5 mV/s using the potentiostat. Fig. 5.5 shows the I–V curve of LSV for conventional anodic oxidation and ultrasonic vibration assisted anodic oxidation of 4H-SiC (0001). The results revealed that the

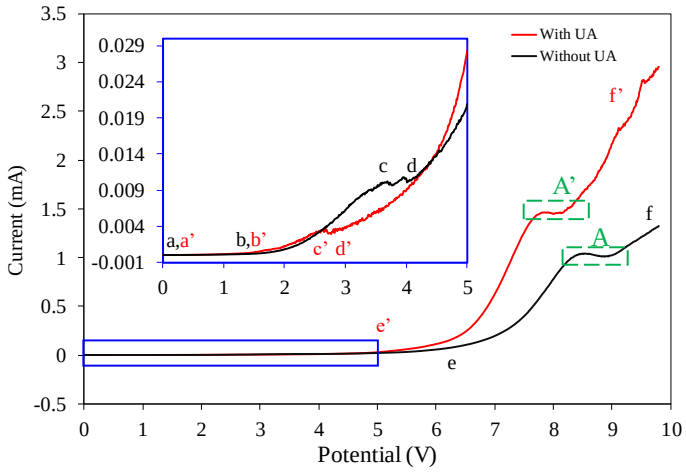



**Fig. 5.5** LSV measurement results; the inset shows a magnified image of the current change from 0 to 5 V.

I–V curve was similar to that for general metal anodization with five oxidation periods. In conventional anodic oxidation, these periods were: the unoxidized state at a–b (0–1.5 V); the active state at b–c (1.5–3.6 V); the passive state at c–d (3.6–4.2 V); the transient state at d–e (4.2–6.5 V); and the transpassive state at e–f (6.5–9.8 V) [1]. In ultrasonic vibration assisted anodic oxidation, the periods were: the unoxidized state at a'–b' (0–1.5 V); the active state at b'–c' (1.5–2.6 V); the passive state at c'–d' (2.6–3.1 V); the transient state at d'–e' (3.1–5 V); and the transpassive state at e'–f' (5–9.8 V). It is obvious that ultrasonic vibration assisted anodic oxidation reached each oxidation state at relatively low voltages compared with conventional anodic oxidation. In addition, the current of ultrasonic vibration assisted anodic oxidation was greater than that of conventional anodic oxidation, except for the c'–d' state, as shown in Fig. 5.5. A passive film is considered to have formed on the SiC surface after ultrasonic vibration assisted anodic oxidation reached the passive state from c', which inhibited the anodic oxidation, decreasing the oxidation rate decreased. However, the conventional anodic oxidation did not reach the passive state at c', so the oxidation current increased continually. The possible reason for this behavior is that the oxide is more uniform in ultrasonic vibration assisted anodic oxidation, which results in the passive film covering the SiC surface in a short time. The ultrasonic vibration assisted anodic oxidation entered into the transient state at d', the passive film was broken down, and the surface oxidation progressed again to increase the current. Similarly, conventional anodic oxidation reached the transition state from d, the passive film was broken down, and anodic oxidation of the SiC surface progressed. Therefore, it was found that in the stage after d, neither conventional anodic oxidation nor ultrasonic vibration assisted anodic oxidation was affected by the passive film and the current of ultrasonic vibration assisted anodic oxidation was always larger than that of conventional anodic oxidation. According to Faraday's law of electrolysis, it was

confirmed that the anodic oxidation rate of SiC is promoted by the application of ultrasonic vibration since the current value can directly reflect the oxidation rate of SiC.

Furthermore, a plateau was observed in the A and A' portions of the LSV current curve, as shown in Fig. 5.5. In order to investigate the cause of the plateau, we observed the oxidation state of the SiC surface via SEM before, during, and after the plateau stage. Fig. 5.6 shows the observation results. Before reaching the plateau stage, the oxide did not cover the entire SiC surface both in conventional and ultrasonic vibration assisted anodic oxidation, as shown in Fig. 5.6(a) and (d). While the entire SiC surface was almost oxidized in the plateau stage, the SiC surface was completely covered by oxide after the plateau stage. From this result, the reason for the appearance of the plateau in the current curve is considered to be the barrier effect of the oxide layer.

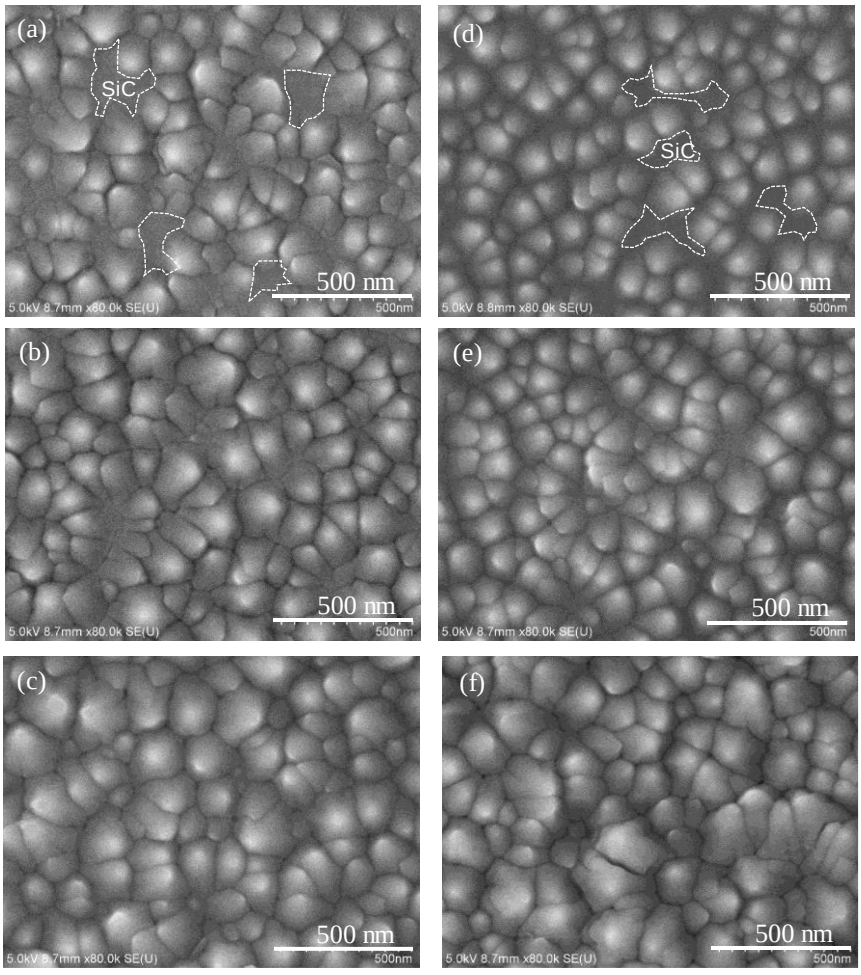



**Fig. 5.6** SEM images of the SiC surfaces at the plateau stage in the transpassive state. Surfaces in conventional anodic oxidation (a) before, (b) during, and (c) after the plateau; surfaces in ultrasonic vibration assisted anodic oxidation (d) before, (e) during, and (f) after the plateau.

In addition, as shown in Fig. 5.6, the oxidation of the SiC surface was not uniform in both conventional and ultrasonic vibration assisted anodic oxidation; many oxide protrusions were generated. However, before the surface was completely covered by oxide, the distribution of the oxide protrusions was more uniform under ultrasonic vibration. The reason for this is considered to be that the ultrasonic vibration assisted anodic oxidation rate is higher than that of conventional anodic oxidation, which makes the current of ultrasonic vibration assisted anodic oxidation larger than that of conventional anodic oxidation, generating a more uniform distribution of oxide protrusions.

### 5.2.4 Discussion of the promotional mechanism of SiC anodic oxidation when applying ultrasonic vibration to the electrolyte

Under ultrasonic vibration, tiny gas bubbles in the liquid violently oscillate and increase in size; these gas bubbles expand rapidly and then collapse when the ultrasound pressure reaches a certain threshold. This phenomenon is called ultrasonic cavitation. During cavitation, intense heating of bubbles occurs. These localized hot spots have extremely high temperatures and pressures that, within a few microseconds, accompany the formation of hydroxyl radicals [2-6]. The temperature of the electrolyte during anodic oxidation intermittently assisted by ultrasonic vibration was observed to be 31 °C at the beginning of the process and increased to 33, 35, and 37 °C after the first, second, and third application of ultrasonic vibration, respectively. In Chapter 4, it was confirmed that the increase of electrolyte temperature and strain on the SiC surface has a promotional effect on the anodic oxidation rate. Therefore, the anodic oxidation of a SiC surface may be promoted by the instantaneous high pressure and temperature created by ultrasonic vibration. The formation of hydroxyl radicals and the enhanced mobility of the electrolyte may also have a promotional effect on the anodic oxidation of the SiC surface [7].

Generally, the anodic oxidation current decreases with increasing oxide layer thickness. In Fig. 5.2, the oxide layer with UA is clearly thicker than that without UA. Thus, in theory, the anodic oxidation current with UA should be lower than that without UA. However, Fig. 5.7(a) shows that the oxidation current with UA is always greater than that without UA at a potential of 3 V. A model was proposed to explain this phenomenon, as shown in Fig. 5.7(b). When the oxide film is relatively thin, it has a dense structure and is a major barrier to the oxidation reaction. Therefore, the electric current decreases rapidly in the initial anodic oxidation stage, as shown in Fig. 5.7(a). With increasing thickness of the oxide layer during oxidation, the upper oxide layer gradually becomes porous, whereas the oxide layer near the interface remains dense and its thickness is maintained. Reactive ions can easily pass through the oxide layer and reach the SiC surface owing to the high ion permeability of the porous oxide layer. Therefore, once the oxidation current is reduced to a certain extent, it remains almost unchanged.

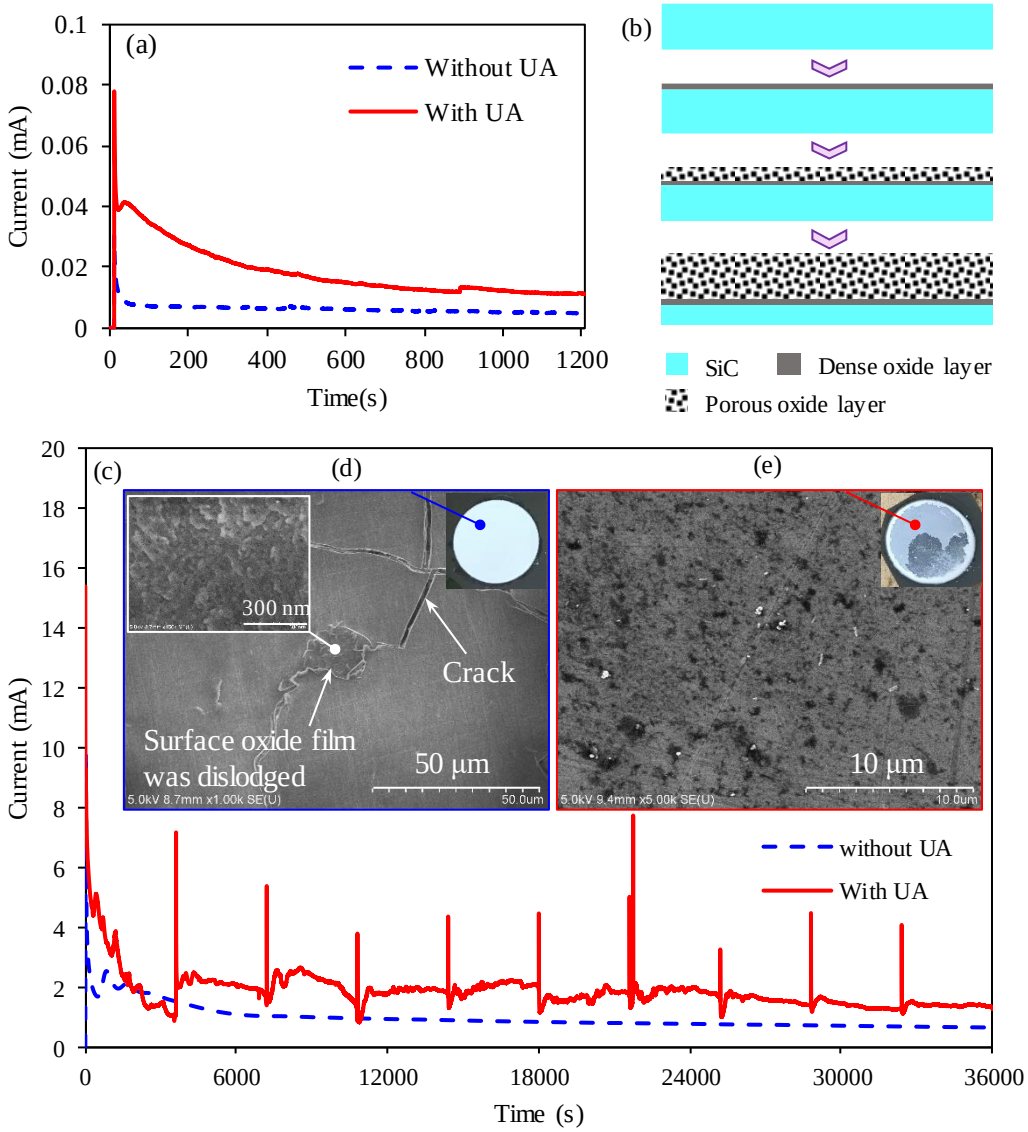



**Fig. 5.7** Structure modeling of the oxide layer. (a) Changes in electric current during anodic oxidation with and without UA at 3 V for 20 min. (b) Structure of the anodically oxidized layer during the progress of oxidation. (c) Changes in current during the anodic oxidation of SiC surfaces at 9 V for 10 h with and without UA. (d) SEM image of the anodically oxidized surface without UA; the insets show the inner structure of the oxide layer and a photo of the oxidized substrate. (e) SEM image of the anodically oxidized surface with UA; the inset shows a photo of the oxidized substrate.

Fig. 5.7(c), (d), and (e) show the changes in electric current during anodic oxidation under 9 V for 10 h with and without UA, and the structure of the anodically oxidized surfaces observed by SEM, respectively. Anodic oxidation with UA for 1 h was repeated ten times to the SiC substrate

owing to the limited operation time of the ultrasonic cleaner. The electric current in anodic oxidation with UA was always greater than that without UA. The current saturated at a constant value of about 1 and 2 mA during oxidation without and with UA, respectively. These results show that, even after 10 h, anodic oxidation continued to occur at a certain rate. The SEM images of the oxidized surface without UA shown in Fig. 5.7(d) indicates that many cracks were generated on the oxide layer and some oxide was dislodged when the cracks were generated, exposing the inner structure of the oxide layer. The inset SEM image of the inner oxide layer indicates that the oxide layer clearly has a porous structure and the oxidized surface became white with the thickening of the oxide layer. A SEM image and a photo of the oxidized surface with UA are shown in Fig. 5.7(e). The oxide layer also has a porous structure, but the porosity and dislodged area of the oxide layer are increased compared to the anodically oxidized surface without UA, indicating that UA affects the porous structure of the oxide layer. Both results with and without UA verify the model proposed in Fig. 5.7(b).

### 5.2.5 Investigation of the promotional mechanism of ultrasonic vibration by electrochemical impedance spectroscopy (EIS)

In order to investigate the promotional mechanism of ultrasonic vibration on the anodic oxidation rate of the 4H-SiC surface, electrochemical impedance spectroscopy (EIS) was used to analyze the change of each resistance in the electrochemical system. EIS is a transient measurement method that analyzes the electrode reaction mechanism by applying a minute sine wave alternating current (or potential) to the target electrode and obtaining the impedance (or admittance) as its transfer function. A physical system, *M*, with an unknown internal structure is like a black box. An excitation signal (disturbance signal) is input to the black box *M* and a response signal can be obtained. If the internal structure of *M* is a linear and stable structure, the response signal would be a linear function of the disturbance signal. The function used to describe the relationship between the disturbance signal and the response signal is called the transfer function. The transfer function of a system is determined by the internal structure of the system. Through the study of the transfer function, the properties of the system can be studied and information about the internal structure of the system can be obtained.

If the disturbance signal, *X*, is a sine wave electrical signal with a small amplitude, the response signal, *Y*, is usually a sine wave electrical signal with the same frequency. The transfer function, G($\omega$), is called the frequency response function. The relationship between *Y* and *X* can be described by the following formula:

$$Y = \mathrm{G}(\omega)X. \tag{5.1}$$

G($\omega$) is a function of angular velocity, $\omega$, and reflects the frequency response characteristics of system *M*. If *X* is a sine wave electric current signal and *Y* is a sine wave potential signal, then

G($\omega$) is the impedance of $M$, which is usually represented by $Z$.

Fig. 5.8(a) shows the ideal equivalent circuit of a three-electrode system. The impedance of this ideal system can be represent by the following formula:

$$Z = R_{sol} + \frac{R_{WE}}{1+j\omega R_{WE}C_{WE}}. \tag{5.2}$$

Furthermore, if $Z$ is divided into real and imaginary parts, it can be expressed as follows.

$$Z = Z' + jZ'', \tag{5.3}$$

$$Z' = R_{sol} + \frac{R_{WE}}{1+\omega^2 {R_{WE}}^2 {C_{WE}}^2}, \tag{5.4}$$

$$Z'' = \frac{\omega {R_{WE}}^2 C_{WE}}{1+\omega^2 {R_{WE}}^2 {C_{WE}}^2}, \tag{5.5}$$

$$\left(Z' - R_{sol} - \frac{R_{WE}}{2}\right)^2 + Z''^2 = \left(\frac{R_{WE}}{2}\right)^2. \tag{5.6}$$

Fig. 5.8(b) shows impedance spectroscopy (also called Nyquist plots) of the three-electrode system, which is obtained by drawing the locus of the semicircle represented by Eq. (5.6). The center of the semicircle is $(R_{sol} + \frac{R_{WE}}{2}, 0)$, the radius is $\frac{R_{WE}}{2}$, and the limit values of high and low frequencies in the spectrum intersect at $R_{Sol}$ and $R_{sol} + R_{WE}$ on the real axis, respectively.

The impedance spectroscopy in Fig. 5.8(b) shows a perfect capacitive semicircle, which is based on an ideal equivalent circuit. However, in an actual measurement, the capacitive semicircle deviates from the perfect circle and shows a locus that collapses in the direction of the real axis; this phenomenon is called the dispersion effect. At present, the exact cause of the dispersion effect is not particularly clear, but it may be related to the inhomogeneity of the

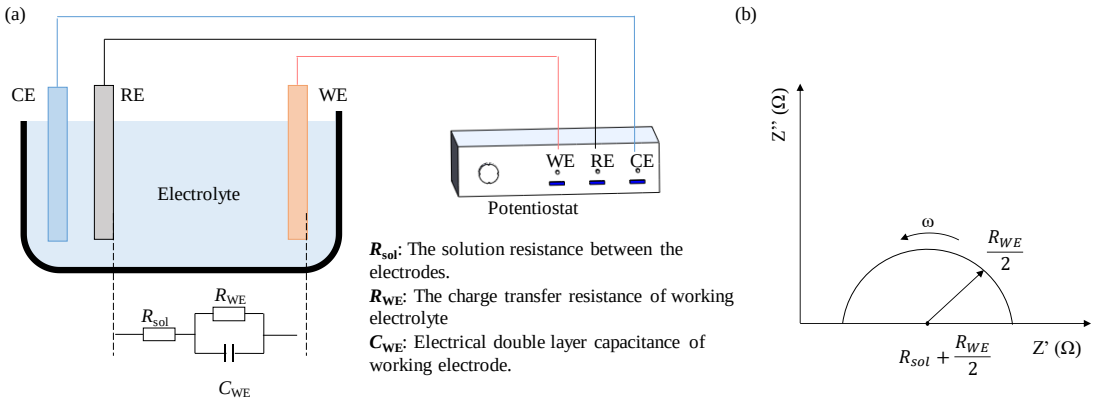



**Fig. 5.8** (a) Ideal equivalent circuit of a three-electrode system and (b) impedance spectroscopy of the three-electrode system in (a).

electrode surface, the adsorption layer on the electrode surface, and the conductivity of the electrolyte. Therefore, the simple equivalent of the electrode interface as a pure capacitor is not sufficiently accurate, so the introduction of a constant phase element (CPE) is necessary. The impedance of the CPE is expressed as:

$$Z = \frac{1}{Y_0}(j\omega)^{-n}. \tag{5.7}$$

The CPE includes two parameters: $Y_0$ and $n$. CPE is an equivalent element used to describe the deviation of the electrode interface from the pure capacitance, $C$, thus the parameter $Y_0$ always takes a positive value (like the parameter $C$ of the capacitance). The other parameter, $n$, is the dispersion index, which is a dimensionless index.

If $n = 0$, the CPE is equivalent to a resistance, $Y_0 = \frac{1}{R}$;

if $n = 1$, the CPE is equivalent to a capacitance, $Y_0 =$ C, $Y = j\omega$C, $Z = -j\frac{1}{\omega C}$;

and if $n = -1$, the CPE is equivalent to an inductance, $Y_0 = \frac{1}{L}$, $Y = -j\frac{1}{\omega L}$, $Z = j\omega$L.

When $0.5 < n < 1$, the CPE has the characteristics of a capacitance and can replace the capacitance as the equivalent element on the electrode surface. The CPE can then be used to fit the impedance spectrum with the dispersion effect in the equivalent circuit.

Fig. 5.9 shows the equivalent circuit and impedance spectroscopy of the three-electrode system after considering the dispersion effect. The impedance of this system can be expressed by the following formula:

$$Z = R_{sol} + \frac{R_{WE}}{1+(j\omega)^n\ Y_0 R_{WE}}. \tag{5.8}$$

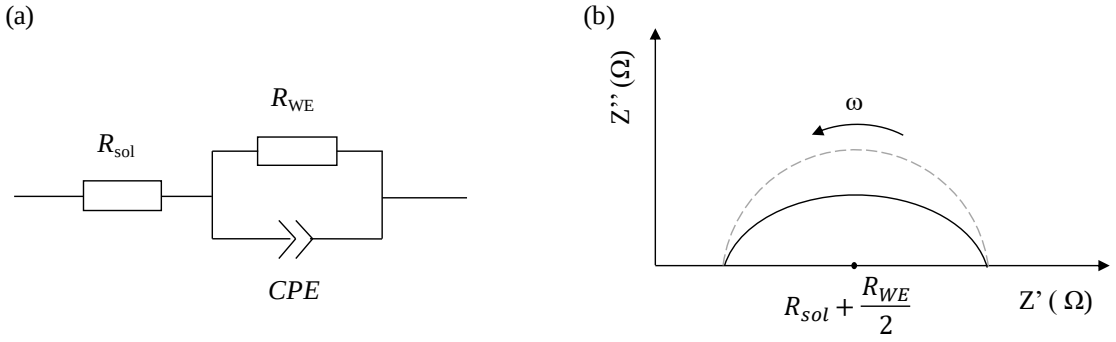



**Fig. 5.9** (a) Equivalent circuit to the schematic diagram of a three-electrode system considering the dispersion effect and (b) impedance spectroscopy of the three-electrode system in (a).

In the anodic oxidation of SiC, an oxide layer with a porous structure is generated, as shown in Fig. 5.10(a). Based on the structure of the oxide layer, the SiC anodic oxidation system can be satisfactorily fitted by an $R0(R1/CPE1)(R2/CPE2)$ circuit, as shown in Fig. 5.10(b) [8]. The series resistance, $R0$, can be attributed to the bulk semiconductor, the Ohmic contact, and the electrolyte. Parallel ($R1/CPE1$) and ($R2/CPE2$) components are the equivalent circuit of the porous oxide layer and the interface of the SiC and electrolyte, respectively.

To conduct EIS, ultrasonic vibration was intermittently applied with the anodic oxidation of SiC at 7 V five times. EIS measurements were conducted with and without ultrasonic vibration during the last three applications. Fig. 5.10(c) shows the changes in current and the schedule of EIS measurements during the anodic oxidation process. The scanning frequencies during EIS measurement ranged from 50 Hz to 50 kHz. The imaginary component of the impedance, $Z$', was plotted as a function of the real component, $Z$', and a somewhat flattened "semicircle" was observed. Fig. 5.10(d) shows that the diameter of the semicircle decreased markedly, from about 3000 to 2000 Ω, with the application of ultrasonic vibration but the start position of the semicircle did not change.

The impedance spectroscopy results in Fig. 5.10(d) were analyzed by the equivalent circuit model, as shown in Fig. 5.10(b). The parameter $n$ of the CPE for both ($R1$/CPE1) and ($R2$/CPE2) circuits were calculated to be greater than 0.5, which suggests that both $CPE1$ and $CPE2$ have capacitor characteristics [8]. Therefore, the current during anodic oxidation was mainly affected by the series resistance of $R0$, $R1$, and $R2$ because direct current is used in the anodic oxidation process. Fig. 5.10(e) shows the changes in $R0$, $R1$, and $R2$ with and without ultrasonic vibration during the three measurements. As shown in Fig. 5.10(e), $R0$ and $R1$ are almost unchanged but $R2$ significantly decreased to about 500 Ω after applying ultrasonic vibration. After applying ultrasonic vibration, the total resistance of the anodic oxidation system significantly decreased, which corresponds to the changes of current in Fig. 5.10(c). This result suggests that the ultrasonic vibration does not affect the resistances of the electrolyte and the oxide layer, but promotes the anodic oxidation process. Generally, an electrochemical process includes four basic processes: the charge transfer process, mass transfer process, changing process of the electric double layer, and the migration process. In the anodic oxidation of SiC, these four processes correspond to: the chemical reactions on the SiC surface, the diffusion process of reactants and products in the electrolyte, the formation of a space charge layer, and the directionally migration of ions between electrodes in the electrolyte, respectively. Thus, charge transfer and mass transfer processes occur at the SiC/electrolyte interface may promoted by the ultrasonic vibration-enhanced flow of the electrolyte and diffusion of the reactants and products. Additionally, the instantaneous high temperature, high pressure, and the hydroxyl radicals generated by ultrasonic cavitation may also promote anodic oxidation of SiC [9].

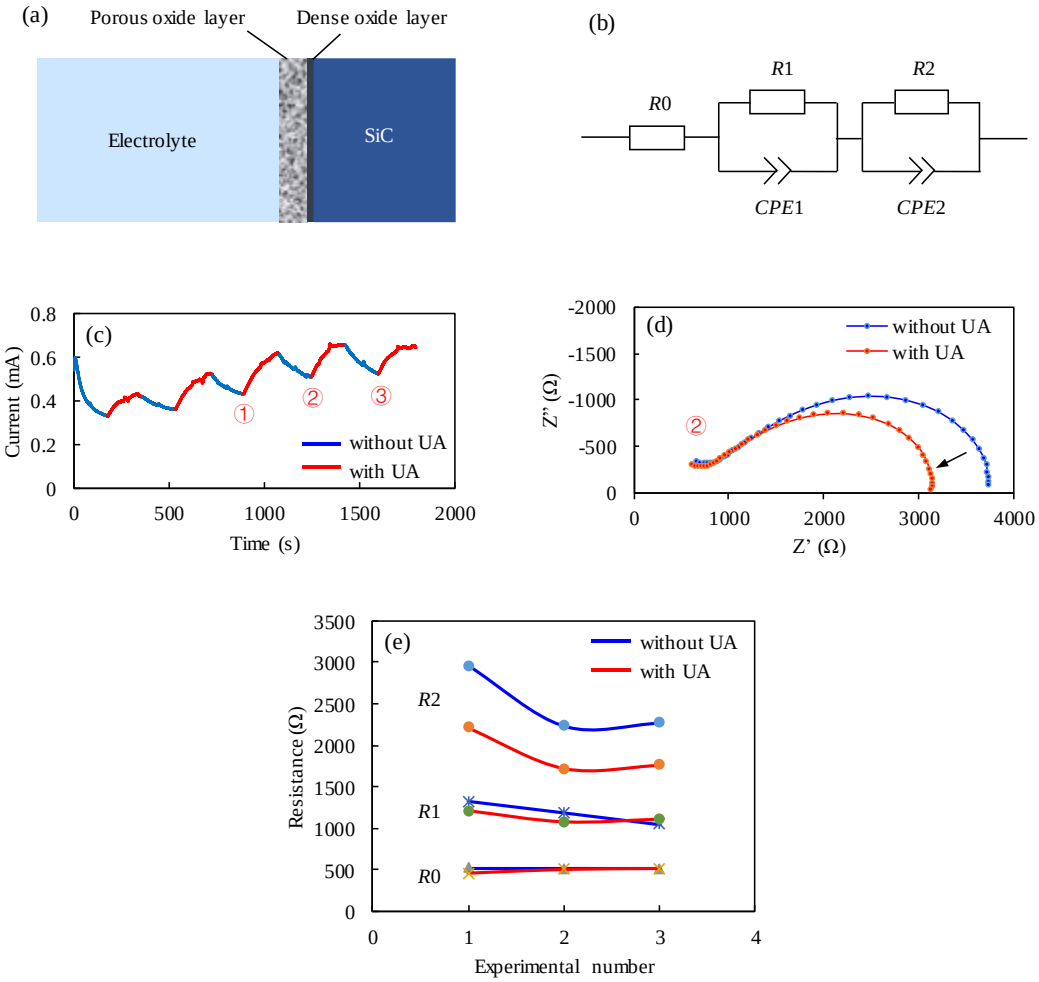



**Fig. 5.10** EIS measurement during anodic oxidation with and without ultrasonic vibration. (a) Schematic diagram of the interface between the electrolyte and SiC. (b) Equivalent circuit of the SiC anodic oxidation system. (c) Changes in current during the EIS measurement. (d) Impedance spectroscopies obtained with and without ultrasonic vibration. (e) Changes in *R*0, *R*1, and *R*2 derived from the fit of the measured impendence spectroscopies.

## 5.3 Application of ultrasonic vibration to the SiC wafer during anodic oxidation

### 5.3.1 Introduction

The above discussion focused on the effect of ultrasonic vibration on the anodic oxidation rate after applying ultrasonic vibration to the electrolyte. Obviously, the method of applying ultrasonic vibration to the electrolyte has a promotional effect on the anodic oxidation rate, whereas the

promotional effect is not particularly significant. Moreover, we want to use ultrasonic vibration to promote the anodic oxidation rate of SiC during the ECMP polishing process, thereby improving the material removal rate (MRR). During the polishing process, the grinding stone is in contact with the SiC surface, resulting in a very small amount of electrolyte between the SiC surface and the grinding stone. Thus, there are certain limitations in applying ultrasonic vibration to the electrolyte. Therefore, applying ultrasonic vibration directly to the SiC wafer was proposed.

### 5.3.2 Anodic oxidation setup

Fig. 5.11 shows the anodic oxidation setup for applying ultrasonic vibration to the SiC wafer. This setup consisted of an anodic oxidation unit, an ultrasonic vibration unit, and a polishing unit for ultrasonic assisted anodic oxidation and UAECMP. The ultrasonic vibration unit (30 W, 42 kHz) was set under the stainless-steel plate. The SiC wafer was fixed on the stainless-steel plate using a conductive glue and served as the WE. The SiC wafer can vibrate with high frequency after turning on the ultrasonic vibrator. The tip of the rotary spindle, which was made of aluminum alloy, was used as the CE. A potentiostat was applied to control the anodic oxidation parameters to anodize the SiC surface. A sodium chloride aqueous solution (NaCl *aq*.) (1 wt%) was used as the electrolyte. The SiC surface and the tip of spindle were immersed in the electrolyte. Therefore, the oxidized area shown in Fig. 5.11(b) was defined. To eliminate the effects of damage and scratches on oxidation performance, CMP-processed wafers were used in this experiment. SiC wafers were anodically oxidized at a potential of 20 V with and without ultrasonic vibration for 20 min. The hardness of oxide layers obtained by the anodic oxidation with and without ultrasonic vibration were measured using a nanoindenter (ENT-2100, Elionix Inc). The oxidation depths and surface topographies after removing the oxide layers with a 50 wt% hydrofluoric acid etching were observed by scanning white light interferometry (SWLI, NewView 8300, Zygo).

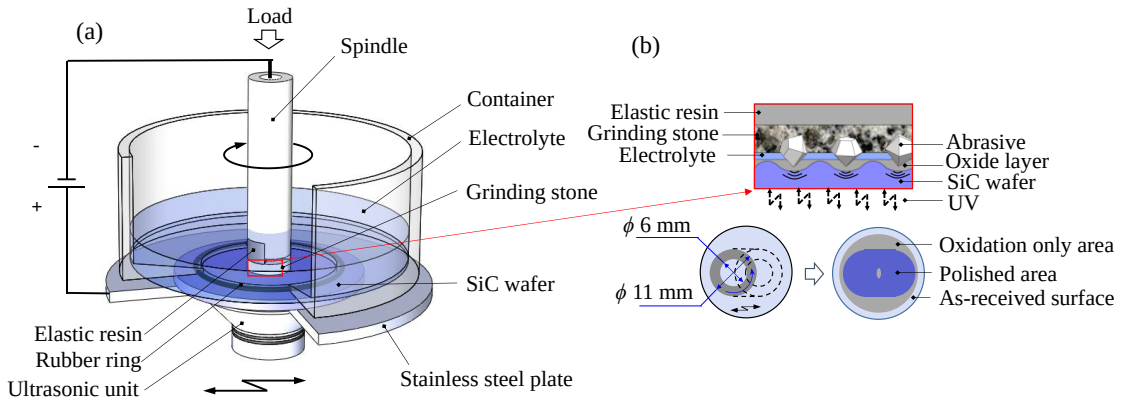



**Fig. 5.11** (a) Anodic oxidation setup for applying ultrasonic vibration to the SiC wafer. (b) Schematic of ultrasonic vibration assisted anodic oxidation.

### 5.3.3 Effects of ultrasonic vibration on the anodic oxidation of the SiC surface

In ECMP and UAECMP process, anodic oxidation was used to soften the surface of the SiC wafer, making it possible for the SiC surface to be polished by soft abrasives. Hardness of the oxide layer is a very important indicator for evaluating surface modification ability. Nanoindentation tests were conducted on the as-received SiC surface and oxide layers obtained by conventional and ultrasonic vibration assisted anodic oxidation to compare their surface hardness. A Berkovich-type indenter made of diamond was used and 100 points were tested on each surface. Fig. 5.12(a) shows the typical load–displacement curves of these three surfaces measured using the nanoindentation method. The surface hardness was calculated by the Oliver–Pharr method [10]. Fig. 5.12(b) shows the hardness of these three surfaces calculated from the load–displacement curves. It was revealed that the hardness of the SiC surface was significantly decreased after conventional anodic oxidation, from 41 to 2.2 GPa, whereas, that of the oxide layer obtained by UA anodic oxidation was only 0.8 GPa. Based on the results in Fig. 5.7, the anodic oxide layer of SiC has a porous structure and its porosity increased after application of ultrasonic vibration. Therefore, the increase in the porosity is considered to have decreased the hardness of the oxide layer; ultrasonic vibration assisted anodic oxidation is more effective for the softening of the SiC surface.

Fig. 5.13(b) shows the oxidation depths obtained by conventional and ultrasonic vibration assisted anodic oxidation at 20 V for 20 min. The oxidation depths in Fig. 5.13(b) are the averages calculated from oxidation depths of eight positions evenly distributed along the edge of the

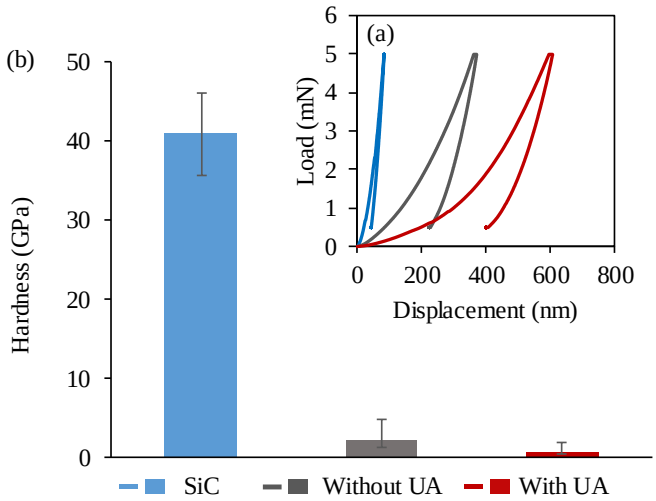



**Fig. 5.12** (a) Load–displacement curves measured by the nanoindentation method. (b) Hardness of SiC, the conventional anodic oxide layer, and the ultrasonic vibration assisted anodic oxide layer calculated from measured data in (a).

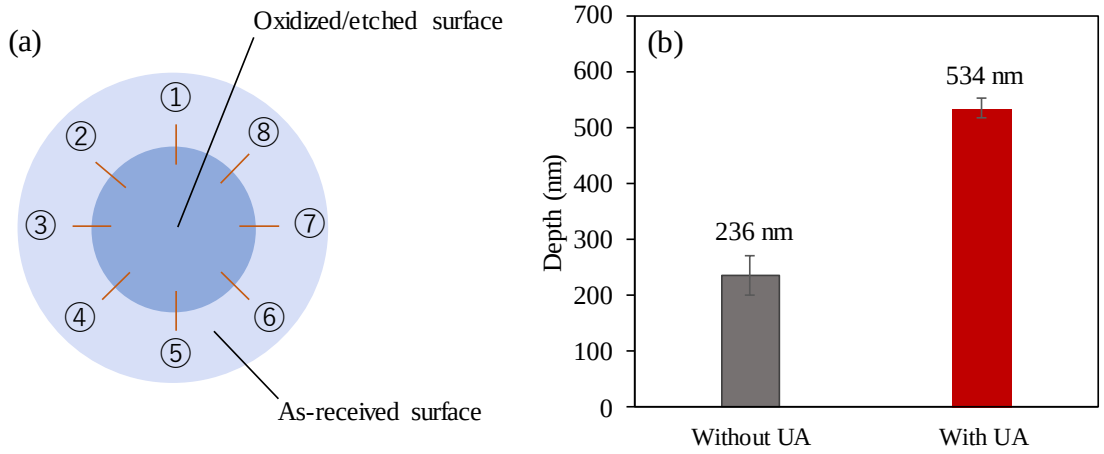



**Fig. 5.13** Oxidation depths of conventional and ultrasonic vibration assisted anodic oxidation. (a) Schematic of oxidation depth observations. (b) Average oxidation depths obtained by conventional and ultrasonic vibration assisted anodic oxidation.

circular oxidation area, as shown in Fig. 5.13(a). These results show that the average oxidation depth of ultrasonic vibration assisted anodic oxidation was more than two times greater than that of conventional anodic oxidation, indicating that ultrasonic vibration increased the anodic oxidation rate. Ultrasonic cavitation can produce localized high-temperature hot spots, high pressures, hydroxyl radicals, and enhance mobility of the electrolyte, which result in an increase in anodic oxidation rate. The increase in anodic oxidation rate when applying ultrasonic vibration to the electrolyte (Section 5.2.2) is much smaller (about 34%) than that obtained when applying ultrasonic vibration to the SiC wafer. When applying ultrasonic vibration to the electrolyte, ultrasonic vibration was not directly applied to the SiC wafer, it was transmitted to the SiC surface through water and the energy of the ultrasonic vibration became very weak after a certain degree of attenuation. Thus, the promotional effect of ultrasonic vibration on the anodic oxidation of the SiC surface was weaker when applied via electrolyte. However, when applying ultrasonic vibration to the SiC wafer, the vibration of the SiC wafer was very strong and resulted in a stronger promotional effect for anodic oxidation of the SiC surface.

Furthermore, the effect of ultrasonic vibration on the uniformity of the anodic oxidation was evaluated by comparing the surface roughness of the oxidized surface after removing the oxide layer by hydrofluoric acid etching. Since the interface between the bulk SiC and the oxide layer becomes rough with increasing oxidation depth [11], controlling the oxidation depth in ultrasonic vibration assisted and conventional anodic oxidation to be the same is necessary for comparing the surface roughness after removing the oxide. As shown in Fig. 5.13(b), the oxidation depth of ultrasonic vibration assisted anodic oxidation for 20 min was 534 nm, which is about twice that of conventional anodic oxidation. Thus, the oxidation time of ultrasonic vibration assisted anodic

oxidation was reduced to 10 min to control its oxidation depth to be equal to that of conventional anodic oxidation.

Fig. 5.14(a) shows that the average oxidation depth of ultrasonic vibration assisted anodic oxidation for 10 min was 242 nm, which was almost the same as that for conventional anodic oxidation for 20 min. Fig. 5.14(b) and (c) show SWLI images of the oxidized/etched surfaces obtained by conventional and ultrasonic vibration assisted anodic oxidation, respectively. The *S*q surface roughness obtained by ultrasonic vibration assisted anodic oxidation was 1.684 nm, while that obtained by conventional anodic oxidation was 2.764 nm. It was also confirmed that ultrasonic vibration can improve anodic oxidation uniformity at the microscopic level. In general, the anodic oxidation of the SiC surface is nonuniform with the generation of oxide protrusions [1)]. However, the oxide protrusions are small and numerous when the anodic oxidation rate is high. Conversely, the size of the oxide protrusions is large and its density is small in the case of a low anodic oxidation rate, which results in a rough interface between the bulk SiC and oxide layer [1)]. Therefore, it is assumed that the smoother surface obtained by UA anodic oxidation is attribute to its higher anodic oxidation rate than conventional anodic oxidation.

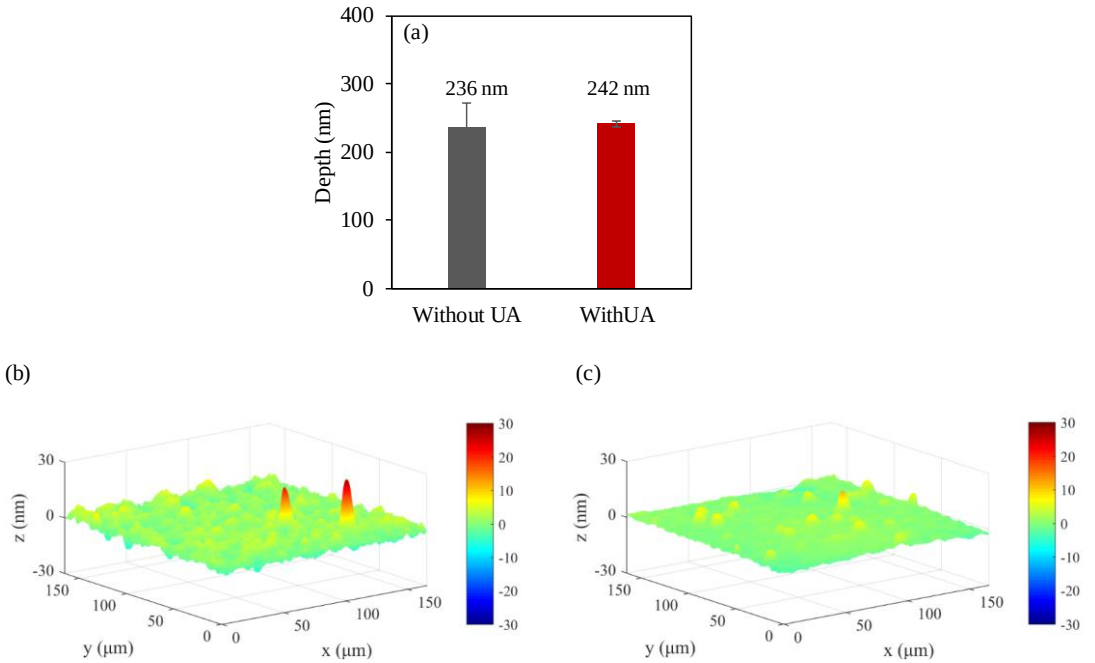



**Fig. 5.14** Evaluation of the anodic oxidation uniformity in conventional and ultrasonic vibration assisted anodic oxidation. (a) Oxidation depths obtained by conventional anodic oxidation for 20 min and by ultrasonic vibration assisted anodic oxidation for 10 min. SWLI images of oxidized/etched surfaces obtained by (b) conventional anodic oxidation (*S*q = 2.764 nm, *S*z = 48.688 nm) and (c) ultrasonic vibration assisted anodic oxidation (*S*q = 1.684 nm, *S*z = 24.677 nm).

## 5.4 Summary

A ultrasonic vibration assisted anodic oxidation setup was developed and the effects of ultrasonic vibration on the anodic oxidation of 4H-SiC (0001) surfaces, including the anodic oxidation rate, the structure of the oxide layer, oxidation uniformity, etc., were investigated. Moreover, the difference between applying ultrasonic vibration to the electrolyte and to the SiC wafer was compared and discussed.

(1) Ultrasonic vibration assisted anodic oxidation of the diamond-lapped 4H-SiC (0001) surface was conducted by applying ultrasonic vibration to the electrolyte. It was confirmed that the anodic oxidation rate increased by about 34% with ultrasonic vibration in the initial oxidation stage and the promotional performance remained at about 11% during subsequent oxidation.

(2) The structure of oxide layers obtained by conventional and ultrasonic vibration assisted anodic oxidation was modeled and observed. The anodic oxide layer has a porous structure, through which the reactive species can pass and reach the interface of the oxide layer and bulk SiC. This resulted in an almost constant oxidation rate after prolonged oxidation. Ultrasonic vibration can increase the porosity of the oxide layer, which decreases the hindrance of the oxide layer during anodic oxidation; therefore the oxidation rate with UA was always greater than that without UA.

(3) The promotional effects of ultrasonic vibration on the anodic oxidation rate of SiC were analyzed by EIS measurements. Ultrasonic vibration enhanced charge transfer and mass transfer processes during anodic oxidation of SiC. This may be due to ultrasonic cavitation, which promotes the flow of electrolyte and the diffusion of reactants and products at the SiC/electrolyte interface. Additionally, the instantaneous high temperature, high pressure, and hydroxyl radicals generated by ultrasonic cavitation also promote anodic oxidation of SiC.

(4) Ultrasonic vibration assisted anodic oxidation experiments were conducted by applying ultrasonic vibration to the SiC wafer and an anodic oxidation rate twice that of conventional anodic oxidation was obtained. Applying ultrasonic vibration to the SiC wafer has a greater promotional effect on the anodic oxidation of SiC than that when applied to the electrolyte.

(5) The oxide layer generated using ultrasonic vibration assisted anodic oxidation is much softer than that generated using conventional anodic oxidation owing to the higher porosity of the oxide layer.

(6) The anodic oxidation uniformity of the SiC surface was improved by the application of ultrasonic vibration.

(7) Applying ultrasonic vibration to the SiC wafer had a stronger promotional effect on the anodic oxidation rate than when applying to the electrolyte due to the higher intensity of ultrasonic vibration near the SiC surface.

# References

1) X. Yang, R. Sun, Y. Ohkubo, K. Kawai, K. Arima, K. Endo, K. Yamamura, Electrochim. Acta 271 (2018) 666–676.
2) K.S. Suslick, Science 247 (1990) 1439–1445.
3) K.S. Suslick, D.A. Hammerton, R.E. Cline, J. Am. Chem. Soc. 108 (1986) 5641–5642.
4) B.E. Noltingk, E.A. Neppiras, Proc. Phys. Soc. B 63 (1950) 674–685.
5) M.E. Fitzgerald, V. Griffing, J. Sullivan, J. Chem. Phys. 25 (1956) 926–933
6) H.G. Flynn, J. Acoust. Soc. Am. 72 (1982) 1926–1932.
7) S. Kentish, A. Muthupandian, Springer, New York, NY (2011) 1–12.
8) D.H. Van Dorp, E.S. Kooij, W.M. Arnoldbik, J.J. Kelly, Chem. Mater. 21 (2009) 3297–3305.
9) L.H. Thompson, L.K Doraiswamy, Ind. Eng. Chem. Res. 38 (1999) 1215–1249.
10) W.C. Oliver, G.M. Pharr, J. Mater. Res. 7 (1992) 1564–1583.
11) X. Yang, X. Yang, R. Sun, K. Kawai, K. Arima, K. Yamamura, Nanomanuf. Metrol. (2019) 5–8.

# Chapter 6
# Application of slurryless UAECMP to SiC wafers

## 6.1 Introduction

It was confirmed in Chapter 5 that anodic oxidation of SiC was promoted under the assistance of ultrasonic vibration. Therefore, the improvement of SiC material removal rate (MRR) is very promising in slurryless ultrasonic vibration assisted electrochemical mechanical polishing (UAECMP). This chapter presents the development of a slurryless UAECMP machine for surface polishing of an entire SiC wafer, followed by a comparison of the performance of slurryless ECMP and slurryless UAECMP using the developed machine. In addition, the promotional mechanism of ultrasonic vibration on the MRR in slurryless UAECMP is investigated and a novel SiC wafer manufacturing process that combines slurryless UAECMP and ECMP is proposed.

## 6.2 Development of a slurryless UAECMP machine

### 6.2.1 Outline of the slurryless UAECMP machine

Ultrasonic vibration assisted anodic oxidation and ultrasonic vibration assisted mechanical polishing are two essential functions in the slurryless UAECMP machine. Fig. 6.1 shows a schematic diagram of the slurryless UAECMP machine developed in this thesis. SiC is fixed on a wafer holder, mounted on a spindle, and serves as a work electrode (WE) while a metal plate acts as a counter electrode (CE). The anodic oxidation parameters can be adjusted by a direct current (DC) power supply. Therefore, the wafer holder, SiC wafer, electrolyte, and DC power supply form an electric circuit. On the other hand, the grinding stone is fixed on the ultrasonic vibrator and makes contact with the SiC surface. During UAECMP, the ultrasonic vibrator drives the pellet grinding stone to perform uniform high-frequency ultrasonic vibration, which makes the abrasives hit the SiC surface at an ultrasonic frequency. In addition, a load is applied on the spindle as the SiC and grinding stone are rotated at specific speeds to remove the oxide layer during the anodic oxidation process. In this way, slurryless UAECMP can be realized.

In fact, the ultrasonic vibrator can be applied to either the SiC wafer or the grinding stone. If the ultrasonic vibrator is applied to the SiC wafer, two difficult problems arise. First, it is very difficult to connect the SiC wafer to the DC power supply while completely insulating it from the ultrasonic vibrator. Second, a large-diameter ultrasonic vibrator is required for the UAECMP of

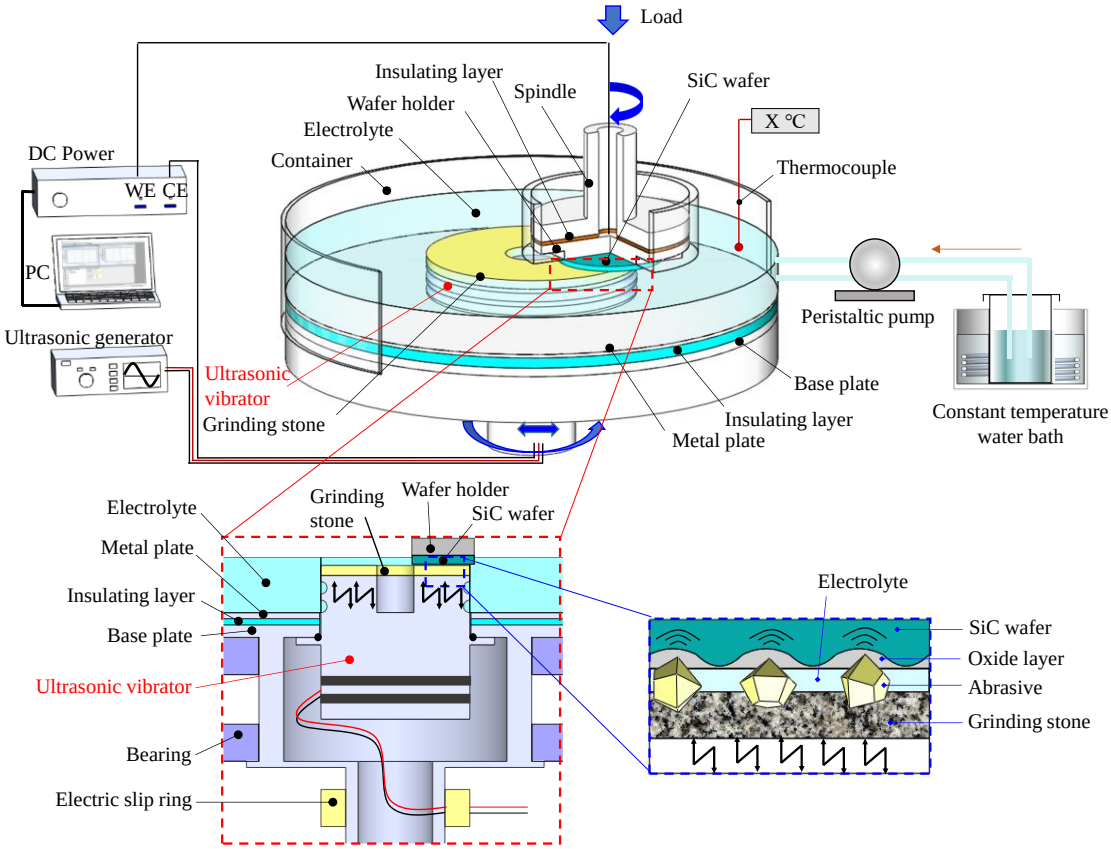



**Fig. 6.1** Schematic diagram of the slurryless UAECMP machine.

large SiC wafers. However, it is difficult to achieve uniform vibration on the end face of large-diameter ultrasonic vibrator, which will cause uneven removal of the SiC surface and even breakage of SiC wafers. In contrast, applying ultrasonic vibration to the grinding stone can significantly decrease difficulties in insulation, and a pellet grinding stone derived from a small-diameter ultrasonic vibrator can ensure uniform grinding stone vibration. Moreover, it is also possible to increase the number of ultrasonic vibrator-pellet grinding stones to form a large polishing disc for processing large SiC wafers. Thus, the machine structure allows SiC wafers with diameters of six inches, eight inches, or larger to be processed.

### 6.2.2 Structure of the slurryless UAECMP machine

The designed slurryless UAECMP machine is shown in Fig. 6.2. It consists of an ultrasonic vibration unit, an anodic oxidation unit, and an MP unit. The ultrasonic vibration unit consists of an ultrasonic vibrator and ultrasonic generator. The ultrasonic vibration unit has a power of 500 W and a frequency of 35 kHz, and the ultrasonic generator is used to adjust the amplitude of the ultrasonic vibrator. A grinding stone is mounted on the end face of the ultrasonic vibrator and was vibrated at the set amplitude. The ultrasonic vibrator is fixed on a rotation sleeve set on a uniaxial

moving table; thus, it can rotate while oscillating along the stage. In the anodic oxidation unit, the SiC wafer is mounted on the wafer holder, which is set opposite to the grinding stone and serves as the WE. The CE is a stainless-steel plate set at the bottom of the electrolyte container. A DC power supply was used to control the anodic oxidation potential. During polishing, the SiC wafer, grinding stone, and stainless plate are immersed in the electrolyte.

In addition, due to the power loss of the ultrasonic transducer, the lost part of the energy is converted into heat. Temperature rise changes the vibration performance of the transducer, which will gradually deviate from the best matching state and weaken the vibration. More seriously, the temperature rise will deteriorate the performance of the piezoelectric ceramic in the vibrator and even cause machine equipment failure. Therefore, cooling is essential to decrease the temperature of the ultrasonic vibrator during polishing. An air-cooling unit in which the air flow is set above 85 L/min is used; the air flow is produced using an air compressor and supplied to the ultrasonic vibrator through an air rotary joint and the center of the spindle. With the application of this cooling system, the effect from the increase in temperature of the ultrasonic vibrator can be suppressed.

The electrolyte temperature has a significant promotional effect on the MRR of ECMP, as discussed in Chapter 4. The heat, which is generated by the ultrasonic vibrator and the friction

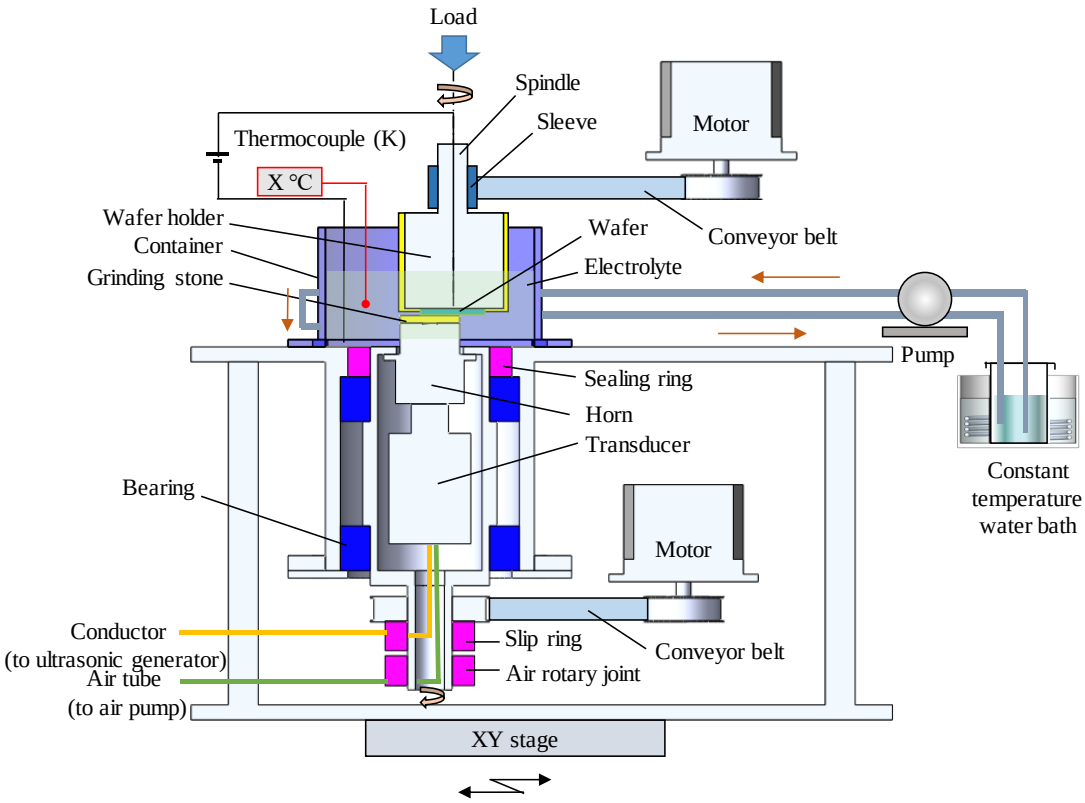



**Fig. 6.2** Design of the slurryless UAECMP machine.

between the grinding stone and the SiC surface, has a non-negligible effect on the change of the electrolyte temperature. Thus, an electrolyte temperature controlling unit is used. A container with electrolyte is placed in a constant temperature water bath, the electrolyte in the UAECMP machine and in the container is circulated using a peristaltic pump, and thus the electrolyte temperature can be controlled. The temperature of the constant-temperature water bath can be set from 0 to 80 °C. During slurryless UAECMP, the electrolyte temperature is monitored by a K-type thermocouple.

Fig. 6.3 shows the structure of the wafer holder and the clamping method used for the SiC wafer. The wafer holder is made of stainless steel. An insulating protective cover is set outside of the wafer holder to prevent oxidation of the holder during UAECMP. The SiC wafer is fixed on the end face of the wafer holder using conductive adhesive. The gap between the SiC wafer and the insulating cover is filled with insulating adhesive to prevent the electrolyte from contacting the wafer holder. SiC wafers with a diameter of 20 mm are cut from a 4-inch 4H-SiC wafer using a fiber laser (with a wavelength of 532 nm and a constant pulse duration about 300 ns). Before the experiments, the SiC wafers were cleaned using a wet chemical method to remove contaminants and native oxide on the surface.

Fig. 6.4 shows the clamping structure of the grinding stone in the UAECMP machine. In order to make grinding stone replacement easy, the grinding stone is pasted on a metal base plate using

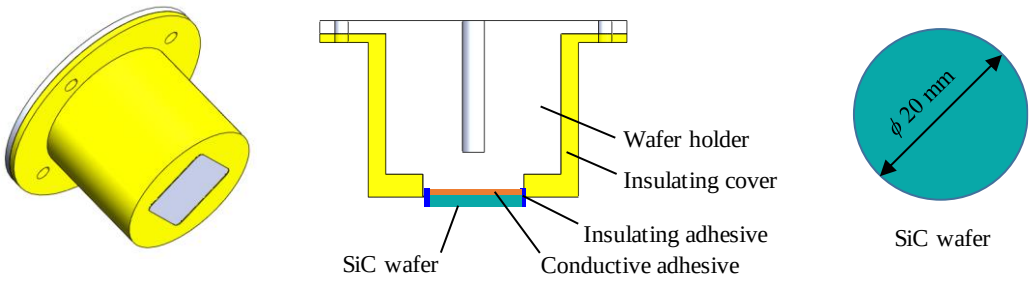



**Fig. 6.3** Wafer holder in the slurryless UAECMP machine.

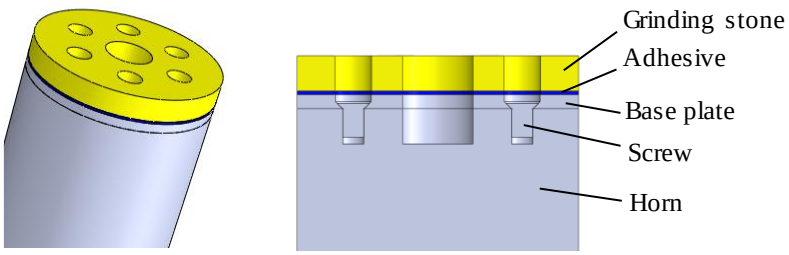



**Fig. 6.4** Grinding stone clamping structure in the slurryless UAECMP machine.

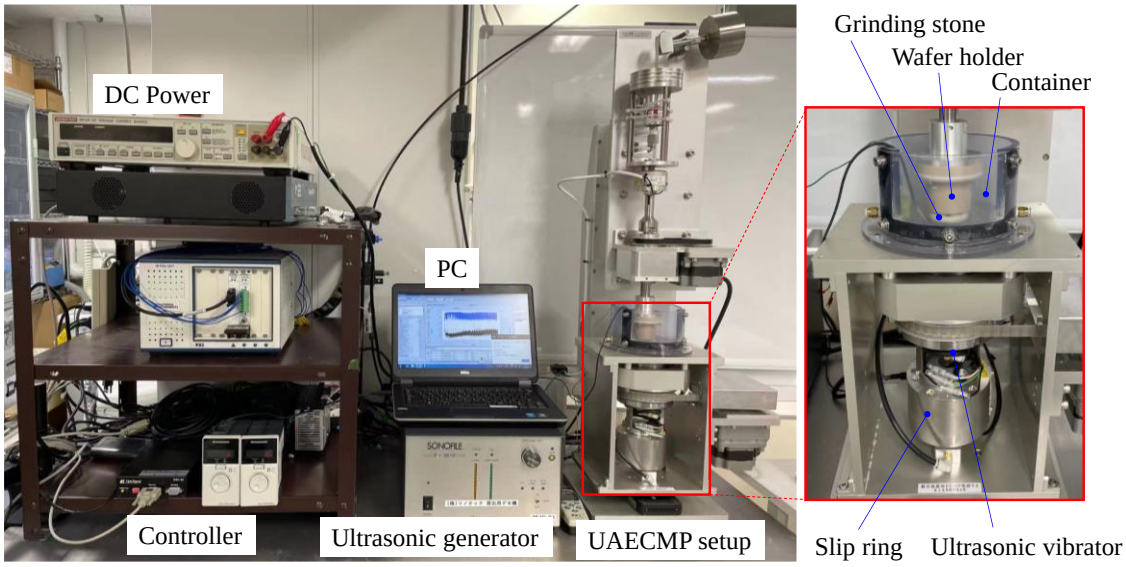



**Fig. 6.5** Photographs of the developed slurryless UAECMP machine.

adhesive and then the metal plate is installed on the end face of the horn using screws, instead of directly pasting the grinding stone to the horn. When replacing the grinding stone, the base plate with the grinding stone is first removed from the horn and then the grinding stone is separated from the metal base plate by heating. In addition, to ensure the integrity of the grinding stone, seven through holes were processed on the grinding stone using a laser. Due to the poor thermal conductivity of the grinding stone, high temperatures would be generated in the process area during laser processing, thus the bottom of the grinding stone is immersed in water to prevent cracks from being generated in the grinding stone. The diameter of the center hole is ϕ10 mm and the diameter of the outer six holes is ϕ6 mm. Fig. 6.5 shows the developed slurryless UAECMP machine.

## 6.3 Slurryless UAECMP of 4H-SiC wafers

### 6.3.1 Experimental parameters

In the polishing experiments, 1 wt% sodium chloride aqueous solution (NaCl *aq*.) with an electrical conductivity of 1.8 S/m was used. A ring-shaped vitrified bonded ceria grinding stone with an inner diameter of 10 mm and an outer diameter of 40 mm was applied to remove the oxide layer. The grinding stone was supplied by Mizuho Co., Ltd. and had an average particle size of 1 μm (#8000). Polishing parameters are summarized in Table 6.1. For UAECMP, the amplitude of the ultrasonic vibrator was set to 1.5 μm without definition.

**Table 6.1** UAECMP parameters.

| | |
|---|---|
| Potential (V) | 25 |
| Wafer rotation speed (rpm) | 50 |
| Grinding stone rotation speed (rpm) | 200 |
| Oscillation rate of grinding stone (mm/s) | 2 |
| Oscillation distance of grinding stone (mm) | 3 |
| Polishing pressure (kPa) | 30 |
| Ultrasonic vibration frequency (kHz) | 35 |
| Ultrasonic vibration power (W) | 500 |
| Grinding stone | Vitrified bonded ceria (ϕ10 × ϕ40) |
| Abrasive particle size (μm) | 0.5–2 (1 on average) |
| Electrolyte | 1 wt% NaCl |

### 6.3.2 Characterization methods

Ultrasonic vibration of the grinding stone was measured using a laser displacement sensor (LK G5000, Keyence Corporation) with a sampling frequency of 200 kHz. Ten points on the end face of the grinding stone were measured and their average vibration amplitude was taken as the vibration amplitude of the grinding stone, as shown in Fig. 6.6(a). The measurement results are shown in Fig. 6.6(b); the vibration of the grinding stone had an average amplitude of about 1.5 μm with a variation of about 0.5 μm.

Surface topography of the SiC wafers was measured using a scanning white-light interferometer (SWLI) (NewView 8300, Zygo). The chemical composition of the processed

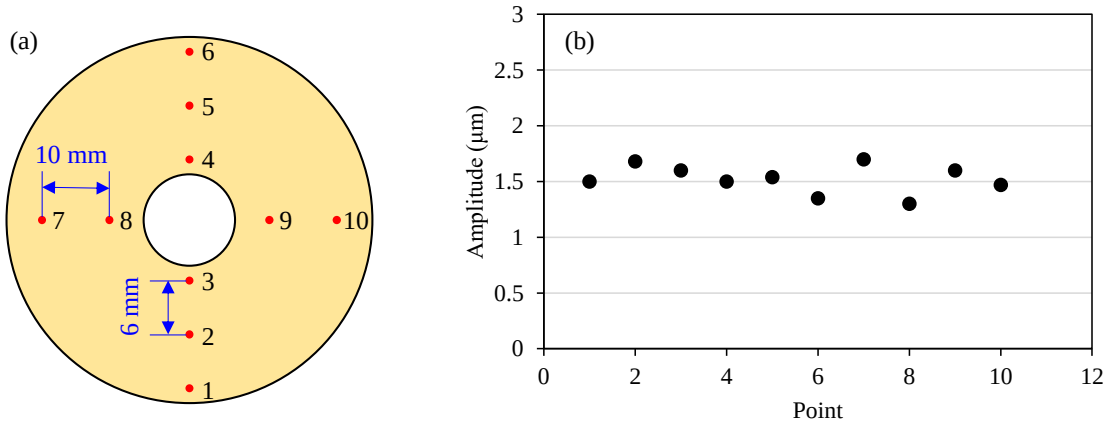



**Fig. 6.6** Measurement of ultrasonic vibration amplitude on the grinding stone. (a) Measurement positions on the surface of grinding stone and (b) vibration amplitude of the grinding stone.

surface was analyzed by X-ray photoelectron spectroscopy (XPS) (Quantum 2000, ULVAC-PHI). The MRR during polishing was evaluated by the change in wafer thicknesses per unit time. The thickness of the SiC wafer was measured by a spectral-interference wafer thickness meter (SF-3/300A, Otsuka Electronics Co., Ltd).

The residual strain on and beneath the processed SiC surface was evaluated by a confocal Raman microscope (RAMANtouch, Nanophoton). The laser used for the Raman spectroscopy had a wavelength of 532 nm. The residual stresses on the SiC surface were evaluated from the shift in the FTO(2/4)E2 peak (777.6 $cm^{-1}$) of 4H-SiC, which can be calculated as follows [1]:

$$\sigma = -510 \times \Delta\nu \ \text{(MPa)}, \tag{6.1}$$

where $\sigma$ is the stress and $\Delta\nu$ is the shift in the FTO(2/4)E2 peak.

When observing the residual strain below the SiC surface, the nominal focus position (NFP) of the laser was changed from the SiC surface to 4-μm below the SiC surface. However, considering that 4H-SiC has a refractive index of 2.7 at the laser wavelength of 532 nm, the actual observation depth for the SiC surface was calculated to be approximately 4 μm × 2.7 = 10.8 μm [2-4].

### 6.3.3 Effect of ultrasonic vibration on MRR

Fig. 6.7 shows the changes in wafer thickness and the removal amount distribution after MP for 5 h, ECMP, and UAECMP at a potential of 25 V for 10 min, along with their MRRs. Because the ceria grinding stone was much softer than SiC, MP removed very little of the wafer surface, with an average of 0.25 μm in 5 h. The removal amount distribution ranged from 0 to 1 μm, as shown in Fig. 6.7(a) and (b). In contrast, ECMP removed about 0.5 μm on average in 10 min and the removal amount distribution ranged from 0 to 1.8 μm, as shown in Fig. 6.7(c) and (d). Meanwhile, UAECMP removed approximately 2–3 μm of the SiC surface in 10 min with a removal amount distribution ranging from 1.6 to 3.4 μm, as shown in Fig. 6.7(e) and (f). ECMP and UAECMP had almost the same removal amount distribution range of 1.8 μm, which indicates that ultrasonic vibration does not affect the material removal distribution or flatness of the SiC surface. UAECMP had a normal material removal amount distribution, while ECMP and MP had semi-normal distributions because the amount of their material removal was very small. Fig. 6.7(g) shows the calculated MRRs for MP, ECMP, and UAECMP. MP and ECMP had average MRRs of 0.05 and 3.20 μm/h, respectively, whereas UAECMP had an average MRR of 14.54 μm/h. These results demonstrate that ultrasonic vibration increased the MRR of UAECMP by more than 4.5 times that of ECMP. In Chapter 5, the promotional effect of ultrasonic vibration on the anodic oxidation rate of the SiC surface in ultrasonic vibration assisted anodic oxidation was confirmed to be 11–34%, which is much lower than the promotional effect of ultrasonic vibration on the MRR in UAECMP. In our previous study, ultrasonic vibration was applied to the electrolyte and its effect on the SiC surface was very weak. That was a pure anodic oxidation experiment

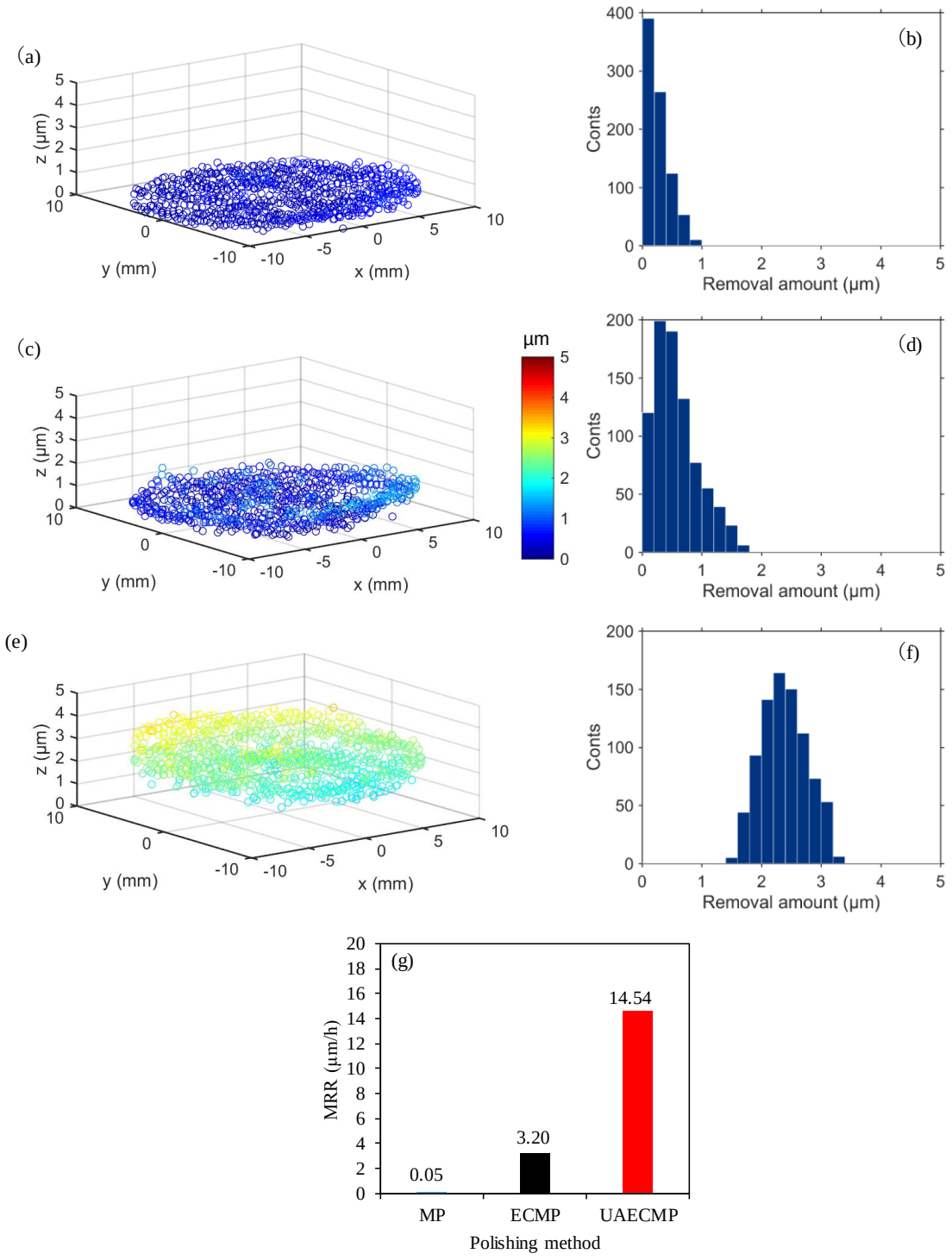



**Fig. 6.7** (a) Removal amount and (b) its distribution on the SiC wafer after MP for 5 h; (c) removal amount and (d) its distribution on the SiC wafer after ECMP at 25 V for 10 min; (e) removal amount and (f) its distribution on the SiC wafer after UAECMP at 25 V for 10 min; (g) average MRRs of MP, ECMP, and UAECMP.

and the generated oxide layer on the SiC surface hindered the promotional effects of the ultrasonic vibration. However, in this study, the ultrasonic vibration was directly applied to the grinding stone, which was in contact with the SiC surface, thus the effect of ultrasonic vibration was more direct and stronger, resulting in a much more significant promotional effect.

On the basis of Faraday's law of electrolysis, the electric current reflects the anodic oxidation rate during anodic oxidation. Fig. 6.8 shows the changes in electric current during ECMP and UAECMP. The electric current significantly increased with the application of ultrasonic vibration, suggesting that ultrasonic vibration made anodic oxidation of the SiC surface easier and increased the anodic oxidation rate. However, the current in UAECMP only increased by about 1.5 times that in ECMP, which is not consistent with the promotional amount of ultrasonic vibration on the MRR (4.5 times) shown in Fig. 6.7(g). In the anodic oxidation of SiC in NaCl aqueous solution, other electrochemical reactions, such as oxidation of water and chloride ions, may occur. The difference between the promotional amount of the electric current and MRR in UAECMP is considered to be caused by the difference in charge utilization efficiency between ECMP and UAECMP. In Chapter 4, it was confirmed that temperature increase and strain on the SiC surface can increase the charge utilization efficiency and promote anodic oxidation of SiC. In anodic oxidation with the same electric current density, anodic oxidation of SiC in a high-temperature electrolyte had a higher anodic oxidation rate than that in a low-temperature electrolyte. Additionally, with the same electric current density, a SiC surface with residual strain had a higher anodic oxidation rate than the strain-free surface. The effects of temperature and strain on the MRR of UAECMP will be investigated in detail in Sections 6.4.1 and 6.4.3.

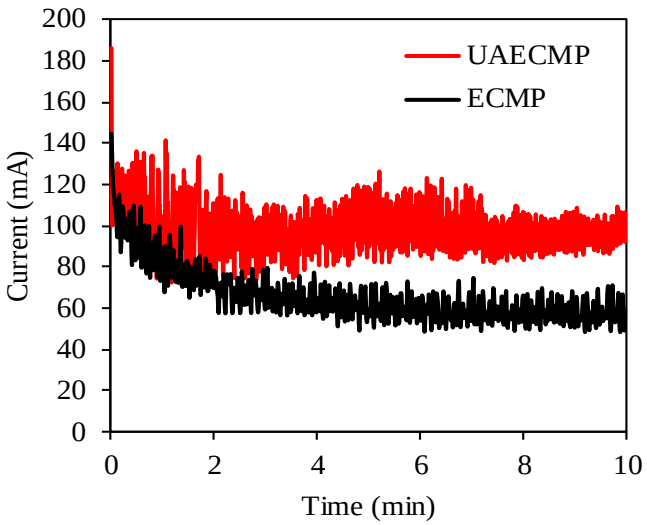



**Fig. 6.8** Changes in the electric current during ECMP and UAECMP.

### 6.3.4 Effect of ultrasonic vibration on SiC surface topography

Fig. 6.9 shows SWLI images of 4H-SiC (0001) surfaces after ECMP and UAECMP, respectively. ECMP resulted in a surface with smooth and continuous polishing marks along the polishing direction. In contrast, UAECMP resulted in polishing marks with obvious fluctuations, which are considered to be caused by impacts between the abrasive and the SiC surface. The surface roughness was less with ECMP (0.528 nm *S*q, 6.220 nm *S*z) than with UAECMP (1.993 nm *S*q, 13.612 nm *S*z).

Fig. 6.10 shows optical microscope images of surfaces after ECMP and UAECMP and the residual stress along the depth (−*z*) direction observed by confocal Raman microscopy. Fig. 6.10(a) and (b) show smooth surfaces after ECMP and UAECMP, and no residual stresses were visible on or beneath these surfaces. It is clear that damage-free surfaces were obtained by both ECMP and UAECMP. Although the MRR was increased 4.5 times with ultrasonic vibration, the SiC surface showed almost no SSD after UAECMP. This indicates that the strain induced by ultrasonic vibration of ceria abrasive on the SiC surface was rapidly removed by anodic oxidation.

Fig. 6.11 shows XPS spectra of the surfaces before polishing (CMP-processed) and after ECMP and UAECMP. Peaks corresponding to the Si–C bond were observed on all three surfaces. However, only a weak peak corresponding to the Si–C–O bond was observed on the CMP- and ECMP-processed surfaces while a strong peak corresponding to the Si–O bond was observed on the UAECMP-processed surface. These results suggest that the oxide layer was sufficiently removed by ECMP, whereas a small amount of oxide remained after UAECMP. The ultrasonic vibration generated many pits on the SiC surface due to the impacts between the fixed abrasive

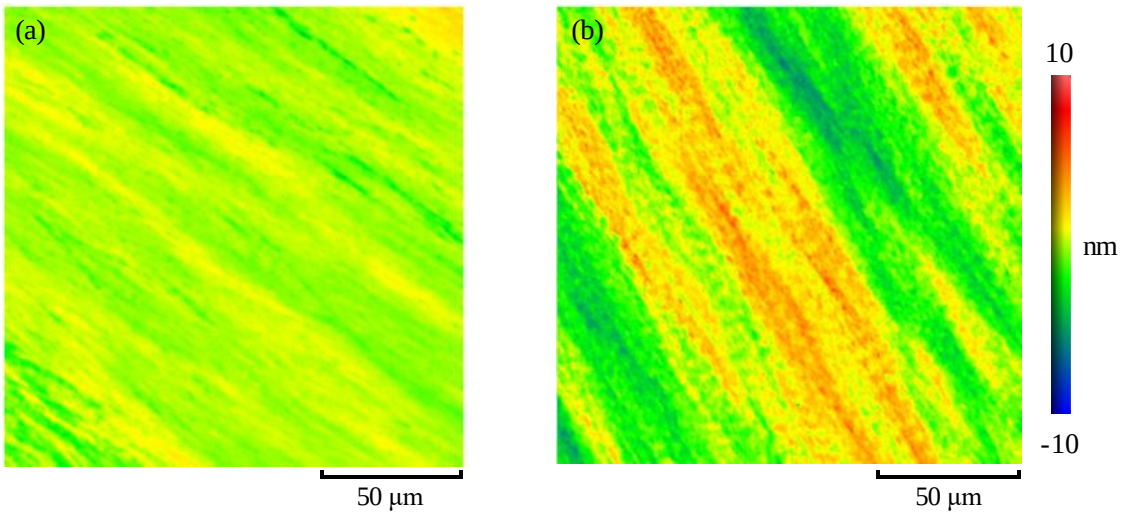



**Fig. 6.9** SWLI images of 4H-SiC (0001) surfaces processed by (a) ECMP (*S*q = 0.528 nm, *S*z = 6.220 nm) and (b) UAECMP with a vibration amplitude of 1.5 μm (*S*q = 1.993 nm, *S*z = 13.612 nm).

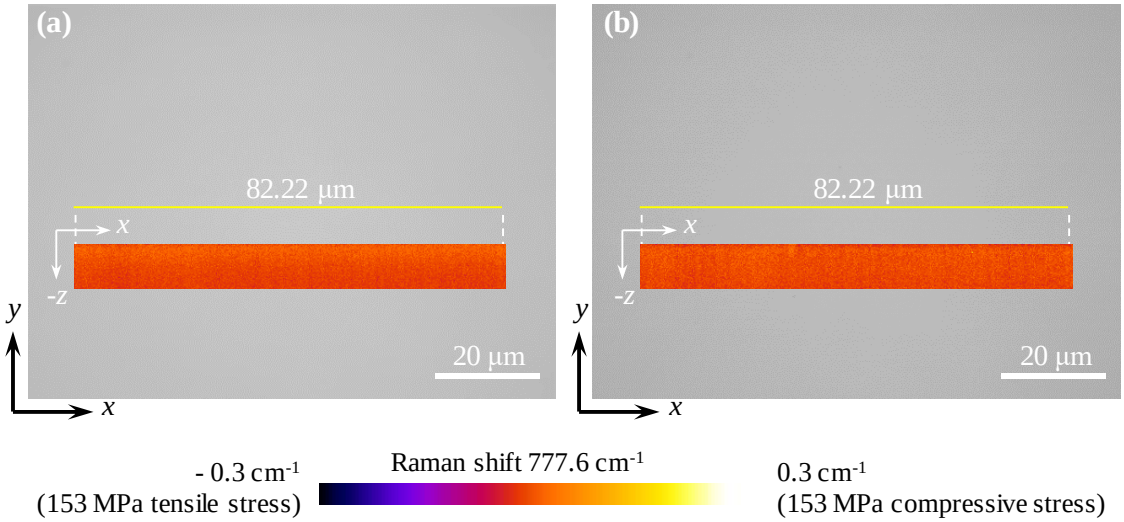



**Fig. 6.10** Optical microscope images of the 4H-SiC (0001) surface after (a) ECMP and (b) UAECMP at 25 V for 10 min. Insets show the cross-sectional residual stress distributions along the depth direction (−*z* direction) measured by confocal Raman microscopy at an observation width of 82.22 μm and depth of about 10.8 μm.

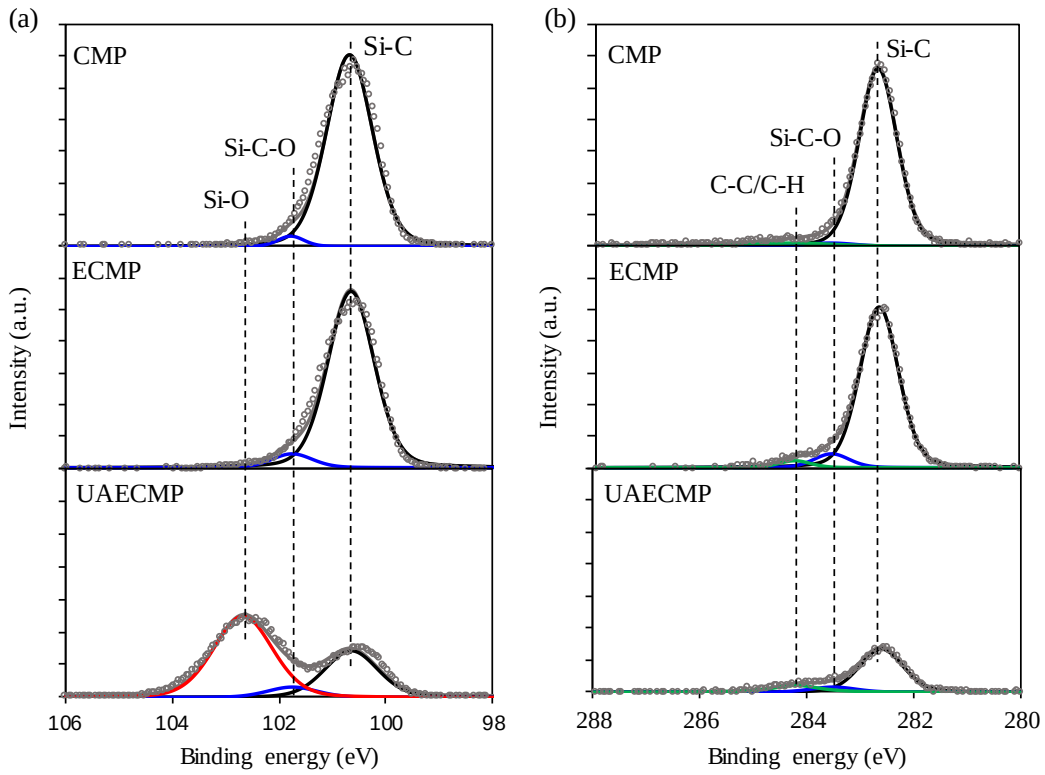



**Fig. 6.11** XPS spectra of 4H-SiC surfaces polished by CMP, ECMP, and UAECMP: (a) Si 2p spectra and (b) C 1s spectra.

and SiC surface. These pits were accompanied by residual strain, which resulted in preferential anodic oxidation of the pits. For deep pits, it was difficult to completely remove the oxide at the bottom with the fixed abrasive. This left small amounts of oxide after UAECMP. The impact force between the grinding stone and the SiC surface increases with ultrasonic vibration amplitude. Therefore, decreasing the amplitude of the ultrasonic vibration may reduce the pit depth and, in turn, the surface roughness after UAECMP.

### 6.3.5 Effects of vibration amplitude on MRR and SiC surface topography

Fig. 6.12(a) and (b) show SWLI images of 4H-SiC (0001) surfaces processed by UAECMP for 10 min at 25 V and vibration amplitudes of 1 and 0.4 μm, respectively. Although discontinuous polishing marks similar to those observed in Fig. 6.9(b) were visible on these two surfaces, the fluctuation of the polishing marks decreased with decreasing ultrasonic vibration amplitude, and the surface roughness decreased significantly. Fig. 6.12(c) and (d) show the XPS spectra of surfaces processed by UAECMP with vibration amplitudes of 1 and 0.4 μm, respectively. Strong peaks corresponding to the Si–C bond were visible on both surfaces. A very weak peak corresponding to the Si–O bond was visible only on the surface after UAECMP at a vibration amplitude of 1 μm; this was much weaker than that observed on the surface after UAECMP at a vibration amplitude of 1.5 μm, as shown in Fig. 6.11. This means that the residual oxide on the surface after UAECMP significantly decreased when the vibration amplitude was dropped from 1.5 to 1 μm. The peak corresponding to the Si–O bond was not observed on the surface after UAECMP at a vibration amplitude of 0.4 μm and only a weak peak, corresponding to the Si–C–O bond, was visible; these are almost the same results as those for ECMP. Thus, decreasing the vibration amplitude can reduce the size and depth of pits generated by impacts between the abrasive and SiC surface, which reduces the residual oxide on the polished surface.

Fig. 6.13(a) and (b) show that UAECMP for 10 min at vibration amplitudes of 1 and 0.4 μm removed approximately 1.5 and 1 μm, respectively. Fig. 6.13(c) shows the MRRs of UAECMP at vibration amplitudes of 0.4, 1, and 1.5 μm. The promotional effect of the ultrasonic vibration increased with increasing vibration amplitude.

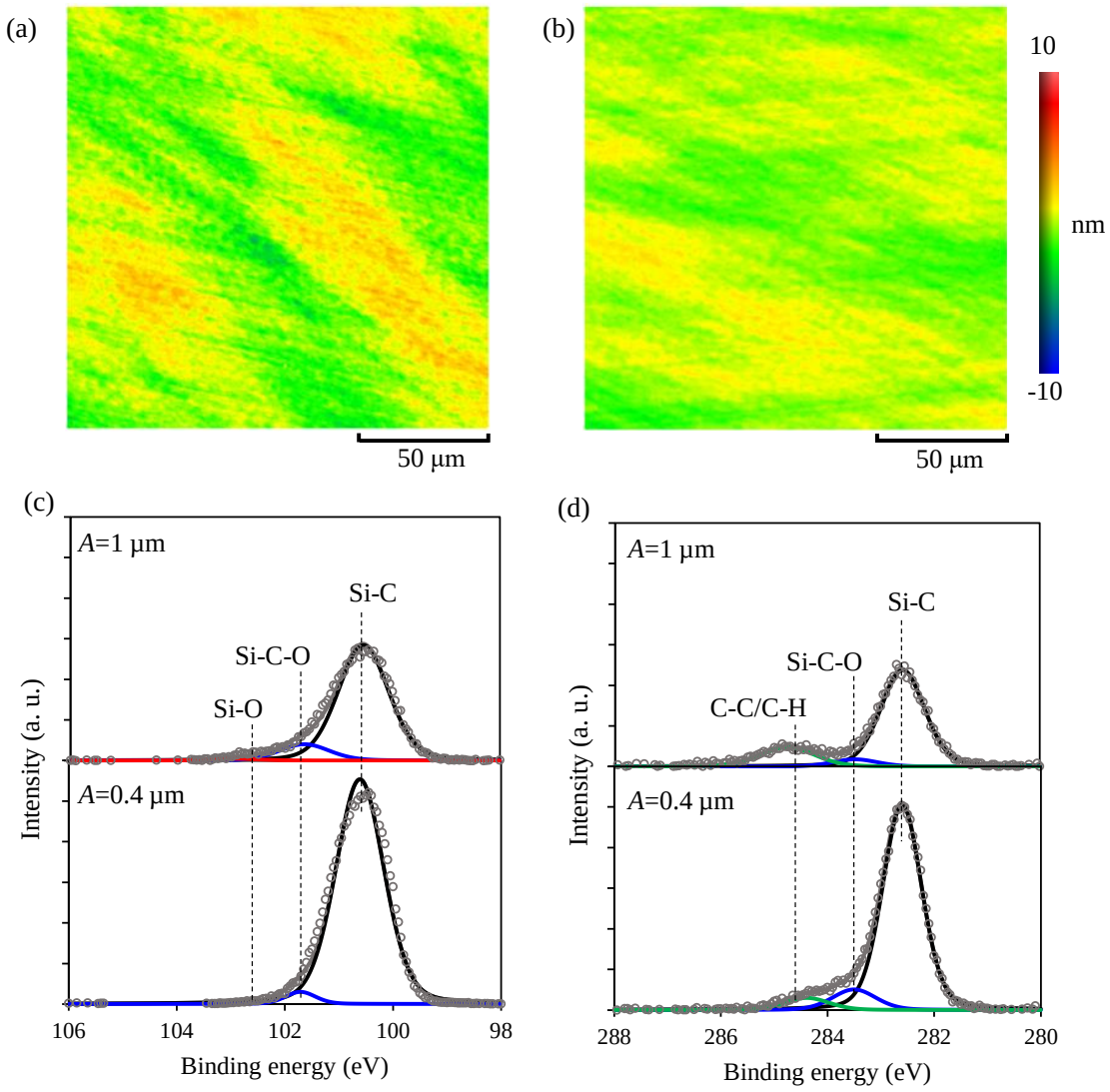



**Fig. 6.12** SWLI images of 4H-SiC (0001) surfaces processed by UAECMP at vibration amplitudes of (a) 1 μm (*Sq* = 1.237 nm, *Sz* = 11.405 nm) and (b) 0.4 μm (*Sq* = 0.733 nm, *Sz* = 5.705 nm). (c) Si 2p and (d) C 1s XPS spectra of surfaces processed by UAECMP with vibration amplitudes of 1 and 0.4 μm.

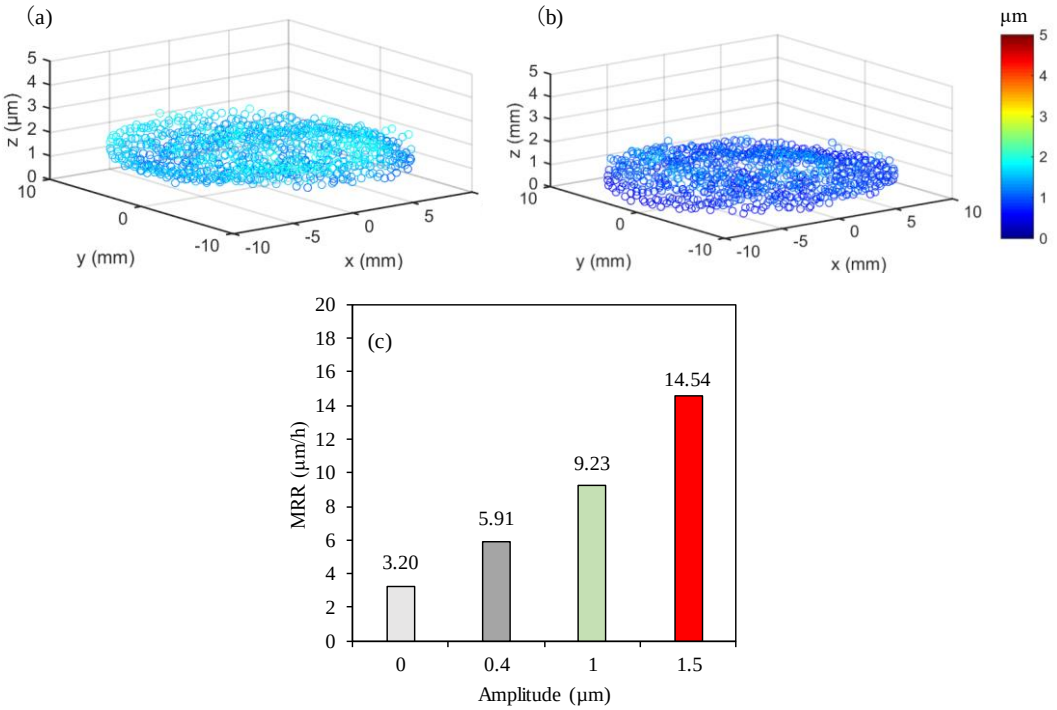



**Fig. 6.13** Amount of SiC surface removed by UAECMP with vibration amplitudes of (a) 1 and (b) 0.4 μm for 10 min. (c) Comparison of MRRs for UAECMP without and with vibration amplitudes of 0.4, 1, and 1.5 μm.

## 6.4 Promotional mechanism of ultrasonic vibration on MRR

### 6.4.1 Temperature increase in UAECMP

Fig. 6.14 shows the changes in the electrolyte temperature during ECMP and UAECMP. During ECMP, the electrolyte temperature increased very slightly and stayed around 24 °C. In contrast, the electrolyte temperature increased significantly during UAECMP, from 24 to 31 °C. This result indicates that the ultrasonic vibration caused a significant increase in electrolyte temperature during UAECMP.

In Chapter 4, increasing the temperature was confirmed to have a strong promotional effect on the anodic oxidation rate of SiC; the anodic oxidation rate increases exponentially with increasing electrolyte temperature and satisfies the Arrhenius equation. To confirm the promotional effect of the electrolyte temperature, ECMP was conducted on 4H-SiC surfaces for 10 min at 25 V and at different electrolyte temperatures: 24 (i.e., room temperature), 30, and 40 °C. Fig. 6.15(a) shows the change in temperature during these experiments. The electrolyte temperature was maintained

at 24, 30, and 40 °C and Fig. 6.15(b) shows the resulting MRRs of 3.20, 3.42, and 8.61 μm/h, respectively. The MRR increased exponentially with increasing electrolyte temperature. These results confirmed the promotional effect of increasing the electrolyte temperature on the MRR of ECMP. The temperature at the SiC/grinding stone interface may be higher than the electrolyte owing to the ultrasonic vibration and thus may has a stronger promotional effect on MRR during UAECMP. Therefore, temperature increase could be considered one of the main promotional mechanisms for ultrasonic vibration on the MRR in UAECMP.

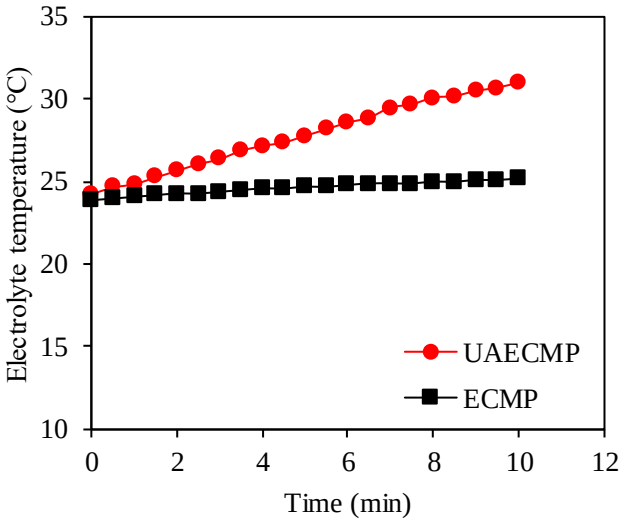



**Fig. 6.14** Changes in electrolyte temperature during ECMP and UAECMP.

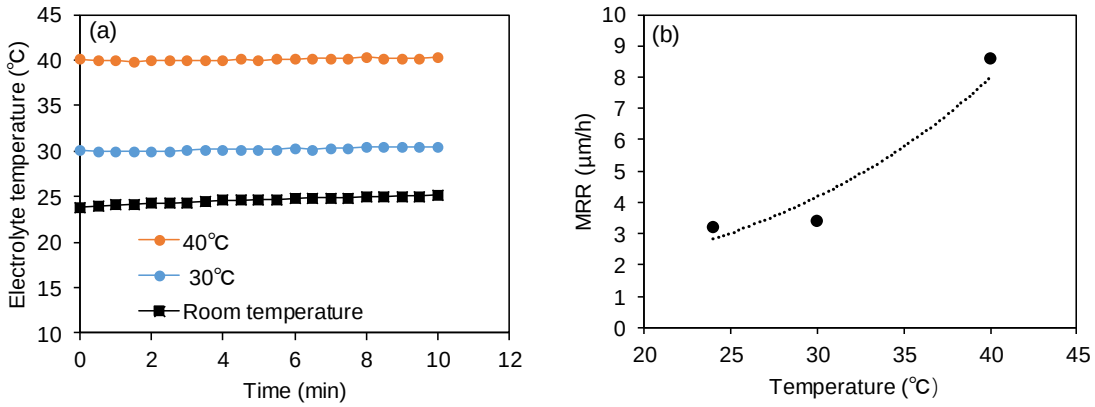



**Fig. 6.15** (a) Changes in electrolyte temperature and (b) MRRs of ECMP at different electrolyte temperatures.

Fig. 6.16 shows the changes in electric current during ECMP with different electrolyte temperatures. The electric current showed the same trend with different electrolyte temperatures for the first 2 min: the electric current was very high in the first few seconds and then dropped slowly. At first, the reactants in the electrolyte near the SiC surface had a high concentration, so anodic oxidation of SiC occurred quickly when the DC power was turned on, resulting in a high electric current. As the anodic oxidation progressed, the reactant concentration near the SiC surface decreased rapidly. The reactants in the bulk solution gradually diffused to the vicinity of the SiC surface and then reached a dynamic equilibrium, which caused the electric current to stabilize. This process took place within a few seconds, resulting in the high electric current peak observed at the initial stage of ECMP. Because the native oxide was removed by the wet chemical method before ECMP, the anodic oxidation rate was initially high without the hindrance of the oxide. This also resulted in a high electric current at the beginning of ECMP. The slow electric current drop after the initial high electric current peak was attributed to changes in the SiC surface. As ECMP progressed, the generation and removal of the oxide layer on the SiC surface gradually reached a dynamic balance and the anodic oxidation rate was affected by oxide that was not immediately removed. Therefore, the electric current was slightly lower at the steady state than at the initial stage of ECMP.

Fig. 6.16 also shows that 2 min after ECMP started, the electric current slightly fluctuated as the polishing time increased. The electric current at 40 °C increased with polishing time. Over long periods of time, the electric current for constant-potential ECMP is not constant and fluctuates but will remain at certain levels according to the polishing condition (as mentioned in Chapter 4). The fluctuation in electric current was attributed to changes in the surface states of the SiC wafer and grinding stone. For both the SiC wafer and grinding stone, their surfaces change

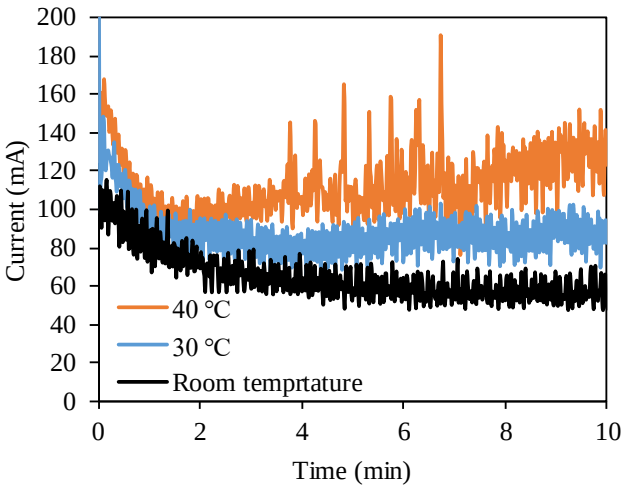



**Fig. 6.16** Changes in electric current at different electrolyte temperatures with ECMP.

as the oxide layer is removed and the grinding stone is worn down, which affects the contact state. The changes in the contact state affect the oxide removal process on the SiC surface, which causes the electric current to fluctuate. In the experiment of the present study, the polishing time was no longer than 10 min, so electric current fluctuations over time were not fully revealed. This is why Fig. 6.16 shows that the electric current increases with the polishing time.

To confirm the initial fluctuations in the electric current, ECMP was applied intermittently to a CMP-processed SiC surface for two 10-min sessions with a 5-min interval between sessions and without changing polishing conditions. Fig. 6.17 shows that the fluctuations in electric current for the first session were almost the same as that shown in Fig. 6.16. The average electric current in the second session was continuous with that in the first session, except for a momentary high electric current peak immediately after resumption. In the first session, the anodic oxidation rate was affected by both the initial change in the reactant concentration near the SiC surface and the initial SiC surface state, as mentioned earlier. At the initial stage of the second session, the SiC surface was in the same state as at the end of the first session, so the electric current was only affected by the change in reactant concentration near the SiC surface when the DC power was turned on. Therefore, the average electric current was continuous with that in the first session.

Overall, Fig. 6.16 clearly shows that the electric current increased with the electrolyte temperature. When the potential remains the same, the electric current can reflect the difficulty of SiC anodic oxidation. Thus, the anodic oxidation of 4H-SiC occurred more easily at higher electrolyte temperatures. This demonstrates that the increase of temperature in the polishing area and electrolyte is greatly account for the promotional effect of ultrasonic vibration on MRR in UAECMP.

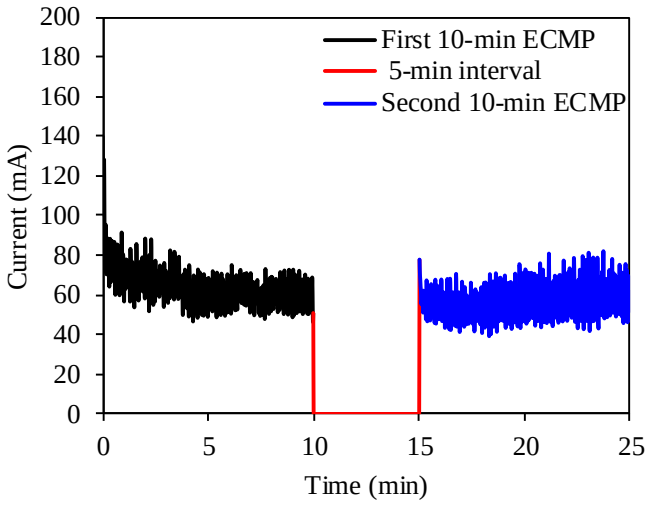



**Fig. 6.17** Changes in electric current during two 10-min sessions of ECMP, their interval was 5 min.

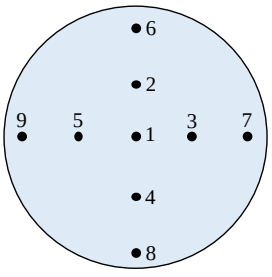
### 6.4.2 Effects of ultrasonic vibration on the removal of oxide layer

In the anodic oxidation of SiC, the oxide layer on the SiC surface has a hindrance effect on the anodic oxidation rate by preventing the diffusion of reactants in the electrolyte to the SiC/oxide interface. Therefore, the promotional effects of ultrasonic vibration on MRR can be attributed to the enhanced removal of the oxide layer during UAECMP. Since the SiC is oxidized to silicon dioxide ($SiO_2$) during anodic oxidation, MP and ultrasonic vibration assisted MP (UAMP) were applied to quartz glass, which has the same chemical composition as the oxide layer, to study the effects of ultrasonic vibration on the removal of the oxide layer. The polishing parameters were the same as that of ECMP and UAECMP described in Section 6.3.3 but without electricity. The thickness changes of nine points on the quartz glass wafer after MP and UAECMP were observed using a height gauge with a resolution of 0.1 μm, as shown in Fig. 6.18(a).

Fig. 6.18(b) and (c) show amount of quartz removed with MP and UAMP for 10 min and the calculated MRRs. MP and UAMP removed 2.5–3.9 μm and 3.4–4.6 μm of quartz glass in 10 min, respectively; their average MRRs were 19.8 and 24.2 μm/h, respectively. The MRR increased by ~22% with the assistance of ultrasonic vibration. This result is similar to that obtained by Li *et al.* in ultrasonic fixed-ceria-abrasive polishing of fused silica [5,6]. These results indicate that the promotional effect of ultrasonic vibration on the MRR of the oxide layer is very limited compared with the promotional effect of ultrasonic vibration on the MRR of SiC in UAECMP (4.5 times), as shown in Fig. 6.7(g).

On the other hand, as the XPS results shown in Fig. 6.11, there was no oxide on the ECMP-processed SiC surface while a very thin dense oxide layer of about 3.04 nm (calculated by the method in Refs. 7) and 8) and based on the XPS result with a take-off angle of 45°) on the UAECMP-processed surface. Since the electric current maintained a constant level after ECMP and UAECMP for 2 min (Fig. 6.8), the generation and removal of the oxide layer on the SiC

(a)




(b)

| No. | MP (μm) | UAMP (μm) |
|---|---|---|
| 1 | 3.8 | 4.1 |
| 2 | 3.8 | 4.2 |
| 3 | 3.9 | 4.2 |
| 4 | 3.7 | 4.3 |
| 5 | 2.6 | 3.7 |
| 6 | 3.6 | 3.6 |
| 7 | 3.0 | 4.6 |
| 8 | 2.5 | 4.2 |
| 9 | 2.8 | 3.4 |

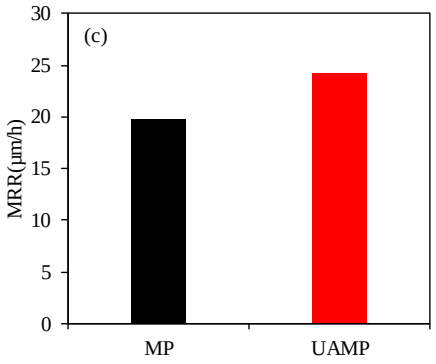



**Fig. 6.18** MP and UAMP of quartz glass. (a) Schematic diagram of thickness change measurement of quartz glass, (b) removal amounts of quartz glass with MP and UAMP for 10 min, and (c) MRRs of quartz glass in MP and UAMP.

surface reached a dynamic balance based on the analysis in Section 6.4.1. The state of the residual oxide on the surface obtained after ECMP and UAECMP can reflect the state of the residual oxide during the ECMP and UAECMP processes. Therefore, the anodic oxide layer was completely removed during ECMP and the application of ultrasonic vibration could not increase the MRR by increasing the oxide layer removal rate.

Fig. 6.11 also shows that the removal rate of the oxide layer in ECMP was greater than the anodic oxidation rate, thus no oxide was observed on the ECMP-processed surface. After application of ultrasonic vibration in UAECMP, the anodic oxidation rate of SiC and the removal rate of the oxide layer both increased. However, the promotional effect on the removal rate of the oxide layer was relatively low, as shown in Fig. 6.18, while the promotional effect on the anodic oxidation rate of SiC was greater. This resulted in the lowering of the oxide layer removal rate compared to the anodic oxidation rate of SiC, thus a thin residue of oxide layer was observed on the UAECMP-processed surface.

### 6.4.3 Impacts between abrasives and the SiC surface in UAECMP

For UAECMP, the SiC surface is in contact with the grinding stone because of the applied polishing pressure. Thus, the ultrasonic vibration imparted an impact force between the SiC surface and the grinding stone. The displacement of the grinding stone in the vertical direction is given by

$$Z = A\sin(\omega t + \phi), \tag{6.2}$$

where $Z$ is the displacement of the grinding stone with time $t$, $A$ is the amplitude, $\omega$ is the angular velocity, and $\phi$ is the initial phase angle of the ultrasonic vibration. The impact force, $F(t)$, induced by ultrasonic vibration between the abrasive and SiC surface can be expressed as [9)]

$$F(t) = N\frac{m\mathrm{d}Z/\mathrm{d}t}{\Delta t} = N\frac{m}{\Delta t}\omega A\cos(\omega t + \phi), \tag{6.3}$$

where $N$ is the number of effective abrasives on the surface of the grinding stone, $m$ is the mass of a single abrasive, and $\Delta t$ is the contact time between the SiC surface and abrasive. Therefore, the contact force, $F$, between the SiC surface and abrasive is given by

$$F = F_{\mathrm{s}} + F(t), \tag{6.4}$$

where $F_{\mathrm{s}}$ is the static polishing pressure (i.e., polishing load).

According to Eq. (6.4), the contact force increases with the upward ultrasonic displacement of the grinding stone. However, the SiC wafer moves downward with the downward displacement of the grinding stone due to the applied polishing pressure; the contact force does not change. Therefore, the contact force between the abrasive and SiC surface can be expressed as follows:

$$F = \begin{cases} F_s \quad \left(2k\pi + \frac{\pi}{2} \le \omega t + \phi \le 2k\pi + \frac{3\pi}{2}\right) \\ F_s + N\frac{m}{\Delta t}\omega A cos(\omega t + \phi) \quad \left(2k\pi - \frac{\pi}{2} \le \omega t + \phi \le 2k\pi + \frac{\pi}{2}\right) \end{cases}, \tag{6.5}$$

where $k$ is a natural number.

Eq. (6.5) indicates that contact force between the abrasive and SiC surface is greater with UAECMP than with ECMP. Owing to the very short contact time between the SiC surface and abrasive, ultrasonic vibration may introduce a huge local transient strain on the SiC surface owing to the high-frequency local impact during UAECMP. Strained areas on the SiC surface have been reported to have higher electrical conductivity than strain-free areas, which would have a promotional effect on the anodic oxidation rate of SiC. Therefore, ultrasonic vibration may increase the MRR by introducing strain to the SiC surface.

MP and ultrasonic vibration assisted mechanical polishing (UAMP) were applied to two different CMP-processed SiC wafers for 5 min to verify the above hypothesis. The polishing setup and parameters were the same as those used for ECMP and UAECMP but without electricity. Fig. 6.19 shows the thickness distributions of the SiC wafers before and after MP and UAMP. The thickness showed almost no change. This may be because the ceria grinding stone is softer than the SiC surface and had difficulty removing it. Therefore, the SiC removal amount was too small to be detected by the spectral-interference wafer thickness meter.

Fig. 6.20 shows SWLI images of the 4H-SiC surfaces before and after MP and UAMP and the bottom profiles of scratches. The surfaces were processed by CMP before MP and UAMP and were smooth without any scratches, as shown in Fig. 6.20(a). However, both MP and UAMP resulted in scratches on the surfaces, as shown in Fig. 6.20(b) and (c). The scratches by MP were

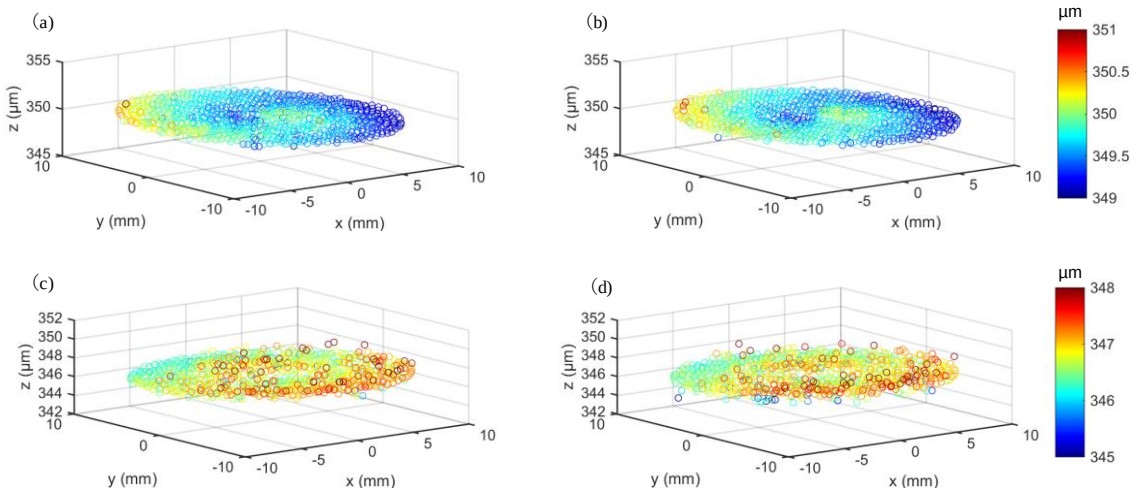



**Fig. 6.19** Thickness distributions of SiC wafers: (a) before and (b) after MP; (c) before and (d) after UAMP.

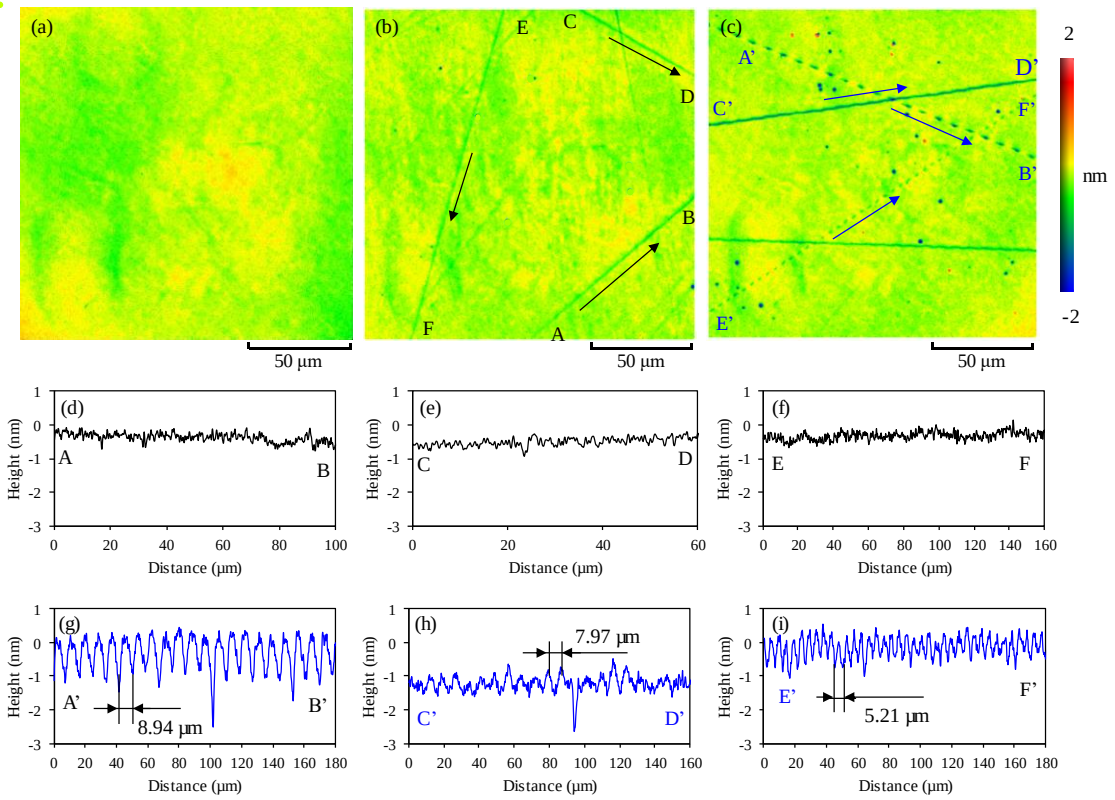



**Fig. 6.20** SWLI images of 4H-SiC (0001) surfaces (a) processed by CMP (*Sq* = 0.155 nm, *Sz* = 1.931 nm), (b) processed by MP (*Sq* = 0.158 nm, *Sz* = 8.719 nm), and (c) processed by UAMP (*Sq* = 0.222 nm, *Sz* = 21.699 nm). Bottom profiles of scratches (d) A–B, (e) C–D, (f) E–F, (g) A'–B', (h) C'–D', and (i) E'–F'.

continuous and shallow, whereas the scratches by UAMP were discontinuous and deep. Fig. 6.20(d)–(f) and (g)–(i) show detailed bottom profiles of scratches on surfaces processed by MP and UAMP. The fluctuation of scratches on the MP-processed surface were small and uniform, while those on the UAMP-processed surface were large and periodic. The fluctuation periods for scratches A'–B', C'–D', and E'–F' in Fig. 6.20(g)–(i) were 8.94, 7.97, and 5.21 µm, respectively. This can be explained by the impact force between the SiC surface and the grinding stone during ultrasonic vibration.

To confirm that the discontinuous scratches on the UAMP-processed SiC surface were caused by ultrasonic vibration, a kinematic model of the wafer polishing process was built, as shown in Fig. 6.21. The model was used to calculate a random abrasive motion trajectory on the grinding stone on the SiC surface. $\omega_1$ and $\omega_2$ are the angular velocities of the SiC wafer and grinding stone, respectively. $r_i$ is the rotation radius of a random abrasive particle A on the grinding stone. $\theta_i$ is the initial phase angle of the random abrasive particle A. $L$ is the uniaxial oscillation distance of the grinding stone during polishing and $e$ is the eccentricity between the SiC wafer and grinding

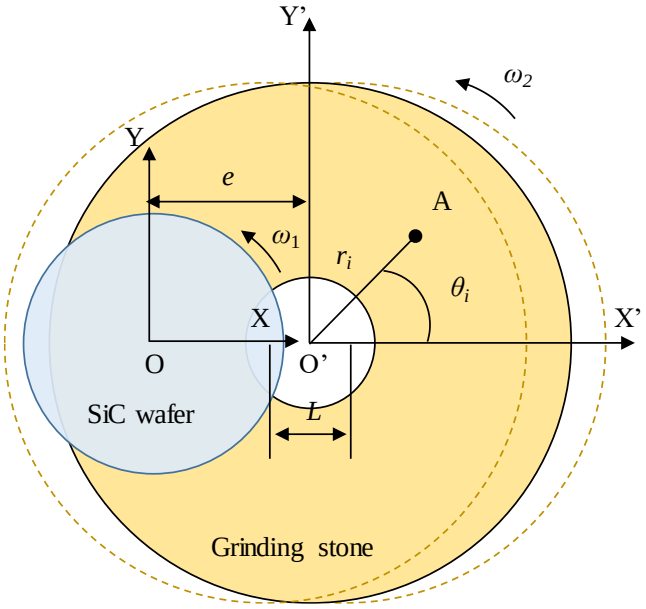



**Fig. 6.21** Kinematic model of the wafer polishing process.

stone centers. XOY is the coordinate system of the SiC wafer and its origin, O, was set at the center of the SiC wafer. X'O'Y' is the coordinate system of the grinding stone and its origin, O', was set at the center of the grinding stone. Thus, the coordinates of the random abrasive particle A in X'O'Y' at polishing time $t$ can be expressed as

$$\begin{cases} x_i = r_i \cos(\theta_i + \omega_2 t) \\ y_i = r_i \sin(\theta_i + \omega_2 t) \end{cases}. \tag{6.6}$$

Then, the coordinates of the random abrasive particle A in XOY can be calculated as

$$\begin{bmatrix} x \\ y \\ 1 \end{bmatrix} = \begin{bmatrix} \cos\omega_1 t & \sin\omega_1 t & 0 \\ -\sin\omega_1 t & \cos\omega_1 t & 0 \\ 0 & 0 & 1 \end{bmatrix} \begin{bmatrix} 1 & 0 & dx \\ 0 & 1 & dy \\ 0 & 0 & 1 \end{bmatrix} \begin{bmatrix} x_i \\ y_i \\ 1 \end{bmatrix}, \tag{6.7}$$

where

$$\begin{cases} dx = -e + \frac{L}{2}\sin(\frac{2\pi}{T}t) \\ dy = 0 \end{cases}. \tag{6.8}$$

If Eqs. (6.6)–(6.8) are combined, the coordinates of the random abrasive particle A in XOY can be written as a function of polishing time $t$:

$$\begin{cases} x = f(t) = r_i \cos(\theta_i + \omega_2 t - \omega_1 t) - e\cos\omega_1 t + \frac{L}{2}\sin(\frac{2\pi}{T}t)\cos\omega_1 t \\ y = g(t) = r_i \sin(\theta_i + \omega_2 t - \omega_1 t) + e\sin\omega_1 t - \frac{L}{2}\sin(\frac{2\pi}{T}t)\sin\omega_1 t \end{cases}. \tag{6.9}$$

Because the SiC wafer had a diameter of 20 mm, the distance $d$ between points A and O should be less than 10 mm:

$$d = \sqrt{x^2 + y^2} < 10. \tag{6.10}$$

If the period of the ultrasonic vibration is $T$, then the distance $\Delta l$ between two adjacent impact

pits on the SiC surface produced by abrasive particle A can be expressed as

$$\Delta l = \sqrt{[f(t+T) - f(t)]^2 + [g(t+T) - g(t)]^2}, \tag{6.11}$$

where

$$T = \frac{1}{f} = \frac{1}{35000} \text{ s}. \tag{6.12}$$

Because a ring-shaped grinding stone (inner diameter of 10 mm and outer diameter of 40 mm) was used in this study, to evenly distribute the abrasive particles on the entire surface of the grinding stone, $r_i$ was set to values ranging from 5 to 20 mm in increments of 1 mm. In addition, $\theta_i$ was set to values ranging from 0 to 2π in increments of π/10. Then, $\Delta l$ was calculated to be 3.44–10.9 μm, which is consistent with the UAMP results shown in Fig. 6.20(g)–(i). This confirms the discontinuous scratches and their fluctuation in depth on the surface polished by UAMP were caused by the ultrasonic vibration of the grinding stone. Eq. (6.5) also indicates that the contact force between the SiC surface and the grinding stone changed periodically, confirming that the contact force between the abrasive particles and the SiC surface increased with the assistance of ultrasonic vibration.

Fig. 6.22 shows Raman images of surfaces after MP and UAMP. Fig. 6.22(c) and (d) show the residual stress distributions. Tensile stress was mainly concentrated at the scratches; the stress induced by MP was continuous, corresponding with the continuous scratches shown in Fig. 6.20(b). The stress inducted by UAMP was discontinuous, which is consistent with the discontinuous and fluctuating scratches shown in Fig. 6.20(c). UAMP induced greater stress than MP. According to Eq. (6.1), the maximum residual stress on the MP- and UAMP-processed surfaces were approximately 15 and 100 MPa, respectively. Fig. 6.22(e) and (f) show the cross-sectional residual stress distributions on the surfaces after MP and UAMP. Both MP and UAMP induced shallow strained layers, but the strain was deeper with UAMP than with MP. This confirms that the ultrasonic vibration increased the contact force between the abrasive particles and the SiC surface, which resulted in greater strain on the SiC surface.

In Chapter 4, both tensile and compressive strains on the SiC surface were confirmed to significantly promote the anodic oxidation rate of SiC; the anodic oxidation rate almost linearly increased with the increase in tensile or compressive strain and compressive strain had a stronger effect on the anodic oxidation rate than tensile strain. The increased amount of anodic oxidation rate reached more than twice when the compressive or tensile strain increased from 0 to 450 με. Thus, the anodic oxidation rate of SiC can be greatly promoted by strong impacts from the abrasives during UAECMP, resulting in an increase in MRR. According to Eq. (6.5), the impact force between the abrasive and the SiC surface increases with increasing vibration amplitude. This is consistent with the relationship between the vibration amplitude and the MRR, as shown in Fig. 6.13(c).

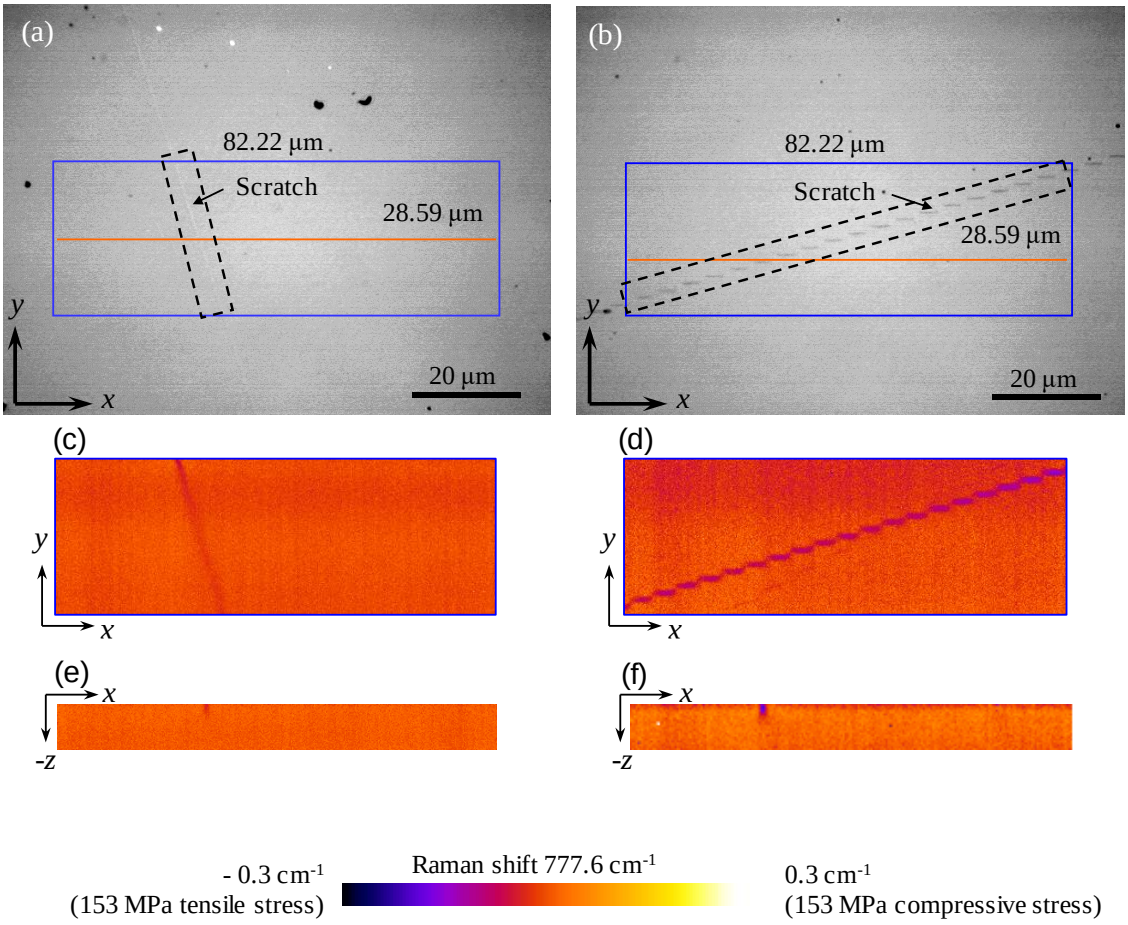



**Fig. 6.22** Raman spectroscopy observations of MP- and UAMP-processed SiC surfaces. Optical microscope images of 4H-SiC (0001) surface processed by (a) MP and (b) UAMP. Residual stress distributions on (c) MP- and (d) UAMP-processed surfaces observed in the rectangular area (82.22 × 28.59 μm$^2$) marked in (a) and (b). Cross-sectional residual stress distribution images of (c) MP- and (d) UAMP-processed surfaces observed at the orange line marked in (a) and (b) (depth of about 10.8 μm).

### 6.4.4 Modeling of the UAECMP process

Based on the above results, the main promotional mechanism of ultrasonic vibration on the MRR can be attributed to the abrasive impact-induced strain on the SiC surface and the temperature increase. The material removal mechanisms of MP, ECMP, and UAECMP using the ceria grinding stone can be modeled, as shown in Fig. 6.23. Fig. 6.23(a) shows the MP process. Because MP removes almost no SiC, it only leaves a few scratches or pits accompanied by residual strain, as shown in Fig. 6.20(b). Fig. 6.23(b) shows the ECMP process. The mechanically induced strain and damage on the SiC surface are quickly oxidized by anodic oxidation and the generated oxide layer is simultaneously removed by the fixed abrasive. Thus, no residual strain

and oxide remain on the SiC surface after ECMP. Fig. 6.23(c) and (d) show the UAECMP process. The ultrasonic vibration increases the degree of strain on the SiC surface induced by the abrasive impact. When the ultrasonic vibration has a large amplitude, the strong impact produces large and deep pits on the SiC surface, as shown in Fig. 6.23(c). These pits are accompanied by large residual strain, which significantly promotes the anodic oxidation rate of the SiC surface. However, it is difficult to completely remove the oxide at the bottom of the deep pits, which results in remaining residual oxide on the polished surface and a relatively rough surface. When the ultrasonic vibration has a small amplitude, as shown in Fig. 6.23(d), the pits become shallower, and the oxide becomes easier to remove, which results in a smoother surface. However, the MRR decreases with decreasing ultrasonic vibration amplitude due to the reduced residual strain induced by the impact between the abrasive and SiC surface. No residual strain was observed in

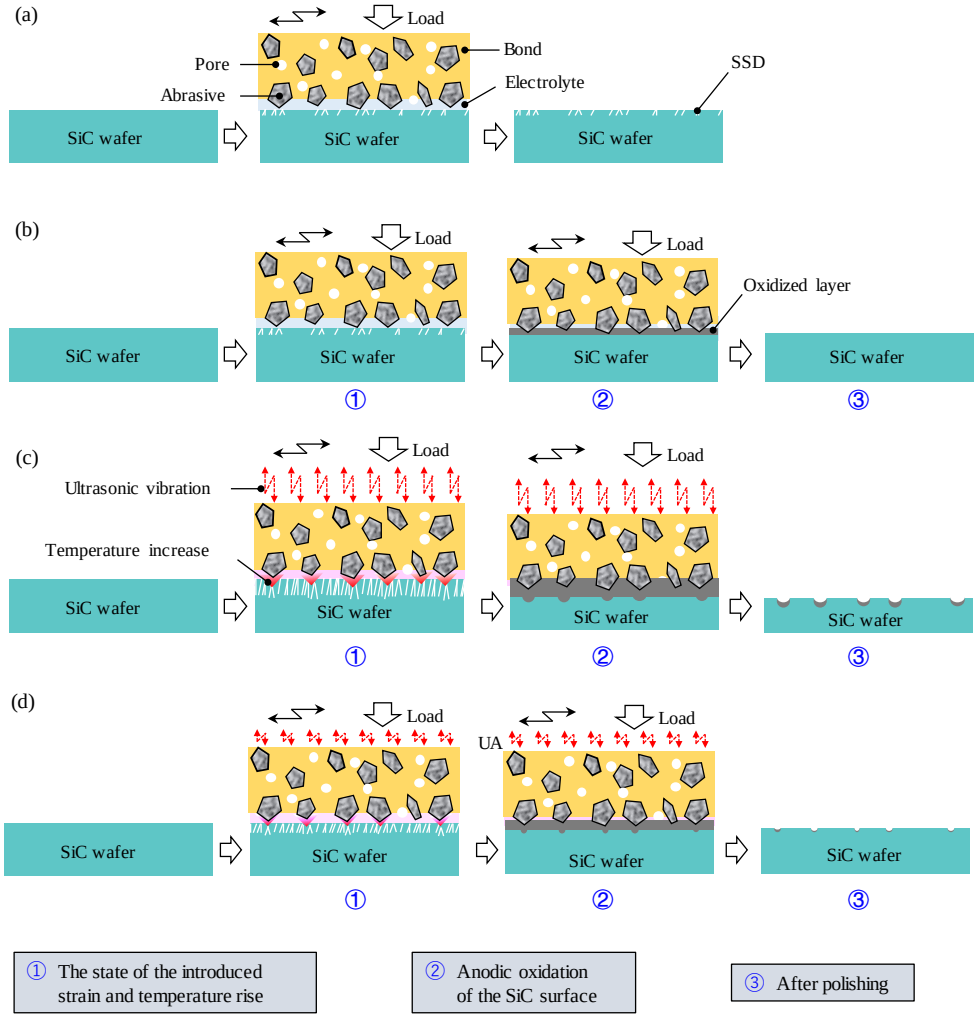



**Fig. 6.23** Material removal mechanisms for (a) MP, (b) ECMP, and UAECMP with (c) large and (d) small vibration amplitude.

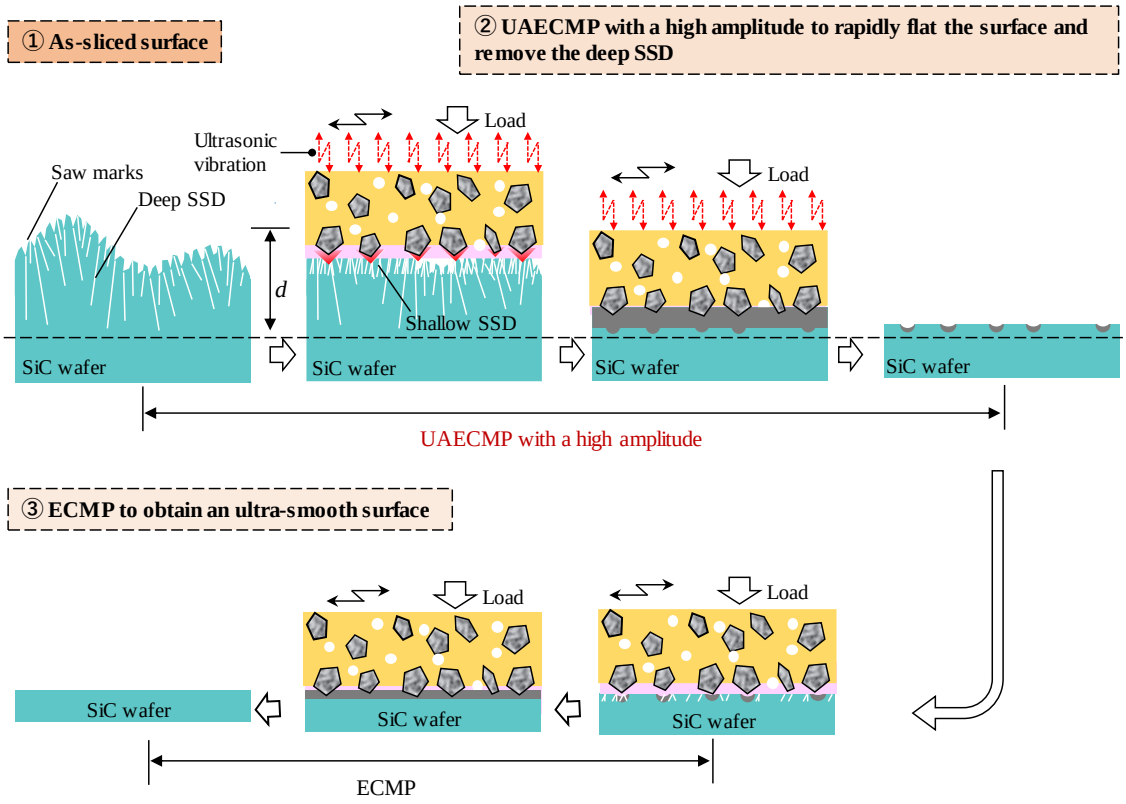



**Fig. 6.24** New manufacturing process for as-sliced SiC wafer combining UAECMP and ECMP.

the Raman image of the polished surface in this study because the strained area was immediately oxidized and the strain was removed regardless of the vibration amplitude.

Because increasing the vibration amplitude of UAECMP increases both the MRR and surface roughness, a high-efficiency and high-quality polishing process for as-sliced SiC wafers can be realized by combining UAECMP and ECMP, as shown in Fig.6.24. First, UAECMP with a high vibration amplitude can be applied to the as-sliced SiC wafer to rapidly remove saw marks and deep strained layers on the SiC surface. Then, the surface can be finished by ECMP with a short polishing time to reduce surface roughness. Therefore, UAECMP is a promising approach for replacing and simplifying the current SiC wafer manufacturing process, which is complex and time-consuming.

## 6.5 Summary

This chapter introduced the developed slurryless UAECMP machine and used it to perform slurryless UAECMP of 4H-SiC wafers. Also, theoretical analyses of the polishing process of slurryless UAECMP were performed to evaluate its performance and clarify the underlying mechanisms. The obtained results in this chapter are summarized as follows.

(1) A slurryless UAECMP machine, which combines an anodic oxidation unit, ultrasonic vibration unit, and mechanical polishing unit, was developed. Ultrasonic vibration assisted anodic oxidation and mechanical polishing were simultaneously realized using the developed machine.

(2) Ultrasonic vibration significantly increased the MRR of SiC. UAECMP of a CMP-processed 4H-SiC (0001) surface at a vibration amplitude of 1.5 μm obtained an extremely high MRR of 14.53 μm/h while that of ECMP was 3.42 μm/h. The MRR increased by 4.5 times after the application of ultrasonic vibration.

(3) The effect of the increase in electrolyte temperature was confirmed in slurryless UAECMP. The increase in temperature accounted for part of the increase in MRR during slurryless UAECMP.

(4) The impact force between the SiC surface and the grinding stone was modeled. It was confirmed that ultrasonic vibration increased the contact force between the SiC surface and the grinding stone. This induced a larger residual strain on the SiC surface, promoting the anodic oxidation of SiC and increasing the MRR in slurryless UAECMP.

(5) It was revealed that the surface roughness obtained by UAECMP is greater than that obtained by ECMP owing to pits generated by impacts between the grinding stone and the SiC surface.

(6) The MRR of SiC in UAECMP is proportional to the amplitude of ultrasonic vibration, whereas the surface roughness obtained by UAECMP was increased with the increase in vibration amplitude.

(7) To realize the benefits of UAECMP while mitigating its disadvantages, a novel polishing process was proposed for SiC wafers that starts with UAECMP and finishes with ECMP.

# References

1) N. Sugiyama, M. Yamada, Y. Urakami, M. Kobayashi, T. Masuda, K. Nishikawa, F. Hirose, S. Onda, MRS Proc. 1693 (2014).
2) S. Hell, G. Reiner, C. Cremer, E.H. Stelzer, J. Microsc. 169(3) (1993) 391–405.
3) P.T. Shaffer, R.G. Naum, JOSA 59(11) (1969) 1498–1498.

4) B. Pégourié, Astron. Astrophys. 194 (1988) 335–339.
5) Y. Li, Y. Wu, L. Zhou, M. Fujimoto, Int. J. Machine Tools Manuf. 77 (2014) 93–102.
6) C. Zhou, Q. Zhang, C. He, Y. Li, Optik 125 (2014) 4064–4068.
7) S. Imai, M. Fujimoto, M. Takahashi, H. Kobayashi, Surf. Sci. 600(3) (2006) 547–550.
8) C. Önneby, C. G. Pantano, J. Vac. Sci. Technol. A 15(3) (1997) 1597–1602.
9) W. Xu, X. Lu, G. Pan, Y. Lei, J. Luo, Appl. Surf. Sci. 257 (2011) 2905–2911.

# Chapter 7
# Summary

A novel, high-efficiency, low-cost, and damage-free polishing technique called slurryless ultrasonic vibration assisted electrochemical mechanical polishing (UAECMP) is proposed and developed in this thesis. Surface modification of difficult-to-machine materials by ultrasonic vibration assisted anodic oxidation and the removal of this modified layer by ultrasonic vibration assisted fixed-soft-abrasive polishing were effectively combined in UAECMP. To investigate the effects and mechanism of ultrasonic vibration on the anodic oxidation of SiC, anodic oxidation of 4H-SiC (0001) was first studied through a series of anodic oxidation and electrochemical mechanical polishing (ECMP) experiments. The effects of ultrasonic vibration on the anodic oxidation of SiC were confirmed using ultrasonic vibration assited anodic oxidation experiments and its effects on the material removal rate (MRR) and surface roughness in slurryless UAECMP were investigated. Additionally, the mechanism behind the UAECMP polishing technique was clarified.

In Chapter 1, the background of this study, includes the properties and applications of the SiC substrates polished in this study, and the aims of this study were described.

In Chapter 2, to realize high-efficiency, high-quality, low-cost manufacturing of single crystal SiC wafers, the current SiC wafer manufacturing process was described and its characteristics were analyzed. Polishing techniques that are applied in the final processing step of SiC wafers were summarized and their advantages and disadvantages were discussed. Furthermore, the application of ultrasonic vibration in the fields of chemical, physical, and machining applications were introduced and the performance of ultrasonic vibration in these applications was reviewed. On the basis of these results, slurryless UAECMP was proposed. The obtained results in this chapter are summarized as follows.

(1) At present, the manufacturing of SiC wafers includes a series of processing steps after slicing: grinding, lapping, rough mechanical polishing, and CMP. This complex process involves the use of a variety of expensive equipment and a lot of manpower, which results in high cost and low efficiency.

(2) Although there are many polishing methods for the final finishing step of SiC wafers, some of these methods are low in efficiency, costly, and cannot obtain high surface quality. Therefore, these methods cannot be used for mass industrial production of SiC wafers. Slurryless ECMP can achieve damage-free and ultra-smooth surfaces with a relatively high MRR compared to other polishing techniques. However, it is necessary to further increase this MRR to replace the entire post-slicing SiC wafer manufacturing process and to simplify the SiC wafer manufacturing process.

(3) Cavitation induced by ultrasonic vibration, which is accompanied by high-energy output phenomenon and different physical mechanisms, such as acoustic streaming, micro-jetting, and shock waves, can enhance the mass transfer and activation (de-passivation) of the surface of an electrode, enhancing chemical and electrochemical processes. Additionally, in fixed-abrasive machining, the application of ultrasonic vibration introduces strong local impact between the tool and the workpiece, which significantly promotes the mechanical removal of the workpiece. In loose-abrasive polishing, the application of ultrasonic vibration can increase the effective number of abrasives and prevent abrasive agglomeration, which can improve the MRR and decrease surface roughness and SSD.

(4) Slurryless UAECMP, which combines ultrasonic vibration-assisted anodic oxidation and ultrasonic vibration-assisted mechanical polishing, was proposed. In this method, both the anodic oxidation rate of SiC and the removal rate of the oxide layer are promoted by ultrasonic vibration. High-efficiency ultra-precision polishing of SiC wafers is expected with this method. In addition, slurryless UAECMP is expected to replace processing steps after slicing in the current SiC wafer manufacturing process and significantly improve efficiency while decreasing cost.

Chapter 3 investigated the role of electrolyte type, electrolyte concentration, and electric current density in the anodic oxidation of SiC, as well as their underlying mechanisms. On the basis of the above results, the anodic oxidation system of SiC in NaCl aqueous solution was modeled and an anodic oxidation mechanism of SiC was proposed. The main results of the chapter are summarized as follows.

(1) NaOH, NaCl, and $NaNO_3$ with different concentrations were used for anodic oxidation of the 4H-SiC (0001) surface. It is found that the changes of anodic oxidation rate were mainly affected by the conductivity, but not by the type of electrolyte in constant-potential anodic oxidation, while the electrolyte conductivity affected the electric current at the beginning of

the anodic oxidation. As the electrolyte conductivity increases, the electric current at the beginning of the anodic oxidation increased, but the anodic oxidation rate of SiC first increased and then decreased.

(2) Anodic oxidation at the same electric current densities with different electrolyte concentrations was applied to 4H-SiC surfaces. When the electric current densities were the same, electrolyte concentration did not affect the surface roughness or anodic oxidation of SiC. It was confirmed that the anodic oxidation of SiC is mainly affected by the flowed current.

(3) It was found that with the increase in electric current during anodic oxidation, pits on the oxidized/etched surface were reduced and gradually disappeared, the surface roughness decreased significantly, and a smooth and flat surface was obtained during anodic oxidation in 5 wt% NaCl electrolyte. The anodic oxidation of the SiC surface changed from non-uniform oxidation to uniform oxidation with the increase in electric current density.

(4) With the increase in flowed electric current during anodic oxidation, the generated oxide layer changed from a porous to a dense structure; the size and number of pores in the oxide layer decreased and the interface between the oxide layer and bulk SiC became smooth. The dense oxide layer more greatly hindered the anodic oxidation of SiC and had higher hardness compared with the porous oxide layer.

(5) Anodic oxidation at the same charge with different electric current densities was applied to 4H-SiC surfaces. The anodic oxidation rate decreased with the increase in electric current density although the amount of charge was the same.

(6) Anodic oxidation for the same period of time and with different electric current densities was applied to 4H-SiC surfaces. The anodic oxidation depths increased linearly with the increase in electronic current densities, then slightly decreased. After the electronic current density increase to a certain degree, the charge utilization efficiency was reduced.

(7) ECMP with different electric current densities was conducted on 4H-SiC (0001) surfaces. The MRRs of the ECMP increased with increasing electric current density and then significantly decreased after the electric current density was increased to a certain level.

(8) The anodic oxidation system of SiC in NaCl electrolyte was modeled. The order of oxidation reactions that may occur on the SiC surface was evaluated from the equilibrium potentials of

each reaction calculated by the Nernst equation. The results showed that the order of oxidation reactions, from easy to difficult, is the anodic oxidation of SiC, oxidation of $H_2O$, and, finally, the oxidation of $Cl^-$.

(9) LSV measurements were applied to CMP-processed SiC surfaces to confirm the potential at which the reaction occurs. The reaction occurring on the SiC surface is mainly the oxidation of SiC from 3.7 to 25 V; the oxidation reaction of $H_2O$ from 25 to 28 V, and the oxidation of $Cl^-$ when the potential is greater than 28 V. The LSV results were verified by the anodic oxidation and ECMP experiments.

(10) The number of holes (electrons) that are needed for anodizing 1 mol SiC was calculated through anodic oxidation experiments. It was found that about 7 mol of holes is required to anodize 1 mol SiC and the reactions of six and eight holes are almost equal to each other in the anodic oxidation of SiC.

(11) The role of $Na^+$ and $Cl^-$ in the anodic oxidation of SiC with NaCl electrolyte was modeled. $Na^+$ and $Cl^-$ ions do not participate in the oxidation reaction of SiC, they only play a role in the transmission of electric current.

In Chapter 4, dominant factors, including temperature, doping concentration, damage, and strain, and their action mechanisms in anodic oxidation and ECMP of the 4H-SiC (0001) surface were investigated experimentally and theoretically. The following results were obtained.

(1) A constant-temperature anodic oxidation set up was developed. Anodic oxidation of 4H-SiC (0001) was performed with different electrolyte temperatures. In constant-current anodic oxidation, there existed a saturated anodic oxidation rate with increasing oxidation current density. This saturated anodic oxidation rate increased exponentially with increasing electrolyte temperature and satisfied the Arrhenius equation.

(2) At the same current density of 20 $mA/cm^2$, the MRR of ECMP increased from 4.5 to 9.5 μm/h as the electrolyte temperature increased from 25 to 60 °C. The surface roughness was not affected by electrolyte temperature. It was mainly affected by the balance between anodic oxidation rate and the removal rate of the oxide layer.

(3) Both N-doping and surface damage increased the anodic oxidation rate of SiC and the current efficiency at high current densities. The activation energies of highly doped and diamond-

lapped SiC were lower than those of low doped CMP-processed SiC; damage showed a greater promotional effect. These observations were attributed to the residual strain on the SiC surface.

(4) The effects of strain on the anodic oxidation rate of SiC were quantitatively investigated using a strain-controllable, constant-temperature anodic oxidation setup. The results showed that both compressive and tensile strains increase the anodic oxidation rate of SiC; the anodic oxidation rate of the SiC surface increased by more than two times when compressive and tensile strains were increased from 0 to 450 με. The promotional effect of compressive strain was stronger than that of tensile strain.

(5) MP with different polishing pressures was conducted on SiC surfaces; almost no material was removed with increasing polishing pressure. The surfaces obtained with different polishing pressures were measured by Raman spectroscopy and no residual stress was observed on these surfaces. It was confirmed that damage was unlikely to be introduced to the SiC surface by increasing the polishing pressure when applying a ceria grinding stone during MP.

(6) Increasing the polishing pressure was an effective method for introducing strain on the SiC surface during ECMP and resulted in an increase in anodic oxidation rate and MRR. The MRR of ECMP was increased from 1.5 to 11.5 μm/h by increasing the polishing pressure from 35 to 175 kPa and the same surface roughness of about 0.6 nm *S*q were obtained.

(7) The promotional mechanism of anodic oxidation by strain on SiC was investigated using C-AFM. The C-AFM results showed that the strained areas had a higher electrical conductivity than the strain-free areas, and the distribution of the anodic oxidation rate was perfectly consistent with the current distribution on the SiC surface. It is considered that the strain changed the electrical property of the SiC.

In Chapter 5, a ultrasonic vibration assisted anodic oxidation setup was developed and the effects of ultrasonic vibration on the anodic oxidation of 4H-SiC (0001) surfaces, including the anodic oxidation rate, the structure of the oxide layer, oxidation uniformity, etc., were investigated. Moreover, the difference between applying ultrasonic vibration to the electrolyte and to the SiC wafer was compared and discussed.

(1) Ultrasonic vibration assisted anodic oxidation of the diamond-lapped 4H-SiC (0001) surface was conducted by applying ultrasonic vibration to the electrolyte. It was confirmed that the

anodic oxidation rate increased by about 34% with ultrasonic vibration in the initial oxidation stage and the promotional performance remained at about 11% during subsequent oxidation.

(2) The structure of oxide layers obtained by conventional and ultrasonic vibration assisted anodic oxidation was modeled and observed. The anodic oxide layer has a porous structure, through which the reactive species can pass and reach the interface of the oxide layer and bulk SiC. This resulted in an almost constant oxidation rate after prolonged oxidation. Ultrasonic vibration can increase the porosity of the oxide layer, which decreases the hindrance of the oxide layer during anodic oxidation; therefore the oxidation rate with UA was always greater than that without UA.

(3) The promotional effects of ultrasonic vibration on the anodic oxidation rate of SiC were analyzed by EIS measurements. Ultrasonic vibration enhanced charge transfer and mass transfer processes during anodic oxidation of SiC. This may be due to ultrasonic cavitation, which promotes the flow of electrolyte and the diffusion of reactants and products at the SiC/electrolyte interface. Additionally, the instantaneous high temperature, high pressure, and hydroxyl radicals generated by ultrasonic cavitation also promote anodic oxidation of SiC.

(4) Ultrasonic vibration assisted anodic oxidation experiments were conducted by applying ultrasonic vibration to the SiC wafer and an anodic oxidation rate twice that of conventional anodic oxidation was obtained. Applying ultrasonic vibration to the SiC wafer has a greater promotional effect on the anodic oxidation of SiC than that when applied to the electrolyte.

(5) The oxide layer generated using ultrasonic vibration assisted anodic oxidation is much softer than that generated using conventional anodic oxidation owing to the higher porosity of the oxide layer.

(6) The anodic oxidation uniformity of the SiC surface was improved by the application of ultrasonic vibration.

(7) Applying ultrasonic vibration to the SiC wafer had a stronger promotional effect on the anodic oxidation rate than when applying to the electrolyte due to the higher intensity of ultrasonic vibration near the SiC surface.

Chapter 6 introduced the developed slurryless UAECMP machine and used it to perform slurryless UAECMP of 4H-SiC wafers. Also, theoretical analyses of the polishing process of

slurryless UAECMP were performed to evaluate its performance and clarify the underlying mechanisms. The obtained results in this chapter are summarized as follows.

(1) A slurryless UAECMP machine, which combines an anodic oxidation unit, ultrasonic vibration unit, and mechanical polishing unit, was developed. Ultrasonic vibration assisted anodic oxidation and mechanical polishing were simultaneously realized using the developed machine.

(2) Ultrasonic vibration significantly increased the MRR of SiC. UAECMP of a CMP-processed 4H-SiC (0001) surface at a vibration amplitude of 1.5 μm obtained an extremely high MRR of 14.53 μm/h while that of ECMP was 3.42 μm/h. The MRR increased by 4.5 times after the application of ultrasonic vibration.

(3) The effect of the increase in electrolyte temperature was confirmed in slurryless UAECMP. The increase in temperature accounted for part of the increase in MRR during slurryless UAECMP.

(4) The impact force between the SiC surface and the grinding stone was modeled. It was confirmed that ultrasonic vibration increased the contact force between the SiC surface and the grinding stone. This induced a larger residual strain on the SiC surface, promoting the anodic oxidation of SiC and increasing the MRR in slurryless UAECMP.

(5) It was revealed that the surface roughness obtained by UAECMP is greater than that obtained by ECMP owing to pits generated by impacts between the grinding stone and the SiC surface.

(6) The MRR of SiC in UAECMP is proportional to the amplitude of ultrasonic vibration, whereas the surface roughness obtained by UAECMP was increased with the increase in vibration amplitude.

(7) To realize the benefits of UAECMP while mitigating its disadvantages, a novel polishing process was proposed for SiC wafers that starts with UAECMP and finishes with ECMP.

Slurryless UAECMP is proposed, developed, and applied to SiC wafers. The anodic oxidation mechanism of SiC is clarified and, moreover, the effects of the dominant factors, which include temperature, doping level, damage, and strain, on anodic oxidation of the 4H-SiC (0001) surface is investigated. These results promote the understanding of the anodic oxidation process of SiC

as well as the mechanism of ultrasonic vibration in SiC anodic oxidation. Rapid anodic oxidation of the SiC surface was realized using ultrasonic vibration assisted anodic oxidation and an extremely high MRR, 4.5 times that of conventional ECMP, was realized using the proposed method. Moreover, a very promising processing method, which combines slurryless UAECMP with ECMP for the manufacture of SiC wafers, is proposed.

Owing to its extremely high efficiency, slurryless UAECMP is very promising as a replacement for the complex processing steps currently implemented in the SiC wafer manufacturing process. These processing steps include grinding, lapping, and rough mechanical polishing. The proposed method allows for the SiC wafer to be processed by only one UAECMP machine, only one ceria grinding stone, and only one wafer clamping process, which will greatly reduce the cost and manpower needed for SiC wafer manufacturing and promote SiC applications. This work marks the beginning of the study of UAECMP for difficult-to-machine materials and the results obtained in this study are expected to promote the research and application of UAECMP to create a low-energy and environmentally friendly green society.

# Acknowledgements

As I wrote the last paragraph of my thesis, the three years of my Ph.D. program gradually came to an end. From my interest in Professor Kazuya Yamamura's article from the other end of the internet three years ago to becoming his student and accepting his careful education and training, to now, when I am about to graduate and leave my Professor's arms. Time flies and the day I first arrived at the Yamamura laboratory seemed like yesterday. How lucky that I could have this magical encounter and such a wonderful journey with laughter and tears. I think the education and knowledge I have obtained here will be some of the most precious wealth obtained in my life.

The most important person I want to thank is my supervisor Professor Kazuya Yamamura, who gave me a taste of the demeanor of Japanese scientists, his wisdom, profound knowledge, and rigorous attitude towards scientific research, which will be worth learning all my life. He always encouraged me to face difficulties and bravely challenge common sense. He guided me to think and patiently explained information when I was confused, giving me constructive suggestions when I really did not know what to do. He also enthusiastically encouraged me when he saw any progress I made. He gave me many chances to participate in conferences at various locations, allowing me to see the bigger world and communicate and learn from many fellow experts. He gave his opinions on every article I wrote and always revised them verbatim… Professor Yamamura has given me so much cultivation and education that I cannot list it all here. He taught me how to become a real scientific researcher and how to face scientific research problems. I am also very grateful to Associate Professor Kenta Arima, who has given me a lot of advice and help over the past three years. He not only always put forward constructive comments about my research projects, but also extended a helping hand when there were any problems with test equipment. I also want to thank Assistant Professor Kentaro Kawai, who always cared about my research progress and generously lent or gave me many experimental consumables. Also, I would like to sincerely thank Ms. Yukari Ogawa, the secretary of our lab, for her patient and kind support and for giving me courage in my daily life.

Thanks very much to Xu Yang, the Specially Appointed Assistant Professor. He is a very earnest, smart, and tough person. In my heart, he is a teacher, an elder brother, and a role model for my life. I am very lucky to be able to work, study, and spend this precious time with such an outstanding person. During my Ph.D. period, he gave me a lot of selfless help and care, taught me how to use various experimental and testing equipment, discussed experimental plans, and provided constructive advice for my research. Thanks to my junior, Haiyang Gu, who just arrived

in the laboratory and actively took on many research tasks of our group and provided assistance towards my graduation.

This research was partially supported JST A-STEP Grant Number JPMJTR20RT, Japan, as well as the Japan Society for the Promotion of Science (JSPS) KAKENHI Grant Number JP20J10524, a research grant from the Machine Tool Engineering Foundation, and a research grant from the Mazak Foundation. We thank MIZUHO Co., Ltd. for providing the vitrified-bonded grinding stone and SONOTEC Co., Ltd. for providing the ultrasonic vibration device.

Finally, I thank my parents, who poured the credo of constantly striving for strength into my soul and always told me that every challenge is a gift from life and that those who bravely face challenges become stronger. All of this has made me never shrink or be weak in any predicament and to be brave to meet challenges. Thanks to their efforts to give me a better educational environment, which provides more opportunities for life choices and allows me the ability devote myself to study and research, without distractions. They gave me an outstanding model of being parents, like spiritual guides, and also a cornerstone to support the growth of a new generation of the family.